Chiroptical Switching in Molecular and Extended Framework Systems

Lyndon Alan Hall

A thesis submitted in fulfilment of the requirements for the degree of Doctor of Philosophy

School of Chemistry

The University of Sydney

February 2025

Statement of Originality

I declare that the content of this thesis is the product of my own, original work. This work has not been submitted in any other form for another dissertation or diploma at any other institution.

Lyndon Hall

February 2025

Abstract

Stimuli-responsive materials are those whose properties can be controllably and reversibly altered through the application of external stimuli. Chiroptical switches are stimuli-responsive chiral materials and are of great interest due to their potential use in technological applications such as optical displays, optoelectronic devices, and chiral sensing. This thesis describes research into the design, synthesis, and characterisation of novel chiroptical switches in both molecular and extended framework systems.

Chapter 3 presents the synthesis of a novel pair of enantiomers (*S*)-1,1′-binaphthalene-2,2′-bis(1,8-naphthalimide) and (*R*)-1,1′-binaphthalene-2,2′-bis(1,8-naphthalimide), (*S*)-BNI and (*R*)-BNI, which combine the axially chiral 1,1′-binaphthalene scaffold and redox-active 1,8-naphthalimide functional groups. The chiroptical and electronic behaviours of (*S*)-BNI and (*R*)-BNI are thoroughly investigated through a combination of UV-vis, CD, and EPR spectroelectrochemistry (SEC) techniques. They are thus shown to be high-performance redox-modulated chiroptical switches exhibiting excellent sensitivity and good reversibility to repeated reduction and oxidation cycles.

In Chapter 4, a pair of ferrocene amino acid bioconjugates, L-Fc(MeLeu)$_2$ and D-Fc(MeLeu)$_2$, are synthesised from 1,1′-ferrocenedicarboxylic acid and methyl ester-protected L/D-leucine. In these molecules, chirality arises from intramolecular hydrogen bonding between leucine residues, which forces the molecule into an axially chiral conformation. The chiroptical response of L-Fc(MeLeu)$_2$ and D-Fc(MeLeu)$_2$ were found to be solvent dependent, with more intense chiroptical signals observed in nonpolar solvents. Owing to the lability of the hydrogen bonds, L-Fc(MeLeu)$_2$ and D-Fc(MeLeu)$_2$ displayed temperature-modulated chiroptical switching, with a linear increase in CD intensity as the temperature was decreased. Additionally, redox-modulated chiroptical switching was demonstrated through successive oxidation and reduction of the ferrocene core, making L-Fc(MeLeu)$_2$ and D-Fc(MeLeu)$_2$ valuable examples of dual-responsive chiroptical switching. The effects of concentration on reversibility and potential decomposition are discussed.

Chapter 5 details the synthesis of an isostructural series of lanthanide MOFs, $[Ln_2(CBA)_2(H_2O)_4]\cdot 4H_2O$ (Ln = La, Ce, Pr, Nd) using the chiral ligand (4-carboxybenzoyl)-L-aspartic acid (H_3CBA). These MOFs were found to be achiral due to racemisation of H_3CBA during solvothermal synthesis. Attempts to prevent racemisation and the potential causes of

racemisation are discussed. An alternate approach to synthesising chiral MOFs was then undertaken with a different chiral ligand, *N*-(4-carboxyphenyl)-L-alanine (H_2CPA), which was intended to be more resistant to racemisation. The reaction of H_2CPA with $Cd(NO_3)_2 \cdot 4H_2O$ successfully yielded a chiral MOF.

This thesis highlights the complex interplay between chirality, spectroscopy, and stimuli-responsive materials and demonstrates the valuable information that can be gained through rigorous investigation of these systems. Thus, this work represents an important contribution to the broader understanding of chiroptical switching and offers key insights into promising areas of future exploration.

Acknowledgements

A PhD is no small undertaking and along the way I have been fortunate enough to have had the support of many wonderful and amazing people.

First and foremost, I extend my sincerest gratitude to my two supervisors, Professor Girish Lakhwani and Professor Deanna D'Alessandro. Throughout all the ups and downs your steadfast support, encouragement, and mentorship has been invaluable. Thank you for believing in me and inspiring me to be a better chemist.

I have also had the pleasure to be part of two fantastic research groups. To the Molecular Materials and Molecular Photophysics groups, thanks for being such a friendly, fun and welcoming group of people. Working in an environment with so many great people made the PhD that much more enjoyable, and I'll cherish all the friendships I've made. Special thanks to Dr Hunter Windsor for your help with all things crystallography. To Sam Wenger for your keen insight into various electrochemical problems. To Katelyn Clutterbuck, for sharing the chiroptics journey with me, you understood the ups and downs better than anyone (and also make a great MOF slice!). To Dr Alison Goldingay, your positive attitude and generous spirit were always a bright spot in my day. To Dr Alexandra Stuart and Dr Inseong Cho, thanks for all the spectroscopy advice, your guidance and help troubleshooting was vital in so many ways. To Dr Marcello Solomon for providing feedback on parts of this thesis.

I would also like to acknowledge the technical staff who have assisted me at various points throughout the last four years. Thanks to Dr William Lewis, Dr Samuel Duyker, and Dr Paul Fitzgerald from the Sydney Analytical X-Ray facilities. Thanks to Dr Nicholas Proschogo from the School of Chemistry Mass Spectrometry facility. Thanks to Dr Ian Luck, Dr Paige Hawkins, and Dr Biswaranjan Mohanty from the Sydney Analytical Magnetic Resonance facility. Thanks also to Dr Bun Chan for performing the Density Functional Theory calculations for this project.

I am also grateful to the Australian Government for supporting my research through a Research Training Program (RTP) Fee Offset and RTP Scholarship.

I also owe a huge thank you to my family, Mum, Dad, and Fraser for your unwavering support and for always believing in me. To all my wonderful friends, thank you for the many good times, laughs, and games nights which always kept my spirits high. Finally, to my amazing partner Lauren, thank you for your incredible love, kindness, and patience throughout my PhD journey.

Statement of Contribution

I declare that all written and experimental work presented in this thesis was carried out by myself except where specified below:

SCXRD data collection and refinement were performed with assistance from Dr Hunter Windsor.

Dr Bun Chan from Nagasaki University performed Density Functional Theory (DFT) calculations.

APCI-MS was performed by staff at The University of Sydney, School of Chemistry Mass Spectrometry facility.

Authorship Attribution

Chapter 1 contains material from the following publication:

Hall, L. A.; D'Alessandro, D. M.; Lakhwani, G. Chiral metal–organic frameworks for photonics. *Chem. Soc. Rev.* **2023**, *52*, 3567-3590.

I wrote the manuscript and created the figures. Dr Girish Lakhwani and Dr Deanna D'Alessandro conceived and supervised the research project. All authors revised and edited the manuscript.

Chapter 3 contains material from the following publication:

Hall, L. A.; Windsor, H. J.; Chan, B.; D'Alessandro, D. M.; Lakhwani, G. Chiroptical Switching in an Enantiomeric Pair of Binaphthylenes Based on Redox-Active 1,8-Naphthalimide Substituents. *J. Phys. Chem. Lett.* **2025**, *16*, 1529-1534.

I designed the study, performed the experiments, analysed the data, wrote the manuscript, and created the figures. Dr Hunter Windsor assisted with SCXRD data collection and refinement. Dr Bun Chan performed the DFT calculations. Dr Girish Lakhwani and Dr Deanna D'Alessandro conceived and supervised the research project. All authors revised and edited the manuscript.

Lyndon Hall

February 2025

As supervisor for the candidature upon which this thesis is based, I can confirm that the authorship attribution and statements of contribution above are correct.

Girish Lakhwani

February 2025

List of Publications and Conference Presentations

Publications From Parts of This Thesis

Hall, L. A.; D'Alessandro, D. M.; Lakhwani, G. Chiral metal–organic frameworks for photonics. *Chem. Soc. Rev.* **2023**, *52*, 3567-3590.

Hall, L. A.; Windsor, H. J.; Chan, B.; D'Alessandro, D. M.; Lakhwani, G. Chiroptical Switching in an Enantiomeric Pair of Binaphthylenes Based on Redox-Active 1,8-Naphthalimide Substituents. *J. Phys. Chem. Lett.* **2025**, *16*, 1529-1534.

Other Publications

Suzuki, H.; Wada, Y.; Usov, P. M.; Zhu, Y.; Chan, B.; **Hall, L. A.**; D'Alessandro, D. M.; Kajiwara, A.; Haga, M.-a.; Kawano, M. Electrochemical proton-coupled electron transfer processes to form neutral radicals of azaphenalenes: pKa values of protonated radicals. *Electrochim. Acta* **2024**, *473*, 143441.

Wenger, S. R.; **Hall, L. A.**; D'Alessandro, D. M. Mechanochemical Impregnation of a Redox-Active Guest into a Metal–Organic Framework for Electrochemical Capture of CO2. *ACS Sustainable Chem. Eng.* **2023**, *11*, 8442-8449

Oanta, A. K.; Collins, K. A.; Evans, A. M.; Pratik, S. M.; **Hall, L. A.**; Strauss, M. J.; Marder, S. R.; D'Alessandro, D. M.; Rajh, T.; Freedman, D. E.; et al. Electronic Spin Qubit Candidates Arrayed within Layered Two-Dimensional Polymers. *J. Am. Chem. Soc.* **2023**, *145*, 689-696

Rashid, R. B.; Evans, A. M.; **Hall, L. A.**; Dasari, R. R.; Roesner, E. K.; Marder, S. R.; D'Allesandro, D. M.; Dichtel, W. R.; Rivnay, J. A Semiconducting Two-Dimensional Polymer as an Organic Electrochemical Transistor Active Layer. *Adv. Mater.* **2022**, *34*, 2110703

Conference Presentations

"*Investigations of a binaphthylene-based redox-active chiroptical switch*", oral presentation at the Royal Australian Chemical Institute 1st NSW Electrochemistry Symposium, Sydney, New South Wales, Australia, July 2024.

"*Investigating Chiral Organic Compounds for Chiroptical Switching*", oral presentation at the 12th Asian Photochemistry Conference (APC), Melbourne, Victoria, Australia, November 2023.

"*Chiral Metal–Organic Frameworks for Nonlinear Optics*", poster presentation at the Australian Research Council Centre of Excellence in Exciton Science annual workshop, Lorne, Victoria, Australia, November 2022.

Table of Contents

List of Figures

List of Tables

List of Abbreviations

AcCl	Acetyl Chloride
AIE	Aggregation-Induced Emission
APCI	Atmospheric Pressure Chemical Ionisation
ATR	Attenuated Total Reflection
BINAM	1,1′-binaphthyl-2,2′-diamine
BINOL	1,1′-binaphthyl-2,2′-diol
BNI	1,1′-binaphthalene-2,2′-bis(1,8-naphthalimide)
CD	Circular Dichroism
$CDCl_3$	Deuterated Chloroform
$(CD_3)_2SO$	Deuterated dimethylsulfoxide
CP	Coordination Polymer
CPL	Circularly Polarised Luminescence
CV	Cyclic Voltammetry
DCM	Dichloromethane
DEF	*N*,*N*-Diethylformamide
DFT	Density Functional Theory
DMF	*N*,*N*-Dimethylformamide
D_2O	Deuterated Water
EPR	Electron Paramagnetic Resonance
ESI	Electrospray Ionisation
EtOH	Ethanol
Et_3N	Triethylamine
Fc	Ferrocene

Fc^+	Ferrocenium ion
FTIR	Fourier-transform Infrared
HATU	1-[bis(dimethylamino)methylene]-1H-1,2,3-triazolo[4,5-b]pyridinium 3-oxide hexafluorophosphate
H_3CBA	(4-carboxybenzoyl)-L-aspartic acid
H_2CBV	(4-carboxybenzoyl)-L-valine
H_3CCA	(E)-((4-carboxy)cinnamoyl)-L-aspartic acid
H_2CPA	*N*-(4-carboxyphenyl)-L-alanine
H_2TDV	Thiophene-2,5-dicarbonyl-bis(L-valine)
ISC	Intersystem Crossing
ITO	Indium Tin Oxide
LED	Light-Emitting Diode
LMCT	Ligand-to-Metal Charge-transfer
MCD	Magnetic Circular Dichroism
MeCN	Acetonitrile
MeOH	Methanol
Me_3CBA	Dimethyl (4-(methoxycarbonyl)benzoyl)-L-aspartate
Me_2CBV	Methyl (4-(methoxycarbonyl)benzoyl)-L-valinate
Me_3CCA	Dimethyl trans-((4-methoxycarbonyl)cinnamoyl)-L-aspartate
Me_2TDV	Dimethyl thiophene-2,5-dicarbonyl-bis(L-valinate)
MOF	Metal–Organic Framework
MS	Mass Spectrometry
NDI	Naphthalene Diimide
NIR	Near Infrared
NMR	Nuclear Magnetic Resonance

NLO	Nonlinear Optics
PDI	Perylene Diimide
PET	Photo-Induced Electron Transfer
PhNI	*N*-phenyl-1,8-naphthalimide
PLQY	Photoluminescent Quantum Yield
PSM	Post-Synthetic Modification
PXRD	Powder X-Ray Diffraction
ROA	Raman Optical Activity
Salox	2-Hydroxybenzaldehyde oxime
SCXRD	Single-Crystal X-Ray Diffraction
SEC	Spectroelectrochemistry
SFG	Sum-Frequency Generation
SHG	Second-Harmonic Generation
SWV	Squarewave voltammetry
TGA	Thermogravimetric Analysis
THF	Tetrahydrofuran
TLC	Thin Layer Chromatography
TTF	Tetrathiafulvalene
UV	Ultraviolet
VCD	Vibrational Circular Dichroism
vis	Visible
VT	Variable Temperature
3 Å MS	3 Å Molecular Sieves

Chapter 1

Introduction

1.1 Stimuli-Responsive Molecules and Materials

Stimuli-responsive molecules and materials are those whose physical, chemical, or optical properties can be altered in response to external stimuli.[1, 2] A range of stimuli can be used including (but not limited to) light, temperature, pH, electric or magnetic field, pressure, host-guest interactions, mechanical force, or solvent. The underlying mechanism by which the applied stimuli change a material's properties include redox processes, isomerisation, conformational changes, host-guest binding, and magnetic ordering, among others. Of particular interest are stimuli-responsive materials which can be controllably, and reversibly, converted back to their original state. This switching behaviour provides additional functionality, allowing switchable molecules and materials to be tailored for specific purposes. The targeted design of switchable, stimuli-responsive materials has thus led to their use in a broad range of areas spanning biomedical,[3] technological,[4, 5] and environmental fields.[6]

Devices whose primary focus is on reversibly altering the optical properties of a molecule or material are known as optical switches. The optical readout – usually absorbance or fluorescence – is typically monitored *in-situ* to provide real-time information on the state of the switch and the progress of the switching process. Optical switches have undoubtedly had a huge impact on our society and have found uses in a variety of applications ranging from fluorescent sensors for the detection of heavy metals,[7] to switchable smart windows which can modulate the transmittance of solar irradiation.[8, 9] These diverse applications underscore the immense functionality of optical switches and highlight the value in designing stimuli-responsive materials for emerging technologies.

Some parts of this chapter appear in the following publication: **Hall, L. A.**; D'Alessandro, D. M.; Lakhwani, G. Chiral metal–organic frameworks for photonics. *Chem. Soc. Rev.* **2023**, *52*, 3567-3590

1.2 Chiroptical Switching

Similar to optical switches, chiroptical switches are molecules or materials which can be controllably and reversibly converted between two (or more) states which have different chiroptical signals.[10-13] In chiroptical switches, the two (or more) states can be distinguished by either a change in the intensity of the chiroptical signal, inversion of signal (opposite handedness), shifts in peak position, or a combination of these (Figure 1.1).[13] By far the most common chiroptical readout is circular dichroism (CD), however the prevalence of circularly polarised luminescence (CPL) based switches has grown in recent years. The design and characterisation of chiroptical switches has attracted a lot of research attention due to their promise for use in applications such as optoelectronic devices, optical displays, and chiral sensing.[11]

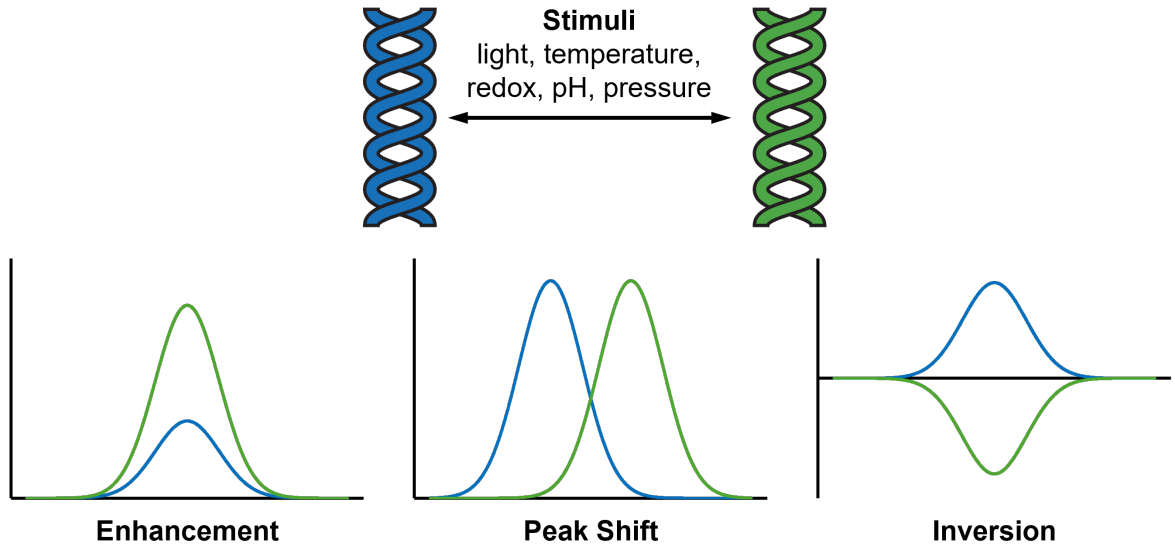

Figure 1.1. Principles of chiroptical switching: application of stimuli leads to an enhancement, peak shift, or inversion of the chiroptical response.

Chiroptical switches have some advantages over purely optical switches, which justifies efforts to make them despite their additional complexity. Firstly, achiral readouts like UV-vis only display positive values and therefore the greatest sensitivity possible in optical switches is an ON/OFF switch. In contrast, chiroptical readouts like CD can be positively or negatively signed, affording comparably better resolution when the switch involves a change in handedness. Additionally, chiroptical readouts can be complemented with a related, achiral readout. For example, when measuring CD, the absorbance of the sample is necessarily obtained as well. Since the CD and absorbance of the switch will be different, there could be spectral regions where one performs better than the other. Such complementarity is not possible

in achiral switches. Finally, chiroptical switches may show greater tolerance to impurities, as only chiral impurities will be able to produce an interfering signal. Beyond these advantages, there are specific applications, such as chiral sensing, which necessitate the use of a chiroptical switch.

In order to properly understand the design, operation, and performance of chiroptical switches, it is first necessary to understand three fundamental concepts: the origins of chirality in physical media, chirality in electromagnetic radiation, and chiral light-matter interactions, i.e., chiroptical techniques.

1.3 Chirality in Matter and Light

An object is said to be chiral if it cannot be superposed onto its mirror image; that is, there is no combination of rotations or translations that would allow a chiral object to be brought into perfect coincidence with its mirror image.[14-16] To fulfill this criteria, a chiral object must not possess either a mirror place, centre of inversion, or an improper axis of rotation.[15] Together, a chiral object and its mirror image partner are referred to as enantiomers.[15] Perhaps the most recognisable example of a chiral object is the human hand, with the right and left hands comprising a pair of enantiomers. Indeed, the word chiral is derived from the Ancient Greek word, χείρ (*cheir*), which means hand. A defining characteristic of enantiomers is that they have the same properties when interacting with achiral media and it is only when interacting with other chiral entities that enantiomers can be distinguished.[16] A mixture containing equal amounts of each enantiomer is called a racemic mixture or racemate.

Chirality plays an essential role in nature and is ubiquitous in all forms of life. Many biological systems are homochiral and exist exclusively in one enantiomeric form; L-amino acids in proteins and 2-deoxy-D-ribose in DNA being prominent examples.[17] This homochirality ensures that enantiospecific interactions between chiral molecules and enzymes form the basis of many biological processes, with wide-ranging implications for biochemistry, medicine, and pharmacology. For example, many drugs designed to target chiral receptors or enzymes are also chiral themselves. Often only one enantiomer can perform the required function while the other enantiomer may be inactive or, in some cases, cause unwanted side-effects.[18]

Light can also be chiral if it is circularly or elliptically polarised. Circularly polarised light is light whose electromagnetic field has a constant magnitude but whose polarisation is rotating in the plane perpendicular to the direction of the wave's propagation.[19] The chirality is due to

the screw pattern traced out by the light as it propagates (Figure 1.2). Circularly polarised light is termed right- or left-handed depending on whether the rotation is clockwise or anticlockwise, respectively. Elliptically polarised light is similarly chiral, however in this case, the magnitude of the electromagnetic field varies during the course of the rotation of polarisation. Chiral media interact differently with right and left circularly (or elliptically) polarised light, generating a chiroptical response.[20] Additionally, the chiroptical response of one enantiomer is equal in magnitude but opposite in sign to the chiroptical response of the other enantiomer.[14] Together, these properties form the basis for many interesting and useful chiroptical phenomena.

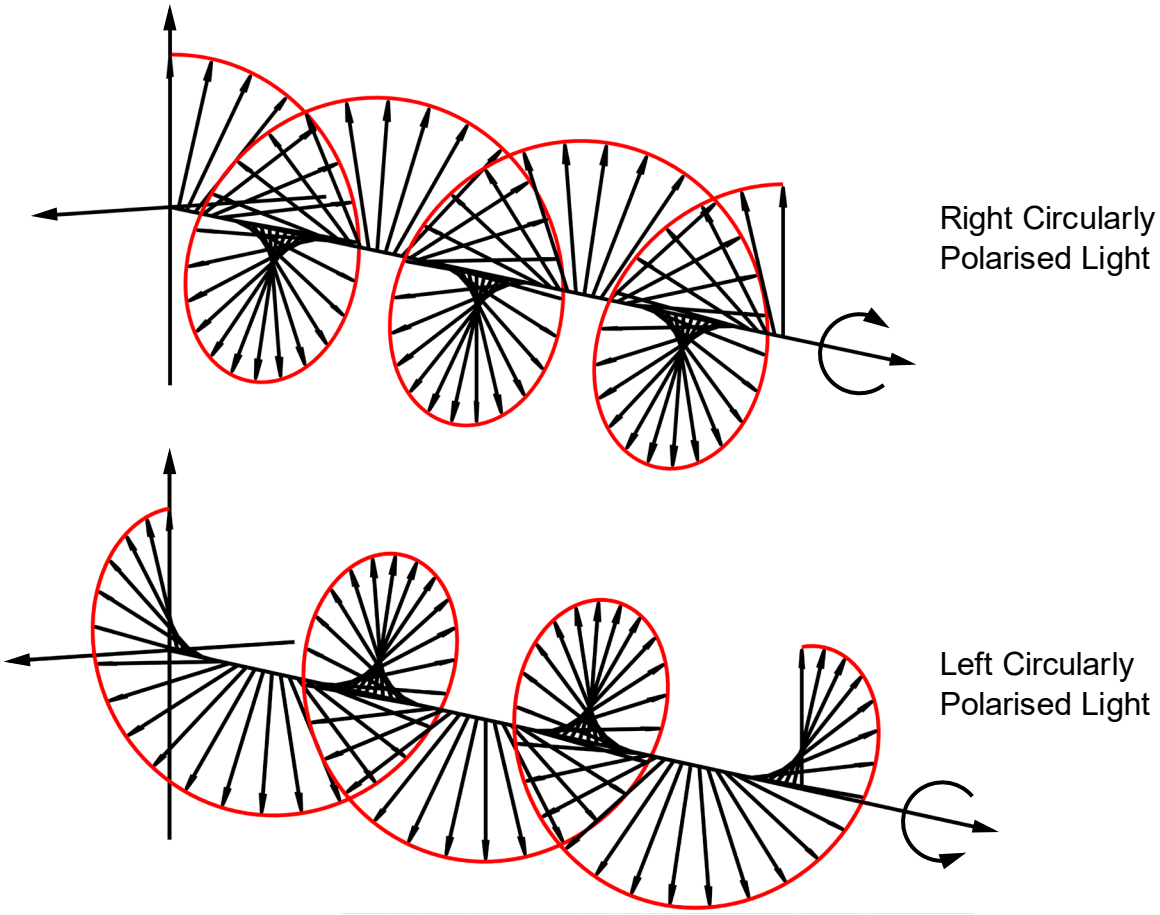

Figure 1.2. Schematic of right and left circularly polarised light. The black arrows represent the vectors describing the electric field of the light. The red line indicates how the ends of these vectors trace out a helical path as the light propagates.

1.4 Chirality at the Molecular Scale

There are several ways in which chirality arises at the molecular scale (Figure 1.3).[15, 21] The most common is point chirality from stereocentres. In organic molecules a stereocentre is a sp^3

hybridised atom – usually, but not always, carbon – bearing four different substituents. It is not uncommon that a molecule may bear two or more stereocentres. In such cases two conformations are only enantiomers if they have the opposite handedness at all stereocentres; otherwise they are diastereomers. In coordination complexes, metal-based stereocentres may have more than four substituents. Another form of molecular chirality is axial chirality (also called atropisomerism) which arises when two pairs of substituents have a non-planar arrangement around an axis of chirality. Axial chirality is typically characterised by hindered rotation around a covalent bond through which the axis of chirality runs through. The barrier to rotation may arise from rigid double bonds such as in allenes, or from steric strain such as in ortho-substituted biphenyls. Helical chirality describes the chirality arising from any propellor or screw-shaped molecule. Helicenes are a common example, as are octahedral metal complexes with three bidentate ligands which form chiral, propellor-like arrangements. The final manifestation of chirality at the molecular scale is planar chirality, which describes chirality resulting from the arrangement of two dissimilar out-of-plane groups with respect to a plane, termed the chirality plane. Many cyclophanes exhibit planar chirality, as do certain metallocenes. In all cases, a molecule is only said to be chiral if its chiral conformation is persistent; chiral conformations that readily interconvert to other forms are not considered chiral.

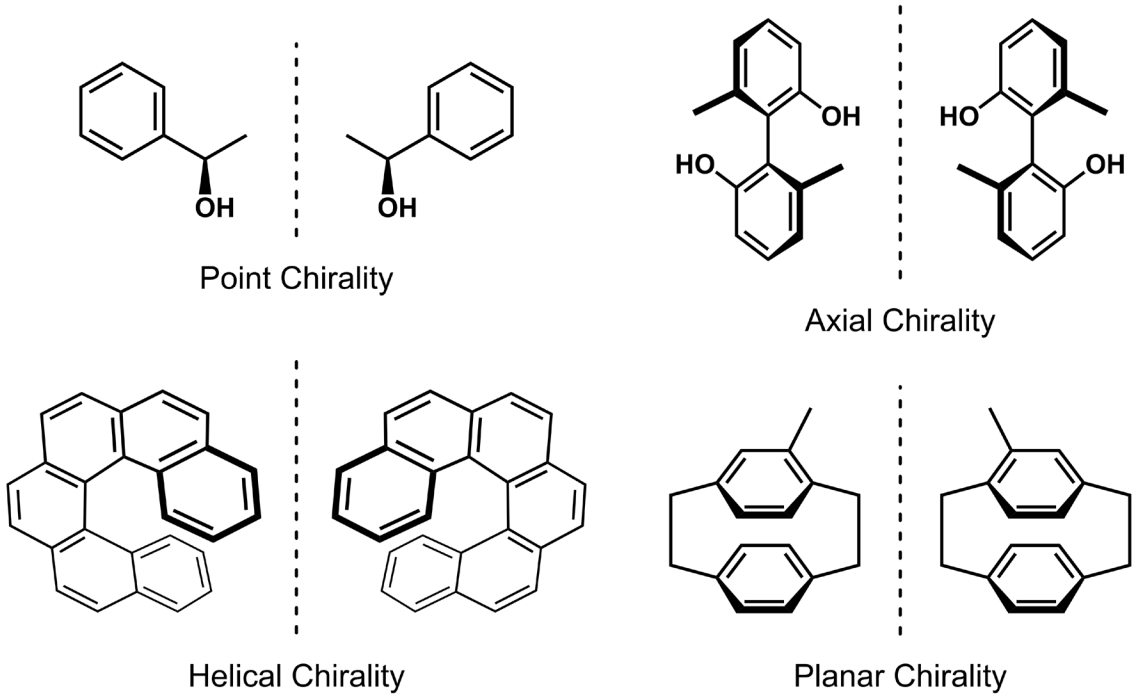

Figure 1.3. Enantiomeric pairs representing different types of chirality at the molecular scale: point, axial, helical, and planar chirality.

1.5 Chirality in Extended Systems

Chirality can also emerge at larger scales. In the solid state, molecules which crystallise into any one of the 65 Sohncke space groups will inevitably form a chiral crystal structure.[22-24] In this case the chirality arises from a chiral arrangement of the molecules in space. Enantiopure chiral molecules will always crystallise in a Sohncke space group. Achiral molecules may crystallise in a Sohncke space group; however, this is not always the case and is difficult to control or predict. Likewise, racemates can crystallise as both chiral and achiral crystals, with the added possibility of attaining a conglomerate containing enantiopure crystals of each enantiomer.[24] In chiral crystals of extended inorganic materials, the chirality typically manifests as helical chains running through the structure. Non-crystalline materials such as polymers and supramolecular assemblies can also exhibit large-scale chirality.[25-27] In these systems the chirality is often due to chiral monomers or chiral inducing agents enforcing a helical twisting of a polymeric or supramolecular strand. Another class of chiral extended materials are Metal–Organic Frameworks (MOFs). Due to their unique advantages (outlined below), further discussion of extended systems will focus on chiral MOFs.

1.5.1 Chiral Metal–Organic Frameworks (MOFs)

Metal–Organic Frameworks (MOFs) are a class of materials which have enormous potential for chiroptical applications. MOFs are constructed through the coordination of metal nodes with multidentate organic ligands, forming repeating coordination entities in one–, two–, or three–dimensions.[28] Additionally, MOFs are defined as having potential voids to distinguish them from coordination polymers (which are analogous to MOFs but lack porosity).[28] The primary appeal of MOFs derives from the essentially unlimited number of possible metal and ligand combinations, the careful selection of which can yield a framework with the desired physical and chemical properties. In many cases, the key characteristics of a given MOF arise specifically due to a synergistic interaction between the constituent components which is only possible in the specific topological confinement of the framework. Therefore, MOFs provide a platform to create and study chemical and optical processes which are inaccessible in conventional purely organic or inorganic media.

Chiral MOFs are those frameworks possessing chiral ligands, chiral guests, or larger-scale chiral topologies such as helical chains. There are four strategies through which chiral MOFs can be synthesised: direct synthesis using enantiopure chiral ligands, spontaneous resolution, post-synthetic modification (PSM), and chiral induction (Figure 1.4).

The most straightforward approach to synthesising homochiral MOFs is to use enantiopure chiral ligands. Since enantioselective syntheses and purifications are often difficult and time-consuming, a common approach is to create a ligand incorporating a commercially-available, enantiopure precursor. While this sacrifices some flexibility in ligand design, the reduced synthetic burden makes this an appealing strategy. A common source of chiral precursors are the so-called 'chiral pool' molecules: naturally occurring molecules containing stereocentres such as amino acids, sugars, tartaric acid, and lactic acid, among others. Chiral pool molecules have been used directly as ligands themselves,[29, 30] as well as functionalised to make larger chiral ligands.[31-33] Derivatives of sterically hindered 1,1′-binaphthalenes with axial chirality have also been used to make chiral MOFs.[34]

In some cases, achiral components spontaneously crystallise in a Sohncke space group through the formation of chiral structures such as helices. The principal benefit of this approach is that it avoids the challenging synthesis of chiral ligands. Spontaneous resolution is highly unpredictable, not guaranteed to work and, in most cases, results in a racemic mixture of individually enantiopure crystals.[35] However, there have been some cases where spontaneous resolution has resulted in an excess of a particular enantiomer.[36]

Chiral MOFs can also be derived through PSM of an achiral framework. For example, MOFs whose ligands contain uncoordinated functional groups such as amines, alcohols, or alkyl halides can undergo reaction with a chiral auxiliary.[37] This essentially generates a chiral ligand *in-situ*, resulting in a homochiral MOF. For frameworks containing unsaturated metal sites, coordination of a chiral guest also yields a chiral MOF.[38] Similarly, encapsulation of a chiral guest in the voids of the framework through noncovalent interactions such as hydrogen bonding and π-π stacking also afford a chiral MOF.[39] Overall, PSM is a versatile way of obtaining enantiopure, chiral MOFs provided the infiltrated chiral moiety is small enough to navigate the pores of the framework. Additionally, it should be noted that the proportion of ligand functionalisation and guest infiltration often fall below maximum theoretical loadings.

Finally, the assembly of achiral components into a chiral MOF can, in some cases, be induced by inclusion of a chiral agent in solution during synthesis. The chiral template is not incorporated into the MOF, but through its inherent asymmetry promotes the preferential formation of metal–ligand chains into right- or left-handed helices in the structure. The resulting batch will contain an enantiomeric excess of individually homochiral crystals.[40] The exact mechanism of chiral induction is poorly understood so multiple chiral templates are

usually trialled until a suitable one is found. Chiral induction is usually performed in solvothermal MOF syntheses, however there is some evidence that it is more effective in layer-by-layer syntheses.[41]

Having outlined the manifestations of chirality in both matter and light, the discussion will now turn to chiral light-matter interactions, which are crucial to the operation of chiroptical switches.

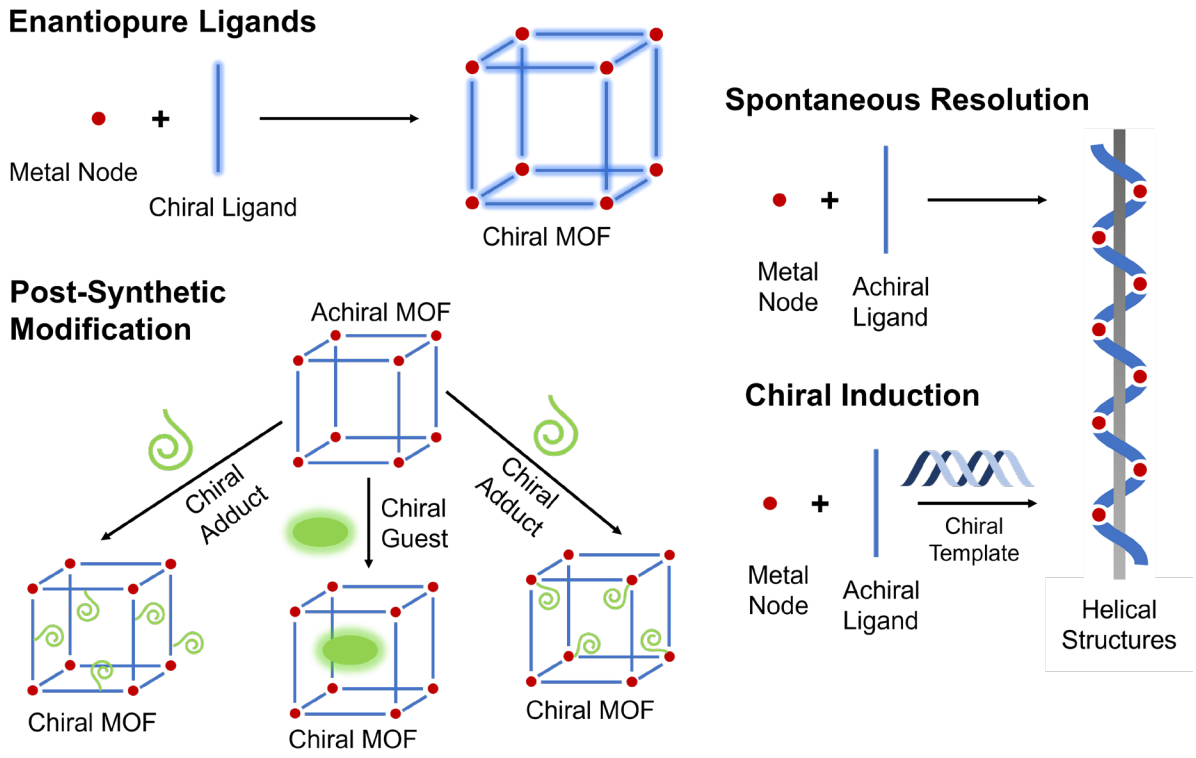

Figure 1.4. Synthesis strategies for chiral MOFs: using enantiopure ligands, spontaneous resolution, post-secondary modification, and chiral induction.

1.6 Chiral Light-Matter Interactions

1.6.1 Electronic Transitions

Before discussing chiral light-matter interactions, it is helpful to first describe the general principles of electronic transitions. When the energy of incident electromagnetic radiation matches the energy difference between two electronic states of a molecule or material, the light may be absorbed, promoting an electronic transition from the ground electronic state to an excited electronic state. Absorbance, A, is defined in relation to the incident, I_0, and transmitted, I, light:[42, 43]

$$A = \log_{10}\left(\frac{I_0}{I}\right) \tag{1.1}$$

Absorbance is related to the molar extinction coefficient, ε, by the Beer-Lambert law:[42, 43]

$$A = \varepsilon c l \tag{1.2}$$

where c is the molar concentration of the absorbing species in mol/L and l is the path length through the sample in cm. The molar extinction coefficient is a fundamental property of a molecule or material that is independent of concentration.

During an electronic transition there is an accompanying redistribution of electron density, reflecting the difference in electron density described by the wavefunctions of the ground and excited states. The electric field of the incident light causes a linear redistribution of charge, termed the electronic transition dipole moment, $\boldsymbol{\mu}$.[42, 43] Meanwhile, the magnetic field of the incident light causes a circular redistribution of charge, termed the magnetic transition dipole moment, $\mathbf{m}$.[42, 43] The overall strength of an electronic transition – whether absorption or emission – is described by the dipole strength D, as follows:[44]

$$D = |\boldsymbol{\mu}|^2 + |\boldsymbol{m}|^2 \tag{1.3}$$

According to the Franck-Condon principle, electronic transitions are essentially instantaneous compared to the timescale of nuclear motion.[45, 46] Therefore, when a photon is absorbed, the electron density rapidly shifts to the arrangement dictated by the excited state wavefunction, while the atoms in the molecule are still in the configuration of the ground state. During an electronic transition, the vibrational energy level, ν, may change as well, with the most probable vibronic transitions those with the greatest wavefunction overlap between the ground and excited state vibrational modes. Since the ground and excited states have different equilibrium nuclear coordinates, this often results in a transition to a higher vibrational level in the excited state. The excited state then rapidly relaxes to its lowest vibrational state before any other photophysical process occur.

There are several ways a molecule in an excited state can relax back to the ground state; here a Jablonski diagram will be used to conveniently represent these processes (Figure 1.5). A brief note on terminology: the ground and excited electronic states are referred to as S_0 and S_1, respectively, reflecting their status as singlet states; the first excited triplet state is called T_1. Nonradiative decay occurs through a process called internal conversion whereby the S_1 state transitions to a high vibrational mode of S_0, which immediately undergoes vibrational

relaxation to its lowest vibrational mode.[47] S_1 can also decay directly to S_0 by the emission of a photon, a process called fluorescence.[48] Finally, intersystem crossing (ISC) can occur between S_1 and the triplet state T_1.[48] ISC involves a change in spin multiplicity and is formally forbidden but weakly allowed due to spin-orbit coupling. The emissive decay of T_1 to S_0 is called phosphorescence and similarly requires a change in spin multiplicity, making it a formally spin-forbidden process.[48] Phosphorescence lifetimes are therefore much longer than fluorescence lifetimes. Additionally, because T_1 is usually lower in energy than S_1, phosphorescence typically occurs at longer wavelengths than fluorescence.[48] ISC from T_1 to S_0 can also occur, allowing for nonradiative deactivation. For both fluorescence and phosphorescence, emission will only occur from the lowest vibrational level of S_1 or T_1, consistent with the rapid relaxation of higher vibrational states. This is termed Kasha's rule.[49] A consequence of this is that the energy of an emitted photon is lower than the energy of the absorbed photon.[48] The energy difference between the maxima of absorbance and emission is termed the Stokes shift.

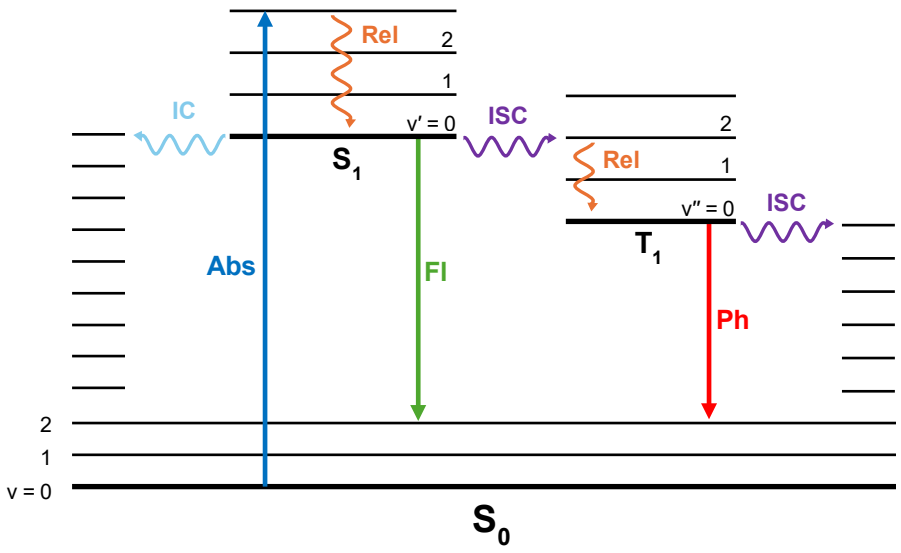

Figure 1.5. Jablonski diagram showing various photophysical phenomena: absorbance (Abs), fluorescence (Fl), phosphorescence (Ph), vibrational relaxation (Rel), internal conversion (IC), and intersystem crossing (ISC).

1.6.2 Chiroptical Techniques

Chiroptical techniques are the primary method by which to investigate the optical properties of chiral media. As such, they are essential tools for quantifying and assessing the performance of chiroptical switches. Therefore, the following sections will provide a thorough description

of the most relevant chiroptical techniques: circular dichroism, magnetic circular dichroism, circularly polarised luminescence, and magneto-chiral dichroism (Figure 1.6).

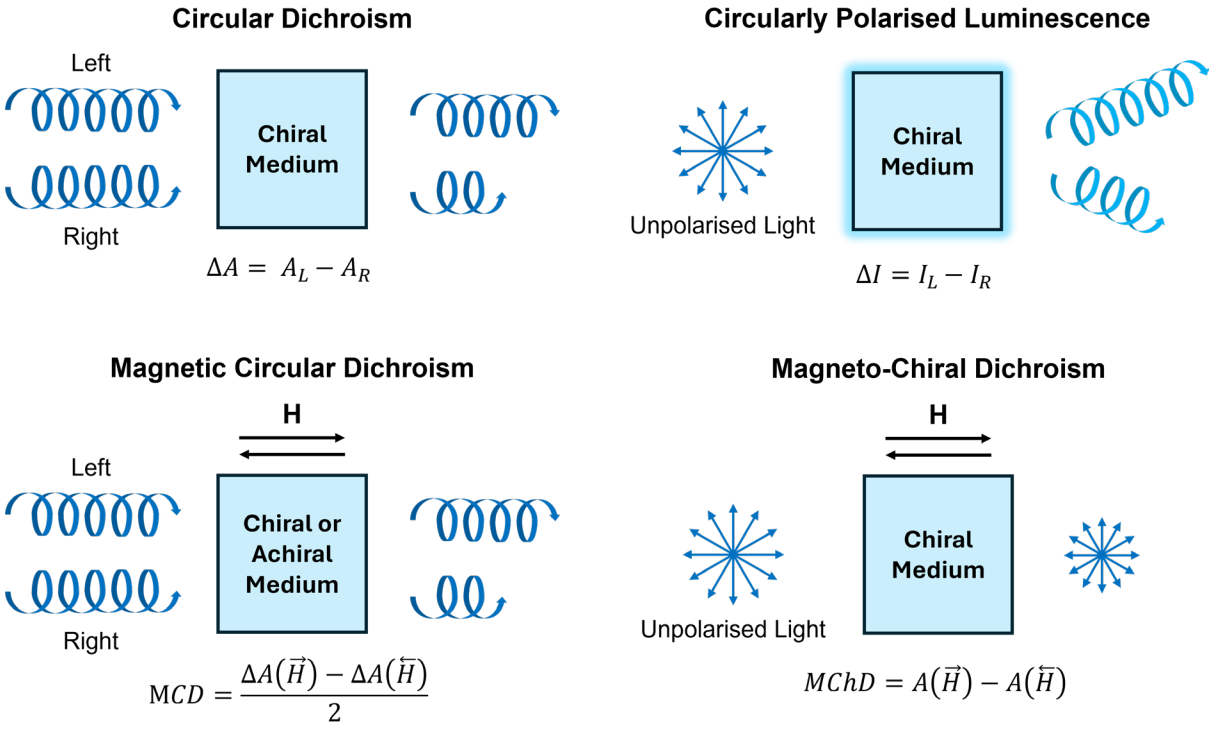

Figure 1.6. Schematic depiction of circular dichroism, magnetic circular dichroism, circularly polarised luminescence, and magneto-chiral dichroism.

1.6.3 Circular Dichroism (CD)

Circular dichroism is defined as the differential absorbance (ΔA) of left and right circularly polarised light:[42, 43]

$$\Delta A = A_L - A_R \tag{1.4}$$

where A_L and A_R are the absorbance when irradiated with left and right circularly polarised light, respectively. As outlined earlier, the rearrangement of electron density is linear for electric dipole allowed transitions and circular for magnetic dipole allowed transitions. If both **μ** and **m** are nonzero then the resulting shift in electron density can be described as a combination of linear and circular motion, tracing out a helical path. Because a helix is chiral, the interaction with left and right circularly polarised light will be different, resulting in the difference in absorbance that is CD.[42, 43] Therefore, in order to display CD, a molecule or material must possess electronic transitions in which both **μ** and **m** are nonzero. This requirement is only fulfilled in chiral systems, making CD a phenomenon exclusive to chiral systems.[42, 43] CD spectroscopy is performed by alternately shining left and right circularly

polarised light on the sample and measuring the difference. The peaks in a CD spectrum are referred to as Cotton effects or signals.

The differential absorbance of left and right circularly polarised light by chiral media results in elliptically polarised light since the amplitude of the left and right components are no longer the same.[50] To quantify the extent of this ellipticity, CD spectra are often reported in units of millidegrees (mdeg), which can be interconverted with ΔA using the following equation:[42, 43]

$$\theta\ (mdeg) = \Delta A \times 32982 \tag{1.5}$$

where the factor of 32982 results from the conversion of radians to millidegrees and from Eulerian to decadic CD. Since the magnitude of a CD signal depends on the concentration of the analyte, the absorbance dissymmetry factor, g_{abs}, is used as a metric of the inherent strength of the differential absorbance of a given transition:[50, 51]

$$g_{abs} = \frac{\Delta A}{A} = \frac{A_L - A_R}{(A_L + A_R)/2} \tag{1.6}$$

The value of g_{abs} ranges from 2 to −2 but is typically $<10^{-2}$ in molecular systems. If the CD is an intensive property of a molecule, g_{abs} will be independent of concentration.[52, 53] However, if large scale chiral aggregates form above a certain concentration, then g_{abs} will vary with concentration and can be considered an extensive property.[54]

The rotational strength (and sign) of a given transition is defined by the Rosenfeld expression as the product of the imaginary component of the scalar product of the electric and magnetic transition dipole moments:[42, 43, 55]

$$R = \mathrm{Im}(\boldsymbol{\mu} \cdot \boldsymbol{m}) \tag{1.7}$$

When the absorbing entities are randomly distributed, R can be expressed in terms of the magnitude and angle (θ) between **μ** and **m**:[42]

$$R = |\boldsymbol{\mu}||\boldsymbol{m}| \cos\theta \tag{1.8}$$

Therefore, if **μ** and **m** are perpendicular to one another the transition will display no CD even if the molecule itself is chiral. Considering both the rotational and dipole strengths of a transition, it can be shown the g_{abs} can also be expressed as:[44]

$$g_{abs} = 4\frac{|\boldsymbol{\mu}||\boldsymbol{m}| \cos\theta}{|\boldsymbol{\mu}|^2 + |\boldsymbol{m}|^2} = 4\frac{R}{D} \tag{1.9}$$

It is important to note that the assumption underpinning equations 1.8–1.9 of a randomly oriented distribution of the absorbing species may not hold in solid-state systems such as MOFs.

Most chiral molecules show relatively small g_{abs} (~10^{-3} or less is not uncommon) when randomly oriented in solution.[44, 50, 56] This has been attributed to the small size of chiral molecules compared to the wavelength of the incident light.[56, 57] Essentially, the circularly polarised light only undergoes a small twist on molecular length scales, meaning that individual molecules do not really 'feel' the helical pitch of the circularly polarised light.[56, 57] As a result, there is only a small difference in the absorption cross sections for left and right circularly polarised light, leading to small g_{abs}.

The strength of the chiroptical response can be increased through the excitonic coupling between the electronic transition dipoles ($\boldsymbol{\mu}_1$ and $\boldsymbol{\mu}_2$) of two chromophores arranged in a chiral orientation (Figure 1.7).[56] This results in the splitting of the degenerate energy levels into two states which give rise to transitions with rotational strengths of equal magnitude but opposite sign.[43, 55, 58] This is called exciton-coupled circular dichroism and is characterised by bisignate CD spectra with both positive and negative Cotton effects.[43, 55, 58] The two transitions have energy slightly above and below the equivalent transition of the isolated chromophore, leading to a null at the absorbance maximum.[55, 58] If the two chromophores form a clockwise (positive) screw sense when viewed down the axis joining them, the CD will be positive at longer wavelengths and negative at shorter wavelengths.[55] The situation is reversed when the chromophores form an anticlockwise (negative) screw sense. The intensity of exciton-coupled CD is proportional to the inverse square of the distance separating the chromophores, therefore a close arrangement is desirable for attaining a strong chiroptical response.[55, 56] The coupled chromophores do not have to be covalently linked, they can also be held together by noncovalent interactions.[56] In cases where more than two chromophores are situated in a chiral arrangement, such as in supramolecular chiral assemblies, the exciton coupling can occur between multiple chromophores.[56, 59, 60]

When an achiral molecule or chromophore is confined in a chiral environment – for example as a guest in a chiral host – it can exhibit CD.[50] This process is known as chirality transfer and the observed chiroptical response is called induced circular dichroism.[50] Induced CD can arise when the confinement leads to a structural change in the guest such that it adopts a chiral geometry that would otherwise rapidly interconvert with its enantiomeric conformation in

solution.[50] As well as structural effects, electronic coupling between the host and guest can also induce a CD response.[50]

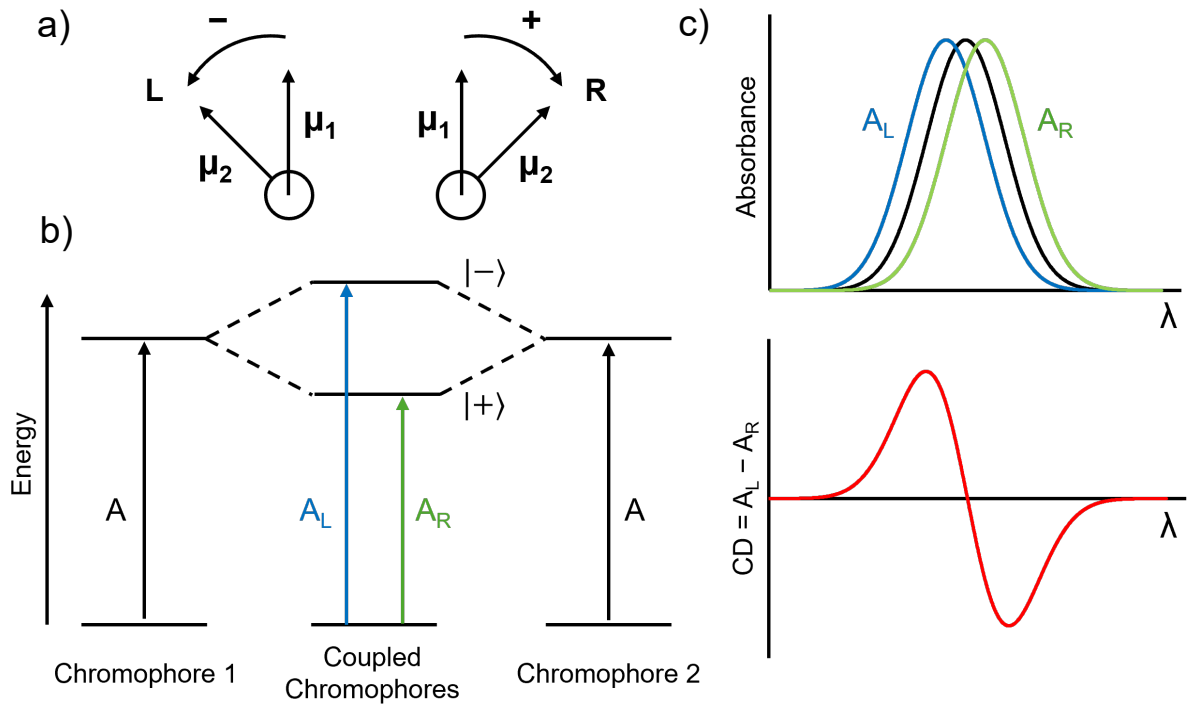

Figure 1.7. Schematic of exciton-coupled circular dichroism in degenerate chromophores. (a) Coupled dipoles arranged with anticlockwise (−) and clockwise (+) screw sense. (b) Energy diagram of exciton coupling of two chromophores showing the two transitions with opposite rotational strength. (c) Absorbance of left (blue) and right (green) circularly polarised light in coupled chromophores with an anticlockwise screw sense, as well as the absorbance of an isolated chromophores (black). The resulting CD (red) is shown below.

1.6.4 Magnetic Circular Dichroism (MCD)

Magnetic circular dichroism is the differential absorbance of left and right circularly polarised light in the presence of a magnetic field oriented parallel to the propagation of the incident light (termed Faraday geometry).[61, 62] MCD spectra acquired at opposite magnetic field orientations will have equal magnitude but opposite sign. In CD, the differential absorption occurs due to the intrinsic asymmetry of chiral analytes. In contrast, MCD arises due to the perturbation of the electronic states involved in an optical transition by the magnetic field. All molecules and materials experience this effect when situated in a magnetic field, therefore all compounds – even achiral ones – display MCD.[61] This means that the differential absorbance of chiral analytes in a magnetic field will be a combination of the CD and MCD components. To remove the CD contribution and obtain the pure MCD spectrum, the following equation is used:

$$MCD = \frac{\Delta A(\vec{H}) - \Delta A(\overleftarrow{H})}{2} \quad 1.10$$

where $\vec{H}$ and $\overleftarrow{H}$ signify measurements performed in the presence of parallel and antiparallel magnetic fields, respectively.

The MCD intensity is proportional to the concentration of the sample, as well as the strength of the magnetic field. Therefore, the MCD absorbance dissymmetry factor, g_{MCD}, is used to provide a measure of the inherent strength of the MCD response:[63]

$$g_{MCD} = \frac{MCD}{(A_L + A_R)/2} \cdot \frac{1}{H} \quad (1.11)$$

where H is the magnetic field strength in tesla.

There are several mechanisms through which MCD can arise, called the Faraday A, B, and C terms (Figure 1.8). Assuming the magnetic field does not change the shape of the bands (Rigid-Shift approximation), the MCD intensity can be described as follows:[61, 64]

$$\frac{\Delta A}{E} = \gamma \mu_B H \left[A_1 \left(\frac{-\partial f(E)}{\partial (E)} \right) + \left(B_0 + \frac{C_0}{k_B T} \right) f(E) \right] \quad (1.12)$$

where γ is a constant, μ_B is the Bohr magneton, H is the magnetic field, E is the energy coordinate in cm^{-1}, $f(E)$ is the line-shape function, k_B is the Boltzmann constant, T is the temperature, and A_1, B_0 and C_0 are parameters defining the MCD A, B, and C terms and whose subscripts denote the order of the spectral moment of their respective band shapes.

The MCD A term originates from Zeeman splitting of degenerate energy levels in the excited state.[42, 61, 64] Consider a doubly degenerate excited state, J, split into two states with magnetic quantum numbers, M_L, of +1 and −1, respectively. Absorbance of left or right circularly polarised light results in a transition with ΔM_L of +1 and −1, respectively, and the selection rule for an allowed transition is that $\Delta M_L = 0, \pm 1$. Therefore, the transition from a nondegenerate ground state A (which has $M_L = 0$) to the +1 state of J is only allowed for left circularly polarised light, while the transition to the −1 state is only allowed for right circularly polarised light. MCD A terms thus have derivative-like spectra with a crossover point corresponding to the absorbance maximum in the absence of a magnetic field. Whether the transition for left or right circularly polarised light is higher in energy depends on the sign of the A term and derives from the energetic ordering of degenerate excited states. By definition, a positive A term is negative on the long wavelength side of the crossing point and positive on

the short wavelength side of the crossing point; this is reversed for negative A terms.[64] In order to have degenerate excited states and thus have A term MCD contributions, a molecule must have three-fold or higher rotational symmetry.[42, 62, 63]

The MCD B term results from the electronic mixing of two non-degenerate energy levels, termed J and K.[42, 61, 64] MCD B terms have gaussian shape, can be either positive or negative, and occur at the peak of the corresponding absorbance bands. The magnitude of B term contributions are inversely proportional to the energy difference between the two mixing states. If the energy gap between the two mixing states is sufficiently small, two closely spaced and oppositely signed B terms can give rise to a derivative shaped pseudo-A term.[42, 64, 65] There are no symmetry requirements for MCD B terms so they are observed in all analytes.[66]

The MCD C term is caused by Zeeman splitting of degenerate ground state energy levels and is therefore only observed in paramagnetic samples.[42, 61, 64] If one considers a doubly degenerate ground state, A, split into two states with $M_L = +1$ and -1, then – analogous to MCD A terms – transitions from the $+1$ and -1 states to a nondegenerate excited state, J (which has $M_L = 0$), will only be allowed for right and left circularly polarised light, respectively. C terms are strongly influenced by the relative population of the nondegenerate ground states, which are determined by the Boltzman distribution. C terms are thus extremely temperature-dependent and their intensity is inversely proportional to k_BT. At low temperatures when only the lowest energy state is populated, MCD C terms have a gaussian shape, however they become more asymmetric at higher temperatures when both nondegenerate ground states are partially populated.

Compared to UV-vis, MCD is a powerful technique for characterising electronic band structures for two key reasons: (1) it emphasises optical transitions with magnetic dipole components which are typically weak and often obscured by much stronger electric dipole allowed transitions in UV-vis; (2) MCD signals arising from different mechanisms have different spectral shapes (e.g. gaussian or derivative) and can be positively or negatively signed, affording greater resolution than UV-vis when there are multiple overlapping bands.[61] In terms of intensity, MCD B terms are generally one to two orders of magnitude smaller than A or C terms at room temperature.[64, 67] At low temperatures, MCD C terms tend to dominate.

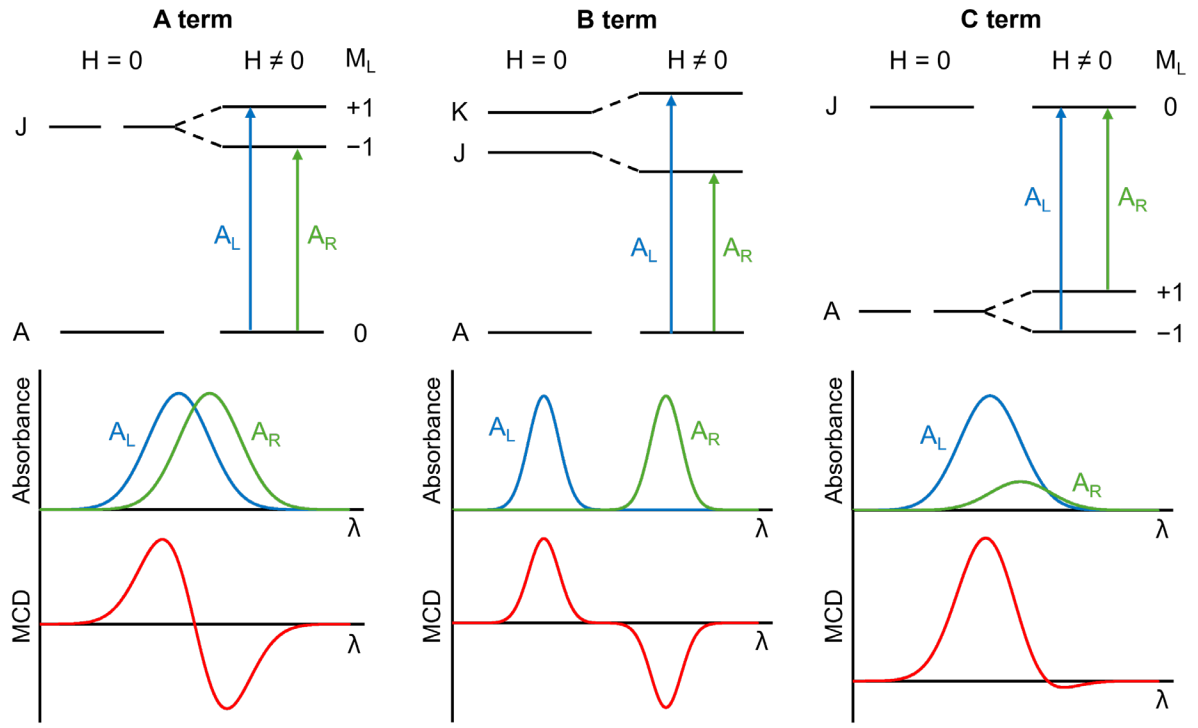

Figure 1.8. Energy level diagrams showing the origin of MCD A, B, and C terms with the corresponding absorbance and MCD spectra depicted beneath.

1.6.5 Circularly Polarised Luminescence (CPL)

Circularly polarised light is of great importance for numerous technological applications such as biomedical imaging and diagnosis,[68] 3D holographic displays,[69] and security devices.[70] The standard method for producing circularly polarised light requires sequentially passing unpolarised light through a linear polariser and a quarter waveplate, which unavoidably leads to much of the original light intensity being lost, making it highly inefficient.[71] This has led to intense research into developing materials which emit circularly polarised light directly. Therefore, as well as a chiroptical technique to characterise chiral emitters, circularly polarised luminescence is a desirable attribute in its own right. CPL can be considered the emission analogue of CD and is defined as the differential emission intensity (ΔI) of left and right circularly polarised light:[72-74]

$$\Delta I = I_L - I_R \tag{1.13}$$

where I_L and I_R are the emission intensity of left and right circularly polarised light, respectively. Like CD, only chiral molecules and materials display CPL due to the requirement than both **μ** and **m** are nonzero. CPL is usually reported in terms of the luminescence dissymmetry factor, g_{lum}:[72-74]

$$g_{lum} = \frac{I_L - I_R}{(I_L + I_R)/2} \tag{1.14}$$

The value of g_{lum} ranges from 2 to −2 and is intended to provide a measure of the net circular polarisation of the emission that is independent of the emission intensity. A g_{lum} of ±2 is obtained for purely left or right CPL, while for unpolarised emission $g_{lum} = 0$.

The rotational and dipole strengths governing absorption in a chiral species are the same as for emission from a chiral species. Therefore, g_{lum} is also defined with an equivalent expression to g_{abs}, assuming a randomly oriented distribution of emitters:[72-74]

$$g_{lum} = 4\frac{|\boldsymbol{\mu}||\boldsymbol{m}|\cos\theta}{|\boldsymbol{\mu}|^2 + |\boldsymbol{m}|^2} = 4\frac{R}{D} \tag{1.15}$$

This similarity in the expression of g_{abs} and g_{lum} does not mean they will have the same value for absorptive and emissive transitions between the same two electronic states, however they are often of the same order of magnitude.[44] Since chiral organic luminophores typically have much larger electronic than magnetic transition dipole moments (*i.e.*, $|\boldsymbol{\mu}| >> |\mathbf{m}|$), they often have small g_{lum} (usually < 10^{-2}).[73, 74] In contrast, transitions which are electric dipole forbidden but magnetic dipole allowed tend to show larger g_{lum}. The most prominent examples being the fluorescent f-f transitions in lanthanide complexes, which have proven to be excellent candidates for achieving large g_{lum} in excess of 0.1.[75-78] Unfortunately, the forbidden nature of the transitions means these complexes typically suffer from poor photoluminescent quantum yields (PLQY).[75, 78] Herein lies the current challenge in designing powerful CPL-active materials: attaining a large g_{lum} without compromising the PLQY.[79]

In some applications, maximising the net handedness of emitted light is most salient, while in other applications the overall amount of emitted circularly polarised light is more important. In the latter case, a more useful metric is the circularly polarised luminescence brightness, B_{CPL}, which takes into account the primary factors which determine overall CPL output:[80]

$$B_{CPL} = \varepsilon \cdot \phi \cdot \frac{|g_{lum}|}{2} \tag{1.16}$$

where ε is the molar extinction coefficient and ϕ is the PLQY of the emissive transition. Therefore, despite often having small g_{lum}, organic luminophores are still viable CPL candidates due to the large extinction coefficients and PLQY that can be attained.

1.6.6 Magneto-Chiral Dichroism (MChD)

In CD the dichroic signal results from a lack of mirror symmetry while in MCD the dichroic response originates from the presence of a magnetic field which breaks time reversal symmetry. When both of these symmetries are simultaneously broken, new magneto-chiral anisotropy effects become possible in both absorbance and refraction of light.[81, 82] When observed in absorbance this effect is termed magneto-chiral dichroism. MChD relies on the wavevector of the incident light, **k**, the applied magnetic field, **H**, and the angle between them. It is formally expressed by the following equation:[81, 82]

$$\varepsilon(\omega, \boldsymbol{k}, \boldsymbol{H}) = \varepsilon_0 \pm \alpha^{r/l}(\omega)\boldsymbol{k} \pm \beta(\omega)\boldsymbol{H} \pm \gamma^{r/l}(\omega)\boldsymbol{kH} \tag{1.17}$$

where ε_0 represents absorption in the absence of a magnetic field, ω is the frequency of the light, $\alpha^{r/l}$ represents CD, β represents MCD, $\gamma^{r/l}$ represents MChD, *r* and *l* refer to right- and left-handed media, and + and – to right and left circularly polarised light, respectively. MChD can thus be considered a nonlinear optical phenomenon since it relies on the product of **k** and **H**.[81-83] Notably, MChD does not depend on the polarisation of the light and can thus be observed with unpolarised light.[81-83] Experimentally, MchD is defined as the differential absorption of unpolarised light by a chiral medium in the presence of a longitudinal magnetic field:[81]

$$\mathrm{MChD} = A_{N\rightarrow S} - A_{S\rightarrow N} \tag{1.18}$$

where N→S and S→N signify the direction of the magnetic field. Enantiomers display MChD with equal magnitude but opposite sign.[81] As with MCD, to normalise the MChD intensity with respect to concentration and magnetic field, the MChD absorbance dissymmetry factor, g_{MChD}, is used to provide a measure of the inherent strength of the MChD response:

$$g_{MChD} = \frac{A_{N\rightarrow S} - A_{S\rightarrow N}}{(A_{N\rightarrow S} + A_{S\rightarrow N})/2} \cdot \frac{1}{H} \tag{1.19}$$

where H is the magnetic field strength in tesla. Furthermore, the approximate magnitude of g_{MChD} can be estimated as the product of g_{abs} and g_{MCD} (equation 1.20) which intuitively aligns with the emergence of MChD as a cross-effect between **k** and **H**.[81, 82, 84]

$$g_{MChD} \approx g_{abs} \cdot g_{MCD} \tag{1.20}$$

This relation emphasises the relative weakness of the MChD response; since g_{abs} and g_{MCD} are often $<10^{-2}$, their product will be very small. Consequently, for MChD to be experimentally

observable, the analyte should display strong CD and MCD in the same spectral region. To date, MChD has predominantly been studied in lanthanide and transition metal complexes because of their large orbital angular momentum and spin-orbit coupling, factors known to enhance MChD. These experiments were often performed at cryogenic temperatures to harness low-temperature ferromagnetic or ferrimagnetic ordering to further boost MChD.[83, 85-87] Nonetheless, the first demonstration of MChD at room temperature in a purely organic compound has recently been reported and displayed a g_{MChD} of approximately 5×10^{-4}.[88]

Materials with strong MChD responses have applications in magneto-optical devices, for example by facilitating optical readout of magnetic data with unpolarised light.[81] Additionally, MChD has been used to facilitate enantioselective photoresolution with unpolarised light.[89]

1.7 Designing Chiroptical Switches

Molecular systems have long been used as platforms for chiroptical switches and a wide variety of structures have been employed to date. One of the most important design features is the choice of stimuli-responsive component, which will inevitably be guided by the choice of stimuli (or vice versa). In this regard, some general trends have emerged amongst the most common classes of chiroptical switches. Light-modulated chiroptical switches have frequently employed well-known moieties which undergo photoisomerization. Prominent examples include *cis-trans* isomerisation in azobenzenes and overcrowded alkenes,[90, 91] spiropyrans,[92] and diarylethenes (Figure 1.9).[93] The construction of redox-modulated chiroptical switches necessarily requires the presence of a redox-active component. This has been achieved using polycyclic aromatic groups such as naphthaline diimides (NDI),[94] tetrathiafulvalene (TTF),[95] and viologens (Figure 1.10).[96] Temperature-modulated chiroptical switches typically exploit noncovalent interactions such as hydrogen bonding and π-π stacking;[97, 98] the formation and breaking of these interactions induce structural changes which are the basis of the chiroptical response. Finally, the use of chemical stimuli such as pH and cation/anion binding naturally requires appropriate acidic/basic functional groups or binding sites.[99-101] Since many stimuli-responsive functional groups are themselves achiral, it is common to covalently link them to chiral scaffolds to ensure a chiroptical response when the stimuli is applied.

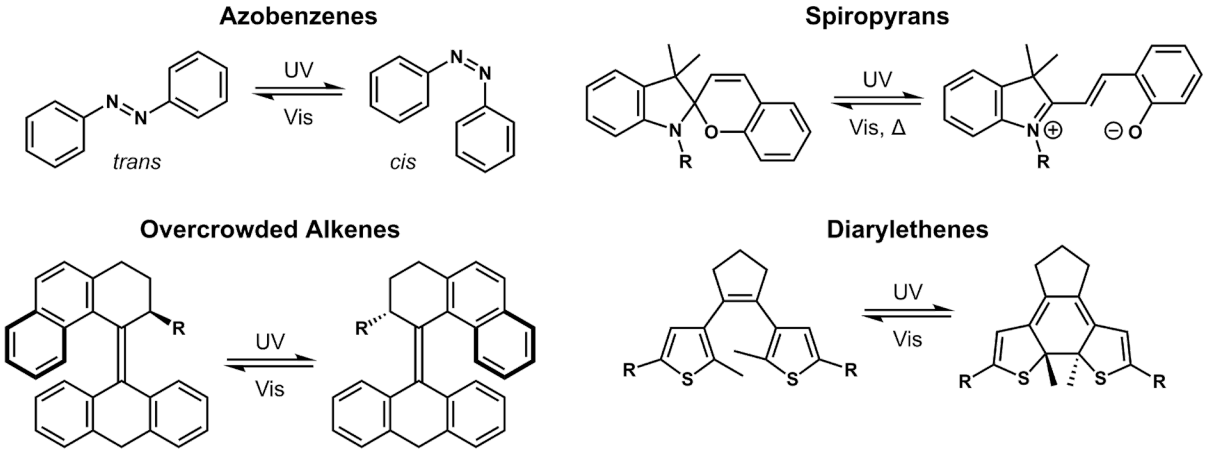

Figure 1.9. Molecular structures of some common photo-responsive molecules.

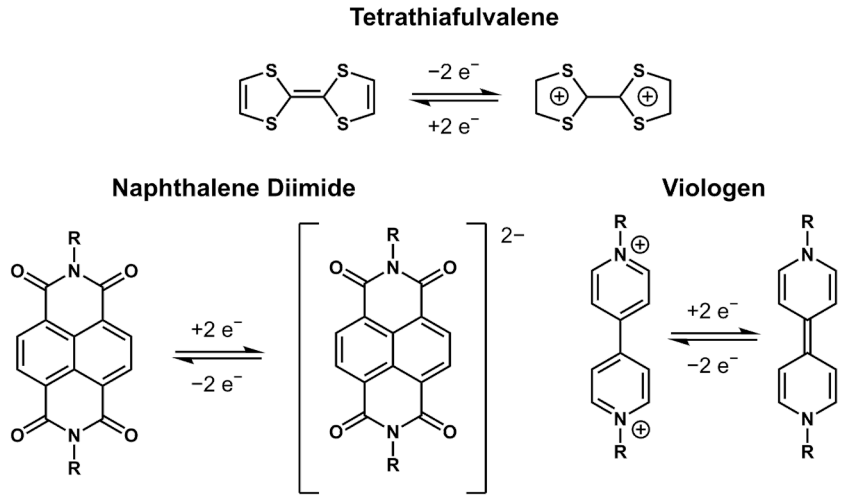

Figure 1.10. Molecular structure of some common redox-active molecules.

While the use of molecular systems for chiroptical switching is well-established, chiroptical switching in chiral MOFs is still relatively underexplored. The aforementioned design criteria still apply to MOF-based switches, however their ordered structure and porosity can also be used to harness switching mechanisms that would be hard to replicate in molecular chiroptical switches. Hu *et al*. demonstrated this by designing a chiroptical switch based on a photochemical [2+2] cycloaddition between double bonds in adjacent ligands.[102] Since photochemical [2+2] cycloaddition reactions are highly sensitive to the relative distance and orientation of the reacting double bonds,[103, 104] the precise structural arrangement provided by the MOF was essential. Additionally, host-guest interactions can be used as a stimulus for chiroptical switching by exploiting chirality transfer from the chiral pore environment of the MOF to a stimuli-responsive guest. This was shown by Zhao *et al*. who incorporated a photoactive diarylethene guest into a chiral MOF to achieve photo-switchable CPL.[105]

1.8 Chiroptical Switches: Performance Metrics

When designing and characterising chiroptical switches, it is important to be able to assess their performance and capability since this directly informs their viability for technological applications. This is done using the following four key metrics:[10-13]

(1) Stability: the two states of the switch should be stable under the conditions of operation and not interconvert without the application of the external stimulus.[11] Furthermore, the readout should be non-destructive *i.e.* the act of measuring the chiroptical signal does not in itself cause interconversion between the two states. This complication is mainly restricted to light-induced switching mechanisms (e.g. photoisomerism) where determining the concentration of the two states invariably involves exposing it to some light.

(2) Sensitivity: the two states should be easily distinguishable from each other such that there is no confusion about which species is present. Furthermore, switches with a strong chiroptical response are desirable since they are better able to discriminate between incremental changes in the applied stimuli.

(3) Reversibility: it should be possible to switch between the two states over many cycles without the loss of sensitivity. Experimentally, reversibility is typically assessed by measuring the signal intensity at a specific wavelength (one with good sensitivity) and monitoring the change in intensity over multiple cycles. Reversibility is particularly important when considering commercial applications of chiroptical switches, which generally require many switching cycles. Due to the time investment required to monitor switching for so many cycles, this is an underexplored feature of many chiroptical switches reported to date. The are two definitions of a cycle found in the literature: the first considers the forwards and reverse processes to count as one cycle each, while the other considers one cycle to consist of both a forwards and reverse switch. Throughout this thesis the latter definition will be used as it is more intuitive and, arguably, more accurate.

(4) Switching time: the switching time needs to be sufficiently fast based on the intended application of the chiroptical switch.

In addition to these key criteria, any chiroptical switch designed to operate in a complex environment should have a high tolerance to impurities. In these cases, impurities should not impede switching and it desirable to have a wide spectral range in which the two states are distinguishable. Designing a chiroptical switch which performs well in all of these categories

is certainly a difficult task and to date only a handful of high-performance chiroptical switches have been reported.[91, 92, 106-109] Generally, the most common difficulty is attaining both good stability and good reversibility. The varied design and structure of the best performing examples indicates that there is no singular pathway to success. However, one notable trend is that many of the best performing chiroptical switches have used electric potential as a stimulus.

1.9 Electric Potential as a Stimulus

Of the many possible stimuli, electric potential is one of the most commonly used for chiroptical switching and has been the basis for some of the best-performing chiroptical switches reported to date.[106-109] This is likely due to several favourable factors which make electric potential a versatile and effective stimulus. Firstly, there are many well-known moieties – both organic and inorganic – that display highly reversible redox behaviour, providing a rich library of building blocks for incorporation into chiroptical switches. Furthermore, redox reactions are often fast and are usually only limited by diffusion of analytes in solution or charge diffusion in bulk phases.[110] Consequently, electroactive thin films are promising since charge diffusion is limited to short distances.[107] Redox reactions generally result in large changes in the optical and magneto-optical properties, and therefore spectra, of a compound. Thus, redox-modulated switches typically display great contrast between states and have high sensitivity. Finally, electric potential is easy to incorporate into devices.

One example of a high-performance redox-modulated chiroptical switch is the PDI-based twistacene, chPDI[2], synthesised by Bao et al. (Figure 1.11).[106] The core redox-active group is comprised of two fused perylene diimides (PDI) which undergo a total of four reversible reduction processes. The chirality is provided by bulky (*S*)-1,2,2-triphenylethylamine substituents which induce helical chirality in the PDI twistacene itself. The large dissymmetry factors of the various redox states ($|g_{abs}|$ ranging from 1.2–3 × 10^{-2}) make chPDI[2] a highly sensitive chiroptical switch, with large differences in CD between the different redox states. When spin-coated on a conductive ITO slide, chiroptical switching between chPDI[2] and its doubly reduced state chPDI[2]$^{2-}$ could be monitored at four different wavelengths spanning visible and near-infrared wavelengths. Furthermore, good reversibility was observed at all four wavelengths for a total of 10 cycles.

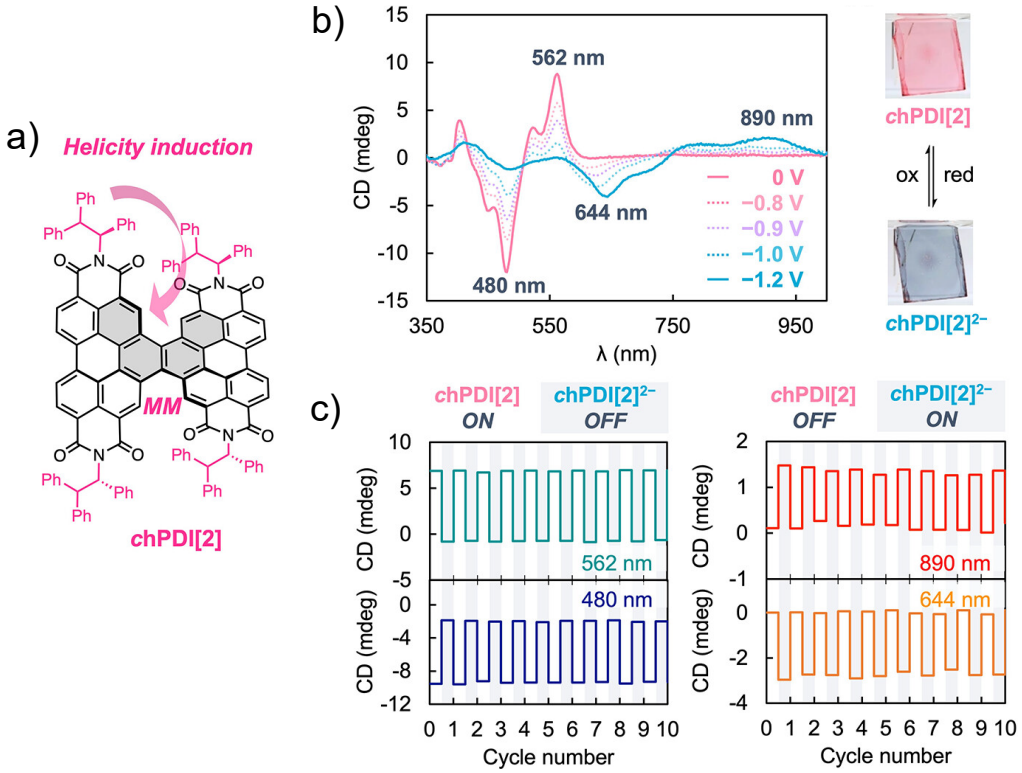

Figure 1.11. Redox-modulated chiroptical switching in chPDI[2]. (a) Structure of chPDI[2]. (b) CD spectra of chPDI[2] during reduction to chPDI[2]$^{2-}$. (c) Reversible CD signal at four different wavelengths during 10 successive reduction and oxidation cycles. Reproduced from ref 106 with permission from the American Chemical Society, copywrite 2023.

An important consideration when designing a redox-modulated chiroptical switch is the stability of the various redox states. This can be a major challenge as many redox species are radicals and thus highly reactive,[111] potentially leading to degradation and/or side reactions. Therefore, while redox-modulated chiroptical switches have great potential, the success of any individual switch is highly conditional on avoiding these pitfalls. Consequently, a key strategy to mitigate this problem is by ensuring operation of the switch under an inert atmosphere and free from protic solvents.

1.10 Spectroelectrochemistry (SEC)

Having identified electric potential as a promising stimulus for chiroptical switching, it is important to discuss how redox-active systems can be characterised spectroscopically so their performance as redox-modulated switches can be assessed. The best way to do this is to generate the oxidised or reduced species *in situ* during a spectroscopic experiment and collect spectra in real-time, a technique called spectroelectrochemistry (SEC).[110, 112-114] SEC is a powerful tool for investigating the properties of electroactive molecules and materials, as well

as providing insight into the kinetics and mechanisms of redox processes. SEC experiments are typically performed by incrementally increasing or decreasing the voltage applied to the sample, with a spectrum acquired at each potential.[110, 112] SEC experiments thus provide a picture of the relative concentration of the various species involved (reactants, intermediates, products) as a function of the applied potential.[115] In this work, three types of SEC experiments will be performed: UV-vis, CD, and EPR SEC. Of these, UV-vis and EPR SEC have seen widespread use to characterise redox processes in a range of materials.[110, 112, 114] In comparison, CD SEC is relatively underexplored, with only a handful of reports to date.[116]

Compared to purely electrochemical experiments such as cyclic voltammetry (CV), in SEC experiments there are additional restrictions on the choice of electrolyte beyond simply being electrochemically inert in the required potential window. Most importantly, the electrolyte solution used in SEC experiments must also not interfere with the spectroscopic technique in question. In UV-vis and CD SEC, this requires the electrolyte solution to be transparent in the required spectral range. This is typically not an issue for experiments in the visible range, however if SEC spectra are required below 250 nm, some common solvents used in electrolytes such as DMF, DMSO, and DCM will be unsuitable. In EPR spectroscopy, the signal intensity is attenuated by solvents with high dielectric constants.[117] Therefore, EPR SEC experiments using aqueous electrolytes may be of limited usefulness, although this can be mitigated somewhat by using narrower cells. As for the supporting electrolyte, tetraalkylammonium salts with noncoordinating anions such as $[ClO_4]^-$, $[BF_4]^-$, and $[PF_6]^-$ are often used due to their inertness, and wide optical windows.[116, 118]

Much like their standard electrochemical cells, typical SEC cell designs feature three-electrode setups consisting of working, counter, and reference electrodes.[110] When SEC experiments are performed in organic solvents it is common to use a Ag/Ag^+ *quasi*-reference electrode due to the challenge of preparing reliable, stable reference electrodes for nonaqueous solvents.[119, 120] Since the potential of *quasi*-reference electrodes are known to be variable,[121-123] it is commonplace to use a well-defined redox couple (e.g. Fc/Fc^+) as an internal standard.[122, 123] However, in SEC experiments this is usually not done because the internal standard may interfere with the spectroscopic measurement. Therefore, the potential at which each spectrum is recorded is only known qualitatively. For this reason, SEC experiments are only intended to highlight spectral changes upon oxidation/reduction, with an accurate determination of the potential of the electrochemical processes being determined with other techniques such as CV. For UV-vis and CD SEC, it is important to generate the oxidised/reduced species directly in

the beam path, in the cuvette part of the cell. This necessitates that the working electrode is also situated in the beam path. To avoid completely blocking the light passing through, semi-transparent working electrodes are used; there are two common types: a fine mesh made of a conductive noble metal such as platinum, or indium tin oxide (ITO) coated glass or quartz slides.[110, 115, 124] The thickness of the cuvette is generally quite narrow (≤1 mm) to decrease the diffusion time of analyte to the working electrode,[110, 115, 124] reducing the time for the cell to reach equilibrium (as dictated by the Nernst equation) each time the potential is changed. The narrow path lengths often require a relatively high sample concentration to attain sufficient spectroscopic response.[112] Detailed descriptions of the SEC cell designs used in this work are presented in Chapter 2.

1.11 Dual-Responsive Chiroptical Switches

Dual-responsive chiroptical switches are those which reversibly, and independently, respond to two different stimuli. Chiroptical switches with this property are of great interest due to their high degree of functionality and tuneability – useful attributes for emerging technologies such as chiroptical logic circuits where having two inputs is necessary for the creation of most fundamental logic gates.[125, 126] It should be noted that dual-responsive chiroptical switches are distinct from switches which use one stimulus for the forwards switch and a different stimulus for the reverse switch. Compared to standard chiroptical switches, the synthesis of dual-responsive chiroptical switches is complicated due to their added complexity. Nonetheless, their utility makes the pursuit of dual-responsive chiroptical switches worthwhile. Overall, relatively few dual-responsive chiroptical switches have been synthesised to date and it is not uncommon for their reversibility to be relatively unexplored for one or both stimuli,[97, 127-129] making it difficult to gain key insights from such examples. However, there are some dual-functional switches whose reversibility has been assessed for both stimuli.[108, 130, 131] Nonetheless, further work is needed towards developing dual-functional chiroptical switches with good reversibility of both switching mechanisms.

1.12 Aims

As we have now seen, chiroptical switching requires the combination of chirality, stimuli-responsiveness, and a chiroptical readout to monitor switching. Many examples of chiroptical switches have been reported, yet enduring challenges remain. Specifically, the number of high-performance and dual-responsive chiroptical switches is still relatively low. Additionally, many

chiroptical switches are synthetically arduous to make, presenting an additional barrier to their roll-out for commercial applications. Finally, it is difficult to know in advance if a particular chiroptical switch will perform well or not.

This thesis aims to investigate critical aspects of chiroptical switching such as stability and reversibility, in order to gain insight into key aspects that underpin successful switching behaviour. This information will identify the targeted design and synthesis of next generation effective chiroptical switches.

In pursuit of these aims, the design and synthesis of novel, high-performance chiroptical switches will be undertaken and their capabilities assessed based on the key metrics of sensitivity, stability, reversibility, and switching time. Both molecular and extended framework systems – specifically MOFs – will be used, with an emphasis on designs which can be made with relatively simple synthetic procedures. A particular focus will be directed towards redox-modulated chiroptical switching, which will be monitored *in-situ* using spectroelectrochemical techniques. Additionally, efforts will be made to achieve dual-functional chiroptical switching. CD will serve as the primary chiroptical readout, however, attempts to use CPL as a chiroptical readout will also be described. A final aim is to investigate the magneto-optical properties of the synthesised materials using MCD and MChD, to assess the applicability of these techniques as chiroptical readouts.

1.13 Thesis Outline

This thesis is comprised of six chapters (including this introduction). Chapter 2 outlines the synthetic procedures and characterisation methods performed during this work.

In Chapter 3, the redox-modulated chiroptical switches (*S*)-BNI and (*R*)-BNI are synthesised from axially chiral 1,1′-binaphthalene-2,2′-diamine and redox-active 1,8-naphthalic anhydride. The fundamental electrochemical and spectroscopic properties of (*S*)- and (*R*)-BNI are first investigated. Then, their performance as redox-modulated chiroptical switches are assessed through a combination of UV-vis and CD SEC experiments. Important practical considerations and limitations of using SEC experiments to measure reversibility in redox-modulated systems will also be discussed. The fundamental electronic structure of (*S*)- and (*R*)-BNI are unveiled through DFT calculations and supported by EPR SEC experiments. Finally, the magneto-optic and thin film properties of (*S*)- and (*R*)-BNI are characterised.

Chapter 4 focuses on the construction of chiroptical switches based on the ferrocene amino acid bioconjugates, L-Fc(MeLeu)$_2$ and D-Fc(MeLeu)$_2$, which contain a redox-active ferrocene core and adopt a chiral orientation through intramolecular hydrogen bonding between the amino acid groups. The solvent-dependent chiroptical response is first studied to provide an insight into the dynamic nature of the intramolecular hydrogen bonding and its relation to the overall chirality of L- and D-Fc(MeLeu)$_2$. Next, temperature and electric potential are both found to be effectively stimuli, with variable temperature (VT) CD and CD SEC experiments used to demonstrate that L- and D-Fc(MeLeu)$_2$ function as dual-responsive temperature- and redox-modulated chiroptical switches. The impact of analyte concentration on the observed electrochemical reversibility of SEC experiments is outlined, as well as the effect of concentration on decomposition rates. Finally, the magneto-optical and thin film properties of L- and D-Fc(MeLeu)$_2$ are characterised.

In Chapter 5, the focus shifts to MOFs. Thus, a series of lanthanide MOFs are made from the chiral ligand (4-carboxybenzoyl)-L-aspartic acid (H_3CBA) and various lanthanides (La, Ce, Pr, Nd). These MOFs are structurally characterised and found to be achiral due to racemisation of H_3CBA. Efforts to prevent racemisation and the possible mechanisms of racemisation are discussed in detail. An alternate chiral ligand, *N*-(4-carboxyphenyl)-L-alanine (H_2CPA), is synthesised in order to avoid racemisation. A chiral MOF is successfully formed from the reaction of H_2CPA with $Cd(NO_3)_2 \cdot 4H_2O$.

Each chapter is accompanied by a discussion of future directions relevant to the specific research presented within that chapter.

Finally, the Epilogue summarised the overall results and findings. Perspectives are also offered on broader trends and promising future directions for optical applications of chiral molecules and materials.

1.14 References

(1) Bril, M.; Fredrich, S.; Kurniawan, N. A. Stimuli-responsive materials: A smart way to study dynamic cell responses. *Smart Mater. Med.* **2022**, *3*, 257-273.
(2) Mellerup, S. K.; Wang, S. Boron-based stimuli responsive materials. *Chem. Soc. Rev.* **2019**, *48*, 3537-3549.
(3) Khizar, S.; Zine, N.; Errachid, A.; Elaissari, A. Introduction to Stimuli-Responsive Materials and Their Biomedical Applications. In *Stimuli-Responsive Materials for Biomedical Applications*, ACS Symposium Series, Vol. 1436; American Chemical Society, 2023; pp 1-30.

(4) Manrique-Juárez, M. D.; Rat, S.; Salmon, L.; Molnár, G.; Quintero, C. M.; Nicu, L.; Shepherd, H. J.; Bousseksou, A. Switchable molecule-based materials for micro- and nanoscale actuating applications: Achievements and prospects. *Coord. Chem. Rev.* **2016**, *308*, 395-408.
(5) Wang, Y.; Zhang, Y.-M.; Zhang, S. X.-A. Stimuli-Induced Reversible Proton Transfer for Stimuli-Responsive Materials and Devices. *Acc. Chem. Res.* **2021**, *54*, 2216-2226.
(6) Abousalman-Rezvani, Z.; Roghani-Mamaqani, H.; Riazi, H.; Abousalman-Rezvani, O. Water treatment using stimuli-responsive polymers. *Polym. Chem.* **2022**, *13*, 5940-5964.
(7) De Acha, N.; Elosúa, C.; Corres, J. M.; Arregui, F. J. Fluorescent Sensors for the Detection of Heavy Metal Ions in Aqueous Media. *Sensors* **2019**, *19*, 599.
(8) Murray, J.; Ma, D.; Munday, J. N. Electrically Controllable Light Trapping for Self-Powered Switchable Solar Windows. *ACS Photonics* **2017**, *4*, 1-7.
(9) Wang, Y.; Runnerstrom, E. L.; Milliron, D. J. Switchable Materials for Smart Windows. *Annu. Rev. Chem. Biomol. Eng.* **2016**, *7*, 283-304.
(10) Canary, J. W.; Mortezaei, S.; Liang, J. Transition metal-based chiroptical switches for nanoscale electronics and sensors. *Coord. Chem. Rev.* **2010**, *254*, 2249-2266.
(11) Feringa, B. L.; van Delden, R. A.; Koumura, N.; Geertsema, E. M. Chiroptical Molecular Switches. *Chem. Rev.* **2000**, *100*, 1789-1816.
(12) Isla, H.; Crassous, J. Helicene-based chiroptical switches. *C. R. Chim.* **2016**, *19*, 39-49.
(13) Zhang, L.; Wang, H.-X.; Li, S.; Liu, M. Supramolecular Chiroptical Switches. *Chem. Soc. Rev.* **2020**, *49*, 9095-9120.
(14) Bradshaw, D. S.; Leeder, J. M.; Coles, M. M.; Andrews, D. L. Signatures of material and optical chirality: Origins and measures. *Chem. Phys. Lett.* **2015**, *626*, 106-110.
(15) Moss, G. P. Basic terminology of stereochemistry (IUPAC Recommendations 1996). *Pure Appl. Chem.* **1996**, *68*, 2193-2222.
(16) Thoonen, S.; Hua, C. Chiral Detection with Coordination Polymers. *Chem. Asian J.* **2021**, *16*, 890-901.
(17) Bonner, W. A. Chirality and life. *Origins Life Evol. Biosphere* **1995**, *25*, 175-190.
(18) Sekhon, B. S. Exploiting the Power of Stereochemistry in Drugs: An Overview of Racemic and Enantiopure Drugs. *J. Mod. Med. Chem.* **2013**, *1*, 10-36.
(19) Warrant, E. J. Polarisation Vision: Beetles See Circularly Polarised Light. *Curr. Biol.* **2010**, *20*, R610-R612.
(20) Ozcelik, A.; Pereira-Cameselle, R.; Poklar Ulrih, N.; Petrovic, A. G.; Alonso-Gómez, J. L. Chiroptical Sensing: A Conceptual Introduction. *Sensors* **2020**, *20*, 974.
(21) Cahn, R. S.; Ingold, C.; Prelog, V. Specification of Molecular Chirality. *Angew. Chem. Int. Ed. Engl.* **1966**, *5*, 385-415.
(22) Fecher, G. H.; Kübler, J.; Felser, C. Chirality in the Solid State: Chiral Crystal Structures in Chiral and Achiral Space Groups. *Materials* **2022**, *15*, 5812.
(23) Nespolo, M.; Aroyo, M. I.; Souvignier, B. Crystallographic shelves: space-group hierarchy explained. *J. Appl. Crystallogr.* **2018**, *51*, 1481-1491.
(24) Rekis, T. Crystallization of chiral molecular compounds: what can be learned from the Cambridge Structural Database? *Acta Cryst. B* **2020**, *76*, 307-315.
(25) Green, M. M.; Cheon, K.-S.; Yang, S.-Y.; Park, J.-W.; Swansburg, S.; Liu, W. Chiral Studies across the Spectrum of Polymer Science. *Acc. Chem. Res.* **2001**, *34*, 672-680.
(26) Liu, M.; Zhang, L.; Wang, T. Supramolecular Chirality in Self-Assembled Systems. *Chem. Rev.* **2015**, *115*, 7304-7397.
(27) Yashima, E.; Maeda, K. Chirality-Responsive Helical Polymers. *Macromolecules* **2008**, *41*, 3-12.
(28) Batten, S. R.; Champness, N. R.; Chen, X.-M.; Garcia-Martinez, J.; Kitagawa, S.; Öhrström, L.; O'Keeffe, M.; Suh, M. P.; Reedijk, J. Terminology of metal–organic frameworks

and coordination polymers (IUPAC Recommendations 2013). *Pure Appl. Chem.* **2013**, *85*, 1715-1724.
(29) Kathalikkattil, A. C.; Babu, R.; Roshan, R. K.; Lee, H.; Kim, H.; Tharun, J.; Suresh, E.; Park, D.-W. An lcy-topology amino acid MOF as eco-friendly catalyst for cyclic carbonate synthesis from CO_2: Structure-DFT corroborated study. *J. Mater. Chem. A* **2015**, *3*, 22636-22647.
(30) Rood, J. A.; Noll, B. C.; Henderson, K. W. Homochiral frameworks derived from magnesium, zinc and copper salts of l-tartaric acid. *J. Solid State Chem.* **2010**, *183*, 270-276.
(31) Boer, S. A.; Hawes, C. S.; Turner, D. R. Engineering entanglement: controlling the formation of polycatenanes and polyrotaxanes using π interactions. *Chem. Commun.* **2014**, *50*, 1125-1127.
(32) Chen, Z.; Liu, X.; Zhang, C.; Zhang, Z.; Liang, F. Structure, adsorption and magnetic properties of chiral metal–organic frameworks bearing linear trinuclear secondary building blocks. *Dalton Trans.* **2011**, *40*, 1911-1918.
(33) Hao, P.; Huang, Q.; Gu, L.; Yu, Y.-H.; Ma, D.-S. Syntheses, structures and properties of three chiral metal–organic coordination polymers based on (R)-4-(4-(1-carboxyethoxy) phenoxy)-3-nitrobenzoic acid. *Polyhedron* **2018**, *149*, 117-125.
(34) Tan, C.; Yang, K.; Dong, J.; Liu, Y.; Liu, Y.; Jiang, J.; Cui, Y. Boosting enantioselectivity of chiral organocatalysts with ultrathin two-dimensional metal–organic framework nanosheets. *J. Am. Chem. Soc.* **2019**, *141*, 17685-17695.
(35) Bisht, K. K.; Suresh, E. Spontaneous Resolution to Absolute Chiral Induction: Pseudo-Kagomé Type Homochiral Zn(II)/Co(II) Coordination Polymers with Achiral Precursors. *J. Am. Chem. Soc.* **2013**, *135*, 15690-15693.
(36) Verma, A.; Tomar, K.; Bharadwaj, P. K. Chiral Cadmium(II) Metal–Organic Framework from an Achiral Ligand by Spontaneous Resolution: An Efficient Heterogeneous Catalyst for the Strecker Reaction of Ketones. *lnorg. Chem.* **2017**, *56*, 13629-13633.
(37) Kou, W.-T.; Yang, C.-X.; Yan, X.-P. Post-synthetic modification of metal–organic frameworks for chiral gas chromatography. *J. Mater. Chem. A* **2018**, *6*, 17861-17866.
(38) Gheorghe, A.; Strudwick, B.; Dawson, D. M.; Ashbrook, S. E.; Woutersen, S.; Dubbeldam, D.; Tanase, S. Synthesis of Chiral MOF-74 Frameworks by Post-Synthetic Modification by Using an Amino Acid. *Chem. Eur. J.* **2020**, *26*, 13957-13965.
(39) Mukhopadhyay, R. D.; Das, G.; Ajayaghosh, A. Stepwise control of host–guest interaction using a coordination polymer gel. *Nat. Commun.* **2018**, *9*, 1987.
(40) Das, S.; Xu, S.; Ben, T.; Qiu, S. Chiral Recognition and Separation by Chirality-Enriched Metal–Organic Frameworks. *Angew. Chem. Int. Ed.* **2018**, *57*, 8629-8633.
(41) Li, C.; Yang, X.-X.; Zheng, M.-Y.; Gu, Z.-G.; Zhang, J. Layer-By-Layer Chiral Induction of Fluorene-Based Metal–Organic Framework Films for Circularly Polarized Luminescence Sensing of Enantiomers. *Adv. Funct. Mater.* **2024**, *34*, 2401102.
(42) Kobayashi, N.; Muranaka, A.; Mack, J. Theory of Optical Spectroscopy. In *Circular Dichroism and Magnetic Circular Dichroism Spectroscopy for Organic Chemists*, The Royal Society of Chemistry, 2012; pp 1-41.
(43) Nordén, B.; Rodger, A.; Dafforn, T. *Linear Dichroism and Circular Dichroism: A Textbook on Polarized-Light Spectroscopy*; The Royal Society of Chemistry, 2010. DOI: 10.1039/9781839168932.
(44) Tanaka, H.; Inoue, Y.; Mori, T. Circularly Polarized Luminescence and Circular Dichroisms in Small Organic Molecules: Correlation between Excitation and Emission Dissymmetry Factors. *ChemPhotoChem* **2018**, *2*, 386-402.
(45) Condon, E. A Theory of Intensity Distribution in Band Systems. *Phys. Rev.* **1926**, *28*, 1182-1201.

(46) Franck, J.; Dymond, E. G. Elementary processes of photochemical reactions. *Trans. Faraday Society* **1926**, *21*, 536-542.
(47) Marconi, G.; Bartocci, G.; Mazzucato, U.; Spalletti, A.; Abbate, F.; Angeloni, L.; Castellucci, E. Role of internal conversion on the excited state properties of trans-styrylpyridines. *Chem. Phys.* **1995**, *196*, 383-393.
(48) Lakowicz, J. R. Introduction to Fluorescence. In *Principles of Fluorescence Spectroscopy*, Lakowicz, J. R. Ed.; Springer US, 2006; pp 1-26.
(49) Kasha, M. Characterization of electronic transitions in complex molecules. *Discuss. Faraday Soc.* **1950**, *9*, 14-19.
(50) Nizar, N. S. S.; Sujith, M.; Swathi, K.; Sissa, C.; Painelli, A.; Thomas, K. G. Emergent chiroptical properties in supramolecular and plasmonic assemblies. *Chem. Soc. Rev.* **2021**, *50*, 11208-11226.
(51) Wakabayashi, M.; Yokojima, S.; Fukaminato, T.; Shiino, K.-i.; Irie, M.; Nakamura, S. Anisotropic Dissymmetry Factor, g: Theoretical Investigation on Single Molecule Chiroptical Spectroscopy. *J. Phys. Chem. A* **2014**, *118*, 5046-5057.
(52) Lakhwani, G.; Gielen, J.; Kemerink, M.; Christianen, P. C. M.; Janssen, R. A. J.; Meskers, S. C. J. Intensive Chiroptical Properties of Chiral Polyfluorenes Associated with Fibril Formation. *J. Phys. Chem. B* **2009**, *113*, 14047-14051.
(53) Lakhwani, G.; Meskers, S. C. J. Insights from Chiral Polyfluorene on the Unification of Molecular Exciton and Cholesteric Liquid Crystal Theories for Chiroptical Phenomena. *J. Phys. Chem. A* **2012**, *116*, 1121-1128.
(54) Sun, Y.; Jiang, Y.; Jiang, J.; Li, T.; Liu, M. Keto-form directed hierarchical chiral self-assembly of Schiff base derivatives with amplified circularly polarized luminescence. *Chin. Chem. Lett.* **2024**, *35*, 108409.
(55) Harada, N.; Nakanishi, K.; Berova, N. Electronic CD Exciton Chirality Method: Principles and Applications. In *Comprehensive Chiroptical Spectroscopy*, 2012; pp 115-166.
(56) Greenfield, J. L.; Wade, J.; Brandt, J. R.; Shi, X.; Penfold, T. J.; Fuchter, M. J. Pathways to increase the dissymmetry in the interaction of chiral light and chiral molecules. *Chem. Sci.* **2021**, *12*, 8589-8602.
(57) Tang, Y.; Cohen, A. E. Enhanced Enantioselectivity in Excitation of Chiral Molecules by Superchiral Light. *Science* **2011**, *332*, 333-336.
(58) Canary, J. W. Redox-triggered chiroptical molecular switches. *Chem. Soc. Rev.* **2009**, *38*, 747-756.
(59) Adelizzi, B.; Van Zee, N. J.; de Windt, L. N. J.; Palmans, A. R. A.; Meijer, E. W. Future of Supramolecular Copolymers Unveiled by Reflecting on Covalent Copolymerization. *J. Am. Chem. Soc.* **2019**, *141*, 6110-6121.
(60) Hoeben, F. J. M.; Jonkheijm, P.; Meijer, E. W.; Schenning, A. P. H. J. About Supramolecular Assemblies of π-Conjugated Systems. *Chem. Rev.* **2005**, *105*, 1491-1546.
(61) Han, B.; Gao, X.; Lv, J.; Tang, Z. Magnetic Circular Dichroism in Nanomaterials: New Opportunity in Understanding and Modulation of Excitonic and Plasmonic Resonances. *Adv. Mater.* **2020**, *32*, 1801491.
(62) Sharma, A.; Wojciechowski, J. P.; Liu, Y.; Pelras, T.; Wallace, C. M.; Müllner, M.; Widmer-Cooper, A.; Thordarson, P.; Lakhwani, G. The Role of Fiber Agglomeration in Formation of Perylene-Based Fiber Networks. *Cell Rep. Phys. Sci.* **2020**, *1*, 100148.
(63) Gabbani, A.; Taddeucci, A.; Bertuolo, M.; Pineider, F.; Aronica, L. A.; Di Bari, L.; Pescitelli, G.; Zinna, F. Magnetic Circular Dichroism Elucidates Molecular Interactions in Aggregated Chiral Organic Materials. *Angew. Chem. Int. Ed.* **2024**, *63*, e202313315.
(64) Mason, W. R. Theoretical Framework: Definition of MCD Terms. In *A practical guide to magnetic circular dichroism spectroscopy*, John Wiley & Sons, 2007; pp 14-35.

(65) Kjærgaard, T.; Coriani, S.; Ruud, K. Ab initio calculation of magnetic circular dichroism. *WIREs Comput Mol Sci.* **2012**, *2*, 443-455.
(66) Sharma, A.; Athanasopoulos, S.; Li, Y.; Sanders, S. N.; Kumarasamy, E.; Campos, L. M.; Lakhwani, G. Probing Through-Bond and Through-Space Interactions in Singlet Fission-Based Pentacene Dimers. *J. Phys. Chem. Lett.* **2022**, *13*, 8978-8986.
(67) Buckingham, A. D.; Stephens, P. J. Magnetic Optical Activity. *Annu. Rev. Phys. Chem.* **1966**, *17*, 399-432.
(68) Kunnen, B.; Macdonald, C.; Doronin, A.; Jacques, S.; Eccles, M.; Meglinski, I. Application of circularly polarized light for non-invasive diagnosis of cancerous tissues and turbid tissue-like scattering media. *J. Biophotonics* **2015**, *8*, 317-323.
(69) Huang, L.; Chen, X.; Mühlenbernd, H.; Zhang, H.; Chen, S.; Bai, B.; Tan, Q.; Jin, G.; Cheah, K.-W.; Qiu, C.-W.; et al. Three-dimensional optical holography using a plasmonic metasurface. *Nat. Commun.* **2013**, *4*, 2808.
(70) Kitagawa, Y.; Wada, S.; Islam, M. D. J.; Saita, K.; Gon, M.; Fushimi, K.; Tanaka, K.; Maeda, S.; Hasegawa, Y. Chiral lanthanide lumino-glass for a circularly polarized light security device. *Commun. Chem.* **2020**, *3*, 119.
(71) Deng, Y.; Wang, M.; Zhuang, Y.; Liu, S.; Huang, W.; Zhao, Q. Circularly polarized luminescence from organic micro-/nano-structures. *Light Sci. Appl.* **2021**, *10*, 76.
(72) Chen, W.; Ma, K.; Duan, P.; Ouyang, G.; Zhu, X.; Zhang, L.; Liu, M. Circularly polarized luminescence of nanoassemblies via multi-dimensional chiral architecture control. *Nanoscale* **2020**, *12*, 19497-19515.
(73) Gong, Z. L.; Li, Z. Q.; Zhong, Y. W. Circularly polarized luminescence of coordination aggregates. *Aggregate* **2022**, *3*, e177.
(74) Sánchez-Carnerero, E. M.; Agarrabeitia, A. R.; Moreno, F.; Maroto, B. L.; Muller, G.; Ortiz, M. J.; de la Moya, S. Circularly Polarized Luminescence from Simple Organic Molecules. *Chem. Eur. J.* **2015**, *21*, 13488-13500.
(75) Harada, T.; Nakano, Y.; Fujiki, M.; Naito, M.; Kawai, T.; Hasegawa, Y. Circularly Polarized Luminescence of Eu(III) Complexes with Point-and Axis-Chiral Ligands Dependent on Coordination Structures. *lnorg. Chem.* **2009**, *48*, 11242-11250.
(76) Islam, M. J.; Kitagawa, Y.; Tsurui, M.; Hasegawa, Y. Strong circularly polarized luminescence of mixed lanthanide coordination polymers with control of 4f electronic structures. *Dalton Trans.* **2021**, *50*, 5433-5436.
(77) Kitagawa, Y.; Tsurui, M.; Hasegawa, Y. Steric and Electronic Control of Chiral Eu(III) Complexes for Effective Circularly Polarized Luminescence. *ACS Omega* **2020**, *5*, 3786-3791.
(78) Kumar, J.; Marydasan, B.; Nakashima, T.; Kawai, T.; Yuasa, J. Chiral supramolecular polymerization leading to eye differentiable circular polarization in luminescence. *Chem. Commun.* **2016**, *52*, 9885-9888.
(79) Furlan, F.; Moreno-Naranjo, J. M.; Gasparini, N.; Feldmann, S.; Wade, J.; Fuchter, M. J. Chiral materials and mechanisms for circularly polarized light-emitting diodes. *Nat. Photonics* **2024**, *18*, 658-668.
(80) Arrico, L.; Di Bari, L.; Zinna, F. Quantifying the Overall Efficiency of Circularly Polarized Emitters. *Chem. Eur. J.* **2021**, *27*, 2920-2934.
(81) Atzori, M.; Rikken, G. L. J. A.; Train, C. Magneto-Chiral Dichroism: A Playground for Molecular Chemists. *Chem. Eur. J.* **2020**, *26*, 9784-9791.
(82) Rikken, G. L. J. A.; Raupach, E. Pure and cascaded magnetochiral anisotropy in optical absorption. *Phys. Rev. E* **1998**, *58*, 5081.
(83) Train, C.; Gheorghe, R.; Krstic, V.; Chamoreau, L.-M.; Ovanesyan, N. S.; Rikken, G. L. J. A.; Gruselle, M.; Verdaguer, M. Strong magneto-chiral dichroism in enantiopure chiral ferromagnets. *Nat. Mater.* **2008**, *7*, 729-734.

(84) Ishii, K.; Hattori, S.; Kitagawa, Y. Recent advances in studies on the magneto-chiral dichroism of organic compounds. *Photochem. Photobiol. Sci.* **2020**, *19*, 9-19.
(85) Atzori, M.; Breslavetz, I.; Paillot, K.; Inoue, K.; Rikken, G. L. J. A.; Train, C. A Chiral Prussian Blue Analogue Pushes Magneto-Chiral Dichroism Limits. *J. Am. Chem. Soc.* **2019**, *141*, 20022-20025.
(86) Cahya Adi, L.; Willis, O. G.; Gabbani, A.; Rikken, G. L. J. A.; Di Bari, L.; Train, C.; Pineider, F.; Zinna, F.; Atzori, M. Magneto-Chiral Dichroism of Chiral Lanthanide Complexes in the Context of Richardson's Theory of Optical Activity. *Angew. Chem. Int. Ed.* **2024**, *63*, e202412521.
(87) Taniguchi, K.; Kishiue, S.; Kimura, S.; Miyasaka, H. Local-Site Dependency of Magneto-Chiral Dichroism in Enantiopure One-Dimensional Copper(II)–Chromium(III) Coordination Polymers. *J. Phys. Soc. Jpn.* **2019**, *88*, 093708.
(88) Kitagawa, Y.; Segawa, H.; Ishii, K. Magneto-Chiral Dichroism of Organic Compounds. *Angew. Chem. Int. Ed.* **2011**, *50*, 9133-9136.
(89) Rikken, G. L. J. A.; Raupach, E. Enantioselective magnetochiral photochemistry. *Nature* **2000**, *405*, 932-935.
(90) Iba, S.; Iwata, K.; Sotani, T.; Ishida, T.; Sano, N.; Sogawa, H.; Sanda, F. Photo-Triggered Chiroptical Switching of Platinum Complexes Bearing Azobenzene Moieties. *Organometallics* **2021**, *40*, 3550-3559.
(91) Jager, W. F.; de Jong, J. C.; de Lange, B.; Huck, N. P. M.; Meetsma, A.; Feringa, B. L. A Highly Stereoselective Optical Switching Process Based on Donor–Acceptor Substituted Dissymmetric Alkenes. *Angew. Chem. Int. Ed. Engl.* **1995**, *34*, 348-350.
(92) Ai, Y.; Fei, Y.; Shu, Z.; Zhu, Y.; Liu, J.; Li, Y. Visible-light-controlled ternary chiroptical switches with high-performance circularly polarized luminescence for advanced optical information storage and anti-counterfeiting materials. *Chem. Eng. J.* **2022**, *450*, 138390.
(93) Li, M.; Chen, L.-J.; Cai, Y.; Luo, Q.; Li, W.; Yang, H.-B.; Tian, H.; Zhu, W.-H. Light-Driven Chiral Switching of Supramolecular Metallacycles with Photoreversibility. *Chem* **2019**, *5*, 634-648.
(94) Zheng, J.; Qiao, W.; Wan, X.; Gao, J. P.; Wang, Z. Y. Near-Infrared Electrochromic and Chiroptical Switching Materials: Design, Synthesis, and Characterization of Chiral Organogels Containing Stacked Naphthalene Diimide Chromophores. *Chem. Mater.* **2008**, *20*, 6163-6168.
(95) Biet, T.; Fihey, A.; Cauchy, T.; Vanthuyne, N.; Roussel, C.; Crassous, J.; Avarvari, N. Ethylenedithio—Tetrathiafulvalene—Helicenes: Electroactive Helical Precursors with Switchable Chiroptical Properties. *Chem. Eur. J.* **2013**, *19*, 13160-13167.
(96) Deng, J.; Song, N.; Liu, W.; Zhou, Q.; Wang, Z. Y. Towards Near-Infrared Chiroptically Switching Materials: Theoretical and Experimental Studies on Viologen-Containing 1,1′-Binaphthyls. *ChemPhysChem* **2008**, *9*, 1265-1269.
(97) Duan, P.; Li, Y.; Li, L.; Deng, J.; Liu, M. Multiresponsive Chiroptical Switch of an Azobenzene-Containing Lipid: Solvent, Temperature, and Photoregulated Supramolecular Chirality. *J. Phys. Chem. B* **2011**, *115*, 3322-3329.
(98) Liu, B.; Hao, A.; Xing, P. Water-Mediated Folding Behaviors and Chiroptical Inversion of Ferrocene-Conjugated Dipeptides. *J. Phys. Chem. Lett.* **2021**, *12*, 6190-6196.
(99) Gao, F.; Yu, X.; Liu, L.; Chen, J.; Lv, Y.; Zhao, T.; Ji, J.; Yao, J.; Wu, W.; Yang, C. Chiroptical switching of molecular universal joint triggered by complexation/release of a cation: A stepwise synergistic complexation. *Chin. Chem. Lett.* **2023**, *34*, 107558.
(100) Pandeeswar, M.; Govindaraju, T. Engineering molecular self-assembly of perylene diimide through pH-responsive chiroptical switching. *Mol. Syst. Des. Eng.* **2016**, *1*, 202-207.
(101) Suk, J.-m.; Naidu, V. R.; Liu, X.; Lah, M. S.; Jeong, K.-S. A Foldamer-Based Chiroptical Molecular Switch That Displays Complete Inversion of the Helical Sense upon Anion Binding. *J. Am. Chem. Soc.* **2011**, *133*, 13938-13941.

(102) Hu, F.-L.; Wang, H.-F.; Guo, D.; Zhang, H.; Lang, J.-P.; Beves, J. E. Controlled formation of chiral networks and their reversible chiroptical switching behaviour by UV/microwave irradiation. *Chem. Commun.* **2016**, *52*, 7990-7993.
(103) Bregman, J.; Osaki, K.; Schmidt, G. M. J.; Sonntag, F. I. 386. Topochemistry. Part IV. The crystal chemistry of some cis-cinnamic acids. *Journal of the Chemical Society (Resumed)* **1964**, 2021-2030.
(104) Schmidt, G. M. J. Topochemistry. Part III. The Crystal Chemistry of some trans-Cinnamic Acids. *J. Chem. Soc.* **1964**, 2014-2021.
(105) Zhao, T.; Han, J.; Shi, Y.; Zhou, J.; Duan, P. Multi-Light-Responsive Upconversion-and-Downshifting-Based Circularly Polarized Luminescent Switches in Chiral Metal–Organic Frameworks. *Adv. Mater.* **2021**, *33*, 2101797.
(106) Bao, S. T.; Louie, S.; Jiang, H.; Jiang, Q.; Sun, S.; Steigerwald, M. L.; Nuckolls, C.; Jin, Z. Near-Infrared, Organic Chiroptic Switch with High Dissymmetry Factors. *J. Am. Chem. Soc.* **2024**, *146*, 51-56.
(107) Bernhard, S.; Goldsmith, J. I.; Takada, K.; Abruña, H. D. Iron(II) and Copper(I) Coordination Polymers: Electrochromic Materials with and without Chiroptical Properties. *lnorg. Chem.* **2003**, *42*, 4389-4393.
(108) Wang, C.; Liu, L.; Wang, J.; Yan, Y. Electrochemically Switchable Circularly Polarized Photoluminescence within Self-Assembled Conducting Polymer Helical Microfibers. *J. Am. Chem. Soc.* **2022**, *144*, 19714-19718.
(109) Yang, G.; Yu, Y.; Yang, B.; Lu, T.; Cai, Y.; Yin, H.; Zhang, H.; Zhang, N.-N.; Li, L.; Zhang, Y.-M.; et al. A Multiple Chirality Switching Device for Spatial Light Modulators. *Angew. Chem. Int. Ed.* **2021**, *60*, 2018-2023.
(110) D'Alessandro, D. M.; Usov, P. M. Spectroelectrochemistry: A Powerful Tool for Studying Fundamental Properties and Emerging Applications of Solid-State Materials Including Metal–Organic Frameworks. *Aust. J. Chem.* **2021**, *74*, 77-93.
(111) Yan, M.; Lo, J. C.; Edwards, J. T.; Baran, P. S. Radicals: Reactive Intermediates with Translational Potential. *J. Am. Chem. Soc.* **2016**, *138*, 12692-12714.
(112) Kaim, W.; Fiedler, J. Spectroelectrochemistry: the best of two worlds. *Chem. Soc. Rev.* **2009**, *38*, 3373-3382.
(113) Karoń, K.; Rode, J. E.; Kaczorek, D.; Kawęcki, R.; Pluczyk-Małek, S.; Łapkowski, M.; Ostrowski, S.; Lyczko, K.; Dobrowolski, J. C. UV–vis and ECD spectroelectrochemistry of atropisomeric naphthalenediimide derivative. *Spectrochim. Acta A* **2023**, *288*, 122089.
(114) Zhai, Y.; Zhu, Z.; Zhou, S.; Zhu, C.; Dong, S. Recent advances in spectroelectrochemistry. *Nanoscale* **2018**, *10*, 3089-3111.
(115) Scherson, D. A.; Sarangapani, S.; Urbach, F. L. Thin-layer spectroelectrochemical cell. *Anal. Chem.* **1985**, *57*, 1501-1503.
(116) Karoń, K.; Łapkowski, M.; Dobrowolski, J. C. ECD spectroelectrochemistry: A review. *Spectrochim. Acta A* **2021**, *250*, 119349.
(117) Glatzhofer, D. T.; Kadam, R. S. Use of Electron Paramagnetic Resonance Spectroscopy to Study Dielectric Properties of Liquids. *Int. Scholarly Res. Not.* **2012**, *2012*, 847102.
(118) Elgrishi, N.; Rountree, K. J.; McCarthy, B. D.; Rountree, E. S.; Eisenhart, T. T.; Dempsey, J. L. A Practical Beginner's Guide to Cyclic Voltammetry. *J. Chem. Educ.* **2018**, *95*, 197-206.
(119) McShane, E. J.; Benedek, P.; Niemann, V. A.; Blair, S. J.; Kamat, G. A.; Nielander, A. C.; Jaramillo, T. F.; Cargnello, M. A Versatile Li0.5FePO4 Reference Electrode for Nonaqueous Electrochemical Conversion Technologies. *ACS Energy Lett.* **2023**, *8*, 230-235.
(120) Smith, T. J.; Stevenson, K. J. 4 - Reference Electrodes. In *Handbook of Electrochemistry*, Zoski, C. G. Ed.; Elsevier, 2007; pp 73-110.

(121) Bond, A. M.; Lay, P. A. Cyclic voltammetry at microelectrodes in the absence of added electrolyte using a platinum quasi-reference electrode. *J. Electroanal. Chem. Interfacial Electrochem.* **1986**, *199*, 285-295.
(122) Huber, B.; Roling, B. Development of a Ag/Ag^+ micro-reference electrode for electrochemical measurements in ionic liquids. *Electrochim. Acta* **2011**, *56*, 6569-6572.
(123) Snook, G. A.; Best, A. S.; Pandolfo, A. G.; Hollenkamp, A. F. Evaluation of a $Ag|Ag^+$ reference electrode for use in room temperature ionic liquids. *Electrochem. Commun.* **2006**, *8*, 1405-1411.
(124) Heineman, W. R. Spectroelectrochemistry: The combination of optical and electrochemical techniques. *J. Chem. Educ.* **1983**, *60*, 305.
(125) de Silva, A. P.; McClenaghan, N. D. Molecular-Scale Logic Gates. *Chem. Eur. J.* **2004**, *10*, 574-586.
(126) Erbas-Cakmak, S.; Kolemen, S.; Sedgwick, A. C.; Gunnlaugsson, T.; James, T. D.; Yoon, J.; Akkaya, E. U. Molecular logic gates: the past, present and future. *Chem. Soc. Rev.* **2018**, *47*, 2228-2248.
(127) Liu, C.; Yang, D.; Jin, Q.; Zhang, L.; Liu, M. A Chiroptical Logic Circuit Based on Self-Assembled Soft Materials Containing Amphiphilic Spiropyran. *Adv. Mater.* **2016**, *28*, 1644-1649.
(128) Sakai, R.; Otsuka, I.; Satoh, T.; Kakuchi, R.; Kaga, H.; Kakuchi, T. Thermoresponsive On−Off Switching of Chiroptical Property Induced in Poly(4‘-ethynylbenzo-15-crown-5)/α-Amino Acid System. *Macromolecules* **2006**, *39*, 4032-4037.
(129) Shang, W.; Zhu, X.; Liang, T.; Du, C.; Hu, L.; Li, T.; Liu, M. Chiral Reticular Self-Assembly of Achiral AIEgen into Optically Pure Metal-Organic Frameworks (MOFs) with Dual Mechano-Switchable Circularly Polarized Luminescence. *Angew. Chem. Int. Ed.* **2020**, *59*, 12811-12816.
(130) Liu, C.; Dong, C.; Liu, S.; Yang, Y.; Zhang, Z. Multiple chiroptical switches and logic circuit based on salicyl– imine–chitosan hydrogel. *Carbohydr. Polym.* **2021**, *257*, 117534.
(131) Shen, C.; He, X.; Toupet, L.; Norel, L.; Rigaut, S.; Crassous, J. Dual Redox and Optical Control of Chiroptical Activity in Photochromic Dithienylethenes Decorated with Hexahelicene and Bis-Ethynyl-Ruthenium Units. *Organometallics* **2018**, *37*, 697-705.

Chapter 2

Experimental Methods

2.1 General

Unless otherwise stated, all reagents and starting materials were purchased from commercial sources and used without further purification. Dry DCM, diethyl ether, MeCN and toluene were obtained from an Innovative Technology Puresolv solvent purification system. Dry Cs_2CO_3 was prepared by grinding with a mortar and pestle and drying overnight at 280 °C.

2.2 Organic Synthesis

(*S*)-1,1′-binaphthalene-2,2′-bis(1,8-naphthalimide) ((*S*)-BNI). (*S*)-1,1′-Binaphthyl-2,2′-diamine (1.14 g, 4.01 mmol), 1,8-naphthalic anhydride (1.91 g, 9.62 mmol), and imidazole (9.01 g, 132 mmol) were combined in a Schlenk tube and stirred at 115 °C under a nitrogen atmosphere. After 7 h a tan-coloured solid had formed and the suspension was left to cool to room temperature. The resulting solid mass was dispersed in water (200 mL) with the aid of sonication, filtered, and washed copiously with water to remove excess imidazole. The solid was then washed with ethanol (3 × 40 mL) and ethyl acetate (30 mL). The crude product was recrystallised from chloroform, washed with chilled chloroform (2 × 40 mL) and diethyl ether (40 mL), and dried to afford a white solid (1.88 g, 73%). Crystals suitable for single crystal X-ray diffraction were obtained by slow evaporation from a 1:1 chloroform/ethyl acetate solution. ^{1}H NMR (500 MHz, $CDCl_3$): δ (ppm) 8.21 (d, J = 8.2 Hz, 2H), 8.11 (d, J = 8.3 Hz, 2H), 8.08 (d, J = 7.2 Hz, 2H), 7.99 (d, J = 7.3 Hz, 2H), 7.91 (d, J = 8.7 Hz, 2H), 7.87 (d, J = 8.2 Hz, 2H), 7.73 (apparent t, J = 7.7 Hz, 2H), 7.55–7.51 (m, 4H), 7.43 (d, J = 8.4 Hz, 2H), 7.35 (m, 2H), 7.23 (d, J = 8.6 Hz, 2H). ^{13}C{^{1}H} NMR (125 MHz, $CDCl_3$): δ (ppm) 165.25, 163.06, 134.19, 134.03, 133.78, 133.20, 133.11, 133.05, 131.77, 131.25, 130.70, 129.74, 128.68, 127.49, 127.16, 126.84, 126.52, 126.21, 125.65, 123.78, 123.11. APCI-MS (positive mode) *m/z* calculated for $C_{44}H_{25}N_2O_4$ $[M + H]^+$ 645.18; found 645.22. IR (ATR): ν_{max} (cm^{-1}) 426 (m), 478 (m), 494 (m), 523 (m), 548 (s), 581 (w), 618 (w), 664 (m), 700 (m), 734 (s), 756 (s), 775 (s), 788 (m), 810 (s), 843 (m), 865 (w), 896 (s), 909 (w), 946 (w), 965 (w), 986 (w), 1026 (m), 1071

(w), 1113 (m), 1151 (w), 1181 (m), 1236 (s), 1267 (w), 1343 (s), 1374 (m), 1405 (w), 1436 (m), 1512 (m), 1590 (s), 1627 (w), 1669 (s), 1704 (s), 3008 (m), 3067 (w).

(*R*)-1,1′-binaphthalene-2,2′-bis(1,8-naphthalimide) ((*R*)-BNI). (*R*)-BNI was synthesised using the same procedure as for (*S*)-BNI except that (*R*)-1,1′-binaphthyl-2,2′-diamine was used instead (1.68 g, 65.0%). Crystals suitable for single crystal X-ray diffraction were obtained by slow evaporation from a 1:1 chloroform/toluene solution. ^{1}H NMR (500 MHz, $CDCl_3$): δ (ppm) 8.21 (d, *J* = 8.3 Hz, 2H), 8.12 (d, *J* = 8.2 Hz, 2H), 8.08 (dd, *J* = 7.3 Hz, *J* = 1.0 Hz, 2H), 7.99 (dd, *J* = 7.3 Hz, *J* = 1.0 Hz, 2H), 7.91 (d, *J* = 8.7 Hz, 2H), 7.87 (d, *J* = 8.1 Hz, 2H), 7.73 (apparent t, *J* = 7.7 Hz, 2H), 7.55–7.51 (m, 4H), 7.43 (d, *J* = 8.5 Hz, 2H), 7.35 (m, 2H), 7.23 (d, *J* = 8.7 Hz, 2H). ^{13}C{^{1}H} NMR (125 MHz, $CDCl_3$): δ (ppm) 165.25, 163.06, 134.19, 134.04, 133.79, 133.20, 133.11, 133.05, 131.77, 131.26, 130.71, 129.74, 128.68, 127.50, 127.15, 126.84, 126.52, 126.21, 125.65, 123.78, 123.10. APCI-MS (positive mode) *m/z* calculated for $C_{44}H_{25}N_2O_4$ $[M + H]^+$ 645.18; found 645.23. IR (ATR): ν_{max} (cm^{-1}) 423 (m), 475 (m), 495 (m), 526 (m), 549 (m), 582 (w), 663 (m), 701 (w), 736 (s), 756 (s), 779 (s), 792 (m), 814 (s), 846 (s), 866 (w), 896 (s), 908 (w), 946 (w), 965 (w), 987 (w), 1025 (m), 1070 (w), 1114 (m), 1155 (w), 1181 (m), 1236 (s), 1272 (w), 1342 (s), 1375 (m), 1406 (w), 1435 (m), 1508 (m), 1589 (s), 1624 (w), 1670 (s), 1704 (s), 1713 (m), 3008 (m), 3065 (w).

***N*-phenyl-1,8-naphthalimide (PhNI)**. Naphthalic anhydride (514 mg, 2.59 mmol) and aniline (15 mL, 15.3 mL, 166 mmol) were stirred at 150 °C under a nitrogen atmosphere for 5 h. The mixture was then cooled to room temperature, poured into water (~75 mL), and acidified to pH 1 with 2 M HCl. The resulting solid was filtered and washed with water until the filtrate was neutral. The brown solid was further washed with methanol (4 × 25 mL) and then diethyl ether (2 × 25 mL). The crude product was purified by column chromatography, eluting with dichloromethane to afford a white solid (368 mg, 52%). ^{1}H NMR (500 MHz, $CDCl_3$): δ (ppm) 8.65 (dd, *J* = 7.3 Hz, 0.9 Hz, 2H), 8.28 (dd, *J* = 8.3 Hz, 0.9 Hz, 2H), 7.80 (dd, *J* = 8.0 Hz, 7.5 Hz, 2H), 7.56 (m, 2H), 7.49 (m, 1H), 7.33 (m, 2H). ^{13}C{^{1}H} NMR (125 MHz, $CDCl_3$): δ (ppm) 164.51, 135.59, 134.41, 131.92, 131.76, 129.53, 128.84, 128.79, 128.72, 127.18, 123.01. APCI-MS (positive mode) *m/z* calculated for $C_{18}H_{12}NO_2$ $[M + H]^+$ 274.09; found 274.14. IR (ATR): ν_{max} (cm^{-1}) 403 (s), 421 (m), 444 (m), 465 (m), 513 (s), 540 (s), 618 (w), 652 (s), 701 (s), 737 (m), 755 (s), 775 (s), 796 (s), 830 (m), 846 (s), 888 (s), 927 (w), 651 (w), 996 (w), 1002 (w), 1025 (m), 1070 (m), 1076 (m), 1116 (m), 1139 (m), 1159 (w), 1178 (m), 1191 (m), 1237 (s), 1269 (w), 1285 (w), 1308 (w), 1355 (s), 1377 (s), 1397 (w), 1434 (m), 1456 (m), 1489 (m),

1504 (m), 1582 (s), 1624 (m), 1659 (s), 1701 (s), 2850 (w), 2918 (w), 3011 (w), 3054 (w), 3072 (w), 3351 (w).

Anthracene-9-carboxylic acid was synthesised according to modified literature procedures.[1] Under an inert atmosphere, magnesium turnings (486 mg, 20.0 mmol) and an iodine crystal (catalytic) were added to dry diethyl ether (5 mL). The mixture was stirred for 10 min and then a solution of 9-bromoanthracene (2.57 g, 9.99 mmol) in dry diethyl ether (40 mL) was added dropwise over 30 min at room temperature. The suspension was then refluxed for 4 h during which time 9-anthracenylmagnesium bromide precipitated as a beige solid. CO_2 was then bubbled through the solution for 30 min, causing the solution to become clear and yellow. The solution was filtered to remove unreacted magnesium and the filtrate poured into a separating funnel. Ethyl acetate (100 mL) and dilute ammonia solution (200 mL) was added and the aqueous layer drained. The organic layer was extracted with a further portion of dilute ammonia solution (100 mL). The combined aqueous fractions were acidified to pH = 1 with 10 M HCl causing the crude product to precipitate. The crude product was filtered and purified by recrystallisation from ethanol to afford pure anthracene-9-carboxylic acid as yellow needles (691 mg, 31%). ^{1}H NMR (500 MHz, $(CD_3)_2SO$): δ (ppm) 13.92 (br s, 0.9 H, partially exchanged with D_2O), 8.73 (s, 1H), 8.16 (d, J = 8.4 Hz, 2H), 8.05 (m, 2H), 7.63 (m, 2H), 7.57 (m, 2H). $^{13}C\{^1H\}$ NMR (125 MHz, $(CD_3)_2SO$): δ (ppm) 170.17, 130.51, 129.71, 128.56, 128.27, 127.03, 126.91, 125.68, 124.87. ESI-MS (negative mode, MeOH): *m/z* calculated for $C_{15}H_9O_2$ $[M - H]^-$ 221.06; found 221.05.

1,1′-Diacetylferrocene was synthesised according to literature procedures.[2] $AlCl_3$ (6.10 g, 45.7 mmol) was suspended in dry DCM (20 mL) and stirred at 0 °C under a nitrogen atmosphere. After 5 min, acetyl chloride (3.10 mL, 43.6 mmol) was added, dissolving the $AlCl_3$. Subsequently, ferrocene (2.70 g, 14.5 mmol, dissolved in 35 mL of dry DCM) was added dropwise through an addition funnel over 15 min. After 1 h the reaction was allowed to warm to room temperature and stirred for a further 4 h. The reaction mixture was then poured onto ice and the organic phase separated in a separating funnel. The aqueous phase was washed with more DCM (2 × 40 mL) then the combined DCM extracts were washed with saturated $NaHCO_3$ solution (30 mL) and brine (30 mL). After drying with $MgSO_4$ the DCM was removed by rotary evaporation to afford a red solid. The crude material was purified by column chromatography (hexane:ethyl acetate 9:1 to 6:4) to afford the pure product as a bright red solid (2.40 g, 61%). ^{1}H NMR (300 MHz, $CDCl_3$): δ (ppm) 4.77 (s, 4H), 4.51 (s, 4H), 2.35 (s, 6H). $^{13}C\{^1H\}$ NMR (75 MHz, $CDCl_3$): δ (ppm) 201.38, 80.76, 73.75, 71.10, 27.79.

1,1′-Ferrocenedicarboxylic acid was synthesised according to literature procedures.[3] 1,1′-Diacetyl ferrocene (1.00 g, 3.70 mmol) was suspended in 5.5% sodium hypochlorite solution (19 mL) and stirred rapidly at 45–50 °C while shielded from light. Additional portions of 5.5% sodium hypochlorite (11 mL) were added after 1.5, 2, and 3 h. Following the last addition the reaction was stirred for another 2 h and then filtered while still warm. The clear orange filtrate was treated with sodium bisulfite until the pH was 7, then acidified with 2 M HCl to form an orange precipitate. The crude material was filtered, washed thoroughly with H_2O, and redissolved with $NaHCO_3$. Reacidification with 2 M HCl precipitated the pure product, with was filtered, washed with H_2O and dried to afford an orange powder (770 mg, 76%). ^{1}H NMR (300 MHz, $(CD_3)_2SO$): δ (ppm) 4.68 (s, 4H), 4.45 (s, 4H), the COOH peak was totally exchanged with D_2O. $^{13}C\{^1H\}$ NMR (75 MHz, $(CD_3)_2SO$): δ (ppm) 171.23, 73.54, 72.70, 71.39.

L-Fc(MeLeu)$_2$. 1,1′-Ferrocenedicarboxylic acid (384 mg, 1.40 mmol) and HATU (1.33 g, 3.50 mmol) were dissolved in DMF (8 mL) and cooled to 0 °C under an N_2 atmosphere. Triethylamine (1.40 mL, 1.02 g, 10.0 mmol) was added and the solution stirred for 30 mins. L-leucine methyl ester hydrochloride (636 mg, 3.50 mmol) was added and the reaction mixture was stirred at room temperature overnight (16 h). The resulting solution was diluted with H_2O (50 mL) and a yellow solid precipitated. The suspension was acidified to pH 2 with 2M HCl. The aqueous layer was then extracted with ethyl acetate (3 × 50 mL). The organic layer was then washed with H_2O (3 × 40 mL), saturated $NaHCO_3$ (30 mL) and brine (30 mL). The organic layer was dried with $MgSO_4$ then evaporated *in vacuo*. The crude material was purified by column chromomatography (5:5:1 hexane:ethyl acetate:DCM) to afford the product as an orange solid (696 mg, 94%). ^{1}H NMR (500 MHz, $CDCl_3$): δ (ppm) 7.76 (d, J = 8.3 Hz, 2H), 4.92 (m, 2H), 4.82–4.77 (m, 4H), 4.56 (m, 2H), 4.34 (m, 2H), 3.81 (s, 6H), 1.80 (m, 2H), 1.56–1.53 (m, 4H), 0.94 (d, J = 6.7 Hz, 6H), 0.92 (d, J = 6.6 Hz, 6H). $^{13}C\{^1H\}$ NMR (125 MHz, $CDCl_3$): δ (ppm) 176.81, 170.63, 75.86, 72.15, 71.45, 70.42, 70.28, 52.73, 50.95, 39.62, 25.02, 23.38, 21.05. ESI-MS (positive mode, MeOH): *m/z* calculated for $C_{26}H_{37}FeN_2O_6$ $[M + H]^+$ 529.20; found 529.17. ESI-MS (negative mode, MeOH): *m/z* calculated for $C_{26}H_{35}FeN_2O_6$ $[M - H]^-$ 527.18; found 527.20. IR (ATR): ν_{max} (cm^{-1}) 509 (s), 560 (m), 590 (m), 669 (m), 775 (m), 805 (m), 842 (m), 895 (w), 927 (w), 986 (m), 1019 (m), 1041 (w), 1096 (w), 1147 (m), 1180 (s), 1210 (s), 1270 (w), 1298 (m), 1377 (m), 1435 (m), 1534 (s), 1631 (s), 1736 (s), 2871 (w), 2956 (m), 3310 (m).

D-Fc(MeLeu)$_2$. Synthesised using the same procedure as for L-Fc(MeLeu)$_2$ except that D-leucine methyl ester hydrochloride was used (703 mg, 95%). ^{1}H NMR (500 MHz, $CDCl_3$): δ (ppm) 7.76 (d, *J* = 8.3 Hz, 2H), 4.92 (m, 2H), 4.82–4.77 (m, 4H), 4.56 (m, 2H), 4.34 (m, 2H), 3.81 (s, 6H), 1.81 (m, 2H), 1.56–1.53 (m, 4H), 0.94 (d, *J* = 6.7 Hz, 6H), 0.92 (d, *J* = 6.6 Hz, 6H). ^{13}C{^{1}H} NMR (125 MHz, $CDCl_3$): δ (ppm) 176.81, 170.64, 75.86, 72.15, 71.45, 70.42, 70.28, 52.73, 50.95, 39.63, 25.03, 23.38, 21.05. ESI-MS (positive mode, MeOH): *m/z* calculated for $C_{26}H_{37}FeN_2O_6$ $[M + H]^+$ 529.20; found 529.21. ESI-MS (negative mode, MeOH): *m/z* calculated for $C_{26}H_{35}FeN_2O_6$ $[M - H]^-$ 527.18; found 527.21. IR (ATR): ν_{max} (cm^{-1}) 510 (s), 561 (m), 591 (m), 667 (m), 777 (m), 805 (m), 843 (m), 895 (w), 927 (w), 986 (m), 1019 (m), 1041 (w), 1097 (w), 1148 (m), 1183 (s), 1212 (s), 1270 (m), 1300 (m), 1379

2-(4-aminophenyl)benzo[d]thiazol was prepared according to literature procedures.[4] Under a nitrogen atmosphere, polyphosphoric acid (10.0 g) was added to 2-aminothiophenol (1.04 g, 8.31 mmol) and 4-aminobenzoic acid (1.14 g, 8.31 mmol). The viscous solution was heated to 170 °C and stirred for 3 h. After cooling to room temperature, the resulting black mixture was poured onto H_2O (150 mL) and became bright yellow. The pH was adjusted to 7 with $NaHCO_3$, then the aqueous solution was poured into a separating funnel and extracted with ethyl acetate (3 × 50 mL). The organic layer was washed with brine (30 mL), dried with $MgSO_4$ and evaporated *in vacuo* to afford the crude product as a yellow solid. Purification by column chromatography (9:1 DCM:ethyl acetate) yielded the pure compound as a slightly green solid (1.14 g, 61%). ^{1}H NMR (300 MHz, $(CD_3)_2SO$): δ (ppm) 8.00 (d, *J* = 7.6 Hz, 1H), 7.90 (d, *J* = 8.0 Hz, 1H), 7.77 (d, *J* = 8.6 Hz, 2H), 7.45 (m, 1H), 7.33 (m, 1H), 6.68 (d, *J* = 8.6 Hz, 2H), 5.89 (s, 2H). ^{13}C{^{1}H} NMR (75 MHz, $(CD_3)_2SO$): δ (ppm) 168.15, 153.90, 152.16, 133.70, 128.76, 126.20, 124.29, 121.86, 121.74, 120.11, 113.60. ESI-MS (positive mode, MeOH): *m/z* calculated for $C_{13}H_{11}N_2S$ $[M + H]^+$ 227.06; found 227.11. ESI-MS (negative mode, MeOH): *m/z* calculated for $C_{13}H_9N_2S$ $[M - H]^-$ 225.05; found 225.04.

Methyl (4-(methoxycarbonyl)benzoyl)-L-valinate (Me$_2$CBV). Monomethyl terephthalic acid (343 mg, 1.90 mmol) and HATU (866 mg, 2.28 mmol) were dissolved in 1:1 THF/DMF (30 mL) and cooled to 0 °C under an Ar atmosphere. Triethylamine (1.20 mL, 871 mg, 8.61 mmol) was added and the solution stirred for 30 min. L-valine methyl ester hydrochloride (319 mg, 1.90 mmol) was added and the reaction mixture was stirred at room temperature for a further 40 h. The solvent was removed *in vacuo* and the residue was dissolved in ethyl acetate and washed with 2M HCl (2 × 30 mL), saturated $NaHCO_3$ (30 mL) and brine (20 mL). The organic layer was dried with $MgSO_4$ then evaporated *in vacuo*. The crude material was purified

by column chromomatography (3:1 hexane:ethyl acetate) to afford the product as a white solid (411 mg, 74%). ^{1}H NMR (300 MHz, $CDCl_3$): δ (ppm) 7.94 (m, 2H), 7.76 (m, 2H), 6.97 (s, 1H), 4.65 (m, 1H), 3.82 (s, 3H), 3.67 (s, 3H), 2.18 (m, 1H), 0.91 (m, 6H). ^{13}C{^{1}H} NMR (75 MHz, $CDCl_3$): δ (ppm) 172.40, 166.53, 166.10, 137.96, 132.69, 129.61, 127.13, 57.67, 52.24, 52.13, 31.32, 18.92, 18.02.

(4-carboxybenzoyl)-L-valine (H_2CBV). Me_2CBV (411 mg, 1.40 mmol) was dissolved in 1:1:1 THF/MeOH/1M $LiOH_{(aq)}$ (25.2 mL) and stirred at room temperature for 2 h. The organics were removed by rotary evaporation and the remaining aqueous portion was acidified to pH 1 with 2M HCl. The aqueous layer was then extracted with ethyl acetate (6 × 20 mL). The organic phase was then washed with brine (20 mL), dried with $MgSO_4$ and evaporated *in vacuo*, yielding the product as a white solid (371 mg, quantitative yield). ^{1}H NMR (300 MHz, $CDCl_3$): δ (ppm) 12.93 (brs, 1.5H, partially exchanged with D_2O), 8.62 (d, J = 8.1 Hz, 1H), 7.99 (m, 4H), 4.29 (m, 1H), 2.19 (m, 1H), 0.98 (d, J = 6.6 Hz, 3H), 0.96 (d, J = 6.6 Hz, 3H). ^{13}C{^{1}H} NMR (75 MHz, $CDCl_3$): δ (ppm) 172.98, 166.82, 166.32, 137.94, 133.10, 129.14, 127.88, 58.47, 29.48, 19.31, 18.79. ESI-MS (positive mode, MeOH): *m/z* calculated for $C_{13}H_{15}NNaO_5$ $[M + Na]^+$ 288.08; found 288.13. ESI-MS (negative mode, MeOH): *m/z* calculated for $C_{13}H_{14}NO_5$ $[M - H]^-$ 264.09; found 264.06.

Dimethyl thiophene-2,5-dicarbonyl-bis(L-valinate) Me_2TDV. Thiophene-2,5-dicarboxylic acid (273 mg, 1.59 mmol) and HATU (1.39 g, 3.66 mmol) were dissolved in DMF (15 mL) and cooled to 0 °C under an Ar atmosphere. Triethylamine (1.60 mL,1.16 g, 11.5 mmol) was added and the solution stirred for 30 mins. L-valine methyl ester hydrochloride (558 mg, 3.33 mmol) was added and the reaction mixture was stirred at room temperature for a further 24 h. The DMF was removed by rotary evaporation and the residue dissolved in ethyl acetate and washed with dilute HCl (2 × 30 mL), saturated $NaHCO_3$ (30 mL) and brine (20 mL). The organic layer was dried with $MgSO_4$ then evaporated *in vacuo*. The crude material was purified by column chromomatography (6:4 hexane:ethyl acetate) to afford the product as a white solid (565 mg, 89%). ^{1}H NMR (300 MHz, $CDCl_3$): δ (ppm) 7.51 (s, 2H), 6. 58 (d, J = 8.6 Hz, 2H), 4.72 (dd, J = 8.6 Hz, 4.9 Hz, 2H), 3.78 (s, 6H), 2.26 (m, 2H), 0.99 (m, 12H). ^{13}C{^{1}H} NMR (75 MHz, $CDCl_3$): δ (ppm) 172.44, 161.03, 142.04, 128.64, 57.69, 52.52, 31.75, 19.09, 18.06.

Thiophene-2,5-dicarbonyl-bis(L-valine) H_2TDV. Me_2TDV (199 mg, 0.50 mmol) was dissolved in 1:1:1 THF/MeOH/1M $LiOH_{(aq)}$ (9 mL) and stirred at room temperature for 2 h. The organics were removed by rotary evaporation and the remaining aqueous portion was

acidified to pH 1 with 2M HCl. The aqueous layer was then extracted with ethyl acetate (5 × 20 mL). The organic phase was then washed with brine (20 mL), dried with $MgSO_4$ and evaporated *in vacuo*, yielding the product as a white solid (185 mg, quantitative yield). ^{1}H NMR (300 MHz, $CDCl_3$): δ (ppm) 12.72 (brs, 1.5H, partially exchanged with D_2O), 8.60 (d, J = 8.2 Hz, 2H), 7.97 (s, 2H), 4.25 (m, 2H), 2.17 (m, 2H), 0.96 (m, 12H). ^{13}C{^{1}H} NMR (75 MHz, $CDCl_3$): δ (ppm) 172.82, 161.06, 142.77, 129.01, 58.34, 29.55, 19.26, 18.75. ESI-MS (negative mode, MeOH): *m/z* calculated for $C_{16}H_{21}N_2O_6S$ $[M - H]^-$ 369.11; found 369.10. IR (ATR): ν_{max} (cm^{-1}) 570 (m), 638 (m), 743 (s), 797 (m), 825 (m), 920 (w), 1023 (m), 1111 (w), 1152 (m), 1201 (m), 1259 (m), 1307 (m), 1394 (m), 1468 (w), 1511 (s), 1539 (s), 1623 (s), 1717 (s), 2963 (m), 3302 (br).

Dimethyl (4-(methoxycarbonyl)benzoyl)-L-aspartate (Me_3CBA). Monomethyl terephthalic acid (447 mg, 2.48 mmol) and HATU (1.08 g, 2.84 mmol) were dissolved DMF (15 mL) and cooled to 0 °C under an Ar atmosphere. Triethylamine (1.20 mL, 871 mg, 8.61 mmol) was added and the solution stirred for 30 mins. L-aspartic acid dimethyl ester hydrochloride (564 mg, 2.85 mmol) was added and the reaction mixture was stirred at room temperature overnight (16 h). The DMF was removed by rotary evaporation and the residue dissolved in water and acidified to pH 1 with 2M HCl. The aqueous layer was then extracted with ethyl acetate (5 × 20 mL). The organic layer was then washed with saturated $NaHCO_3$ (30 mL) and brine (20 mL). The organic layer was dried with $MgSO_4$ then evaporated *in vacuo*. The crude material was purified by column chromomatography (4:6 hexane:ethyl acetate) to afford the product as an off-white solid (719 mg, 90%). ^{1}H NMR (300 MHz, $CDCl_3$): δ (ppm) 8.08 (m, 2H), 7.85 (m, 2H), 7.32 (d, J = 7.7 Hz, 1H), 5.04 (m, 1H), 3.92 (s, 3H), 3.78 (s, 3H), 3.68 (s, 3H), 3.12 and 2.97 (ABq, J_{AB} = 17.4 Hz, J_{AX} = 4.3 Hz, J_{BX} = 4.5 Hz, 2H). ^{13}C{^{1}H} NMR (75 MHz, $CDCl_3$): δ (ppm) 171.76, 171.14, 166.29, 166.18, 137.56, 133.17, 129.94, 127.33, 53.07, 52.49, 52.22, 49.10, 36.03.

(4-carboxybenzoyl)-L-aspartic acid (H_3CBA). Me_3CBA (719 mg, 2.22 mmol) was dissolved in 1:1:1 THF/MeOH/1M $LiOH_{(aq)}$ (30 mL) and stirred at room temperature for 2 h. The organics were removed by rotary evaporation and the remaining aqueous portion was acidified to pH 1 with 2M HCl. The aqueous layer was then extracted with ethyl acetate (10 × 20 mL). The organic phase was then washed with brine (20 mL), dried with $MgSO_4$ and evaporated *in vacuo*, yielding the product as a white solid (614 mg, 98%). ^{1}H NMR (300 MHz, $(CD_3)_2SO$): δ (ppm) 12.78 (brs, 2.4H, partially exchanged with D_2O), 8.91 (d, J = 7.8 Hz, 1H), 8.03 (m, 2H), 7.94 (m, 2H), 4.76 (m, 1H), 2.85 and 2.72 (ABq, J_{AB} = 16.4 Hz, J_{AX} = 5.7 Hz, J_{BX} = 8.1

Hz, 2H). $^{13}C\{^{1}H\}$ NMR (75 MHz, $(CD_3)_2SO$): δ (ppm) 172.37, 171.72, 166.76, 165.44, 137.56, 133.23, 129.29, 127.59, 49.47, 35.73. ESI-MS (positive mode, MeOH): *m/z* calculated for $C_{12}H_{11}NNaO_7$ $[M + Na]^+$ 304.04; found 304.11. ESI-MS (negative mode, MeOH): *m/z* calculated for $C_{12}H_{10}NO_7$ $[M - H]^-$ 280.05; found 280.03. IR (ATR): ν_{max} (cm^{-1}) 460 (m), 531 (m), 539 (m), 639 (m), 652 (m), 693 (m), 725 (s), 795 (w), 831 (w), 873 (m), 957 (m), 1017 (m), 1117 (m), 1132 (w), 1163 (m), 1189 (s), 1285 (s), 1419 (s), 1442 (m), 1503 (w), 1533 (s), 1571 (m), 1635 (s), 1700 (s), 1748 (m), 2553 (br), 2673 (br), 2845 (br), 3416 (m).

Methyl *N*-((4-methoxycarbonyl)phenyl)-L-alaninate (Me_2CPA) was synthesised according to modified literature procedures.[5, 6] Methyl 4-iodobenzoate (786 mg, 3.0 mmol), L-alanine methyl ester hydrochloride (628 mg, 4.5 mmol), CuI (286 mg, 1.5 mmol), K_2CO_3 (829 mg, 6.0 mmol), and L-proline (172 mg, 1.5mmol) were suspended in DMSO (3 mL) under an inert atmosphere. The mixture was then stirred at 60 °C for 24 h, at which point TLC indicated the reaction was complete. The reaction mixture was then filtered through celite and washed with ethyl acetate (3 × 40 mL). The filtrate was then washed with H_2O (1 × 50 mL), saturated $NaHCO_3$ (1 × 50 mL), and brine (1 × 50 mL). The organic phase was dried with $MgSO_4$ then evaporated *in vacuo*. The crude material was purified by column chromatography (9:1 to 7:3 hexane:ethyl acetate) to afford the product as an off-white solid (250 mg, 35%). ^{1}H NMR (300 MHz, $CDCl_3$): δ (ppm) 7.88 (d, J = 8.5 Hz, 2H), 6.59 (d, J = 8.5 Hz, 2H), 5.17 (s, 1H), 4.20 (m, 1H), 3.86 (s, 3H), 3.74 (s, 3H), 1.48 (d, J = 6.9 Hz, 3H). $^{13}C\{^{1}H\}$ NMR (75 MHz, $CDCl_3$): δ (ppm) 174.05, 166.91, 150.43, 131.20, 118.49, 111.57, 51.90, 51.12, 50.88, 18.02.

***N*-(4-carboxyphenyl)-L-alanine (H_2CPA)**. Me_2CPA (250 mg, 1.05 mmol) was dissolved in 1:1:1 THF/MeOH/1M $LiOH_{(aq)}$ (15 mL) and stirred at room temperature for 2 h. The organics were removed by rotary evaporation and the remaining aqueous portion was acidified to pH 1 with 2M HCl. A beige solid precipitated which was collected by centrifugation (2500 rpm, 1 min). The supernatant was removed and replaced with fresh H_2O (5 mL) for two more centrifugal washes. The final product was dried under vacuum overnight to afford an off-white solid (74 mg, 35%). ^{1}H NMR (300 MHz, $(CD_3)_2SO$): δ (ppm) 12.33 (brs, 1.5H, partially exchanged with D_2O), 7.67 (d, J = 8.2 Hz, 2H), 6.65 (s, 1H), 6.56 (d, J = 8.2 Hz, 2H), 4.03 (m, 1H), 1.39 (d, J = 6.9 Hz, 3H). $^{13}C\{^{1}H\}$ NMR (75 MHz, $(CD_3)_2SO$): δ (ppm) 175.18, 167.44, 151.65, 131.05, 117.66, 111.29, 50.64, 17.95. ESI-MS (positive mode, MeOH): *m/z* calculated for $C_{10}H_{11}NNaO_4$ $[M + Na]^+$ 232.06; found 232.08. ESI-MS (negative mode, MeOH): *m/z* calculated for $C_{10}H_{10}NO_4$ $[M - H]^-$ 208.06; found 208.04.

Diethyl 4-bromopyridine-2,6-dicarboxylate was synthesised according to modified literature procedures.[7] PBr_5 (6.78 g, 15.7 mmol) and chelidamic acid monohydrate (702 mg, 3.49 mmol) were added to a flask under an inert atmosphere. The temperature was slowly increased to 90 °C to melt the reagents, taking care to keep the temperature below 100 °C. The reaction mixture was then stirred for 2.5 h and then cooled to room temperature. EtOH (25 mL) was added dropwise while the temperature was kept below 10 °C with an ice bath. The residual EtOH was then removed *in vacuo*, to afford a brown solid. The solid was dissolved in diethyl ether (50 mL) and saturated $NaHCO_3$ was added until the acid was neutralised (pH = 7). The mixture was poured into a separating funnel and the aqueous portion was extracted with diethyl ether (3 × 40 mL). The organic extracts were combined and washed with brine (1 × 30 mL). The organic layer was dried with $MgSO_4$ then evaporated *in vacuo*, yielding the final product as a light yellow solid (840 mg, 80%). ^{1}H NMR (300 MHz, $CDCl_3$): δ 8.42 (s, 2H), 4.49 (q, J = 7.1 Hz, 4H), 1.45 (t, J = 7.1 Hz, 6H). $^{13}C\{^1H\}$ NMR (75 MHz, $CDCl_3$): δ 163.69, 149.68, 135.04, 131.19, 62.86, 14.33. ESI-MS (negative mode, MeOH): *m/z* calculated for $C_{11}H_{13}BrNO_4$ $[M + H]^+$ 302.00/304.00; found 302.06/304.08.

2-hydroxybenzaldehyde oxime (salox) was synthesised according to modified literature procedures.[8] 2-hydroxybenzaldehyde (4.12 g, 33.7 mmol) was dissolved in ethanol (45 mL) and H_2O (5 mL) with stirring. $NaHCO_3$ (5.67 g, 67.4 mmol) and hydroxylamine hydrochloride (3.52 g, 50.6 mmol) were added, and the reaction heated to 45 °C for 2.5 h. The ethanol was removed by rotary evaporation and the residue diluted with H_2O (100 mL) and extracted with ethyl acetate (4 × 40 mL). The organic layer was washed with brine (30 mL), dried with $MgSO_4$ and evaporated *in vacuo*. The crude product was purified by column chromatography (8:2 hexane:ethyl acetate) to afford the pure 2-hydroxybenzaldehyde oxime as a light pink solid (4.53 g, 98%). ^{1}H NMR (300 MHz, $CDCl_3$): δ (ppm) 10.13 (brs, 1H), 9.12 (brs, 1H), 8.20 (s, 1H), 7.24 (m, 1H), 7.14 (dd, J = 7.7 Hz, 1.4 Hz, 1H), 6.96 (d, J = 8.2 Hz, 1H), 6.88 (t, J = 7.5 Hz, 1H). $^{13}C\{^1H\}$ NMR (75 MHz, $CDCl_3$): δ (ppm) 157.06, 152.60, 131.04, 130.63, 119.76, 116.66, 116.58. ESI-MS (negative mode, MeOH): *m/z* calculated for $C_7H_6NO_2$ $[M - H]^-$ 136.04; found 136.07.

(*S*)-2,2′-bis((2,6-diethoxycarbonylpyridin-4-yl)oxy)-1,1′-binaphthalene ((*S*)-Et$_4$DCPB) was synthesised according to modified literature procedures.[9] (*S*)-BINOL (287 mg, 1.0 mmol), diethyl 4-bromopyridine-2,6-dicarboxylate (906 mg, 3.0 mmol), CuI (190 mg, 1.0 mmol), dried Cs_2CO_3 (1.30 g, 4.0 mmol), salox (137 mg, 1.0 mmol), and dried, powdered 3 Å molecular sieves (400 mg) were suspended in dry MeCN (12 mL) under an inert atmosphere. The reaction

mixture was stirred at reflux for 24 h, turning red in colour. A further portion of dry MeCN (12 mL) was added and the reaction refluxed for a further 24 h, at which point TLC indicated the reaction was complete. After cooling to room temperature, the reaction mixture was filtered through celite and washed with DCM (4 × 20 mL). The DCM was removed *in vacuo* to afford the crude product as a brown oil. The crude material was purified by column chromatography (8:1 to 1:1 hexane:ethyl acetate) to yield the final product (182 mg, 25%). ^{1}H NMR (300 MHz, $CDCl_3$): δ (ppm) 8.01 (d, J = 8.6 Hz, 2H), 7.92 (d, J = 8.2 Hz, 2H), 7.60 (s, 4H), 7.46 (m, 2H), 7.36–7.27 (m, 6H), 4.39 (q, J = 7.0 Hz, 8H), 1.39 (t, J = 7.1 Hz, 12H). ^{13}C{^{1}H} NMR (75 MHz, $CDCl_3$): δ (ppm) 165.87, 164.13, 150.13, 148.97, 133.56, 131.52, 131.38, 128.41, 127.39, 126.21, 125.67, 123.24, 119.75, 115.87, 62.28, 14.11.

(*S*)-2,2′-bis((2,6-dicarboxypyridin-4-yl)oxy)-1,1′-binaphthalene ((*S*)-H$_4$DCPB). This synthesis was ultimately unsuccessful, however is include for completeness. (*S*)-Et4DCPB (182 mg, 0.25 mmol), was dissolved in 1:1:1 THF/MeOH/1M $LiOH_{(aq)}$ (15 mL) and stirred at room temperature for 2 h and at 60 °C for 3 h. The organics were removed by rotary evaporation and the remaining aqueous portion was acidified to pH 4 with 2 M HCl. This formed a gel which was collected by centrifugation (4000 rpm, 5 min). The supernatant was removed and replaced with fresh H_2O (10 mL) for two more centrifugal washes. The gel was dried overnight at 95 °C, reducing to a tiny amount of insoluble beige powder.

1,3,5-benzenetricarbonyl chloride. Under an inert atmosphere, trimesic acid (871 mg, 4.1 mmol) was suspended in $SOCl_2$ (9 mL, 124 mmol) and 1 drop of DMF was added. The suspension was stirred at 70 °C for 3 h and then refluxed for 2 h during which time all the solids had dissolved. The $SOCl_2$ was removed by rotary evaporation to afford a slightly yellow oil. Residual $SOCl_2$ was removed by adding dry toluene (2 × 10 mL) and removing solvent by rotary evaporation. The synthesised 1,3,5-benzenetricarbonyl chloride was not characterised and instead used immediately in the next step.

Triemthyl trimesoyl(trialaninate) (Me$_3$TMTA). L-alanine methyl ester hydrochloride (2.58 g, 18.5 mmol) and triethylamine (6.86 mL, 49.2 mmol) were suspended in dry DCM (20 mL). The just-synthesised 1,3,5-benzenetricarbonyl chloride was added dropwise over 10 min at 0 °C. The suspension was stirred for 21 h at room temperature and became beige/off white. The reaction mixture was poured into a separating funnel and water added. The aqueous layer was acidified to pH~1 with 2M HCl. The DCM layer was then drained, and the aqueous layer was further extracted with DCM (4 × 30 mL). The combined DCM extracts were then washed with

saturated $NaHCO_3$ (40 mL) and brine (40 mL). The DCM layer was dried with $MgSO_4$ and then evaporated *in vacuo*. The crude product was purified by column chromatography (hexane:ethyl acetate, gradient) yielding the product as a white solid (870 mg, 45%). ^{1}H NMR (500 MHz, $CDCl_3$): δ (ppm) 8.11 (s, 3H), 7.71 (d, J = 7.6 Hz, 3H), 4.77 (m, 3H), 3.80 (s, 9H), 1.58 (d, J = 7.3 Hz, 9H). ^{13}C{^{1}H} NMR (125 MHz, $CDCl_3$): δ (ppm) 173.92, 166.17, 135.09, 128.77, 52.65, 48.96, 17.53. ESI-MS (positive mode, MeOH): *m/z* calculated for $C_{21}H_{27}N_3NaO_9$ $[M + Na]^+$ 488.16; found 488.17. ESI-MS (negative mode, MeOH): *m/z* calculated for $C_{21}H_{26}N_3O_9$ $[M - H]^-$ 464.17; found 464.15.

Trimesoyl tris(L-alanine) (H_3TMTA). Me_3TMRA (870 mg, 1.87 mmol) was dissolved in 4:1 MeOH:H_2O (25 mL) and NaOH (336 mg, 8.40 mmol) was added. The solution was stirred at room temperature overnight and then at 45 °C for 1 h. The MeOH was then removed in vacuo and the remaining aqueous solution acidified to pH = 1 with 2M HCl. The acidified solution was cooled in an ice bath, causing a solid to precipitate. The solid was filtered, washed with ice-cold H_2O (2 × 20 mL), and dried to afford the pure product as a white solid (520 mg, 66%). ^{1}H NMR (500 MHz, $(CD_3)_2SO$): δ (ppm) 12.59 (s, 2.6 H, partially exchanged with D_2O), 8.95 (d, J = 7.2 Hz, 3H), 8.47 (s, 3H), 4.46 (m, 3H), 1.42 (d, J = 7.4 Hz, 9H). ^{13}C{^{1}H} NMR (125 MHz, $(CD_3)_2SO$): δ (ppm) 173.98, 165.44, 134.45, 129.14, 48.32, 16.86. ESI-MS (positive mode, MeOH): *m/z* calculated for $C_{18}H_{22}N_3O_9$ $[M+H]^+$ 424.14; found 424.05. ESI-MS (negative mode, MeOH): *m/z* calculated for $C_{18}H_{20}N_3O_9$ $[M - H]^-$ 422.12; found 422.15. IR (ATR): ν_{max} (cm^{-1}) 434 (w), 519 (m), 538 (m), 605 (m), 691 (m), 719 (m), 816 (w), 836 (w), 884 (w), 921 (m), 967 (w), 1053 (m), 1125 (w), 1133 (w), 1163 (s), 1238 (s), 1290 (m), 1310 (w), 1327 (w), 1383 (w), 1411 (w), 1456 (m), 1549 (s), 1627 (s), 1714 (s), 2552 (br), 2641 (w), 2904 (br), 2990 (w), 3056 (m), 3218 (m), 3390 (m).

2.3 Thin Films

All thin films were prepared by spin coating onto quartz slides. Before spin coating, the quartz slides were cleaned using the following procedure: sonication in acetone for 10 min, sonication in 2-propanol for 10 min, treatment with ozone cleaner for 10 min.

Thin films of (*S*)- and (*R*)-BNI were prepared by pipetting 50 µL of a 11.5 mM chloroform solution onto the quartz slide and spinning at 1000 rpm for 1 min. Thin films of D- and L-Fc(MeLeu)$_2$ were prepared by pipetting 50 µL of a 30 mM chloroform solution onto the quartz slide and spinning at 500 rpm for 1 min. When acquiring UV-vis and CD spectra of thin films, the slides were aligned such that the film was on the side of the slide facing the detector. When

acquiring fluorescence and CPL spectra of thin films, the slides were aligned such that film was on the side of the slide facing the excitation source.

2.4 MOF Synthesis

2.4.1 Solvothermal Syntheses

General method for the synthesis of $[Ln_2(CBA)_2(H_2O)_4]\cdot 4H_2O$ MOFs. H_3CBA (8 mg, 28.4 μmol) was dissolved in DEF (1 mL) and H_2O (3 mL). $Ln(NO_3)_3\cdot 6H_2O$ (28.4 μmol) was dissolved in H_2O (50 μL) and added to the H_3CBA solution. The resulting solution was sealed and heated at 75 °C for 18 h. The resulting MOF crystals were purified by soaking in H_2O, which was replaced with fresh solvent after 12 h a total of three times. The obtained crystals were suitable for SCXRD analysis.

$[La_2(CBA)_2(H_2O)_4]\cdot 4H_2O$ (La-1) formed as colourless crystals (13 mg, 47%). IR (ATR): ν_{max} (cm^{-1}) 428 (w), 466 (m), 513 (m), 579 (w), 659 (w), 734 (m), 805 (w), 850 (m), 877 (w), 902 (w), 946 (w), 984 (w), 1016 (w), 1053 (w), 1098 (w), 1204 (w), 1241 (w), 1296 (w), 1333 (w), 1358 (m), 1407 (s), 1550 (s), 1576 (w), 1616 (w), 3349 (br).

$[Ce_2(CBA)_2(H_2O)_4]\cdot 4H_2O$ (Ce-1) formed as colourless crystals (12 mg, 43%). IR (ATR): ν_{max} (cm^{-1}) 429 (w), 468 (m), 514 (m), 580 (w), 660 (w), 733 (m), 805 (w), 851 (m), 878 (w), 902 (w), 948 (w), 986 (w), 1016 (w), 1052 (w), 1101 (w), 1205 (w), 1242 (w), 1294 (w), 1332 (w), 1357 (w), 1409 (s), 1550 (s), 1576 (w), 1616 (w), 3356 (br).

$[Pr_2(CBA)_2(H_2O)_4]\cdot 4H_2O$ (Pr-1) formed as light green crystals (10 mg, 36%). IR (ATR): ν_{max} (cm^{-1}) 425 (w), 469 (m), 514 (m), 580 (w), 659 (w), 733 (m), 805 (w), 851 (m), 877 (w), 902 (w), 947 (w), 985 (w), 1015 (w), 1052 (w), 1099 (w), 1207 (w), 1240 (w), 1296 (w), 1332 (w), 1357 (m), 1410 (s), 1550 (s), 1576 (w), 1612 (w), 3355 (br).

$[Nd_2(CBA)_2(H_2O)_4]\cdot 4H_2O$ (Nd-1) formed as light purple crystals (9 mg, 32%). IR (ATR): ν_{max} (cm^{-1}) 429 (w), 469 (m), 513 (m), 579 (w), 661 (m), 733 (m), 805 (w), 850 (m), 877 (w), 902 (w), 948 (w), 987 (w), 1016 (w), 1054 (w), 1100 (w), 1203 (w), 1239 (w), 1293 (w), 1330 (w), 1356 (m), 1409 (s), 1547 (s), 1571 (w), 1611 (w), 3356 (br).

$[Sm_2(CBA)_2(H_2O)_4]\cdot 4H_2O$ (Sm-1) and **Sm-2** formed as a mixed batch of colourless crystals of Sm-1 alongside opaque white chunks of Sm-2. A yield was not calculated because the relative amounts of Sm-1 and Sm-2 could not be determined.

Eu-2 and **Gd-2** formed as opaque white chunks. A yield was not calculated because the composition of Eu-2 and Gd-2 could not be determined.

Cd-1. The MOF formed from H_2CPA and Cd was synthesised with the following procedure: H_2CPA (2.0 mg, 9.6 μmol) was dissolved in DMF (3 mL) and EtOH (1 mL). $Cd(NO_3)_2 \cdot 4H_2O$ (2.9 mg, 9.4 μmol) was dissolved in DMF (100 μL) and added to the H_2CPA solution. The solution was sealed and heated at 80 °C for 21 h. The resulting product was purified by soaking in EtOH, which was replaced with fresh solvent after 12 h a total of three times. A yield was not calculated because the composition of Cd-1 could not be determined.

2.4.2 Diffusion Syntheses

La-3. Diffusion syntheses were carried out with a vial-in-vial approach. H_3CBA (7.0 mg, 25 μmol) was weighed into a small 2 mL open-topped vial and placed inside a larger 21 mL vial. To this small vial was added 2M LiOH(aq) (37.3 μL, 3 equivalents) to deprotonate H_3CBA. $La(NO_3)_3 \cdot 6H_2O$ (10.8, 25 μmol) was dissolved in H_2O and the solution added to the larger vial. The small vial was then very slowly filled with solvent (typically two-solvent mixtures of DMF, EtOH, and H_2O) until the solvent level was just below the top of the small vial. The solvent addition was carefully controlled by use of a syringe and needle, to allow the solvent to run down the side of the vial. The large vial was then gently filled with the same solvent so as not to disturb the denser, aqueous $La(NO_3)_3 \cdot$layer until the solvent level was just above the top of the small vial to enable diffusion between the two. The large vial was then sealed, and the diffusions were left for 8 weeks, affording crystals of La-3. A yield was not calculated because the composition of La-3 could not be determined.

2.5 Characterisation Techniques

Nuclear Magnetic Resonance (NMR)

Solution state ^{1}H and $^{13}C\{^1H\}$ NMR spectra were collected on a Bruker NEO 300 MHz or Bruker NEO 500 MHz spectrometer at 298 K. Chemical shifts (δ) are reported in parts per million (ppm) and are referenced relative to the deuterated solvent residual peaks.[10] Data are reported with the following notation: s = singlet, d = doublet, t = triplet, q = quartet, m = multiplet, br = broad, ABq = AB quartet. Spectra were analysed using TopSpin v3.6.5.

Electrospray Ionisation Mass Spectrometry (ESI-MS)

Mass spectra were collected on a Bruker amazon SL mass spectrometer running in either positive or negative ESI mode. Samples were dissolved in mass spectrometry grade methanol.

Atmospheric Pressure Chemical Ionisation Mass Spectrometry (APCI-MS)

APCI-MS was performed by staff at The University of Sydney, School of Chemistry Mass Spectrometry facility. Low resolution mass spectra were collected on a Bruker amazon SL ion trap mass spectrometer running in APCI direct probe mode.

Attenuated Total Reflection (ATR) Fourier-Transform Infrared (FTIR) Spectroscopy

Solid state FTIR spectra were obtained with a Perkin Elmer Spectrum Two FTIR spectrometer equipped with a UATR accessory with a diamond window. Spectra were measured over the range of 400–4000 cm^{-1} with a resolution of 2 cm^{-1}, averaged over 16 accumulations. Data are reported with the following notation: s = strong, m = medium, w = weak, br = broad.

Solution State Fourier-Transform Infrared (FTIR) Spectroscopy

Solution state FTIR spectra were obtained with a Shimadzu IRAffinity-1S FTIR spectrometer. Samples were dissolved in DCM and a small amount was sandwiched between two glass slides in a demountable liquid cell holder. Spectra were measured over the range of 2000–4000 cm^{-1} with a resolution of 2 cm^{-1}, averaged over 16 accumulations.

Electrochemistry

Cyclic voltammetry (CV) and squarewave voltammetry (SWV) experiments were conducted at room temperature with a BASi Epsilon Electrochemical Analyser.

Solution state experiments were performed in a degassed 0.1 M $[(n\text{-}C_4H_9)_4N]PF_6$/MeCN electrolyte solution under an Ar atmosphere. A three-electrode setup was used, consisting of a glassy carbon working electrode (1 mm diameter), a Pt counter electrode, and Ag wire *quasi*-reference electrode. Squarewave experiments were run with an amplitude of 25 mV, frequency of 15 Hz and step size of 4 mV. The ferrocene/ferrocenium ion (Fc/Fc^+) redox couple was used as an internal reference.

Solid state CV of (*S*)-BNI was performed in a degassed 0.25 M $NaCl_{(aq)}$ electrolyte under an Ar atmosphere. A three-electrode setup was used, consisting of a glassy carbon working electrode (1 mm diameter), a Pt counter electrode, and Ag/AgCl reference electrode. Prior to

measurement, (*S*)-BNI was drop-casted onto the glassy carbon electrode from a 11.5 mM chloroform solution.

Solution State Ultraviolet-Visible (UV-vis) Spectroscopy

Solution state UV-vis spectra were collected with an Agilent Cary 60 UV-vis spectrometer operating in dual beam mode. Spectra were acquired at a scan rate of 600 nm/min and a spectral bandwidth of 1 nm. A quartz cuvette (1 cm pathlength) was used for all experiments.

Solid State Ultraviolet-Visible-Near Infrared (UV-vis-NIR) Spectroscopy

UV-vis-NIR spectra were collected with an Agilent Cary 5000 spectrometer equipped with a Harrick Praying Mantis™ attachment. A background measurement was performed on powdered $BaSO_4$. Samples were prepared as finely ground powders, homogenously mixed at <5% w/w with a $BaSO_4$ matrix. Spectra were acquired at a scan rate of 600 nm/min and a spectral bandwidth of 1 nm.

Fluorescence Spectroscopy

Excitation and emission spectra were obtained with a Shimadzu RF-6000 fluorescence spectrometer. Solution state measurements were performed on samples with a measured absorbance of less than 0.1. For solid-state measurements the sample was immobilised between two quartz slides and inserted into the sample compartment at a 90° angle. In all experiments the excitation and emission bandwidths were tuned to give acceptable signal intensity. A quartz cuvette (1 cm pathlength) was used for all experiments.

Circular Dichroism (CD) Spectroscopy

CD spectra were obtained with a Jasco J-1500 CD spectrometer. Spectra were collected at a scan rate of 100 nm/min, data interval time of 0.5 s, and a spectral bandwidth of 1 nm. The number of accumulations was chosen to attain suitable signal-to-noise levels. The sample compartment was continuously purged with nitrogen during all spectral acquisitions. A quartz cuvette (1 cm pathlength) was used for all solution state experiments. When acquiring spectra of thin films, the films were aligned such that the film was on the side of the slide facing the detector. CD spectra of MOFs were acquired on a small amount of powdered sample sandwiched between two quarts slides.

Magnetic Circular Dichroism (MCD) Spectroscopy

MCD spectra were acquired with a Jasco J-1500 CD spectrometer with either a 1.6 T PM-491 magnet or 0.4 T PM-409 magnet in the sample compartment. The acquisition parameters were the same as for CD. A quartz cuvette (0.5 cm path length) was used for all experiments. Each sample was measured for both magnet orientations, i.e. N→S and S→N. When measuring chiral analytes, the observed difference in absorbance, ΔA (ΔA = A_L – A_R), will be a combination of both the CD response and the MCD response:

$$\Delta A_{N\to S} = CD + MCD_{N\to S} \tag{2.1}$$

$$\Delta A_{S\to N} = CD + MCD_{S\to N} \tag{2.2}$$

Additionally, the MCD response is equal in magnitude but opposite in sign for opposing magnetic field orientations:

$$MCD_{N\to S} = -MCD_{S\to N} \tag{2.3}$$

Therefore, the isolated MCD signal is obtained using the following equations:

$$MCD_{N\to S} = \frac{\Delta A_{N\to S} - \Delta A_{S\to N}}{2} \tag{2.4}$$

$$MCD_{S\to N} = \frac{\Delta A_{S\to N} - \Delta A_{N\to S}}{2} \tag{2.5}$$

In this thesis, the MCD spectra displayed in all figures were calculated according to equations 2.4 and 2.5.

Variable Temperature Circular Dichroism (VT CD)

VT CD experiments were performed with a Jasco J-1500 CD spectrometer containing a Peltier thermostat-controlled cell holder PTC-510. The temperature ramp rate was 0.75 °C/min with a rest time of 60 s and stabilisation time of 10 s before each spectrum was recorded. The spectral acquisition parameters were the same as for CD. A quartz cuvette (1 cm pathlength) was used for all experiments. Even temperature distribution was maintained by a small stirrer bar in the bottom of the cuvette rotating at 100 rpm.

Circularly Polarised Luminescence (CPL)

CPL spectra were acquired with an Olis CPL Solo spectrometer. Spectra were collected at a scan rate of 100 nm/min, a spectral bandwidth of 2 nm. A quartz cuvette (1 cm pathlength) was

used for all solution state experiments. When acquiring spectra of thin films, the films were aligned at a 35° angle to the source to minimise specular reflection of the excitation light to the detector. The slides were orientated such that the excitation light would directly illuminate the film without passing through the rest of the slide.

Magneto-Chiral Dichroism (MChD)

MChD spectra were acquired at room temperature with an Agilent Cary 5000 spectrometer with a 1.6 T PM-491 magnet in the sample compartment. Each sample was measured for both magnet orientations, i.e. N→S and S→N. A quartz cuvette (0.5 cm path length) was used for all experiments.

UV-vis Spectroelectrochemistry (UV-vis SEC) and Circular Dichroism Spectroelectrochemistry (CD SEC)

UV-vis SEC experiments were obtained at room temperature with an Agilent Cary 5000 UV-vis-NIR spectrometer. Spectra were collected at a scan rate of 200 nm/min and a spectral bandwidth of 1 nm. CD SEC experiments were obtained at room temperature with a Jasco J-1500 CD spectrometer. Spectra were collected at a scan rate of 100 nm/min and a spectral bandwidth of 1 nm. Both UV-vis SEC and CD SEC experiments used the same electrochemical cell and electrode setup. The electrochemical cell consisted of a quartz cuvette (0.068 cm path length) fused to an upper solvent reservoir and filled with a 0.25 M $[(n\text{-}C_4H_9)_4N]PF_6$/MeCN electrolyte solution. A working electrode consisting of a Pt mesh attached to Pt wire was inserted into the cuvette part of the cell. For UV-vis SEC experiments operating in dual beam mode, a matching piece of Pt mesh was placed in the reference beam. A coiled Pt wire and an Ag wire acted as the counter and *quasi*-reference electrodes, respectively. These two electrodes were placed in separate glass tubes capped by a glass frit. These tubes were then placed into the reservoir part of the cell. The analyte solution was degassed with N_2 prior to measurement and the apparatus was enclosed by a Teflon lid to allow an inert atmosphere to be maintained. A schematic of the setup is shown below (Figure 2.1). The voltage was controlled with an eDAQ e-corder 410 potentiostat or PalmSens EmStat4S high range potentiostat. Internal calibration with a redox standard (e.g. Fc/Fc^+) was not possible for these experiments. Therefore, given the inherent variability of *quasi*-reference electrodes,[11-13] the exact potential at which each spectrum was obtained is not reported. Instead, the potential was incrementally changed from an initial point corresponding to the neutral species, until no further spectral changes were observed, corresponding to the fully oxidised/reduced species.

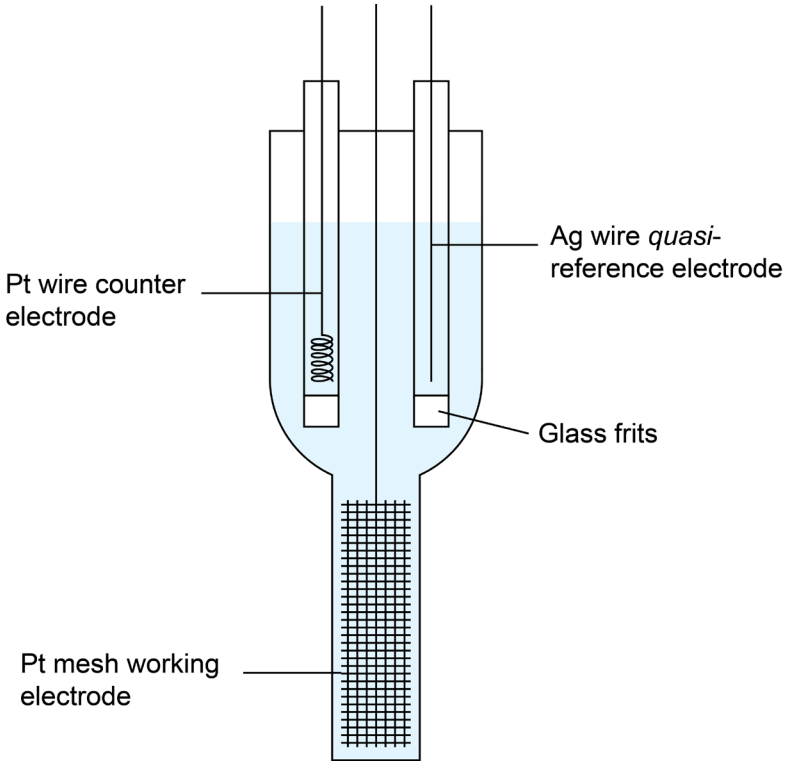

Figure 2.1. Schematic of the SEC cell used for UV-vis and CD SEC experiments. Cell lid not shown for clarity.

Electron Paramagnetic Resonance (EPR) Spectroscopy

Continuous wave EPR spectra were recorded with a Bruker EMXnano X-band spectrometer operating at room temperature. Acquisition parameters such as receiver gain, modulation amplitude, microwave power, and number of scans were adjusted for each sample as required. The magnetic field was calibrated using a strong pitch reference standard (g = 2.0028). Simulated spectra were generated using the EasySpin software package.[14]

Electron Paramagnetic Resonance Spectroelectrochemistry (EPR SEC)

Continuous wave EPR SEC spectra were measured at room temperature with a Bruker EMXnano X-band spectrometer. The electrochemical cell was made from a glass pipette, flame sealed at the narrow end and filled with a degassed 0.1 M [(n-C_4H_9)$_4$N]PF_6/MeCN or 0.1 M [(n-C_4H_9)$_4$N]PF_6/DMF electrolyte solution. The electrodes consisted of a Pt working electrode, a Pt counter electrode, and Ag *quasi*-reference electrode. The ends of both the working and counter electrodes were coiled to increase their surface area. All three electrodes were Teflon-coated, leaving just the ends exposed, and arranged in a staggered format to prevent them from touching. A schematic of the setup is shown below (Figure 2.2). Once the cell was setup it was immediately sealed with parafilm to prevent exposure to atmospheric oxygen and water.

Acquisition parameters such as receiver gain, modulation amplitude, microwave power, and number of scans were adjusted for each sample as required. The magnetic field was calibrated using a strong pitch reference standard (g = 2.0028). The voltage was controlled with an eDAQ e-corder 410 potentiostat or PalmSens EmStat4S high range potentiostat. As with UV-vis and CD SEC, internal calibration with a redox standard was not possible for these experiments, hence the exact potential at which each spectrum was obtained is not reported. Instead, the potential was incrementally changed from an initial point corresponding to the neutral species, until a sufficient radical signal was generated. Simulated spectra were generated using the EasySpin software package.

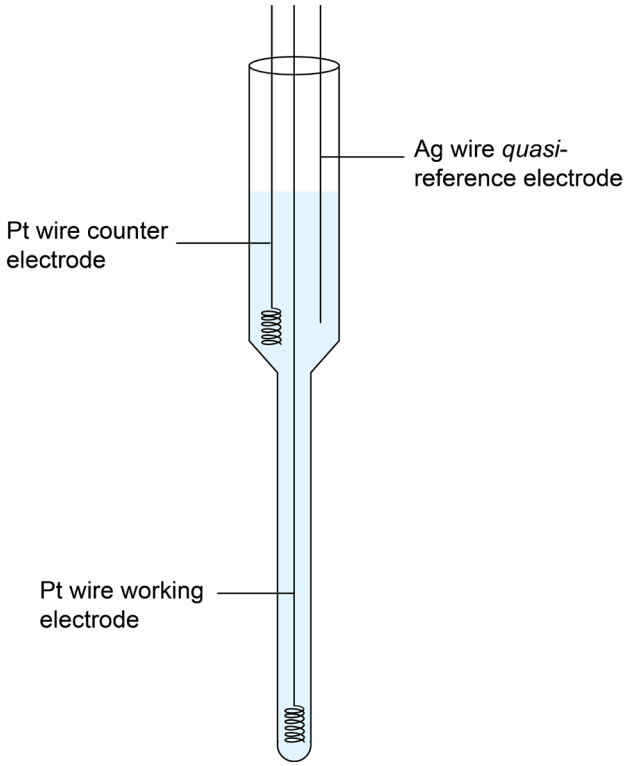

Figure 2.2. Schematic of the SEC cell used for EPR SEC experiments.

Powder X-Ray Diffraction (PXRD)

PXRD patterns were collected with a PANalytical X'Pert PRO diffractometer equipped with a solid-sate PIXcel detector using Cu-$K_{\alpha 1}$ (1.5406 Å) radiation. Samples were loaded into glass capillaries which were rotated during data collection. Pawley refinements were performed using the GSAS-II software package.[15] Simulated powder patterns were generated from single crystal structures with the Mercury software package.[16]

Single Crystal X-Ray Diffraction (SCXRD)

SCXRD data collection and refinement were performed with assistance from Dr Hunter Windsor. Single crystal X-ray data collections were performed using a Rigaku XtaLAB Synergy-DW Custom diffractometer equipped with an FR-X rotating-anode source outputting confocal mirror-monochromated Cu-Kα radiation (λ = 1.54184 Å) and fitted with a Rigaku HyPix-6000HE detector. Crystals were isolated directly from the crystallisation mother liquor using Paratone-N oil as a cryoprotectant before being attached to the instrument goniometer and cooled to 150 K. Data were collected about ω scans and then were integrated and reduced with absorption corrections (Gaussian grid face-indexed numerical integration with beam profile) being applied using CrysAlisPro. Structure solutions were obtained by intrinsic phasing using SHELXT[17] and were refined by full-matrix least-squares on all unique F^2 values using SHELXL[18] as implemented within the OLEX2-1.5 GUI.[19] Molecular and crystal structure drawings were made using CrystalMaker 11 version 11.0.2.

Thermogravimetric Analysis (TGA)

Experiments were performed on a TA Instruments Discovery TGA. Approximately 5 mg of sample was loaded onto a platinum pan and heated from room temperature to 650 °C at a ramp rate of 2 °C/min under a nitrogen flow of 20 mL/min.

2.6 Density Functional Theory (DFT) Calculations

Density Functional Theory (DFT) calculations were performed by Dr Bun Chan. Standard density functional theory calculations were carried out with ORCA 6.[20] All computations included the effect of solvation in acetonitrile with the CPCM model.[21] Geometries were optimized with the ωB97X-3c method.[22] For (*S*/*R*)-BNI^{2-}, we computed both the biradical and the triplet species, with the former being somewhat lower in energy, which is consistent with experimental observations. Refined single-point energies were obtained at the ωB97X-D4(rev)/ma-def2-TZVP level for the calculation of redox potentials.[22, 23] In addition to the (*S*/*R*)-BNI and PhNI species, we also computed the energies for Fc and Fc$^+$ for a direct comparison with experiment. The TDA approach was used for the calculation of electronic transitions.[24] The ωB97X-3c method was used as the use of ωB97X-D4(rev)/ma-def2-TZVP was computationally unfeasible with our computational resources for many larger ((*S*/*R*)-BNI) species in the present study. To account for the systematic deviations in the TDA-ωB97X-3c calculations, we calibrated the energies of the electronic transitions against those of TD-

ωB97X-D4(rev)/ma-def2-TZVP for the neutral PhNI molecule, for which the computations were feasible with the higher-level method. Accordingly, the TDA-ωB97X-3c transitions were uniformly shifted downward by 2000 cm^{-1}. The simulated spectra were obtained by assuming a Gaussian shape for each transition with a half-width of 1000 cm^{-1}.

2.7 References

(1) Bachmann, W. E.; Kloetzel, M. C. PREPARATION AND REACTIONS OF 9-ANTHRYLMAGNESIUM BROMIDE. *J. Org. Chem.* **1938**, *03*, 55-61.

(2) Wen, Y.; Cheng, Z.; Li, W.; Li, Z.; Liao, D.; Hu, X.; Pan, N.; Wang, D.; Hull, T. R. A novel oligomer containing DOPO and ferrocene groups: Synthesis, characterization, and its application in fire retardant epoxy resin. *Polym. Degrad. Stab.* **2018**, *156*, 111-124.

(3) Knobloch, F. W.; Rauscher, W. H. Condensation polymers of ferrocene derivatives. *J. Polym. Sci.* **1961**, *54*, 651-656.

(4) Ankenbruck, N.; Kumbhare, R.; Naro, Y.; Thomas, M.; Gardner, L.; Emanuelson, C.; Deiters, A. Small molecule inhibition of microRNA-21 expression reduces cell viability and microtumor formation. *Biorg. Med. Chem.* **2019**, *27*, 3735-3743.

(5) Ma, D.; Cai, Q.; Zhang, H. Mild Method for Ullmann Coupling Reaction of Amines and Aryl Halides. *Org. Lett.* **2003**, *5*, 2453-2455.

(6) Zhang, H.; Cai, Q.; Ma, D. Amino Acid Promoted CuI-Catalyzed C−N Bond Formation between Aryl Halides and Amines or N-Containing Heterocycles. *J. Org. Chem.* **2005**, *70*, 5164-5173.

(7) Pryor, K. E.; Shipps, G. W.; Skyler, D. A.; Rebek, J. The activated core approach to combinatorial chemistry: A selection of new core molecules. *Tetrahedron* **1998**, *54*, 4107-4124.

(8) Zhu, J.; Ye, Y.; Ning, M.; Mándi, A.; Feng, Y.; Zou, Q.; Kurtán, T.; Leng, Y.; Shen, J. Design, Synthesis, and Structure–Activity Relationships of 3,4,5-Trisubstituted 4,5-Dihydro-1,2,4-oxadiazoles as TGR5 Agonists. *ChemMedChem* **2013**, *8*, 1210-1223.

(9) Cristau, H.-J.; Cellier, P. P.; Hamada, S.; Spindler, J.-F.; Taillefer, M. A General and Mild Ullmann-Type Synthesis of Diaryl Ethers. *Org. Lett.* **2004**, *6*, 913-916.

(10) Gottlieb, H. E.; Kotlyar, V.; Nudelman, A. NMR Chemical Shifts of Common Laboratory Solvents as Trace Impurities. *J. Org. Chem.* **1997**, *62*, 7512-7515.

(11) Bond, A. M.; Lay, P. A. Cyclic voltammetry at microelectrodes in the absence of added electrolyte using a platinum quasi-reference electrode. *J. Electroanal. Chem. Interfacial Electrochem.* **1986**, *199*, 285-295.

(12) Huber, B.; Roling, B. Development of a Ag/Ag^+ micro-reference electrode for electrochemical measurements in ionic liquids. *Electrochim. Acta* **2011**, *56*, 6569-6572.

(13) Snook, G. A.; Best, A. S.; Pandolfo, A. G.; Hollenkamp, A. F. Evaluation of a $Ag|Ag^+$ reference electrode for use in room temperature ionic liquids. *Electrochem. Commun.* **2006**, *8*, 1405-1411.

(14) Stoll, S.; Schweiger, A. EasySpin, a comprehensive software package for spectral simulation and analysis in EPR. *J. Magn. Reson.* **2006**, *178*, 42-55.

(15) Toby, B. H.; Von Dreele, R. B. GSAS-II: the genesis of a modern open-source all purpose crystallography software package. *J. Appl. Crystallogr.* **2013**, *46*, 544-549.

(16) Macrae, C. F.; Sovago, I.; Cottrell, S. J.; Galek, P. T. A.; McCabe, P.; Pidcock, E.; Platings, M.; Shields, G. P.; Stevens, J. S.; Towler, M.; et al. Mercury 4.0: from visualization to analysis, design and prediction. *J. Appl. Crystallogr.* **2020**, *53*, 226-235.

(17) Sheldrick, G. M. SHELXT - Integrated space-group and crystal-structure determination. *Acta Crystallogr. A* **2015**, *71*, 3-8.

(18) Sheldrick, G. M. Crystal structure refinement with SHELXL. *Acta Crystallogr. C* **2015**, *71*, 3-8.

(19) Dolomanov, O. V.; Bourhis, L. J.; Gildea, R. J.; Howard, J. A. K.; Puschmann, H. OLEX2: a complete structure solution, refinement and analysis program. *J. Appl. Crystallogr.* **2009**, *42*, 339-341.

(20) Neese, F. Software update: The ORCA program system—Version 5.0. *WIREs Comput Mol Sci.* **2022**, *12*, e1606.

(21) Cossi, M.; Rega, N.; Scalmani, G.; Barone, V. Energies, structures, and electronic properties of molecules in solution with the C-PCM solvation model. *J. Comput. Chem.* **2003**, *24*, 669-681.

(22) Müller, M.; Hansen, A.; Grimme, S. ωB97X-3c: A composite range-separated hybrid DFT method with a molecule-optimized polarized valence double-ζ basis set. *J. Chem. Phys.* **2023**, *158*.

(23) Zheng, J.; Xu, X.; Truhlar, D. G. Minimally augmented Karlsruhe basis sets. *Theor. Chem. Acc.* **2011**, *128*, 295-305.

(24) Hirata, S.; Head-Gordon, M. Time-dependent density functional theory within the Tamm–Dancoff approximation. *Chem. Phys. Lett.* **1999**, *314*, 291-299.

Chapter 3

Redox-Modulated Chiroptical Switching in (*S*)- and (*R*)-1,1′-binaphthylene-2,2′-bis(1,8-naphthalimide)

3.1 Overview

The construction of a redox-modulated chiroptical switch requires two essential features: chirality and reversible redox activity. In the case of purely organic switches, this inevitably means linking the chiral component with the redox-active component through some synthetic procedure. A commonly used chiral scaffold is 1,1′-binaphthalene, which possesses axial chirality (atropisomerism) when rotation of the single bond linking the naphthalene rings is hindered, typically achieved by substitution at the 2,2′ positions. To be used in chiroptical switches, sterically hindered binaphthyls need to be functionalised to make them redox-active. Both the 1,1′-binaphtalene core itself and the 2,2′ substituents (often hydroxy or amine groups) provide many options for functionalisation with redox-active groups. This synthetic versatility – as well as the commercial availability of several sterically hindered binaphthyls – makes them ideal candidates for redox-modulated chiroptical switching. Multiple examples of chiroptical switches based on 1,1′-binaphtyls have been reported to date.[1-4]

A class of well-known redox-active molecules are 1,8-naphthalimides, which have been shown to undergo a reversible, one-electron reduction.[5, 6] The synthesis of 1,8-naphthalimides is straightforward and many derivatives with various ring and N substituents have been synthesised. Despite this suitability, 1,8-naphthalimides have not yet been used in redox-modulated chiroptical switches. Additionally, 1,8-naphthalimides are often fluorescent and have regularly been employed as fluorophores.[7-9] In a chiral environment this raises the possibility that CPL could be observed.

Some of the work presented in this chapter appears in the following publication: **Hall, L. A.**; Windsor, H. J.; Chan, B.; D'Alessandro, D. M.; Lakhwani, G. Chiroptical Switching in an Enantiomeric Pair of Binaphthylenes Based on Redox-Active 1,8-Naphthalimide Substituents. *J. Phys. Chem. Lett.* **2025**, *16*, 1529-1534.

This chapter begins with an investigation of the chiroptical and electrochemical properties of 1,1′-binaphthelene-2,2′-diamine (BINAM). Next, a targeted design of a redox-modulated chiroptical switch is undertaken, yielding a pair of chiral enantiomers: (*S*)-1,1′-binaphthalene-2,2′-bis(1,8-naphthalimide) and (*R*)-1,1′-binaphthalene-2,2′-bis(1,8-naphthalimide), hereafter referred to as (*S*)-BNI and (*R*)-BNI, respectively. Their behaviour as high-performance redox-modulated chiroptical switches are demonstrated through a detailed investigation of their electrochemical and optical properties using UV-vis, CD, and EPR spectroelectrochemistry techniques. The magneto-optical properties of (*S*)-BNI and (*R*)-BNI are also investigated using MCD and MChD spectroscopies. Finally, the solid-state chiroptical properties and aggregation-induced emission of (*S*)-BNI and (*R*)-BNI are explored through analysis of their thin films.

3.2 (*S*)- and (*R*)-1,1′-binaphthalene-2,2′-diamine ((*S*/*R*)-BINAM)

(*S*/*R*)-BINAM are sterically hindered 1,1′-binaphthyls with amine substituents at the 2,2′ positions (Figure 3.1). BINAM is a promising compound for chiroptical switching and CPL applications for several reasons: it is relatively cheap and commercially available, it is highly resistant to racemisation with a racemisation half-life of 740 h at 210 °C,[10] it is fluorescent,[11, 12] and the amine sites provide scope for further functionalisation. Despite this, there are only a few examples of BINAM derivatives being used for chiroptical switching and CPL.[2, 3, 13, 14] Additionally, to date the basic optical and electrochemical properties of (*S*/*R*)-BINAM itself have only received a cursory discussion in the literature.[11, 12, 15, 16]

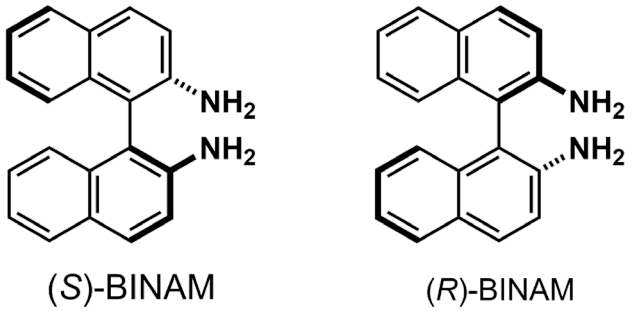

Figure 3.1. Structures of (*S*)- and (*R*)-BINAM.

3.2.1 Optical and Chiroptical Properties of (*S*/*R*)-BINAM

The absorption spectra of (*S*)-BINAM and (*R*)-BINAM in MeCN are identical (Figure 3.2), featuring a broad absorbance band at 310–380 (λ_{max} = 351 nm, ε = 6510 $M^{-1}cm^{-1}$) and a structured absorption band at 265–310 nm (λ_{max} = 283 nm, ε = 13200 $M^{-1}cm^{-1}$), assigned to the $S_0 \rightarrow S_1$ and $S_0 \rightarrow S_2$ transitions, respectively. Similar transitions have been observed in the

spectrum of 2-aminonaphthalene and were assessed as having partial intramolecular charge-transfer character due to the electron donating effect of the amine lone pair.[17, 18]

As expected of enantiomers, the CD spectra of (*S*)-BINAM and (*R*)-BINAM are mirror images and feature two major Cotton signals at 295 nm and 341 nm (Figure 3.2). For (*S*/*R*)-BINAM the absorbance dissymmetry factors, g_{abs}, are $\pm 1.8 \times 10^{-3}$ and $\pm 2.5 \times 10^{-3}$ at 295 nm and 341 nm, respectively, in line with typical values observed for chiral organic molecules.[19, 20]

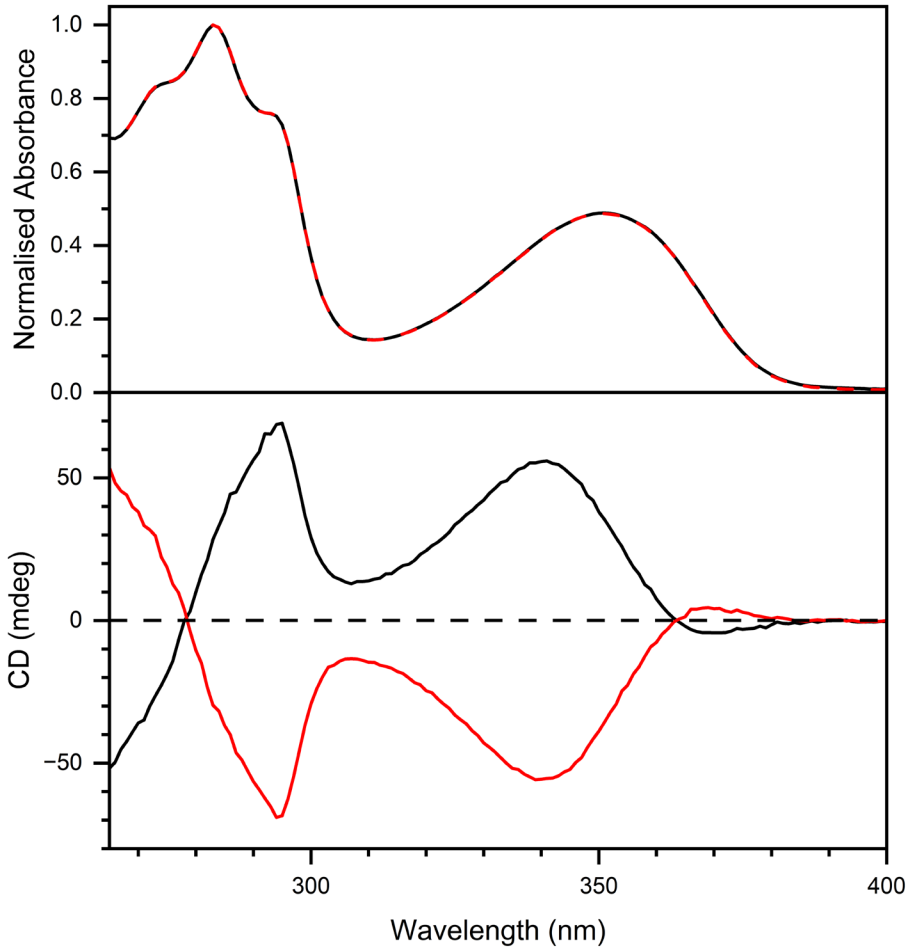

Figure 3.2. Normalised absorbance (top) and CD (bottom) of (*S*)-BINAM (red) and (*R*)-BINAM (black) in MeCN. Sample concentrations were approximately 120 μM.

The fluorescence spectrum of (*S*)-BINAM is presented in Figure 3.3. A single, broad emission band is observed with an emission maximum of 403 nm and a Stokes shift of 3680 cm^{-1}, also very similar to the fluorescence of 2-aminonaphthalene.[17] (*R*)-BINAM displayed identical fluorescent properties to (*S*)-BINAM (Figure A1). The similarity of the absorbance and fluorescence spectra of (*S*/*R*)-BINAM and 2-aminonaphthalene suggests that in (*S*/*R*)-BINAM the two naphthylamine rings behave as separate chromophores rather than a single

chromophore. This could be due to the disruption of π-electron delocalisation caused by the twist between the two naphthyl rings.

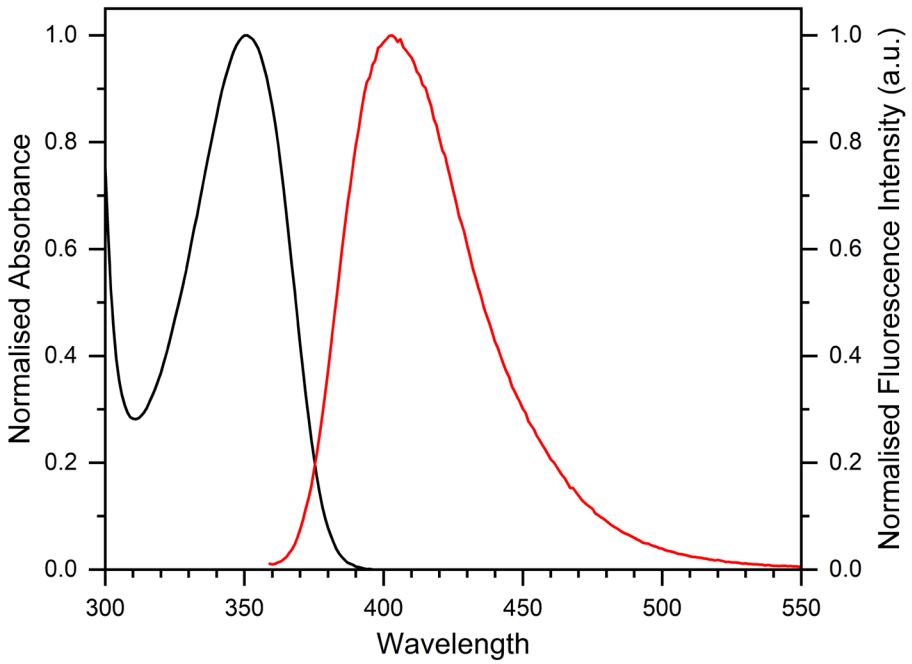

Figure 3.3. Normalised absorbance (black) and normalised fluorescence emission intensity (red) of (*S*)-BINAM in MeCN. Excitation wavelength was 351 nm. Spectra were acquired at 120 μM for absorbance and 6 μM for fluorescence.

Given their inherent chirality and luminescent behaviour, it was assumed that (*S*/*R*)-BINAM would display CPL. Unfortunately, (*S*/*R*)-BINAM showed no detectable CPL in solution (Figure 3.4). In contrast, (*S*/*R*)-BINAM have been reported to show CPL with a luminescence dissymmetry factor, g_{lum}, of $\pm 1.3 \times 10^{-3}$ in the solid state.[16] A possible explanation of this discrepancy is that the g_{lum} is simply smaller in solution such that it cannot be detected above the baseline level of noise in the experiment. This could arise through aggregation-induced emission (AIE), in which the rigidity of molecules in the solid-state hampers nonradiative decay pathways and boosts luminescent transitions. There are many examples of chiral luminophores with this property and there can be a significant increase in g_{lum} in cases where the aggregates form chiral superstructures.[21-24]

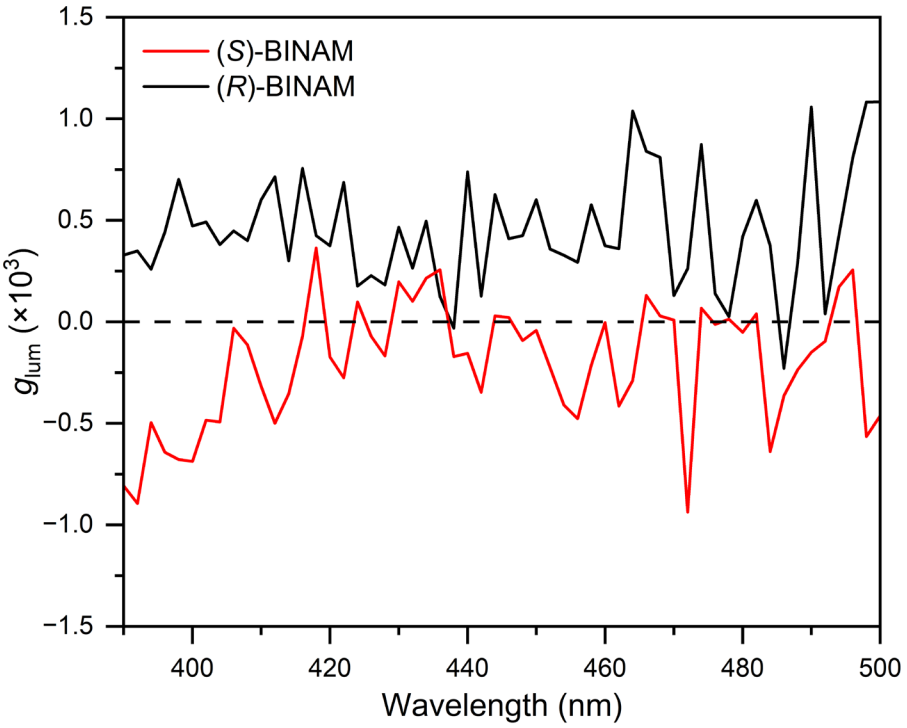

Figure 3.4. CPL of (*S*)-BINAM (red) and (*R*)-BINAM (black) in MeCN. Spectra are averaged over 25 scans and excitation was performed with a 380 nm LED. The sample concentrations were approximately 15 μM.

3.2.2 Electrochemistry of (*S*)-BINAM

The cyclic voltammogram (CV) of (*S*)-BINAM shows two electrochemically irreversible processes with anodic peak currents of 0.62 and 0.99 V vs Fc/Fc^+, respectively (Figure 3.5). This is in line with 2-aminonaphthalene itself and other analogues containing the 2-aminonaphthalene moiety.[25, 26] No electrochemical reduction processes were observed on the negative potential sweep. Since CV is not a chiroptical technique, it can be expected that (*R*)-BINAM would exhibit similarly irreversible electrochemical behaviour. For this reason, CV experiments were not performed on (*R*)-BINAM. Overall, these results indicate (*S*/*R*)-BINAM are unsuitable for redox-modulated chiroptical switching.

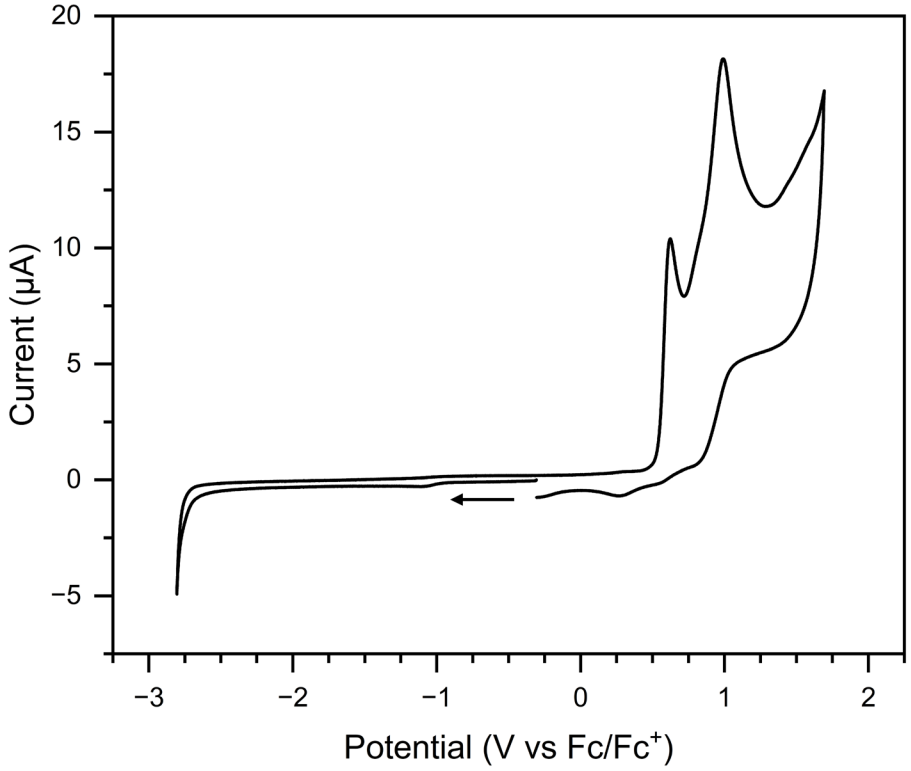

Figure 3.5. Cyclic voltammogram of (*S*)-BINAM in MeCN with 0.1 M $[(n\text{-}C_4H_9)_4N]PF_6$ supporting electrolyte. The arrow shows the direction of the potential sweep. Scan rate = 100 mV/s and the potentials are referenced to Fc/Fc^+ at 0.V.

3.3 (*S*)- and (*R*)-1,1′-binaphthylene-2,2′-bis(1,8-naphthalimide) ((*S*/*R*)-BNI)

3.3.1 Synthesis of (*S*/*R*)-BNI

The rationale behind the design of (*S/R*)-BNI was to functionalise (*S/R*)-BINAM with a redox-active functional group which displays reversable electrochemistry. It was hoped that the fluorescence of (*S/R*)-BINAM would also be retained to achieve a dual-functional CPL-active chiroptical switch. The 1,8-naphthalimide moiety appeared to fit these criteria, being well-known to undergo a reversible one-electron reduction as well as seeing widespread use as a fluorophore.[5-7, 9] Despite this suitability, 1,8-naphthalimides have not yet been used in redox-modulated chiroptical switches, although the related naphthalenediimides have.[27]

It was envisioned that a condensation reaction between the BINAM amino groups and 1,8-naphthalimide would yield a chiral molecule bearing two redox-active and fluorescent 1,8-naphthalimide moieties. Therefore, (*S*)-BNI and (*R*)-BNI were synthesised by the condensation reaction between (*S*)-BINAM or (*R*)-BINAM and 1,8-naphthalic anhydride in a molten

imidazole solvent (Figure 3.6). Following purification by recrystallisation from chloroform, the products were obtained in 73% and 65% yield, respectively. Additionally, *N*-phenyl-1,8-naphthalimide (PhNI) was synthesised via a similar method and serves as a simple model compound to help interpret the spectra and properties of (*S*/*R*)-BNI.

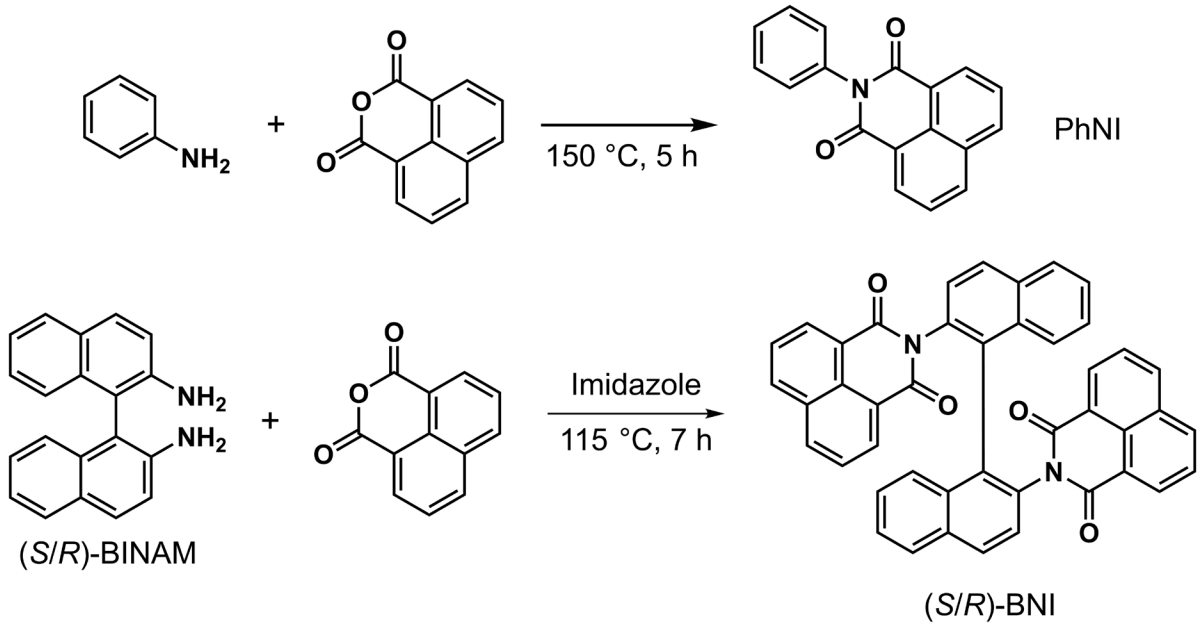

Figure 3.6. Synthesis scheme for PhNI and (*S*/*R*)-BNI.

3.3.2 Crystal Structures of (*S*/*R*)-BNI

Single crystals of (*S*)-BNI suitable for X-ray diffraction analysis were obtained by slow evaporation from a 1:1 chloroform/ethyl acetate solution (Figure 3.7). From these conditions (*S*)-BNI crystallises in the non-centrosymmetric monoclinic space group $P2_1$. The crystal structure possesses a high degree of enantiopurity, with a measured Flack parameter of 0.02(11). The molecular structure of (*S*)-BNI shows a large twist between the naphthyl rings with a C2–C1–C23–C24 torsion angle of 79.2(5)°. The two naphthalimide moieties display significant torsional offset from the binaphtyl core with C11–N1–C2–C3 and C33–N2–C24–C25 torsion angles of 64.0(5)° and 69.0(5)°, respectively. The molecular packing consists of 1D chains projected along the crystallographic *a*-axis wherein each naphthalimide unit partially overlaps with a naphthalimide of a neighbouring molecule in an offset π–π stacking mode (centroid–centroid distance of 3.521(3) Å). Overall, the 1D chains are assembled such that they adopt a conventional herringbone packing structure. Detailed crystallographic information of (*S*)-BNI is presented in Table A1.

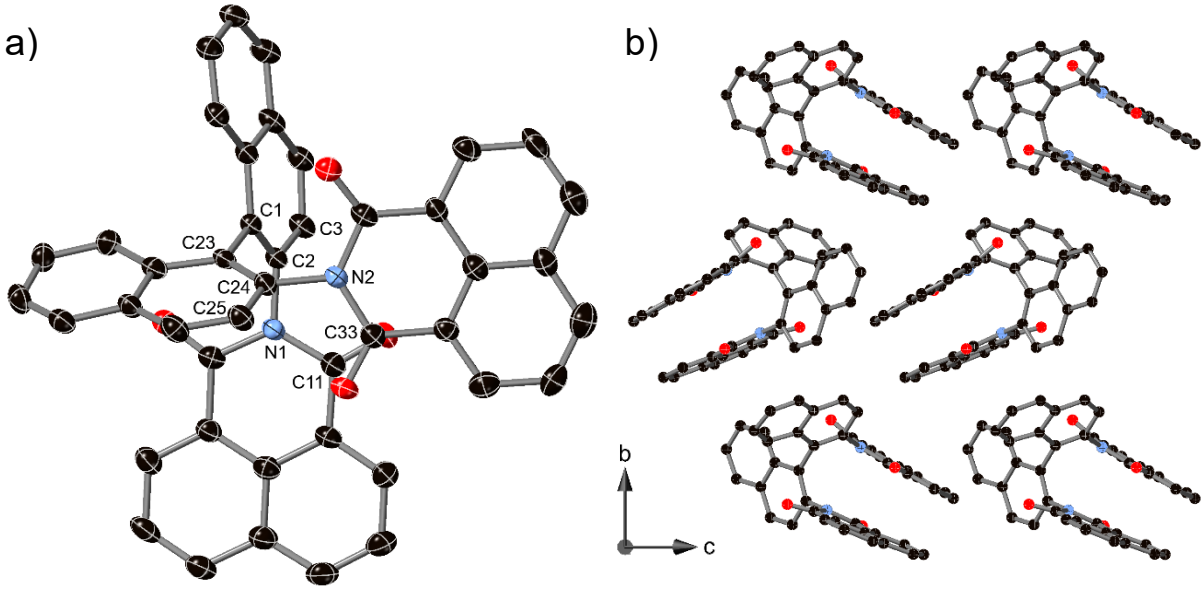

Figure 3.7. (a) Molecular structure and asymmetric unit of (*S*)-BNI with displacement ellipsoids drawn at the 50% probability level. (b) Crystal packing of (*S*)-BNI as viewed down the crystallographic *a*-axis. Hydrogen atoms have been omitted for clarity. Black = carbon, red = oxygen, blue = nitrogen.

Despite repeated efforts, X-ray diffraction-quality crystals of (*R*)-BNI could not be obtained from the same chloroform/ethyl acetate solvent system as for (*S*)-BNI. However, suitable crystals were obtained from slow evaporation of a 1:1 chloroform/toluene solution. Under these conditions, (*R*)-BNI crystallises in the non-centrosymmetric monoclinic space group *C*2 and notably contains a toluene molecule as a solvent of crystallisation (Figure 3.8). A Flack parameter of −0.1(4) confirms the enantiopurity of the crystal structure. The twist between the binaphthyl rings is slightly smaller in the crystal of (*R*)-BNI compared to that for (*S*)-BNI, with a C10–C1–C23–C32 torsion angle of −76.1(6)°. However, the two naphthalimide moieties are slightly more offset from the binaphthyl core, with C22–N1–C2–C3 and C33–N2–C24–C25 torsion angles of −66.8(6)° and −70.4(6)°, respectively. The molecular packing is comprised of 1D chains of (*R*)-BNI projected along the crystallographic *b*-axis wherein each naphthalimide moiety partially overlaps with a naphthalimide of a neighbouring molecule – much like in (*S*)-BNI – in an offset π–π stacking mode (centroid–centroid distance of 3.439(3) Å). The 1D chains are assembled into pairs of rows with adjacent rows having opposite orientation. There is an additional π–π stacking interaction between naphthalimide pendants of (*R*)-BNI molecules in adjacent 1D chains (centroid–centroid distance of 3.660(4) Å). This contrasts with the packing of (*S*)-BNI, in which there were only π–π stacking interactions within 1D chains but not between then. Finally, the pairs of rows are separated by solvent toluene molecules, which are positionally disordered over two positions with occupancies of

60(2)% and 40(2)%. Detailed crystallographic information of (*R*)-BNI is presented in Table A2.

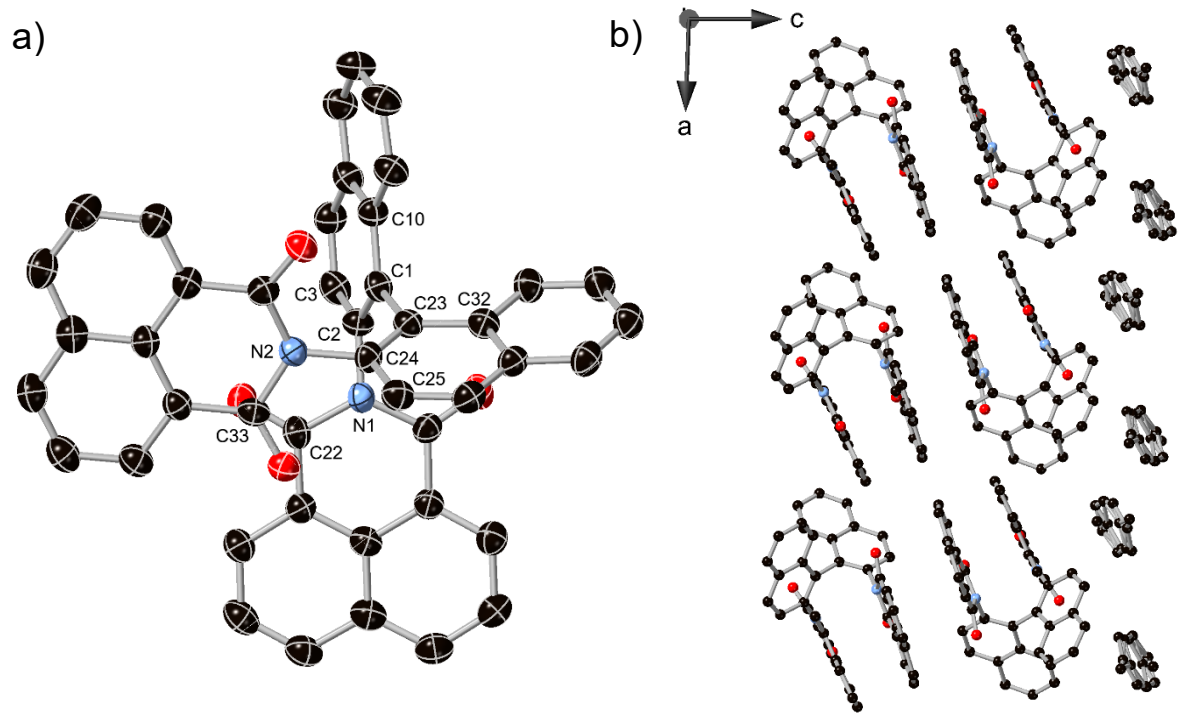

Figure 3.8. (a) Molecular structure of (*R*)-BNI with displacement ellipsoids drawn at the 50% probability level. Interstitial toluene omitted for clarity. (b) Crystal packing of (*R*)-BNI as viewed along the crystallographic *b*-axis including interstitial disordered toluene solvent molecules. Hydrogen atoms are excluded for clarity. Black = carbon, red = oxygen, blue = nitrogen.

Given the similarities between (*S*)- and (*R*)-BNI, the following discussion will focus primarily on (*S*)-BNI with the relevant details for (*R*)-BNI provided in Appendix A.

3.3.3 Electrochemistry of (*S*/*R*)-BNI

To confirm the redox activity of (*S*/*R*)-BNI, cyclic voltammetry experiments were performed in MeCN using 0.1 M $[(n\text{-}C_4H_9)_4N]PF_6$ as the supporting electrolyte. The cyclic voltammogram of (*S*)-BNI shows two reduction processes with $E_{1/2} = -1.74$ and -1.91 V vs Fc/Fc^+ (Figure 3.9a). Both processes are electrochemically reversible with a ΔE of 62 mV and 64 mV for the first and second reductions, respectively. Additionally, both redox processes are diffusion-limited due to the linear relationship between the cathodic peak current and the square root of the scan rate according to the Randles-Sevcik equation (Figure 3.9b).[28] These processes are assigned to the reduction of each naphthalimide ring of (*S*)-BNI and are consistent with the redox behaviour of other N-substituted naphthalimides.[29] This is further supported by comparison with the cyclic voltammogram of PhNI, which shows a single, diffusion-limited

reduction process with $E_{1/2} = -1.71$ vs Fc/Fc^+ (Figure 3.10). As expected, (*R*)-BNI showed the same electrochemical behaviour as (*S*)-BNI, featuring two diffusion-limited reduction processes with $E_{1/2} = -1.74$ and -1.89 V vs Fc/Fc^+ and ΔE of 64 mV and 62 mV for the first and second reductions, respectively. (Figure A2).

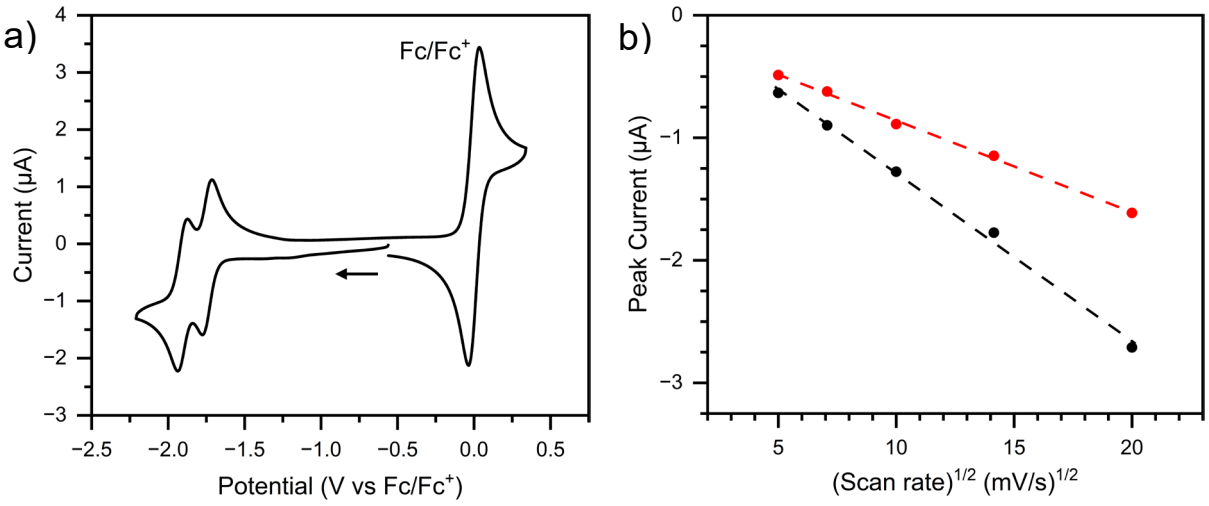

Figure 3.9. (a) Cyclic voltammogram of (*S*)-BNI in MeCN with 0.1 M $[(n\text{-}C_4H_9)_4N]PF_6$ supporting electrolyte. The arrow shows the direction of the potential sweep. Scan rate = 100 mV/s and the potentials are referenced to Fc/Fc^+ at 0 V. (b) Linear fits of cathodic peak current vs the square root of scan rate for (*S*)-BNI in MeCN with 0.1 M $[(n\text{-}C_4H_9)_4N]PF_6$ supporting electrolyte. Black = first reduction process, red = second reduction process. The first and second reductions have R^2 values of 0.9961 and 0.9979, respectively.

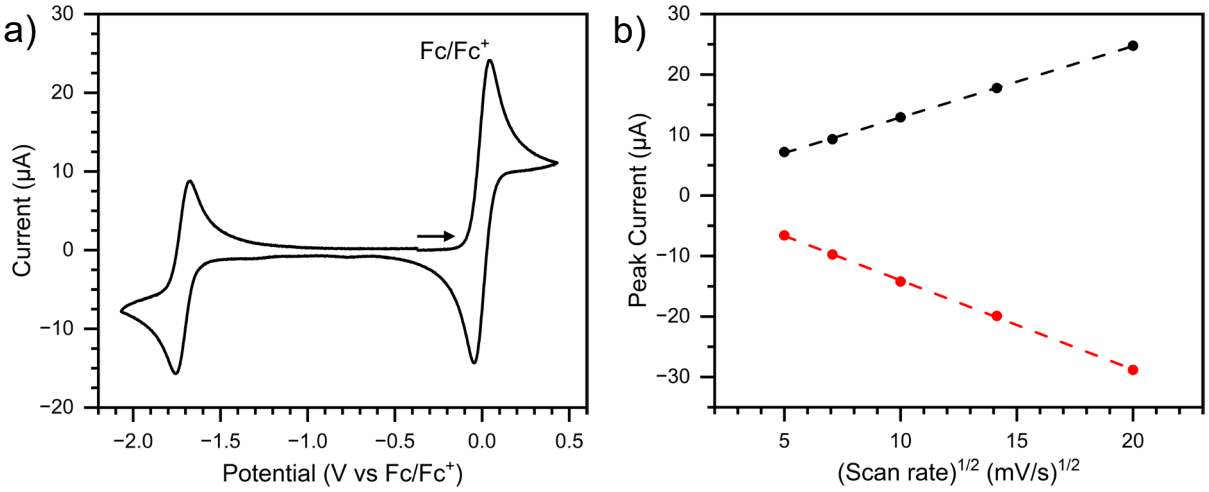

Figure 3.10. (a) Cyclic voltammogram of PhNI in MeCN with 0.1 M $[(n\text{-}C_4H_9)_4N]PF_6$ supporting electrolyte. The arrow shows the direction of the potential sweep. Scan rate = 100 mV/s and the potentials are referenced to Fc/Fc^+ at 0 V. (b) Linear fit of cathodic peak current vs the square root of scan rate for PhNI in MeCN with 0.1 M $[(n\text{-}C_4H_9)_4N]PF_6$ supporting electrolyte. Black = anodic peak currents, red = cathodic peak current. The anodic and cathodic processes have R^2 values of = 0.9997 and 0.9997, respectively.

The reduction of each naphthalimide is proposed to be a one-electron process resulting in a delocalised radical anion, as depicted in Figure 3.11. The formation of delocalised radicals is typical of highly conjugated organic molecules, including aromatic imides.[30, 31] Comprehensive evidence supporting this assignment is presented below in section 3.6.

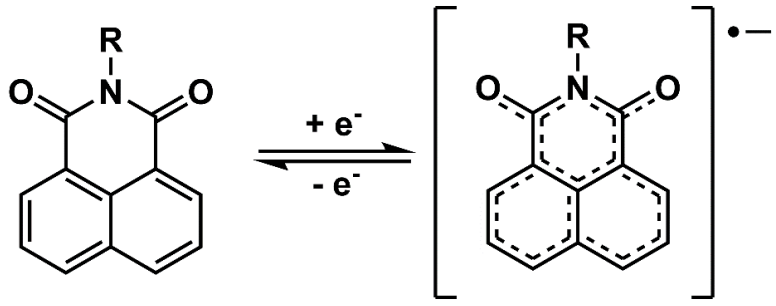

Figure 3.11. Proposed mechanism of reduction of the naphthalimide moieties in (*S*/*R*)-BNI and PhNI.

3.3.4 Optical and Chiroptical Properties of (*S*/*R*)-BNI

The absorption spectra of (*S*)-BNI and (*R*)-BNI are identical, featuring a prominent absorption band in the 310–360 nm range (λ_{max} = 333 nm, ε = 27200 $M^{-1}cm^{-1}$) that is assigned to the absorbance of the naphthalimide units (Figure 3.12). This is supported by the similar absorption of PhNI in the same region (λ_{max} = 331 nm, ε = 14300 $M^{-1}cm^{-1}$, Figure 3.13). The higher energy band between 280–300 nm (λ_{max} = 293 nm, ε = 16100 $M^{-1}cm^{-1}$) is attributed to absorbance of the binaphthyl moiety.[32] The CD spectra of (*S*)-BNI and (*R*)-BNI are mirror images and feature both positive and negative Cotton signals in the 280–370 nm region with prominent peaks at 316 and 354 nm (Figure 3.12). Additionally, the CD spectra display a null corresponding to the absorbance maxima; this is typical of exciton-coupled CD and confirms that the two naphthalimide moieties are both electronically coupled and situated in a chiral orientation with respect to one another.[33-35] Furthermore, the CD spectrum of (*S*)-BNI is positive on the long wavelength side of the null and negative on the short wavelength side of the null, indicating the positions of the naphthalimide groups from a clockwise screw sense,[34] consistent with its stereochemical (*S*) assignment. The situation is reversed for (*R*)-BNI, indicating an anticlockwise arrangement. For (*S*)-BNI and (*R*)-BNI, their absorbance dissymmetry factors, g_{abs}, at 354 nm are $\pm 2.8 \times 10^{-3}$ respectively, slightly larger than for (*S*/*R*)-BINAM and in line with typical values observed for chiral organic molecules.[19, 20]

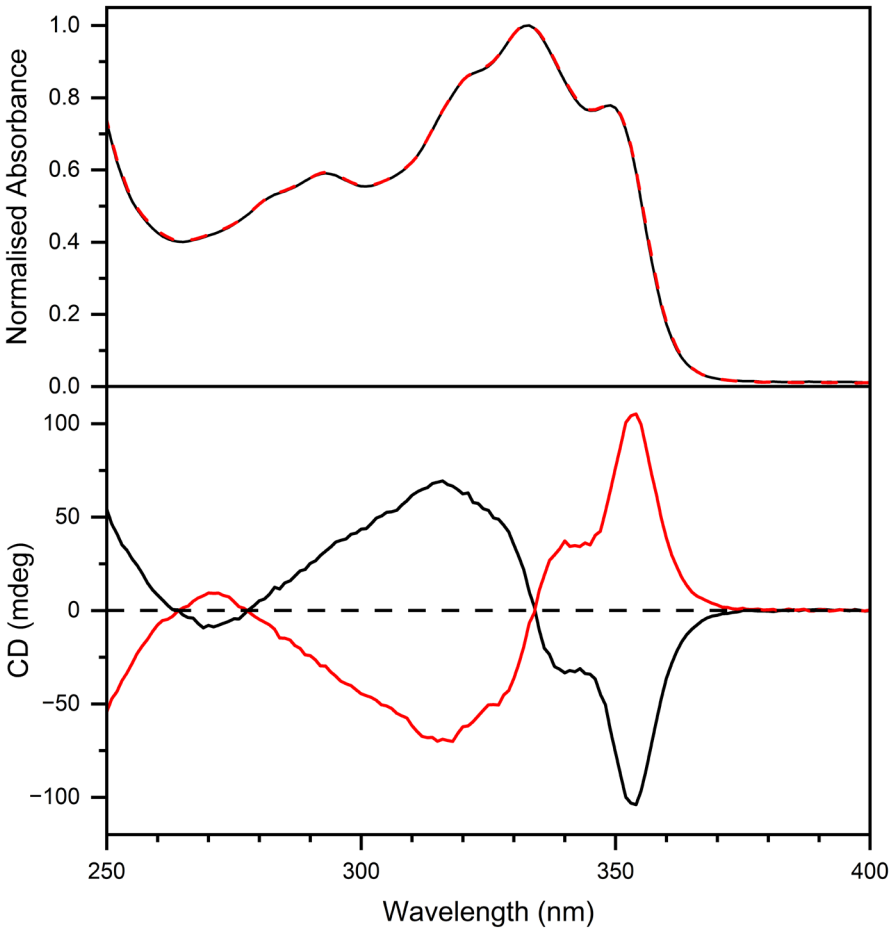

Figure 3.12. Normalised absorbance (top) and CD (bottom) of (*S*)-BNI (red) and (*R*)-BNI (black) in MeCN. Sample concentrations were 70 μM.

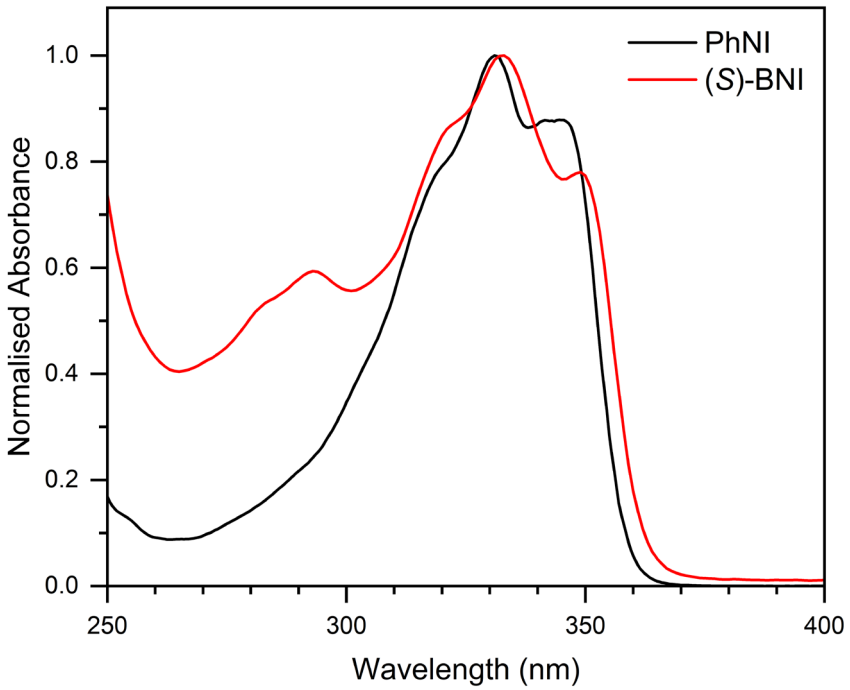

Figure 3.13. Normalised UV-vis spectra of PhNI (black) with (*S*)-BNI (red) for comparison, acquired in MeCN. The concentration of PhNI was 85 μM and the concentration of (*S*)-BNI was 70 μM.

Given the π–π stacking interactions observed in the solid state, it was worth investigating whether these interactions were also occurring in solution and driving the formation of chiral supramolecular aggregates. If such chiral superstructures were forming and contributing to the observed CD, g_{abs} would be expected to dramatically increase above a threshold concentration were nucleation of aggregates could begin.[36] Therefore, the of g_{abs} of (*S*)-BNI was measured at a range of concentrations spanning two orders of magnitude from 10 µM to 1000 µM (close to the solubility limit of (*S*)-BNI in acetonitrile). As shown in Figure 3.14, g_{abs} is independent of concentration, indicating that chiral aggregates did not form and consequently that the observed CD is an intensive property of (*S*)-BNI.[37, 38]

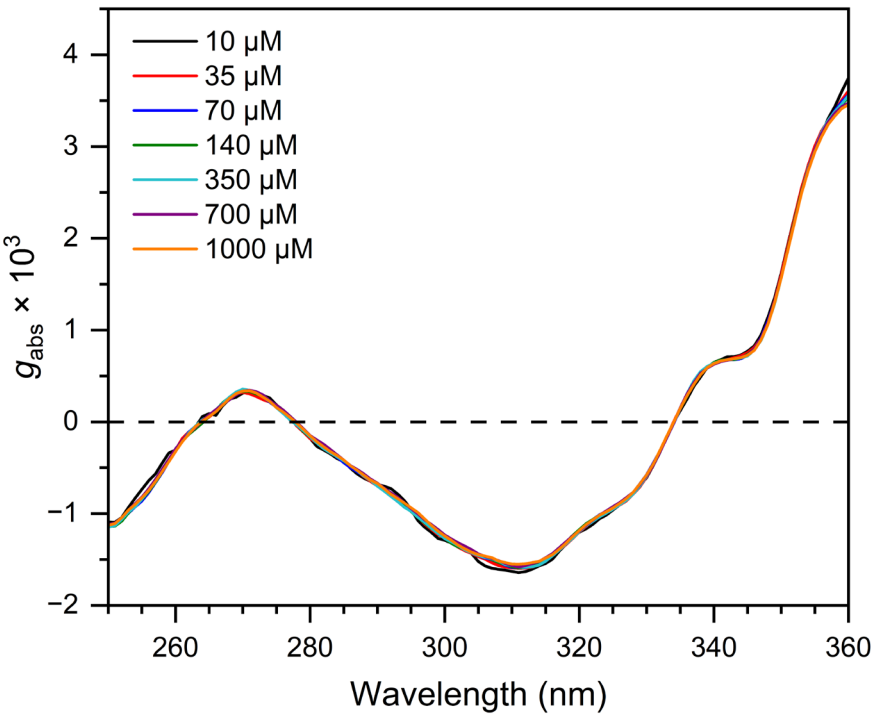

Figure 3.14. g_{abs} of (*S*)-BNI in MeCN at different concentrations.

Due to their 1,8-naphthalimide chromophores, it was expected that (*S*/*R*)-BNI would show strong fluorescence in the solution-state. However, they were found to be non-emissive in MeCN solution. This is likely because of highly efficient internal conversion due to a pseudo Jahn-Teller effect induced by solvent cage relaxation and geometrical relaxation in the S_1 state.[39] As a result, (*S*/*R*)-BNI are not suitable candidates for CPL in the solution state.

3.4 Redox-Modulated Chiroptical Switching of (*S*/*R*)-BNI

The strong chiroptical signal and reversible redox behaviour of (*S*/*R*)-BNI make them suitable for redox-modulated chiroptical switching. To demonstrate this capability and assess their performance, spectroelectrochemical experiments were performed on both (*S*)- and (*R*)-BNI.

The UV-vis and CD spectroelectrochemistry of (*S*)-BNI are presented in Figure 3.15. The spectroelectrochemical data for (*R*)-BNI are analogous to that of (*S*)-BNI and are shown in Figure A3. While (*S*)-BNI undergoes two reduction processes, the $E_{1/2}$ potentials are too close together for the singly reduced species to be the only species present in solution. Therefore, the initial and final spectra can be considered to represent the neutral and doubly reduced species, while the other spectra are some combination of multiple species. Upon reduction, the absorbance band at 333 nm was diminished while new bands appeared at 489 nm (ε = 6800 $M^{-1}cm^{-1}$), 419 nm (ε = 40900 $M^{-1}cm^{-1}$), and 273 nm (ε = 35900 $M^{-1}cm^{-1}$), corresponding to doubly reduced (*S*)-BNI^{2-}. This behaviour is closely mirrored by the UV-vis SEC of PhNI which exhibits a decrease in absorbance at 331 nm and the emergence of new absorption bands at 490 nm (ε = 3620 $M^{-1}cm^{-1}$), 415 nm (ε = 29200 $M^{-1}cm^{-1}$), and 270 nm (ε = 19600 $M^{-1}cm^{-1}$), assigned to the $PhNI^{-}$ anion species (Figure 3.16). The spectra of (*S*)-BNI^{2-} and $PhNI^{-}$ are almost identical (Figure 3.17), indicating that the binaphthyl core is not contributing to the spectrum of the reduced species and hence the spectral changes can be wholly attributed to the reduction of naphthalimide groups.

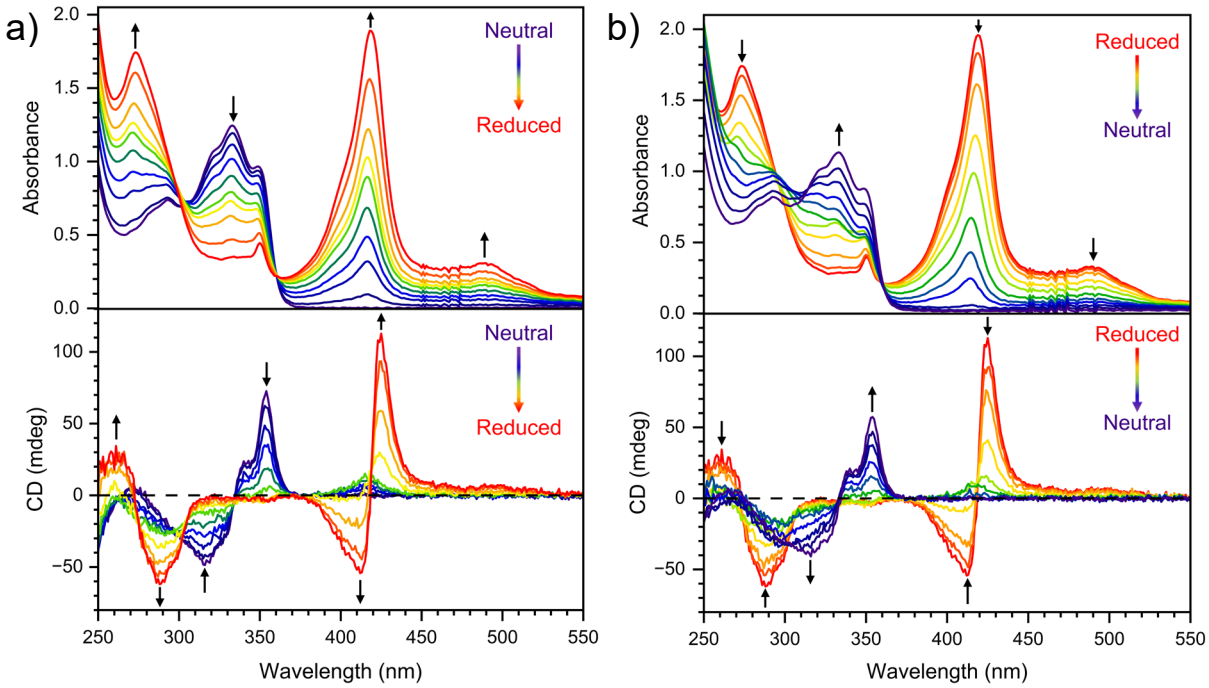

Figure 3.15. (a) UV-vis (top) and CD (bottom) spectra of (*S*)-BNI during reduction from the neutral to the dianion state over a 60 min time interval. (b) UV-vis (top) and CD (bottom) spectra of (*S*)-BNI during subsequent oxidation from the dianion to the neutral state over an 80 min time interval. The concentration of (*S*)-BNI was approximately 0.73 mM. Spectra were acquired in MeCN with 0.25 M $[(n\text{-}C_4H_9)_4N]PF_6$ as supporting electrolyte.

The CD SEC spectra of (*S*)-BNI also show large changes upon reduction, with the peaks at 354 and 316 nm decreasing and new peaks emerging at 425, 412, 288, and 261 nm (Figure 3.15a). These bands align with those observed in the absorbance spectrum and can be considered the CD spectrum of the doubly reduced species (*S*)-BNI^{2-}, rather than signifying any change in the inherent chirality of the system, which comes from the binaphthyl backbone which is not itself involved in the redox processes. This assessment is supported by the clear exciton-coupled CD in the visible region (centred on the 419 nm optical transition) which confirms the clockwise screw sense is retained. The g_{abs} of (*S*)-BNI^{2-} is 2.2×10^{-3} at 425 nm in the visible region and -1.5×10^{-3} at 288 nm in the UV region, indicating that the doubly reduced species has a slightly lower intrinsic absorption chirality than the neutral species. Furthermore, the largest difference in g_{abs} between the neutral and doubly reduced species, Δg_{abs}, is 4.2×10^{-3} at 363 nm. As expected, the CD spectra of (*S*)-BNI^{2-} and (*R*)-BNI^{2-} are mirror images (Figure 3.18).

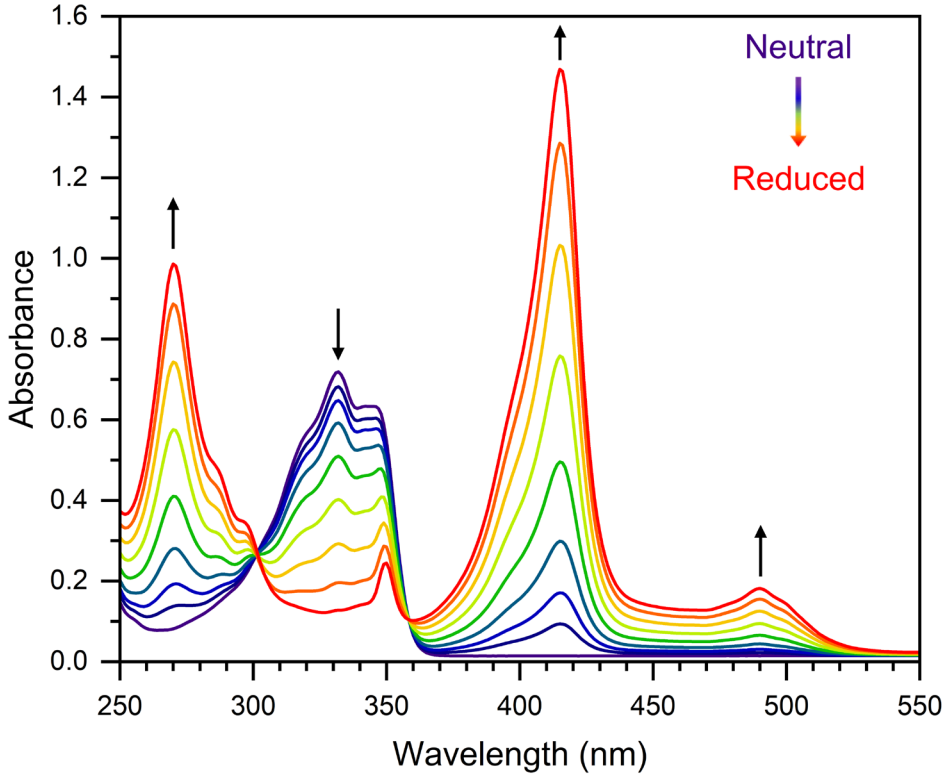

Figure 3.16. UV-vis SEC of PhNI during reduction from the neutral to the reduced state over a 30 min interval. The concentration of PhNI was approximately 0.74 mM. Spectra were measured in MeCN with 0.25 M $[(n\text{-}C_4H_9)_4N]PF_6$ as supporting electrolyte.

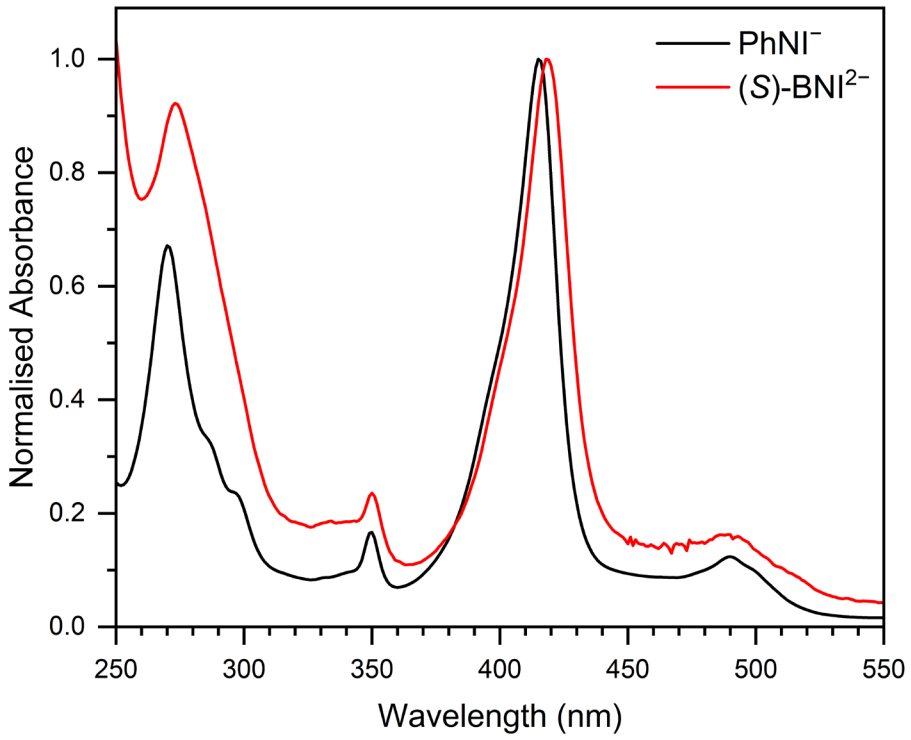

Figure 3.17. Normalised UV-vis spectra of fully reduced $PhNI^{-}$ (black) and (*S*)-BNI^{2-} (red) from SEC experiments.

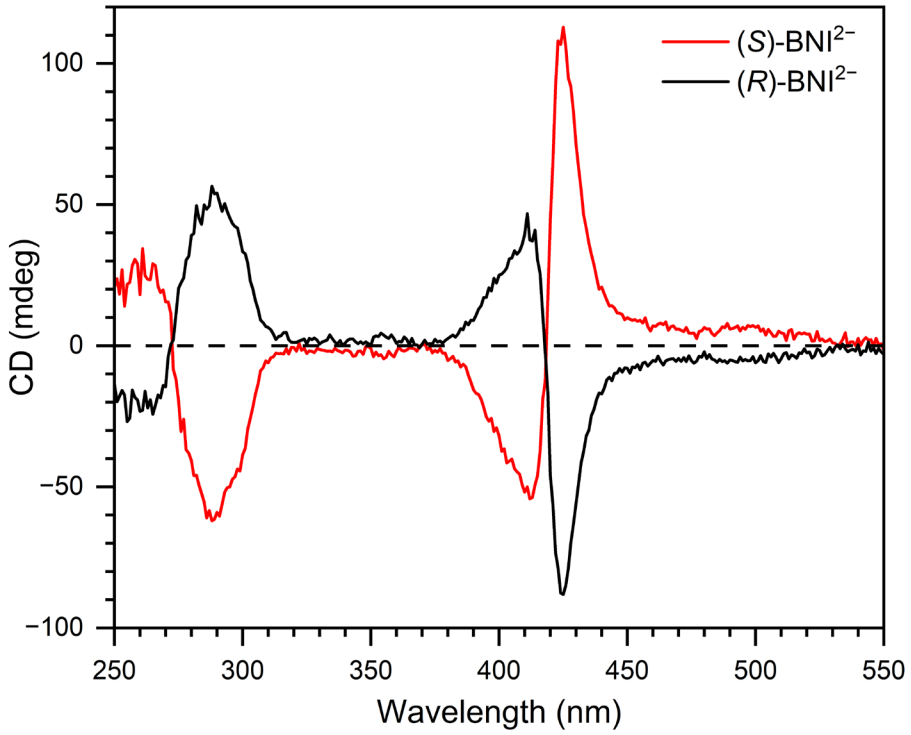

Figure 3.18. CD spectra of (*S*)-BNI^{2-} (red) and (*R*)-BNI^{2-} (black) from SEC experiments. The concentrations of (*S*)-BNI^{2-} and (*R*)-BNI^{2-} were approximately 0.73 mM and 0.68 mM, respectively.

For both UV-vis and CD SEC, the original spectra are regained following oxidation back to the neutral state (Figure 3.15b), confirming that (*S*)-BNI can function as both an optical and

chiroptical switch. The CD spectra of the neutral and doubly reduced species are easily distinguishable across numerous wavelengths in the visible and UV range, as summarised in Table 3.1. The wavelengths 425 nm ($|\Delta\Delta\varepsilon|$ = 69.3 $M^{-}1cm^{-}1$) and 354 nm ($|\Delta\Delta\varepsilon|$ = 46.6 $M^{-}1cm^{-}1$) were identified as displaying a particularly sharp contrast and therefore the best wavelengths to monitor the chiroptical readout during switching experiments, as discussed below. Similar values were obtained for (*R*)-BNI (Table A3). These results confirm that (*S*/*R*)-BNI are highly sensitive chiroptical switches. Moreover, there are certain spectral regions where the contrast between the two states is relatively greater in CD than UV-vis; for example, around 360 nm (isosbestic point in UV-vis). This complementarity highlights the versatility of chiroptical switches over purely optical switches. Another advantage of chiroptical switches lies in their greater resistance to interference as only chiral impurities will be able to produce an interfering signal.

Table 3.1. $\Delta\varepsilon$ of (*S*)-BNI and (*S*)-BNI^{2-} and corresponding $|\Delta\Delta\varepsilon|$ at selected wavelengths as calculated from CD SEC measurements.

Wavelength (nm)	(*S*)-BNI $\Delta\varepsilon$ ($M^{-}1cm^{-}1$)	(*S*)-BNI^{2-} $\Delta\varepsilon$ ($M^{-1}cm^{-1}$)	$\lvert\Delta\Delta\varepsilon\rvert$ ($M^{-1}cm^{-1}$)
261	−2.6	21.1	23.7
288	−8.1	−38.1	30.0
316	−29.9	−1.8	28.1
354	44.6	−2.0	46.6
412	0	−33.3	33.3
425	0	69.3	69.3

3.4.1 Chiroptical Switching of (*S*/*R*)-BNI Over Multiple Cycles

Given the large spectral changes between the neutral and doubly reduced states at 425 nm and 354 nm, the switching behaviour of (*S*)-BNI was successfully demonstrated over 10 reduction and oxidation cycles at both wavelengths (Figure 3.19). At 425 nm, (*S*)-BNI functions as an "OFF/ON" switch with only a 5% decrease in signal intensity over the 10 cycles. At 354 nm, (*S*)-BNI functions as an "ON/OFF" switch and displays an initial drop in signal intensity of 10% after one cycle, with the remaining nine cycles recording an average drop of 0.9% per cycle. For both wavelengths, switching times were on the order of a few minutes for each half cycle. Since the electrochemical reduction/oxidation of (*S*)-BNI is diffusion limited, the switching times simply reflect the rate of diffusion of (*S*)-BNI to the surface of the working

electrode. However, faster cycling may be possible by simply switching the polarity of the applied potential at shorter time intervals at the cost of some signal intensity. Despite some reduction in signal intensity, the neutral and doubly reduced states were still easily distinguishable after 10 cycles at both 425 nm and 354 nm, demonstrating that (*S*)-BNI is an effective chiroptical switch with good reversibility and a strong chiroptical response. (*R*)-BNI showed similar switching capabilities over the same number of cycles and at the same wavelengths (Figure A4).

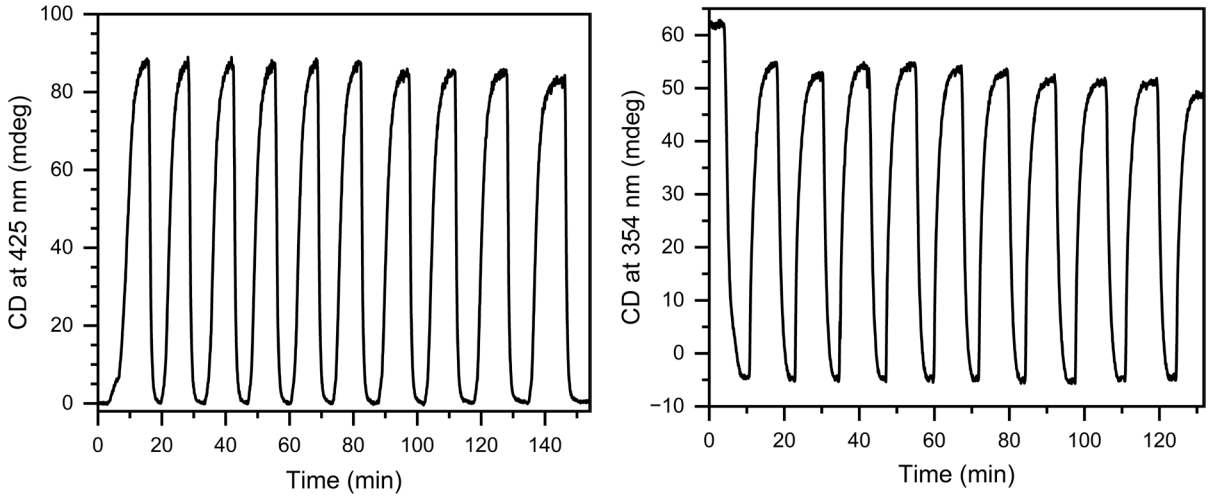

Figure 3.19. CD response of (*S*)-BNI at 425 nm (left) and 354 nm (right) during 10 consecutive reduction and oxidation cycles. The concentration of (*S*)-BNI was approximately 0.68 mM. Spectra were acquired in MeCN with 0.25 M $[(n\text{-}C_4H_9)_4N]PF_6$ as supporting electrolyte.

It is important to note that SEC experiments are not necessarily an accurate measure of the optimal performance of a system's electrochemical reversibility. This is because typical SEC experiments are not designed to realistically measure electrochemical reversibility. During a SEC experiment, a species is oxidised/reduced at the working electrode, which requires a corresponding reduction/oxidation at the counter electrode to maintain charge balance. However, in SEC experiments, suitable redox-active counter electrolyte species are not typically added to the solution because they could diffuse into the beam path and interfere with the measurement. While this is prudent from a spectroscopic perspective, it leads to suboptimal conditions for assessing the electrochemical reversibility over many cycles because the electrochemical reactions at the counter electrode may not be reversible themselves. Furthermore, even when a redox counter species is present, the time taken for each oxidation/reduction cycle, the rest time between cycles, and the proportion of material oxidised/reduced are important parameters that require fine-tuning in order to maximise the electrochemical reversibility of a system.[40-43] These aspects of reversibility must be considered

when incorporating any redox-modulated switch – chiroptical or otherwise – into device applications where many switching cycles are required.

To more accurately determine the electrochemical reversibility of an analyte, alternate experiments should be conducted which explicitly include an appropriate, electrochemically reversible counter species at the counter electrode. Compared to other estimates of cycling stability such as performing multiple CV cycles, having a counter species present allows the effects of bulk oxidation/reduction to be understood. This is important because certain decomposition pathways of electrochemically generated species such as disproportionation and dimerisation are bimolecular and thus are influenced by their concentration in solution – something CV cycling cannot assess since only a tiny fraction of material is ever oxidised/reduced.[41] To avoid spectral interference, the counter species should remain isolated from the beam path, for example using an ion-exchange membrane. Such membranes are routinely used in redox-flow batteries to prevent the anolyte and catholyte solutions from mixing and could be incorporated into an improved SEC cell design.[44, 45]

Designing a SEC cell or device which keeps the analyte (in the beam path) and counter species (at the counter electrode) separate may prove to be a difficult or cumbersome engineering challenge. Thus, two alternate approaches in which a counter species is present but allowed to diffuse into the beam path are suggested. The first approach is to design a molecular switch which is able to reversibly undergo both oxidation and reduction. For example, if the analyte is being oxidised at the working electrode, the analyte itself can act as the redox counter-species at the counter electrode by being reduced. If any of these reduced molecules diffuse into the beam path, they will quickly contact the working electrode (to which they are coulombically attracted) and be converted to the oxidised state. In this way, the potential set by the working electrode will determine the dominant species in the beam path without significant interference by counter species. This approach does impose additional design constraints, but chiroptical switches which are stable to both oxidation and reduction have been synthesised.[46] Alternately, a redox counter species could be chosen in which both its neutral and oxidised/reduced states absorb outside the spectral range of both the neutral and reduced/oxidised states of the analyte. For purely optical switches this is likely to be quite difficult in practice but could be suitable for switches with working wavelengths in the NIR region, which is far removed from where many highly reversible redox-active molecules (such as ferrocene and phenazine) absorb.[47-49] For chiroptical switches this is presumably much simpler as an achiral redox counter species

could be chosen. However, any chiral chirality transfer from the analyte to the redox-counter species – or other interactions that influence the CD signal – would still need to be considered.

3.5 Density Functional Theory Calculations

To better understand the nature of the observed UV-vis and CD transitions of PhNI and (*S*)-BNI in their various reduced states, DFT modelling was undertaken to predict their spectra (Figure 3.20 and Figure 3.22). In all cases, the predicted spectra are in qualitative agreement with the experimental spectra, with the computational results blueshifted by approximately 30-40 nm for most transitions. Furthermore, examination of the natural transition orbitals illustrates the origin of all the observed transitions (Figure 3.21 and Figure 3.23). For PhNI and $PhNI^{-}$, their transitions are all localized on the naphthalimide moiety, consistent with our prior analysis. For the three different redox states of (*S*)-BNI, the highest energy transition involves the binaphthyl backbones, while all other lower energy transitions are confined to the naphthalimide moieties. In (*S*)-BNI and (*S*)-BNI^{2-}, these lower energy transitions are delocalised across both naphthalimide units, while in (*S*)-BNI^{-} they are confined to a single naphthalimide. Notably, the transitions of (*S*)-BNI^{-} all occur at energies matching a transition of either (*S*)-BNI or (*S*)-BNI^{2-}, making it hard to distinguish in UV-vis SEC. However, the predicted CD spectrum of (*S*)-BNI^{-} exhibits a unique feature consisting of a positive Cotton signal where (*S*)-BNI^{2-} shows a CD response with both positive and negative Cotton signals; this feature can be observed in Figure 3.15 with a small peak at 417 nm.

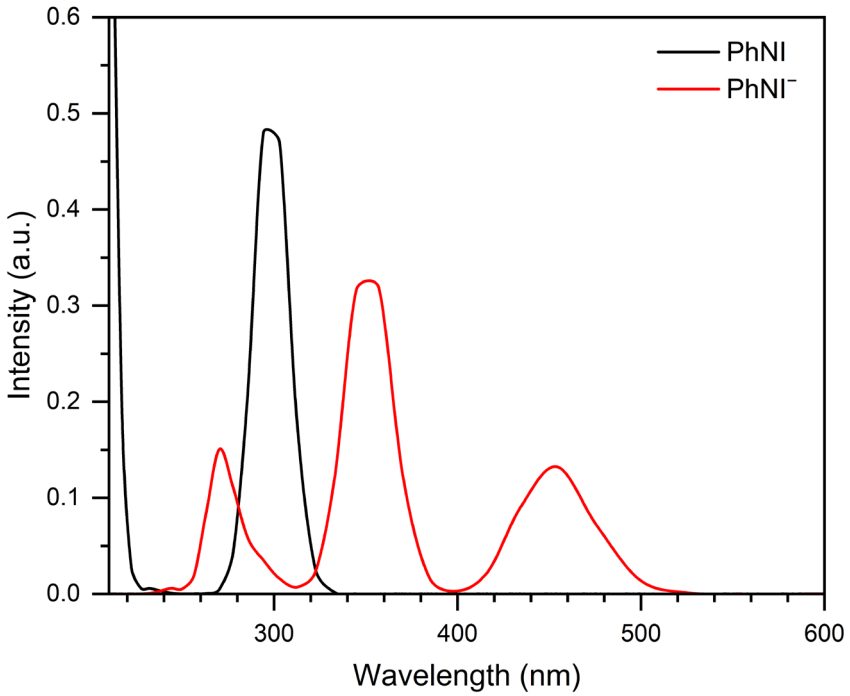

Figure 3.20. Calculated UV-vis spectra for PhNI (black) and $PhNI^{-}$ (red).

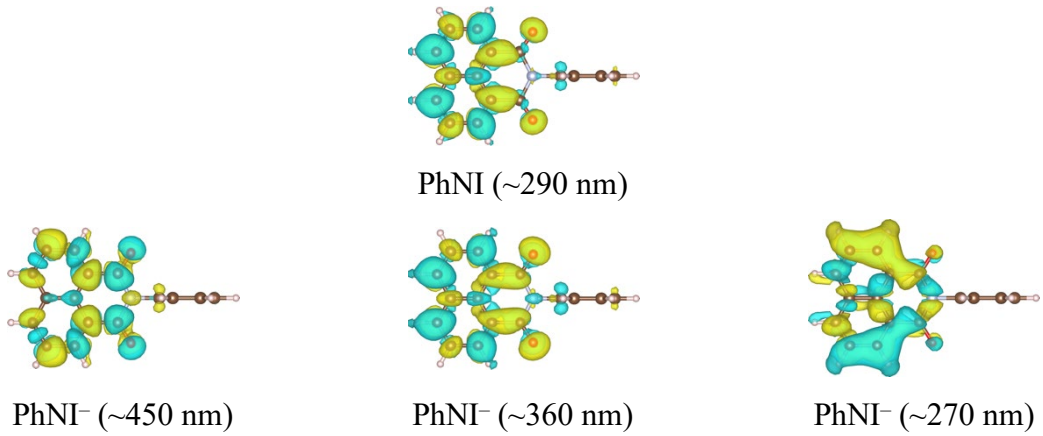

Figure 3.21. Natural transition orbitals for PhNI (top) and $PhNI^-$ (bottom) corresponding to the major peaks in the calculated UV-vis spectra. Yellow and turquoise sections signify positive and negative regions, respectively.

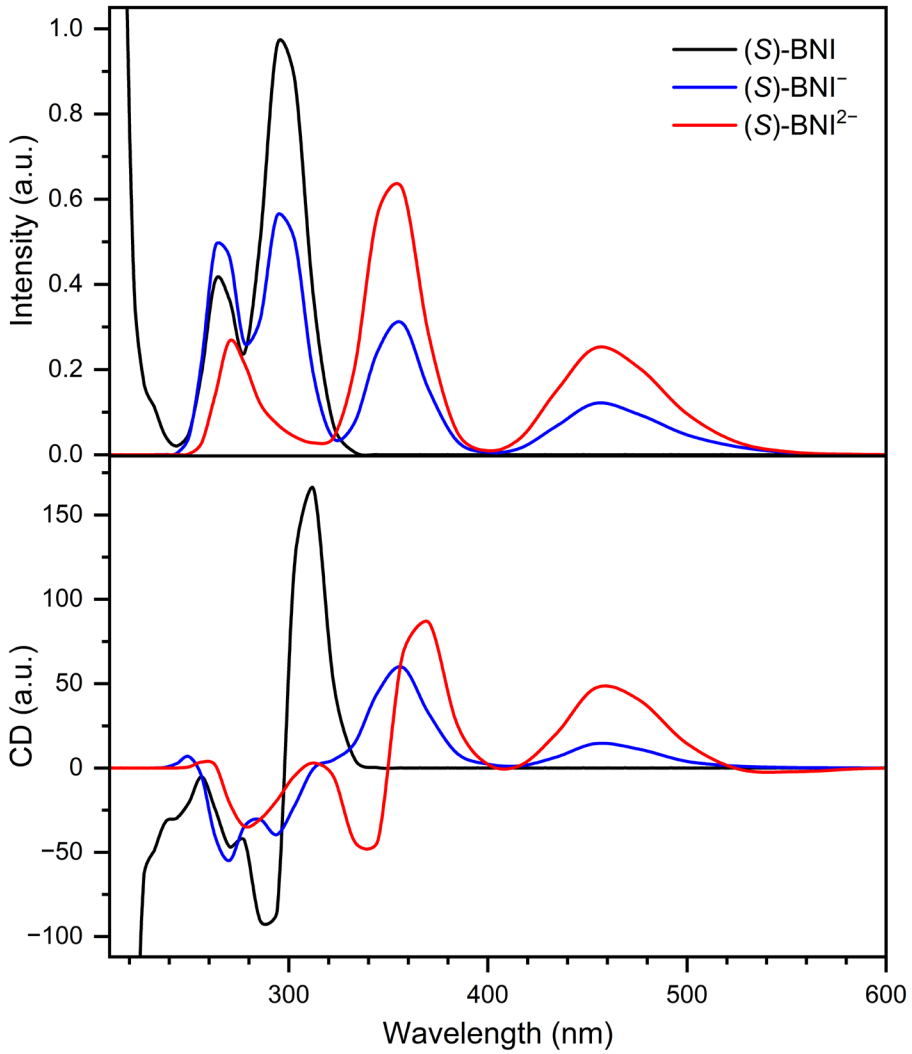

Figure 3.22. Calculated UV-vis (top) and CD (bottom) for (*S*)-BNI (black), (*S*)-BNI^- (blue), and (*S*)-BNI^{2-} (red).

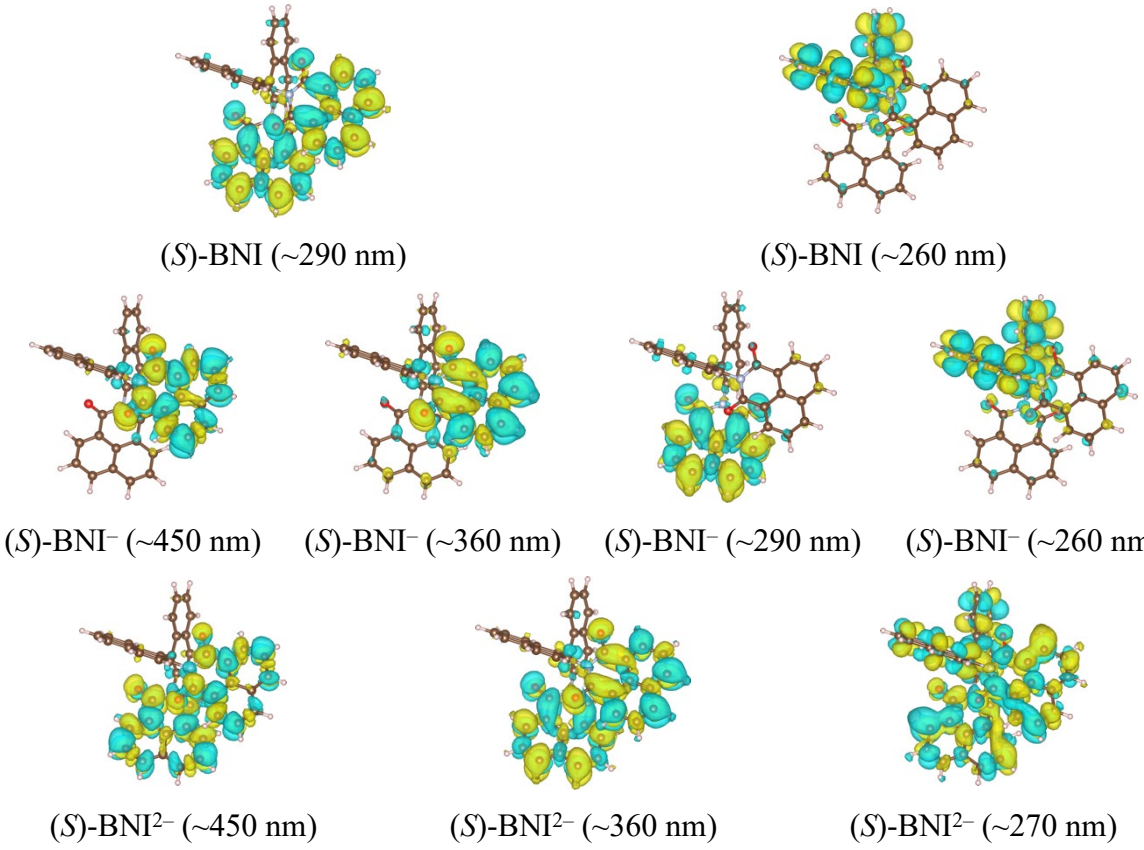

Figure 3.23. Natural transition orbitals for (*S*)-BNI (top), (*S*)-BNI^{-} (middle), and (*S*)-BNI^{2-} corresponding to the major peaks in the calculated UV-vis and CD spectra. Yellow and turquoise sections signify positive and negative regions, respectively.

3.6 Further Investigations of the doubly reduced state of (*S*/*R*)-BNI

To further characterise the reduced states of PhNI and (*S*/*R*)-BNI, EPR SEC was performed. Beginning with PhNI, reduction produced a clear radical signal with a g-factor of 2.0032, confirming reduction is a single-electron process generating the PhNI^{-} radical anion species (Figure 3.24). The EPR spectrum of PhNI^{-} contained numerous hyperfine splittings, with the coupling constants determined through simulation and least-squares fitting analysis as follows: aH = 2.10 MHz (2H), aH = 13.8 MHz (2H), aH = 16.2 MHz (2H), aN = 3.87 MHz (1N). This hyperfine splitting pattern is consistent with three pairs of symmetry equivalent hydrogen environments and one nitrogen environment and confirms the delocalised nature of the radical anion.

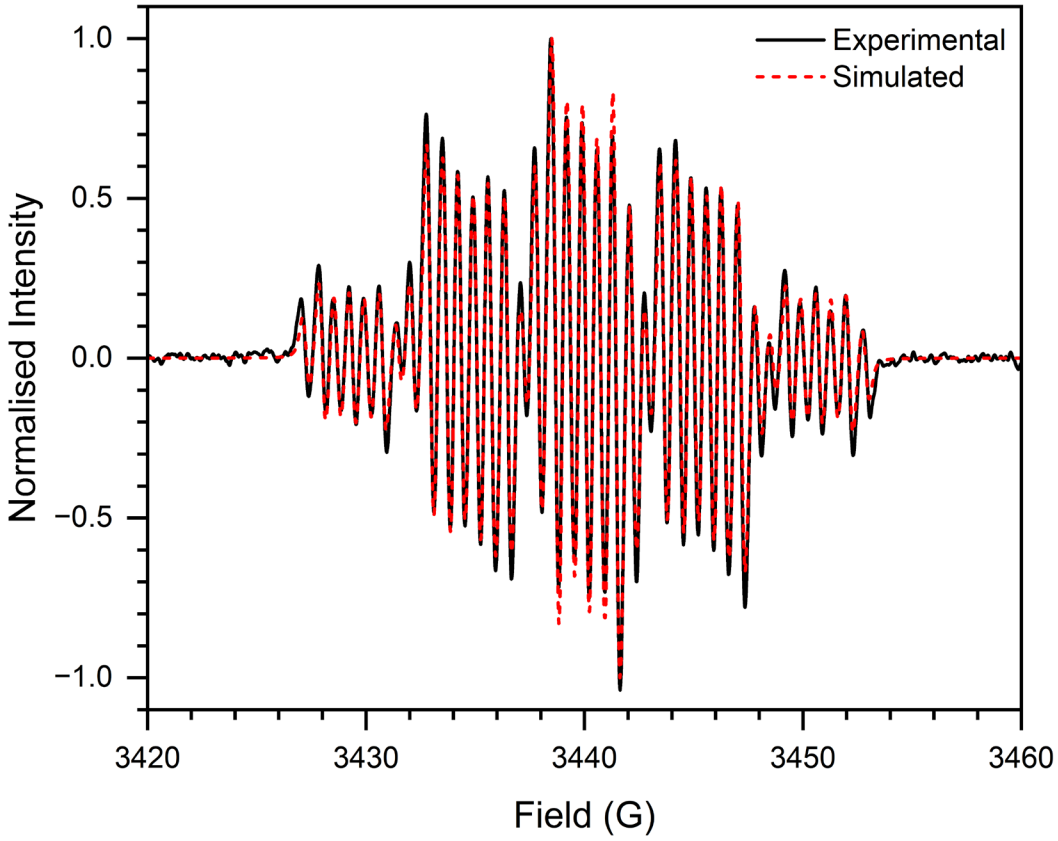

Figure 3.24. Experimental EPR spectrum of $PhNI^{-}$ (black) and the simulated spectrum (red dashed line). $PhNI^{-}$ was generated by reduction of a 1 mM solution of PhNI in DMF with 0.1 M $[(n\text{-}C_4H_9)_4N]PF_6$ as supporting electrolyte. Instrument parameters: microwave frequency = 9.645 GHz; modulation amplitude = 0.2 G; modulation frequency = 100 kHz; microwave power = 10 mW.

The EPR spectrum of (*S*)-BNI^{2-} also shows a radical signal with a g-factor of 2.0032 (Figure 3.25). The spectrum shows clear differences to that obtained for $PhNI^{-}$, likely due to the presence of two radical sites, one for each naphthalimide moiety. Unfortunately, a satisfactory simulation of this spectrum to obtain hyperfine coupling constants was not possible, likely due to the complexity of the spin system, which presumably contains two unpaired electrons plus a large number of coupled nuclei. Nevertheless, the system is tentatively assigned as a biradical system (two coupled S = ½ spins) rather than a triplet state (S = 1) for the following two reasons: (1) the absence of a detectable 'half field' resonance peak, a characteristic marker of a triplet state;[50, 51] (2) in the case of a strong exchange interaction between identical spin systems, the hyperfine couplings are expected to be half that of the analogous monoradical.[51, 52] In the EPR spectrum of (*S*)-BNI^{2-}, the smallest observed hyperfine coupling is 0.93 MHz, roughly half of the smallest coupling in the $PhNI^{-}$ radical anion. These results are also supported by DFT calculations which found the biradical state to be lower in energy than the

triplet state. As expected, the EPR spectrum of (*R*)-BNI^{2-} matched that of (*S*)-BNI^{2-} under identical conditions (Figure A5).

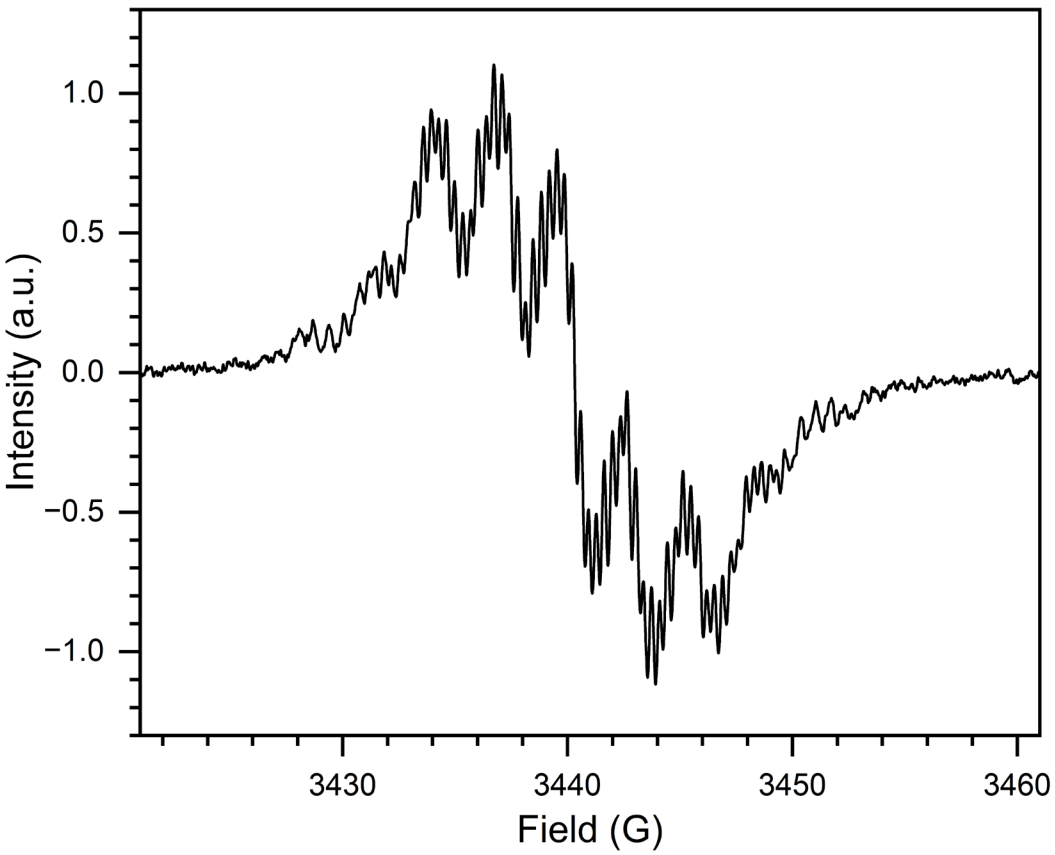

Figure 3.25. EPR spectrum of (*S*)-BNI^{2-} generated by reduction of a 2 mM solution of (*S*)-BNI in DMF with 0.1 M [(*n*-C_4H_9)$_4$N]PF_6 as supporting electrolyte. Instrument parameters: microwave frequency = 9.646 GHz; modulation amplitude = 75 mG; modulation frequency = 100 kHz; microwave power = 10 mW.

In contrast to the UV-vis and CD SEC experiments, the EPR SEC measurements were performed in DMF due to solubility limitations of (*S*/*R*)-BNI in MeCN. To confirm that the fundamental nature of the radical species is the same in both MeCN and DMF – and therefore that the EPR SEC and UV-vis/CD SEC experiments are analysing the same doubly reduced species – EPR SEC of PhNI was performed in MeCN (Figure 3.26). In MeCN, the PhNI^{-} radical anion exhibited a similar spectrum to that observed in DMF, with a g-factor of 2.0029 and hyperfine couplings of aH = 2.34 MHz (2H), aH = 14.1 MHz (2H), aH = 16.2 MHz (2H), aN = 3.97 MHz (1N), as determined by spectral simulation least-squares fitting analysis. The small differences between DMF and MeCN are easily attributed to differences in solvent polarity rather than a fundamental change in the identity of the radical species. Therefore, given that PhNI and (*S*/*R*)-BNI contain the same redox-active chromophore, it is presumed that the EPR SEC and UV-vis/CD SEC experiments are indeed measuring the same species.

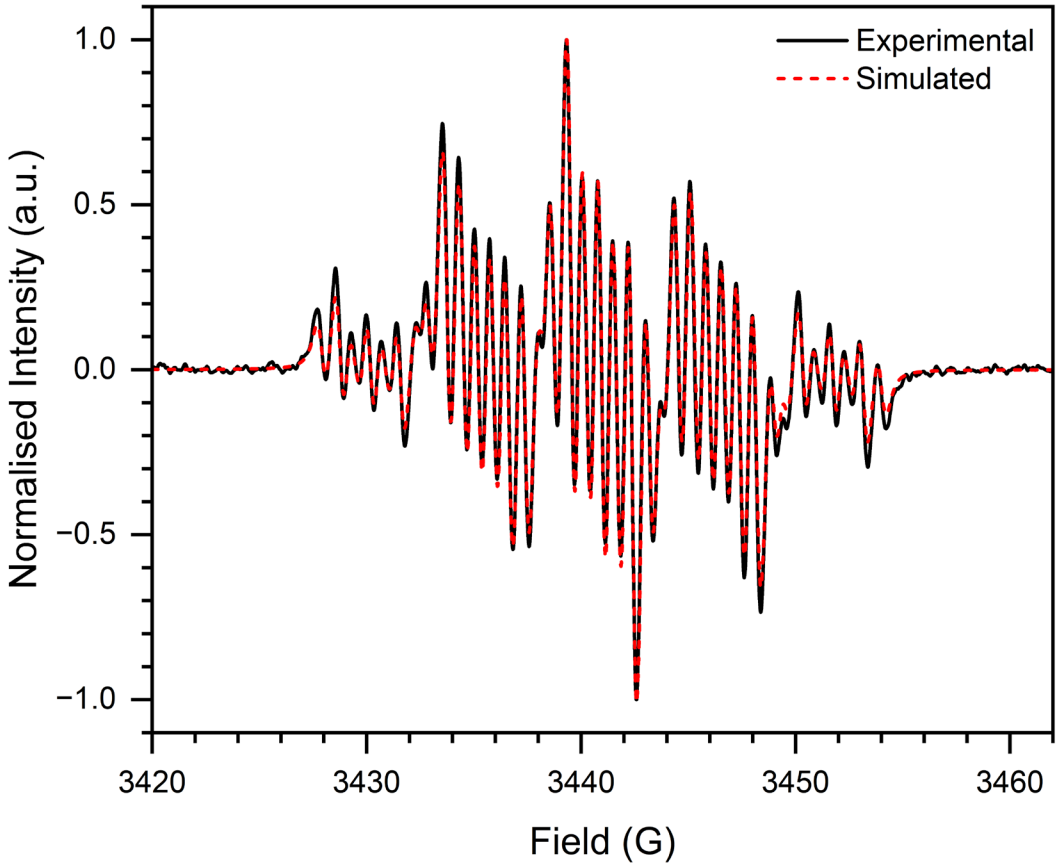

Figure 3.26. Experimental EPR spectrum of $PhNI^{-}$ (black) and the simulated spectrum (red dashed line). $PhNI^{-}$ was generated by reduction of a 1 mM solution of PhNI in MeCN with 0.1 M $[(n\text{-}C_4H_9)_4N]PF_6$ as supporting electrolyte. Instrument parameters: microwave frequency = 9.646 GHz; modulation amplitude = 0.2 G; modulation frequency = 100 kHz; microwave power = 10 mW.

3.7 Magneto-Optical Properties of (*S*/*R*)-BNI

The magneto-optical properties of (*S*/*R*)-BNI were investigated by magnetic circular dichroism (MCD) spectroscopy (Figure 3.27). The $MCD_{N\rightarrow S}$ spectra of (*S*)-BNI show a derivative-like signal with peaks at 347 nm and 316 nm. The magnetic field normalised MCD dissymmetry factors, g_{MCD}, were 4.7×10^{-4} at 347 nm and -3.6×10^{-4} at 316 nm. These g_{MCD} values are intermediate compared to those for other organic molecules,[53, 54] however some metal complexes have exhibited g_{MCD} values several orders of magnitude larger.[55-58] As expected, the MCD spectra have equal magnitude but opposite sign when the magnetic field direction is reversed.[59, 60] Additionally, the MCD intensity was approximately four times larger when using a 1.6 T magnet compared to a 0.4 T magnet, in agreement with the expected linear response to magnetic field strength.[59, 60] These results demonstrate how magnetic field could also be used as a stimulus for chiroptical switching since both increasing/decreasing the magnetic field strength or reversing the polarity of the magnetic field cause clear changes in the MCD signal.

These measurements were performed using permanent magnets, which require manual work to either reverse their orientation or install a magnet with a different field strength. To achieve chiroptical switching in a practical sense, an electromagnet is preferable as the strength and polarity of the magnetic field can be easily adjusted.

The origin of the MCD signals is simple. Since (*S*)-BNI is diamagnetic and lacks three-fold or higher rotational symmetry, it cannot possess degenerate ground- or excited-states and therefore can only exhibit B term MCD contributions.[53, 59, 61] The derivative-like MCD spectral features seen in Figure 3.27 are typical of MCD A-terms, however they are also observed for B-term contributions when the two mixing excited states are close in energy.[59, 60, 62] Such cases are referred to as pseudo-A terms. Identical results were obtained for (*R*)-BNI (Figure A6).

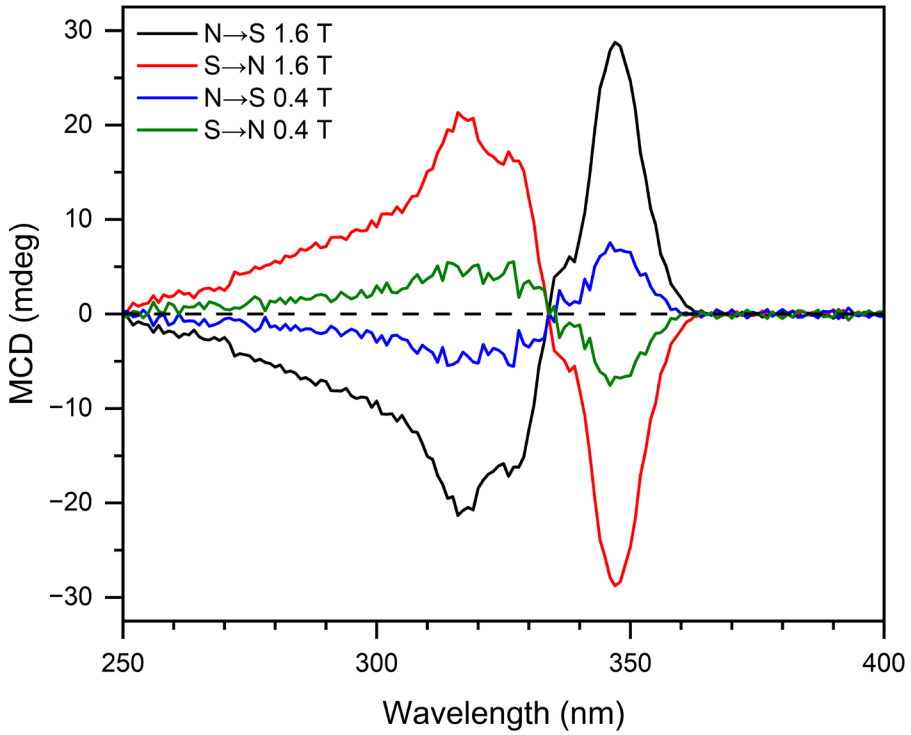

Figure 3.27. MCD spectra of (*S*)-BNI in MeCN with different magnetic field strengths and orientations. Sample concentration was 110 μM.

Since (*S*/*R*)-BNI displayed both CD and MCD responses, it was hoped that magneto-chiral dichroism (MChD) could also be observed. Unfortunately, no MChD signal was observed. The likely explanation for this is that the intensity of any MChD response was too low to be detected. Indeed, MChD is known to be weak and can be approximated as the product of CD and MCD, that is, $g_{MChD} \approx g_{abs} \times g_{MCD}$.[63, 64] For (*S*)-BNI this would equate to a very small g_{MChD} with a 10^{-7} magnitude. In this case even repeating the experiment in a stronger magnetic field may not be sufficient to observe a signal. Furthermore, it has been observed that MChD is

intensified by large orbital angular momentum;[54, 64] hence the prominence of d- and f-block metals in MChD studies. In organic compounds, orbital angular momentum increases with increasing π-conjugation.[54, 64] To date there have been very few examples of purely organic molecules which display detectable MChD, with the most prominent being a porphyrin-based system containing extensive π-conjugation.[54] Compared to porphyrin, (*S*/*R*)-BNI clearly possess much smaller effective conjugation due to the twisting between the naphthalene and naphthalimide rings, which disrupts the planarity that would be needed to enable more extensive π-conjugation and thus orbital angular momentum.

3.8 (*S*/*R*)-BNI Thin Films

Given the promising solution-state performance of (*S*/*R*)-BNI, spin-coated thin films of (*S*/*R*)-BNI were prepared to investigate their solid-state behaviour (Figure 3.28). Compared to MeCN solution, the absorbance is redshifted by 13 nm in the solid state (λ_{max} = 346 nm) but retains the same general features (Figure 3.29). The films displayed nonzero absorbance at long wavelengths which were too low in energy to cause electronic excitation. This was ascribed to scattering of incident light by the films and could not be precisely modelled but was partially accounted for by a baseline subtraction (~0.075) to make the absorbance zero at 450 nm. The CD of the films were similarly redshifted – with peaks at 367 nm and 336 nm – but were otherwise aligned with the CD measured in solution (Figure 3.29). The thin films of (*S*)- and (*R*)-BNI have g_{abs} of 1.4×10^{-3} and -1.2×10^{-3} at 367 nm, respectively. While slightly less than the analogous solution-state g_{abs}, these values are in reality an underestimate due to residual scattering contributions to the absorbance.

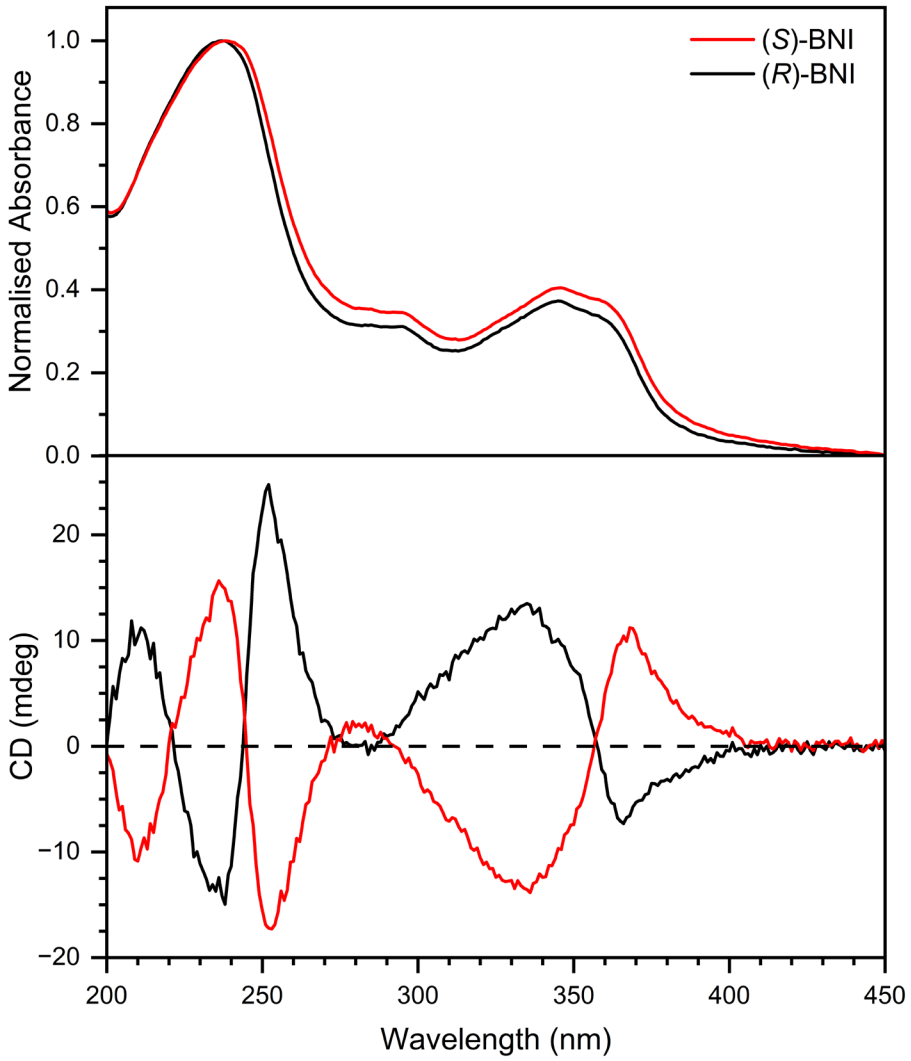

Figure 3.28. Normalised absorbance (top) and CD (bottom) of (*S*)-BNI (red) and (*R*)-BNI (black) thin films.

As noted previously, (*S*/*R*)-BNI were found to be nonemissive in solution due to due to highly efficient internal conversion stemming from solvent cage and geometrical relaxation.[39] It was expected that these nonradiative decay pathways would be suppressed in the solid state and facilitate aggregation-induced emission. This was confirmed by fluorescence measurements of (*S*/*R*)-BNI thin films, which exhibited turquoise fluorescence (emission maximum = 467 nm) when excited with UV light (Figure 3.30 and Figure A7). The large Stokes shift of 7490 cm^{-1} can likely be attributed to the formation of aggregates, which often causes a redshift in fluorescence compared to isolated monomers because the excited state wave function extends over a larger volume, lowering the transition energy. The absence of a higher energy monomeric fluorescence peak indicates that all (*S*/*R*)-BNI molecules are in an aggregated state, as expected in a neat film. This result is consistent with the reported fluorescence of PhNI aggregates in the solid state, which exhibited an emission maximum similar to that observed

here for the (*S*/*R*)-BNI thin films.[65] Preparing thin films of (*S*/*R*)-BNI at different weight fractions in a polymer matrix could reduce the amount of aggregation and potentially allow monomeric fluorescence to be observed.

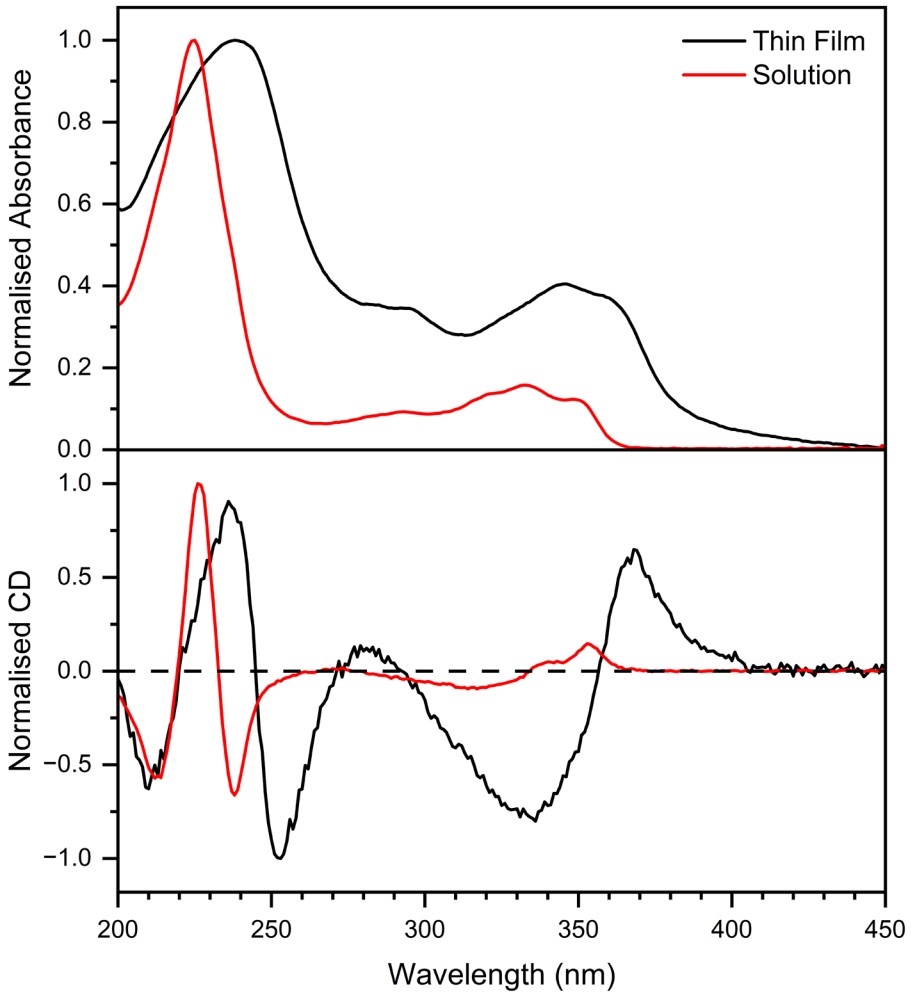

Figure 3.29. Normalised absorbance (top) and CD (bottom) of (*S*)-BNI in a thin film (black) and in 10 μM MeCN solution (red).

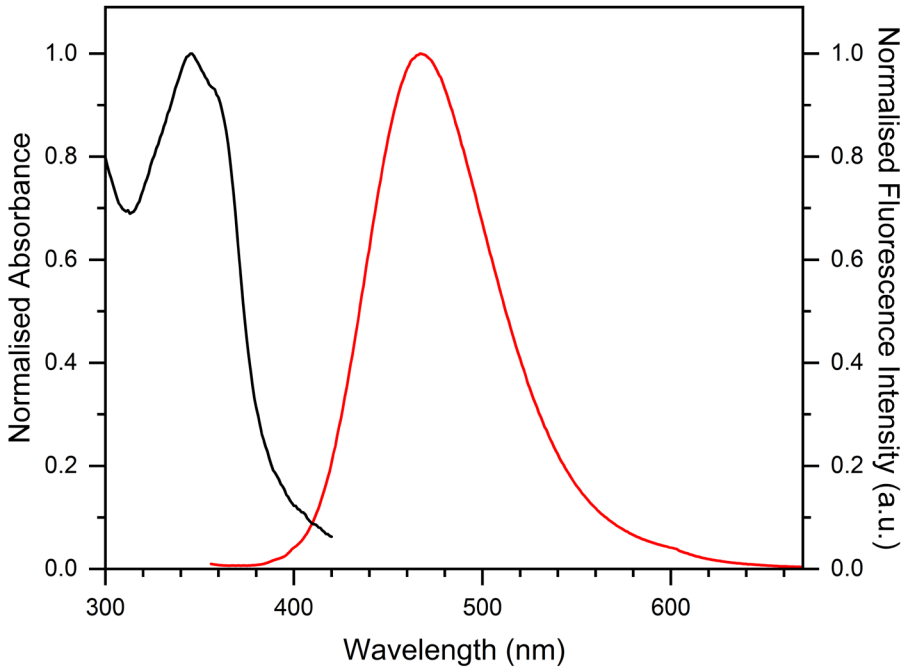

Figure 3.30. Normalised absorbance (black) and normalised fluorescence emission intensity (red) of (*S*)-BNI thin films. Excitation wavelength = 344 nm.

Given their promising fluorescence behaviour, CPL measurements were performed on the (*S*/*R*)-BNI thin films (Figure 3.31). While (*S*)- and (*R*)-BNI displayed differences in their spectra, they were not mirror images as would be expected of enantiomers. This indicates that additional effects were also occurring, however these features could not be deconvoluted to isolate the pure CPL spectra of (*S*/*R*)-BNI. Circularly polarised light scattering is one possible explanation as there is a difference in how chiral materials scatter circularly polarised light.[66] This effect could be more pronounced at longer wavelengths where the proportion of scattered light to emitted light is much larger.

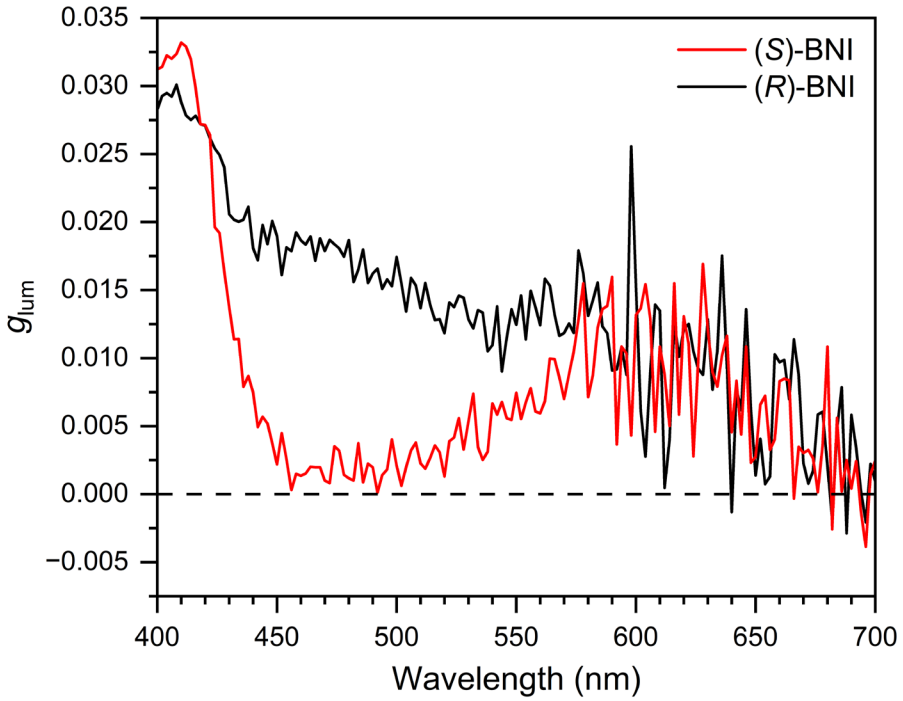

Figure 3.31. CPL spectra of (*S*)-BNI (red) and (*R*)-BNI (black) thin films. The excitation source was a 380 nm LED.

It was also envisioned that spin coating (*S*/*R*)-BNI onto conductive ITO slides would facilitate redox-modulated chiroptical switching in the solid-state. Unfortunately, this was not possible for the following reasons: (1) (*S*/*R*)-BNI show at least some degree of solubility in organic solvents meaning that use of an organic electrolyte would simply result in dissolution of the film. (2) Aqueous electrolytes are also unsuitable because the reduced states of (*S*/*R*)-BNI are unstable in aqueous solution, as demonstrated by lack of reversibility in solid-state CV measurements performed in water (Figure 3.32). Such dilemmas are likely applicable to many organic-based redox switches in the solid state. A possible solution is to incorporate a relevant functional group into the molecule to facilitate covalent binding to a conductive substrate, allowing organic electrolytes to be used.

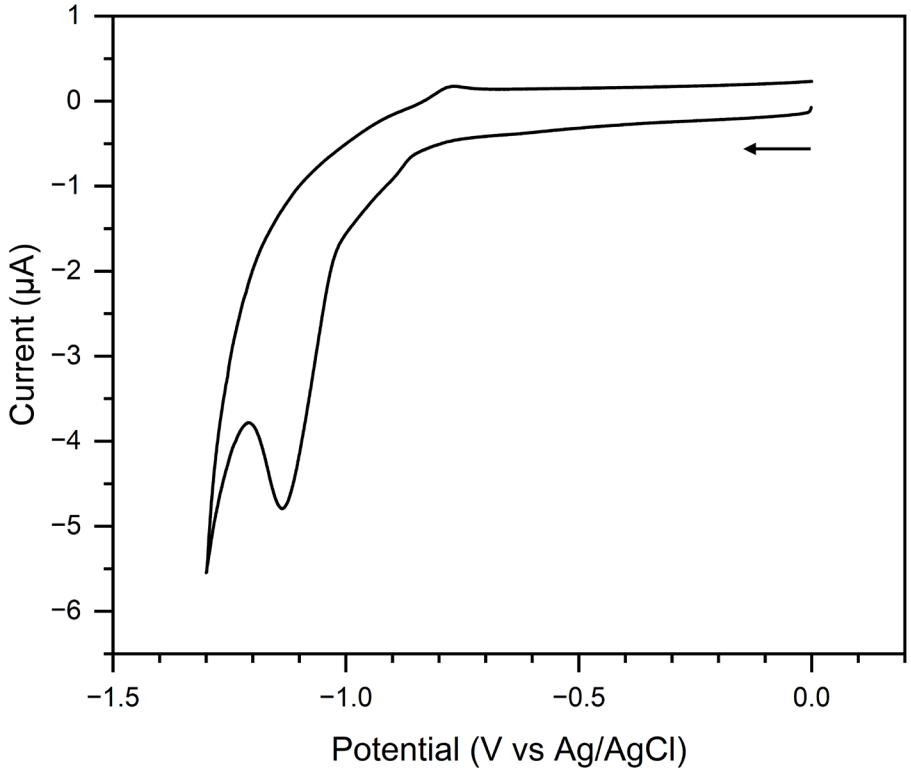

Figure 3.32. Solid-state cyclic voltammogram of (*S*)-BNI with aqueous 0.25 M NaCl supporting electrolyte. The scan rate = 100 mV/s and the arrow shows the direction of the potential sweep.

3.9 Conclusions

In conclusion, this chapter describes the successful synthesis and characterisation of a novel pair of redox-modulated chiroptical switches, (*S*)-BNI and (*R*)-BNI, combining both an axially chiral 1,1′-binaphthyl core and pendant redox-active 1,8-naphthalimide groups. Reduction of the naphthalimide moieties leads to significant changes in their UV-vis, CD, and EPR spectra, as observed through *in situ* spectroelectrochemical measurements. Therefore, repeated cycles of reduction and oxidation allowed (*S*)- and (*R*)-BNI to function as chiroptical switches with both visible (425 nm) and UV (354 nm) chiroptic readouts. A detailed assessment of the optical transitions was carried out through DFT modelling, indicating that the observed transitions in all redox states of (*S*)-BNI were highly localised to the naphthalimide groups, except for the highest energy transitions, which involved the binaphthyl backbone. Furthermore, an analysis of the EPR spectrum of doubly reduced (*S*)-BNI^{2-} revealed that it is best described as a biradical species rather than a triplet species, in agreement with other spectroscopic data.

The magneto-optical properties of (*S*)-BNI and (*R*)-BNI were also investigated, revealing clear positive and negative MCD signals ascribed to MCD B terms. Unfortunately, the expected strength of any MChD response was very weak, and no MChD was detected. Nonetheless, it

would be interesting to perform MCD on the singly and doubly reduced states of (*S*/*R*)-BNI as this would allow temperature-dependent MCD C terms to be observed. It is possible that the strength of MCD would be larger for these reduced states and therefore make detection and analysis of MChD possible. Regardless, these results indicated that magnetic field-modulated chiroptical switching would be possible, provided a facile way to modulate the magnetic field was employed. This would enable dual-responsive chiroptical switching, a useful capability which will be explored in greater detail in Chapter 4.

The solid-state properties of (*S*)-BNI and (*R*)-BNI were also studied. Thin films were prepared by spin coating and their CD spectra replicated the observed solution state spectra well. Interestingly, the films of (*S*/*R*)-BNI displayed aggregation-induced emission – a stark contrast with their nonemissive solution state behaviour. CPL measurements were thus performed, with (*S*)-BNI and (*R*)-BNI displaying different CPL responses. It is likely that other effects such as chiral scattering also contributed to the observed CPL spectra, therefore the pure CPL contributions could not be reliably identified. Additionally, the (*S*/*R*)-BNI thin films were unsuitable for measuring solid-state redox-modulated chiroptical switching due to the experimental difficulties of identifying an appropriate electrolyte solution.

3.10 Future Work

The work presented in this chapter provides ample scope for future research directions. A natural extension would be to synthesise a derivative of (*S*/*R*)-BNI in which one naphthalimide moiety is functionalised with an electron-withdrawing group and the other with an electron-donating group (see Figure 3.33a for an example structure). The resulting $E_{1/2}$ of each naphthalimide would thus be sufficiently separated that the intermediate, singly reduced state could be electrochemically generated as the sole species in solution. This would allow the creation of a 3-tiered, redox-modulated chiroptical switch. Furthermore, electron donating groups such as methoxy and dimethylamino are known to enhance the fluorescence of 1,8-naphthalimides in solution.[67, 68] This would enable CPL in the solution state and the possibility of performing CPL SEC experiments.

More significant changes to the structure of (*S*)-BNI and (*R*)-BNI could also combine solution-state chirality, redox-activity, and fluorescence into one molecule. For example, the naphthalimide units could be replaced with anthracene, a widely studied fluorophore which is also redox-active. A proposed structure is shown in Figure 3.33b in which anthracene-9-carboxylic acid is anchored to the binaphthyl backbone by the formation of amide bonds. This

synthesis is relatively straightforward, and some anthracene-9-carboxylic acid has already been prepared via a Grignard reaction of 9-bromoanthracene.

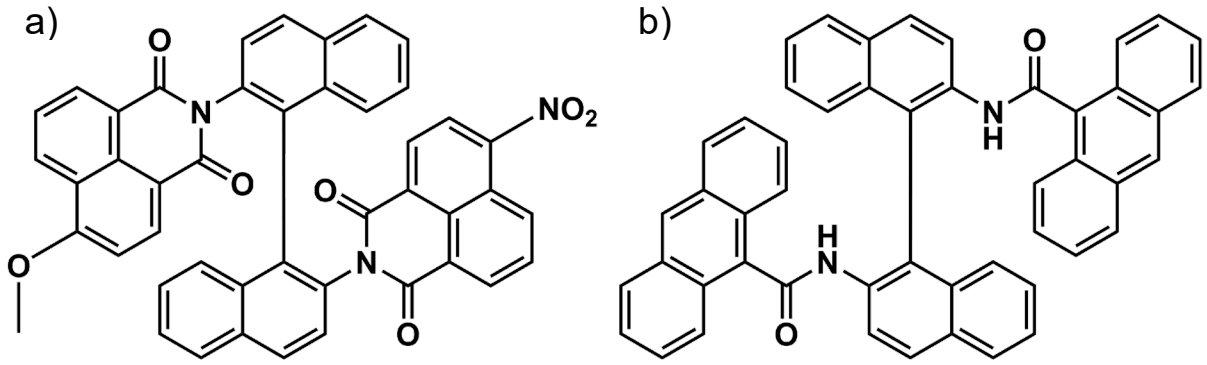

Figure 3.33. (a) A derivative of (*S*/*R*)-BNI with an electron donating methoxy group and electron withdrawing nitro group. (b) A BINAM derivative containing pendant anthracenes.

As previously described, SEC experiments are unsuited for determining the 'true' electrochemical reversibility of a particular redox process. Despite the importance of these characteristics to real-world applications, such measurements receive almost no focus in the literature on redox-modulated chiroptical (or optical) switching. However, the field of redox-flow batteries have already seen the widespread adoption of key metrics for bulk-scale electrochemical cycling. These are coulombic efficiency (the ratio of discharge capacity to charge capacity within one cycle) and capacity retention (the discharge capacity of a cycle divided by the discharge capacity of the previous cycle).[45, 69, 70] Undertaking such experiments to determine the coulombic efficiency and capacity retention of (*S*/*R*)-BNI would therefore provide a more valid measure of its potential performance over long-term redox cycling.

3.11 References

(1) Beer, G.; Niederalt, C.; Grimme, S.; Daub, J. Redox Switches with Chiroptical Signal Expression Based on Binaphthyl Boron Dipyrromethene Conjugates. *Angew. Chem. Int. Ed.* **2000**, *39*, 3252-3255.

(2) Chen, X.-M.; Chen, Y.; Liang, L.; Liu, Q.-J.; Liu, Y. Chiral Binaphthylbis(4,4′-Bipyridin-1-Ium)/Cucurbit[8]Uril Supramolecular System and Its Induced Circularly Polarized Luminescence. *Macromol. Rapid Commun.* **2018**, *39*, 1700869.

(3) Sun, Z.-B.; Liu, J.-K.; Yuan, D.-F.; Zhao, Z.-H.; Zhu, X.-Z.; Liu, D.-H.; Peng, Q.; Zhao, C.-H. 2,2′-Diamino-6,6′-diboryl-1,1′-binaphthyl: A Versatile Building Block for Temperature-Dependent Dual Fluorescence and Switchable Circularly Polarized Luminescence. *Angew. Chem. Int. Ed.* **2019**, *58*, 4840-4846.

(4) van Vliet, S.; Alachouzos, G.; de Vries, F.; Pfeifer, L.; Feringa, B. L. Visible light activated BINOL-derived chiroptical switches based on boron integrated hydrazone complexes. *Chem. Sci.* **2022**, *13*, 9713-9718.

(5) Barooah, N.; Tamuly, C.; Baruah, J. B. Synthesis, characterisation of few N-substituted 1,8-naphthalimide derivatives and their copper(II) complexes. *J. Chem. Sci.* **2005**, *117*, 117-122.

(6) Rogers, J. E.; Kelly, L. A. Nucleic Acid Oxidation Mediated by Naphthalene and Benzophenone Imide and Diimide Derivatives: Consequences for DNA Redox Chemistry. *J. Am. Chem. Soc.* **1999**, *121*, 3854-3861.

(7) Dong, H.-Q.; Wei, T.-B.; Ma, X.-Q.; Yang, Q.-Y.; Zhang, Y.-F.; Sun, Y.-J.; Shi, B.-B.; Yao, H.; Zhang, Y.-M.; Lin, Q. 1,8-Naphthalimide-based fluorescent chemosensors: recent advances and perspectives. *J. Mater. Chem. C* **2020**, *8*, 13501-13529.

(8) Gopikrishna, P.; Meher, N.; Iyer, P. K. Functional 1,8-Naphthalimide AIE/AIEEgens: Recent Advances and Prospects. *ACS Appl. Mater. Interfaces* **2018**, *10*, 12081-12111.

(9) Srivastava, A. K.; Singh, A.; Mishra, L. Tuning of Aggregation Enhanced Emission and Solid State Emission from 1,8-Naphthalimide Derivatives: Nanoaggregates, Spectra, and DFT Calculations. *J. Phys. Chem. A* **2016**, *120*, 4490-4504.

(10) Patel, D. C.; Woods, R. M.; Breitbach, Z. S.; Berthod, A.; Armstrong, D. W. Thermal racemization of biaryl atropisomers. *Tetrahedron: Asymmetry* **2017**, *28*, 1557-1561.

(11) Liu, Z.; Lu, X.; Liu, M.; Wang, W. Blue, Yellow, and Red Carbon Dots from Aromatic Precursors for Light-Emitting Diodes. *Molecules* **2023**, *28*, 2957.

(12) Xu, X.; Qu, L.; Song, J.; Wu, D.; Zhou, X.; Xiang, H. A simple and visual approach for enantioselective recognition through supramolecular gels with specific selectivity. *Chem. Commun.* **2019**, *55*, 9873-9876.

(13) Meng, Q.; Feng, Q.; Cui, L.; Li, F.; Cheng, Y.; Li, Y.; Wang, Y. Chiral binaphthylamine based emitters with donor-acceptor structures: Facile synthesis and circularly polarized luminescence. *Dyes Pigm.* **2022**, *199*, 110085.

(14) Yan, Z.-P.; Liu, T.-T.; Wu, R.; Liang, X.; Li, Z.-Q.; Zhou, L.; Zheng, Y.-X.; Zuo, J.-L. Chiral Thermally Activated Delayed Fluorescence Materials Based on R/S-N2,N2′-Diphenyl-[1,1′-binaphthalene]-2,2′-diamine Donor with Narrow Emission Spectra for Highly Efficient Circularly Polarized Electroluminescence. *Adv. Funct. Mater.* **2021**, *31*, 2103875.

(15) Sun, C.; Liu, W.; Mu, Y.; Wang, X. 1,1′-binaphthyl-2,2′-diamine as a novel MALDI matrix to enhance the in situ imaging of metabolic heterogeneity in lung cancer. *Talanta* **2020**, *209*, 120557.

(16) Zheng, M.-Y.; Jin, Z.-B.; Ma, Z.-Z.; Gu, Z.-G.; Zhang, J. Photo-Curable 3D Printing of Circularly Polarized Afterglow Metal–Organic Framework Monoliths. *Adv. Mater.* **2024**, *36*, 2313749.

(17) Seliskar, C. J.; Brand, L. Electronic spectra of 2-aminonaphthalene-6-sulfonate and related molecules. I. General properties and excited-state reactions. *J. Am. Chem. Soc.* **1971**, *93*, 5405-5414.

(18) Soltermann, A. T.; Luiz, M.; Biasutti, M. A.; Carrascoso, M.; Amat-Guerri, F.; García, N. A. Monosubstituted naphthalenes as quenchers and generators of singlet molecular oxygen. *J. Photochem. Photobiol., A* **1999**, *129*, 25-32.

(19) Nizar, N. S. S.; Sujith, M.; Swathi, K.; Sissa, C.; Painelli, A.; Thomas, K. G. Emergent chiroptical properties in supramolecular and plasmonic assemblies. *Chem. Soc. Rev.* **2021**, *50*, 11208-11226.

(20) Wakabayashi, M.; Yokojima, S.; Fukaminato, T.; Shiino, K.-i.; Irie, M.; Nakamura, S. Anisotropic Dissymmetry Factor, g: Theoretical Investigation on Single Molecule Chiroptical Spectroscopy. *J. Phys. Chem. A* **2014**, *118*, 5046-5057.

(21) Liu, C.; Yang, J.-C.; Lam, J. W. Y.; Feng, H.-T.; Tang, B. Z. Chiral assembly of organic luminogens with aggregation-induced emission. *Chem. Sci.* **2022**, *13*, 611-632.

(22) Liu, J.; Su, H.; Meng, L.; Zhao, Y.; Deng, C.; Ng, J. C. Y.; Lu, P.; Faisal, M.; Lam, J. W. Y.; Huang, X.; et al. What makes efficient circularly polarised luminescence in the condensed phase: aggregation-induced circular dichroism and light emission. *Chem. Sci.* **2012**, *3*, 2737-2747.

(23) Song, F.; Xu, Z.; Zhang, Q.; Zhao, Z.; Zhang, H.; Zhao, W.; Qiu, Z.; Qi, C.; Zhang, H.; Sung, H. H. Y.; et al. Highly Efficient Circularly Polarized Electroluminescence from Aggregation-Induced Emission Luminogens with Amplified Chirality and Delayed Fluorescence. *Adv. Funct. Mater.* **2018**, *28*, 1800051.

(24) Yuan, Y.-X.; Hu, M.; Zhang, K.-R.; Zhou, T.-T.; Wang, S.; Liu, M.; Zheng, Y.-S. The largest CPL enhancement by further assembly of self-assembled superhelices based on the helical TPE macrocycle. *Mater. Horiz.* **2020**, *7*, 3209-3216.

(25) Karoń, K.; Łapkowski, M.; Dobrowolski, J. C. ECD spectroelectrochemistry: A review. *Spectrochim. Acta A* **2021**, *250*, 119349.

(26) Zhu, G.; Yi, Y.; Han, Z.; Liu, J.; Gai, Z. 3,4,9,10-Perylene Tetracarboxylic Acid Noncovalently Modified Multiwalled Carbon Nanotubes: Synthesis, Characterization, and Application for Electrochemical Determination of 2-Aminonaphthalene. *Anal. Lett.* **2014**, *47*, 2370-2383.

(27) Zheng, J.; Qiao, W.; Wan, X.; Gao, J. P.; Wang, Z. Y. Near-Infrared Electrochromic and Chiroptical Switching Materials: Design, Synthesis, and Characterization of Chiral Organogels Containing Stacked Naphthalene Diimide Chromophores. *Chem. Mater.* **2008**, *20*, 6163-6168.

(28) Elgrishi, N.; Rountree, K. J.; McCarthy, B. D.; Rountree, E. S.; Eisenhart, T. T.; Dempsey, J. L. A Practical Beginner's Guide to Cyclic Voltammetry. *J. Chem. Educ.* **2018**, *95*, 197-206.

(29) Martín, E.; Weigand, R. A correlation between redox potentials and photophysical behaviour of compounds with intramolecular charge transfer: application to N-substituted 1,8-naphthalimide derivatives. *Chem. Phys. Lett.* **1998**, *288*, 52-58.

(30) Gao, J.; Berden, G.; Oomens, J. LABORATORY INFRARED SPECTROSCOPY OF GASEOUS NEGATIVELY CHARGED POLYAROMATIC HYDROCARBONS. *Astrophys. J.* **2014**, *787*, 170.

(31) Rak, S. F.; Miller, L. L. Mixed-valence, conjugated quinone and imide anion radicals. An ESR investigation. *J. Am. Chem. Soc.* **1992**, *114*, 1388-1394.

(32) Friedel, R. A.; Orchin, M.; Reggel, L. Steric Hindrance and Short Wave Length Bands in the Ultraviolet Spectra of Some Naphthalene and Diphenyl Derivatives. *J. Am. Chem. Soc.* **1948**, *70*, 199-204.

(33) Canary, J. W. Redox-triggered chiroptical molecular switches. *Chem. Soc. Rev.* **2009**, *38*, 747-756.

(34) Harada, N.; Nakanishi, K.; Berova, N. Electronic CD Exciton Chirality Method: Principles and Applications. In *Comprehensive Chiroptical Spectroscopy*, 2012; pp 115-166.

(35) Nordén, B.; Rodger, A.; Dafforn, T. *Linear Dichroism and Circular Dichroism: A Textbook on Polarized-Light Spectroscopy*; The Royal Society of Chemistry, 2010. DOI: 10.1039/9781839168932.

(36) Sun, Y.; Jiang, Y.; Jiang, J.; Li, T.; Liu, M. Keto-form directed hierarchical chiral self-assembly of Schiff base derivatives with amplified circularly polarized luminescence. *Chin. Chem. Lett.* **2024**, *35*, 108409.

(37) Lakhwani, G.; Gielen, J.; Kemerink, M.; Christianen, P. C. M.; Janssen, R. A. J.; Meskers, S. C. J. Intensive Chiroptical Properties of Chiral Polyfluorenes Associated with Fibril Formation. *J. Phys. Chem. B* **2009**, *113*, 14047-14051.

(38) Lakhwani, G.; Meskers, S. C. J. Insights from Chiral Polyfluorene on the Unification of Molecular Exciton and Cholesteric Liquid Crystal Theories for Chiroptical Phenomena. *J. Phys. Chem. A* **2012**, *116*, 1121-1128.

(39) Demeter, A.; Bérces, T.; Biczók, L.; Wintgens, V.; Valat, P.; Kossanyi, J. Comprehensive Model of the Photophysics of N-Phenylnaphthalimides: The Role of Solvent and Rotational Relaxation. *J. Phys. Chem.* **1996**, *100*, 2001-2011.

(40) Kowalski, J. A.; Neyhouse, B. J.; Brushett, F. R. The impact of bulk electrolysis cycling conditions on the perceived stability of redox active materials. *Electrochem. Commun.* **2020**, *111*, 106625.

(41) Kwabi, D. G.; Ji, Y.; Aziz, M. J. Electrolyte Lifetime in Aqueous Organic Redox Flow Batteries: A Critical Review. *Chem. Rev.* **2020**, *120*, 6467-6489.

(42) Murali, A.; Nirmalchandar, A.; Krishnamoorthy, S.; Hoober-Burkhardt, L.; Yang, B.; Soloveichik, G.; Prakash, G. K. S.; Narayanan, S. R. Understanding and Mitigating Capacity Fade in Aqueous Organic Redox Flow Batteries. *J. Electrochem. Soc.* **2018**, *165*, A1193.

(43) Sharma, S.; Andrade, G. A.; Maurya, S.; Popov, I. A.; Batista, E. R.; Davis, B. L.; Mukundan, R.; Smythe, N. C.; Tondreau, A. M.; Yang, P.; et al. Iron-iminopyridine complexes as charge carriers for non-aqueous redox flow battery applications. *Energy Storage Mater.* **2021**, *37*, 576-586.

(44) Peltier, C. R.; Rhodes, Z.; Macbeth, A. J.; Milam, A.; Carroll, E.; Coates, G. W.; Minteer, S. D. Suppressing Crossover in Nonaqueous Redox Flow Batteries with Polyethylene-Based Anion-Exchange Membranes. *ACS Energy Lett.* **2022**, *7*, 4118-4128.

(45) Wenger, S. R.; D'Alessandro, D. M. Improving the Sustainability of Electrochemical Direct Air Capture in a 3D Printed Redox Flow Cell. *ACS Sustainable Chem. Eng.* **2024**, *12*, 4789-4794.

(46) Cortijo, M.; Viala, C.; Reynaldo, T.; Favereau, L.; Fabing, I.; Srebro-Hooper, M.; Autschbach, J.; Ratel-Ramond, N.; Crassous, J.; Bonvoisin, J. Synthesis, Spectroelectrochemical Behavior, and Chiroptical Switching of Tris(β-diketonato) Complexes of Ruthenium(III), Chromium(III), and Cobalt(III). *lnorg. Chem.* **2017**, *56*, 4555-4567.

(47) Feng, S.; Wang, L.; Tian, L.; Liu, Y.; Hu, K.; Xu, H.; Wang, H.; Hua, J. Leveraging phenazine and dihydrophenazine redox dynamics in conjugated microporous polymers for high-efficiency overall photosynthesis of hydrogen peroxide. *Chem. Sci.* **2024**, *15*, 11972-11980.

(48) Paul, A.; Borrelli, R.; Bouyanfif, H.; Gottis, S.; Sauvage, F. Tunable Redox Potential, Optical Properties, and Enhanced Stability of Modified Ferrocene-Based Complexes. *ACS Omega* **2019**, *4*, 14780-14789.

(49) Swearingen, C.; Wu, J.; Stucki, J.; Fitch, A. Use of Ferrocenyl Surfactants of Varying Chain Lengths To Study Electron Transfer Reactions in Native Montmorillonite Clay. *Environ. Sci. Technol.* **2004**, *38*, 5598-5603.

(50) Bertrand, P. The zero-field splitting term. EPR spectrum for paramagnetic centres of spin greater than ½. In *Electron Paramagnetic Resonance Spectroscopy*, Springer Nature Switzerland AG, 2020; pp 197-239.

(51) Weil, J. A.; Bolton, J. R. Systems With More Than One Unpaired Electron. In *Electron Paramagnetic Resonance: Elementary Theory and Practical Applications*, John Wiley & Sons, 2006; pp 158-207.

(52) Bertrand, P. Effects of dipolar and exchange interactions on the EPR spectrum. Biradicals and polynuclear complexes. In *Electron Paramagnetic Resonance Spectroscopy*, Springer Nature Switzerland AG, 2020; pp 241-287.

(53) Gabbani, A.; Taddeucci, A.; Bertuolo, M.; Pineider, F.; Aronica, L. A.; Di Bari, L.; Pescitelli, G.; Zinna, F. Magnetic Circular Dichroism Elucidates Molecular Interactions in Aggregated Chiral Organic Materials. *Angew. Chem. Int. Ed.* **2024**, *63*, e202313315.

(54) Kitagawa, Y.; Segawa, H.; Ishii, K. Magneto-Chiral Dichroism of Organic Compounds. *Angew. Chem. Int. Ed.* **2011**, *50*, 9133-9136.

(55) Cahya Adi, L.; Willis, O. G.; Gabbani, A.; Rikken, G. L. J. A.; Di Bari, L.; Train, C.; Pineider, F.; Zinna, F.; Atzori, M. Magneto-Chiral Dichroism of Chiral Lanthanide Complexes in the Context of Richardson's Theory of Optical Activity. *Angew. Chem. Int. Ed.* **2024**, *63*, e202412521.

(56) Kitagawa, Y.; Miyatake, T.; Ishii, K. Magneto-chiral dichroism of artificial light-harvesting antenna. *Chem. Commun.* **2012**, *48*, 5091-5093.

(57) Lu, H.; Qi, F.; Wang, H.; He, T.; Sun, B.; Gao, X.; Comstock, A. H.; Gull, S.; Zhang, Y.; Qiao, T.; et al. Strong Magneto-Chiroptical Effects through Introducing Chiral Transition-Metal Complex Cations to Lead Halide. *Angew. Chem. Int. Ed.* **2024**, e202415363.

(58) Raupach, E.; Rikken, G. L. J. A.; Train, C.; Malézieux, B. Modelling of magneto-chiral enantioselective photochemistry. *Chem. Phys.* **2000**, *261*, 373-380.

(59) Kobayashi, N.; Muranaka, A.; Mack, J. Theory of Optical Spectroscopy. In *Circular Dichroism and Magnetic Circular Dichroism Spectroscopy for Organic Chemists*, The Royal Society of Chemistry, 2012; pp 1-41.

(60) Mason, W. R. Theoretical Framework: Definition of MCD Terms. In *A practical guide to magnetic circular dichroism spectroscopy*, John Wiley & Sons, 2007; pp 14-35.

(61) Sharma, A.; Wojciechowski, J. P.; Liu, Y.; Pelras, T.; Wallace, C. M.; Müllner, M.; Widmer-Cooper, A.; Thordarson, P.; Lakhwani, G. The Role of Fiber Agglomeration in Formation of Perylene-Based Fiber Networks. *Cell Rep. Phys. Sci.* **2020**, *1*, 100148.

(62) Kjærgaard, T.; Coriani, S.; Ruud, K. Ab initio calculation of magnetic circular dichroism. *WIREs Comput Mol Sci.* **2012**, *2*, 443-455.

(63) Atzori, M.; Rikken, G. L. J. A.; Train, C. Magneto-Chiral Dichroism: A Playground for Molecular Chemists. *Chem. Eur. J.* **2020**, *26*, 9784-9791.

(64) Ishii, K.; Hattori, S.; Kitagawa, Y. Recent advances in studies on the magneto-chiral dichroism of organic compounds. *Photochem. Photobiol. Sci.* **2020**, *19*, 9-19.

(65) Ge, S.; Li, B.; Meng, X.; Yan, H.; Yang, M.; Dong, B.; Lu, Y. Aggregation-induced emission, multiple chromisms and self-organization of *N*-substituted-1,8-naphthalimides. *Dyes Pigm.* **2018**, *148*, 147-153.

(66) Kwon, J.; Park, K. H.; Choi, W. J.; Kotov, N. A.; Yeom, J. Chiral Spectroscopy of Nanostructures. *Acc. Chem. Res.* **2023**, *56*, 1359-1372.

(67) Jin, R.; Tang, S. Theoretical investigation into optical and electronic properties of 1,8-naphthalimide derivatives. *J. Mol. Model.* **2013**, *19*, 1685-1693.

(68) Kagatikar, S.; Sunil, D. A systematic review on 1,8-naphthalimide derivatives as emissive materials in organic light-emitting diodes. *J. Mater. Sci.* **2022**, *57*, 105-139.

(69) Nagde, K. R.; Dhoble, S. J. Chapter 12 - Li-S ion batteries: a substitute for Li-ion storage batteries. In *Energy Materials Fundamentals to Applications*, Dhoble, S. J., Kalyani, N. T., Vengadaesvaran, B., Kariem Arof, A. Eds.; Elsevier, 2021; pp 335-371.

(70) Tornheim, A.; O'Hanlon, D. C. What do Coulombic Efficiency and Capacity Retention Truly Measure? A Deep Dive into Cyclable Lithium Inventory, Limitation Type, and Redox Side Reactions. *J. Electrochem. Soc.* **2020**, *167*, 110520.

Chapter 5

Design and Synthesis of Chiral Metal–Organic Frameworks (MOFs) for Chiroptical Switching

5.1 Overview

The versatility of molecular systems as the basis for chiroptical switches was convincingly demonstrated in Chapters 3 and 4. However, one drawback of molecular systems is that they often display small dissymmetry factors due to the random orientation of molecules in solution.[1] In contrast, the long-range ordering in supramolecular, polymeric, and framework materials can facilitate constructive interactions between many aligned chromophores which can boost the chiroptical signal,[1] in some cases resulting in large dissymmetry factors (> 0.1).[2-5] Chiral MOFs are one class of framework material and are promising candidates for studying chiroptical phenomena due to the high degree of functionality provided by the diversity of possible ligand and metal combinations.

A prominent feature of MOFs is their porosity. Guest species that are encapsulated within the pores can interact with the host framework through a variety of mechanisms such as π-π interactions,[6] hydrogen bonding,[7] electrostatic interactions,[8] energy transfer,[9] and coordination to open metal sites.[10] Since the pore spaces are themselves chiral, this can facilitate chirality transfer from the chiral MOF to an achiral guest, allowing the guest exhibit chiroptical phenomena such as CPL.[9, 11, 12] Conversely, the guest can also influence the chiroptical signal of the host framework.[13] Host-guest interactions can be harnessed to achieve chiroptical switching. For example, infiltration of a stimuli-responsive, achiral guest could allow chiroptical switching to be observed in the induced chiroptical response of the guest.[14] A key consideration for any chiroptical switch incorporating host-guest interactions is that chirality transfer is more efficient when the guest fits tightly within the pores and has limited freedom of movement.[12] This is important because a strong chirality transfer will enhance the strength of the chiroptical response and afford a more sensitive chiroptical switch.

The photophysical and fluorescent properties of lanthanide MOFs have allowed them to be used in a range of technological applications such as barcodes,[15] anticounterfeiting,[16] and luminescent sensors.[17] For chiral lanthanide MOFs, a major focus has been on developing frameworks for CPL since the large magnetic dipole moments of some f-f transitions have been shown to exhibit large g_{lum} values.[18-20] While strong CPL is desirable in its own right, CPL can also serve as a readout for chiroptical switching in chiral lanthanide MOFs. For example, through infiltration of a guest which either enhances or quenches CPL. Temperature could also be used as a stimulus for chiroptical switching by exploiting temperature-dependent lanthanide fluorescence. Temperature-dependent fluorescence has been well-established in achiral lanthanide MOFs;[21-23] expanding this strategy to a chiral framework could lead to temperature-modulated chiroptical switching of CPL.

Chapter 1 outlined the various ways in which to synthesise chiral MOFs.[24, 25] The strategy pursued in this chapter is to use enantiopure, chiral ligands. This was done using chiral precursors to avoid the burdensome chiral purification needed when synthesising new stereocentres. Amino acids are well-suited to this task because they are cheap, readily functionalisable, contain functional groups for coordinating to metals, and possess a great diversity of side chains.

This chapter first describes the synthesis of several chiral *N*-functionalised amino acid-based ligands. The solvothermal reaction between the chiral ligand (4-carboxybenzoyl)-L-aspartic acid (H_3CBA) and $Ln(NO_3)_3 \cdot 6H_2O$ yielded four novel, isostructural lanthanide MOFs with the composition $[Ln_2(CBA)_2(H_2O)_4] \cdot 4H_2O$ (Ln = La, Ce, Pr, Nd). Structural characterisation of these MOFs revealed they were achiral due to racemisation of H_3CBA during synthesis. The possible mechanism of racemisation and efforts to prevent it are discussed. Reaction of H_3CBA with later lanthanides (Eu, Gd) resulted in MOFs with a different topology, however the structure of this new phase could not be determined due to poor crystallinity of the crystals. When Sm was used, a mixture of both topologies was formed.

Subsequently, a new chiral ligand, *N*-(4-carboxyphenyl)-L-alanine (H_2CPA), intended to be less susceptible to racemisation, was synthesised. Reaction of H_2CPA and $Cd(NO_3)_2 \cdot 4H_2O$ successfully resulted in the formation of a novel, chiral MOF.

5.2 Synthesis and Characterisation of Chiral Ligands Derived from Amino Acids

5.2.1 Synthetic Procedures

There are many ways to synthesise a chiral ligand based on an amino acid. In this chapter, the approach taken was to perform an amide coupling between the amine of an amino acid and an aromatic carboxylic acid. This leaves the amino acid carboxylic acid free to bind to metals. Three chiral ligands were thus synthesised: (4-carboxybenzoyl)-L-valine (H_2CBV), 2,5-thiophenedicarbonyl-L-valine (H_2TDV), and (4-carboxybenzoyl)-L-aspartic acid (H_3CBA) whose structures are shown in Figure 5.1. These ligands were all synthesised via the same two-step process consisting of an amide coupling followed by a deprotection step. Methyl ester-protected amino acids were used to avoid self-coupling. The synthesis of H_3CBA is described below as an example.

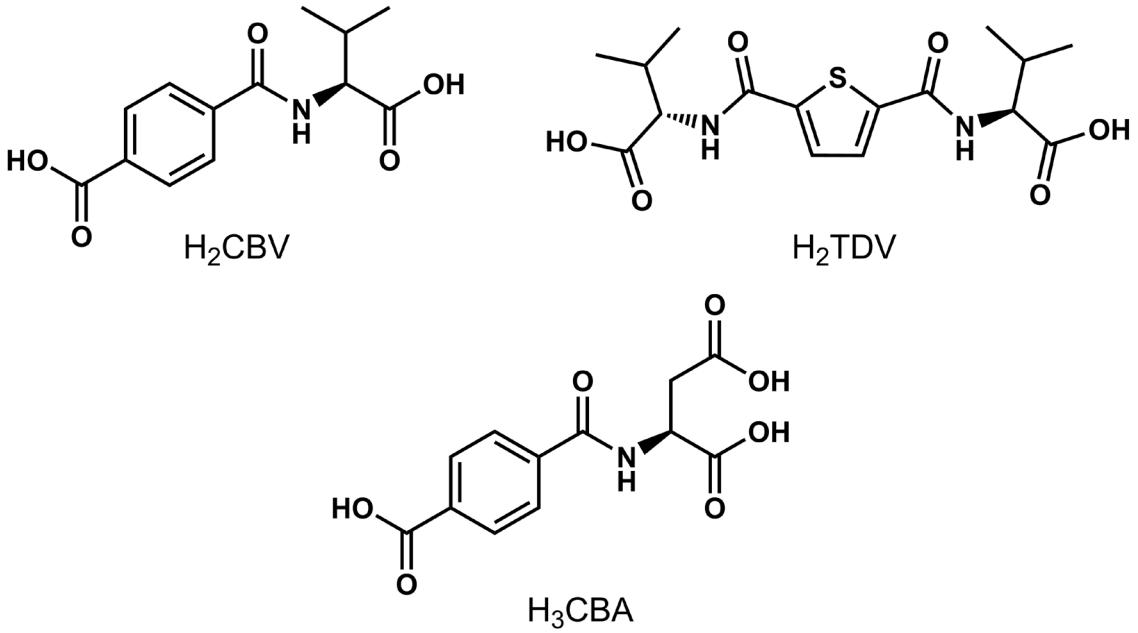

Figure 5.1. Chiral ligands synthesised by an amide coupling between an amino acid and an aromatic acid.

H_3CBA was synthesised from monomethyl terephthalic acid and dimethyl ester-protected L-aspartic acid (Figure 5.2). The initial amide coupling was accomplished with the peptide coupling agent HATU in DMF with triethylamine as the base, yielding the protected Me_3CBA intermediate. Next, deprotection of the ester groups was performed with LiOH to afford H_3CBA with an overall yield of 88% for both steps.

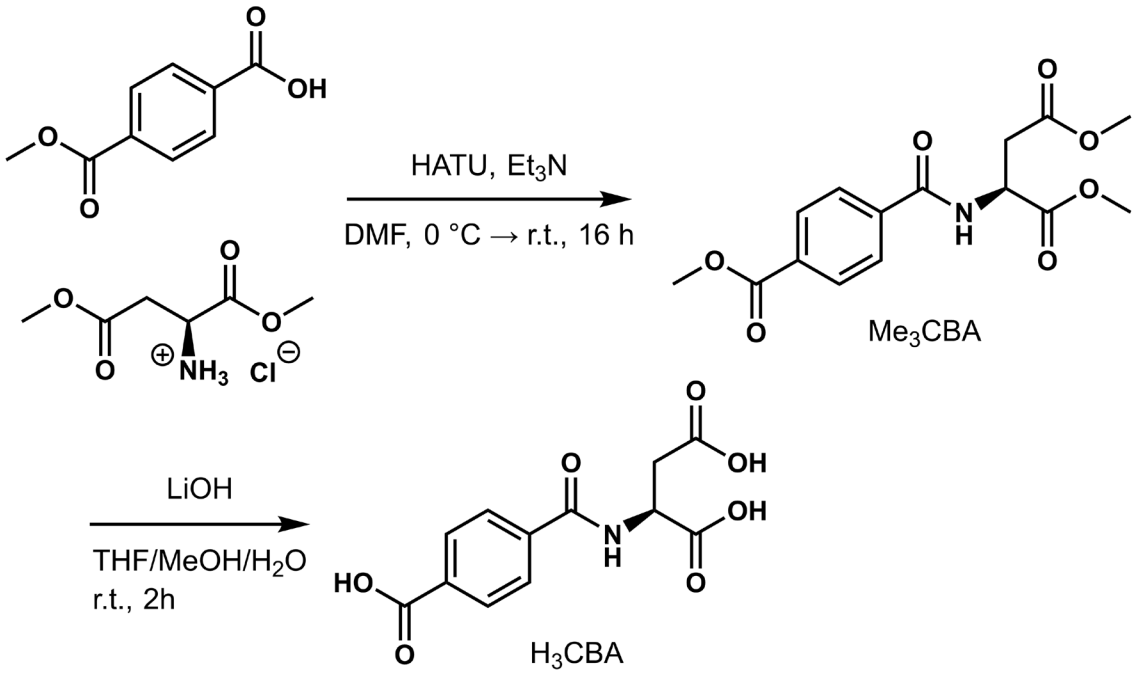

Figure 5.2. Synthesis scheme for H_3CBA.

Attempts to synthesise MOFs with H_2CBV and H_2TDV were ultimately unsuccessful despite a wide range of solvents, metals, concentrations, and temperatures trialled. The exact reason for this could not be discerned, but one potential explanation is the close proximity of the isopropyl side chain of valine to the bonding carboxylate group presenting a steric barrier to MOF formation. In contrast, H_3CBA, with its less sterically hindered side chain was able to form a series of MOFs with various lanthanides (La–Nd). Since no MOFs could be formed from H_2CBV and H_2TDV, they will not be discussed further.

5.2.2 Optical Properties of H_3CBA

The UV-vis spectrum of H_3CBA shows an absorbance peak at 238 nm ($\varepsilon = 5680\ M^{-1}cm^{-1}$) and a shoulder between 260–300 nm (Figure 5.3). The CD spectrum confirms that H_3CBA is chiral with a negative Cotton signal at ~244 nm and a positive Cotton signal at ~218 nm (Figure 5.3). The absorbance dissymmetry factor, g_{abs}, was 1.4×10^{-4} at 218 nm, which is quite small – hence the poor signal-to-noise – but not especially unusual for small, non-aggregated organic molecules.[26-29]

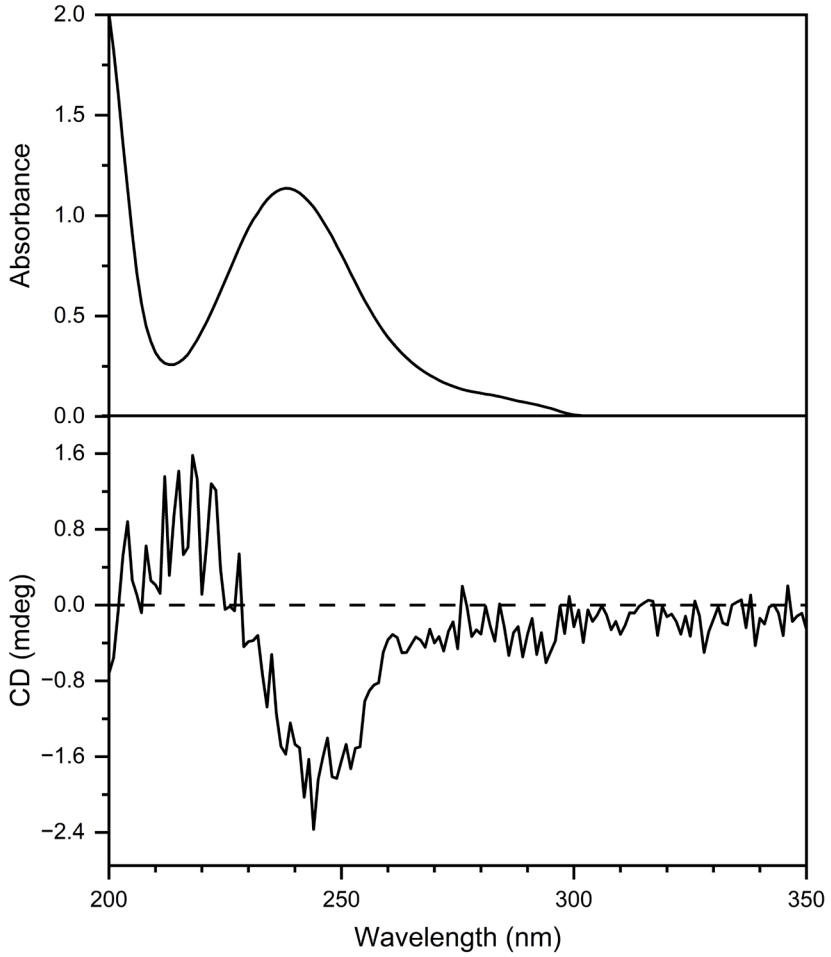

Figure 5.3. Absorbance (top) and CD (bottom) spectra of H_3CBA in MeCN, averaged over 10 accumulations. Sample concentration was 200 μM.

5.3 Synthesis and Characterisation of $[Ln_2(CBA)_2(H_2O)_2]$ MOFs

5.3.1 MOF Synthesis

The most common oxidation state of lanthanide ions is +3. H_3CBA, which has a −3 charge when deprotonated, would thus provide charge balance when reacted with Ln^{3+} ions in a 1:1 ratio, making it a promising ligand for obtaining chiral lanthanide MOFs. Various solvent systems based on DMF, DEF, H_2O, EtOH, MeOH, and MeCN were tested, with MOF crystals obtained using DMF/H_2O and DEF/H_2O mixtures. In syntheses without the presence of DMF or DEF, the H_3CBA amide linkage was found to hydrolyse, forming terephthalic acid and aspartic acid. DMF and DEF thus play a crucial role during MOF synthesis: acting as sacrificial amides that get hydrolysed in place of H_3CBA due to their significantly higher concentration in the solvothermal reaction mixture. It was also qualitatively observed that there is a trade-off between yield and crystallinity based on the ratio of DMF/H_2O or DEF/H_2O. Increasing the proportion of H_2O afforded larger, better-quality crystals, while also reducing the yield. This

suggests that higher proportions of DMF/DEF increased the rate of MOF formation, with the corresponding reduction in the time for error-correction leading to a less crystalline product. The reduced yield at higher water fractions is attributed to more hydrolysis of H_3CBA as there is less DMF/DEF to get preferentially hydrolysed. It was also observed that using DEF instead of DMF resulted in larger crystals. Combining these observations, optimised solvothermal synthesis conditions were subsequently developed. Thus the reaction between $Ln(NO_3)_3 \cdot 6H_2O$ and H_3CBA in a DEF/H_2O (1:3) solution at 75 °C for 18 h yielded an isostructural series of MOFs of the form $[Ln_2(CBA)_2(H_2O)_4] \cdot 4H_2O$ (Ln = La, Ce, Pr, Nd), hereafter referred to as La-1, Ce-1, Pr-1, and Nd-1, respectively.

5.3.2 Structure of La-1–Nd-1

Solvothermal synthesis afforded block crystals of La-1, Ce-1, and Pr-1 suitable for SCXRD analysis. Since they are isostructural, only La-1 will be described in detail. Surprisingly, La-1 crystallises in the centrosymmetric triclinic space group *P*-1, meaning that the structure contains an inversion centre and is therefore achiral. The crystal structure of La-1 contains equal numbers of L-and D-enantiomers of CBA^{3-} (Figure 5.4), indicating that H_3CBA had racemised during the solvothermal reaction. When a MOF is formed from a racemic ligand mixture there are two possible outcomes. The first is that the different enantiomers are incorporated into entirely different crystals, yielding equal amounts of individually enantiopure MOF crystals in an overall racemic batch.[30] The second possibility is that both enantiomers are incorporated into the same crystals such that the individual MOF crystals are achiral.[30] This latter scenario was the case for the La-1–Pr-1 series of MOFs reported here. The racemisation of H_3CBA is discussed in more detail in section 5.3.5.

The unit cell parameters of La-1 are a = 8.5061(5) Å, b = 9.0168(5) Å, c = 11.9108(6) Å, α = 80.884(4)°, β = 75.074(5)°, γ = 68.722(5)°, and V = 820.39(8) Å^3. Each unit cell contains two La nodes and two CBA^{3-} ligands, one of each handedness. In La-1 each CBA^{3-} ligand binds to five La nodes, with the benzoate carboxylate chelating one La, the aspartate carboxylates each coordinating two La in a monodentate fashion, and the amide oxygen bonding to one La (Figure 5.4a). Each La is 9-coordinate and is coordinated by five CBA^{3-} ligands, as well as two H_2O molecules (Figure 5.4b). The overall structure consists of 2D layers of La nodes linked by aspartate carboxylates, with adjacent layers joined through coordination by the benzoate groups (Figure 5.4c). Moreover, adjacent CBA^{3-} ligands have alternating orientation and handedness. The structure contains narrow channels parallel to the crystallographic *a*-axis which contained

four highly disordered H_2O molecules per unit cell, which could not be precisely modelled (Figure 5.4d). Therefore, a solvent mask was used during the refinement. The pores were approximately 5.0 Å wide, which entails a maximum accessible width of 2.8 Å when the van der Waals radii of the framework atoms are taken into account.[31] Therefore, even if the pore and coordinated H_2O molecules were removed, the channels would likely be too small to accommodate even simple aromatic guests without appreciable framework reorganisation. Detailed crystallographic information of La-1, Ce-1, and Pr-1 are presented in Tables C1–C3.

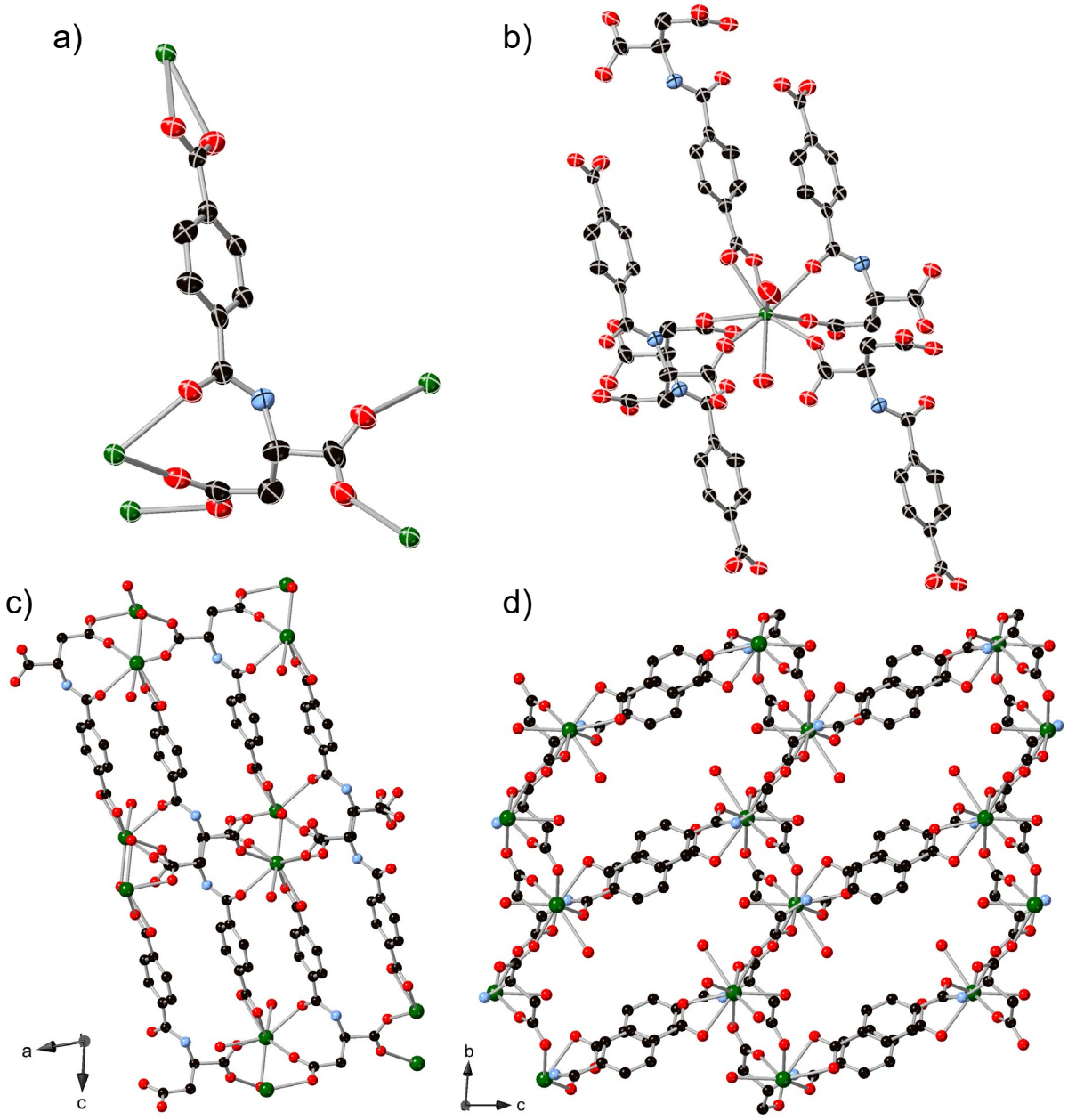

Figure 5.4. (a) and (b) Coordination environment of CBA^{3-} and La in La-1 with displacement ellipsoids drawn at the 50% probability level. (c) and (d) La-1 viewed along the crystallographic *b*-axis and *a*-axis, respectively. Pore solvent molecules and hydrogen atoms are omitted for clarity. Black = carbon, red = oxygen, blue = nitrogen, green = lanthanum.

The structure of Nd-1 could not be determined by SCXRD, however comparing the PXRD patterns of La-1–Nd-1 clearly indicates that they are all isostructural (Figure 5.5). Furthermore, the experimental PXRD patterns are in good agreement with the simulated pattern derived from the single-crystal structure of La-1.

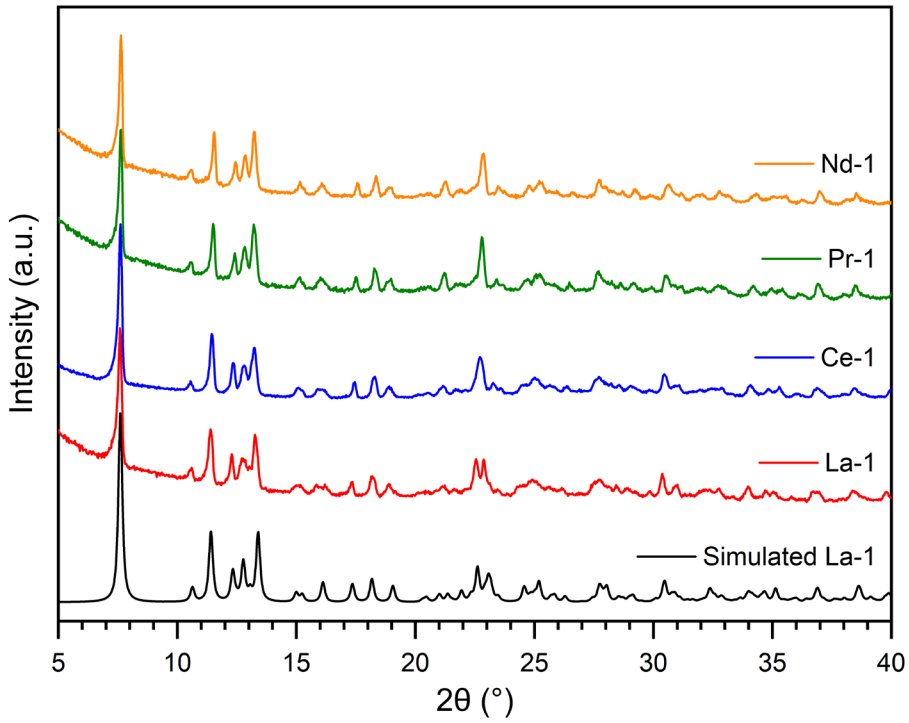

Figure 5.5. PXRD patterns of La-1 (red), Ce-1 (blue), Pr-1 (green), and Nd-1 (orange), as well as the simulated PXRD pattern of La-1 (black).

The comparison of simulated and experimental patterns gives a qualitative metric of batch purity. To obtain a more comprehensive measure of batch purity, Pawley refinements were performed on La-1–Nd-1 (Figures C1–4). For each MOF a good fit (Rw values ranging from 3.390–5.238) was obtained with the refined unit cell parameters closely matching those determined from SCXRD (Table C4), providing further evidence that the single-crystal structure is representative of the bulk material. Moving along the lanthanides from La to Nd, there is a consistent decrease in the unit cell dimensions and volume (except for the *c* dimension for Ce-1, which was slightly larger than La-1). The *a*, *b*, and *c* unit cell lengths declined by 1.44%, 0.65%, and 0.44%, respectively, while the volume declined by 2.02% over this range (Figure 5.6). This is attributed to the decreasing radii of the Ln^{3+} ions due to the lanthanide contraction.[32-34]

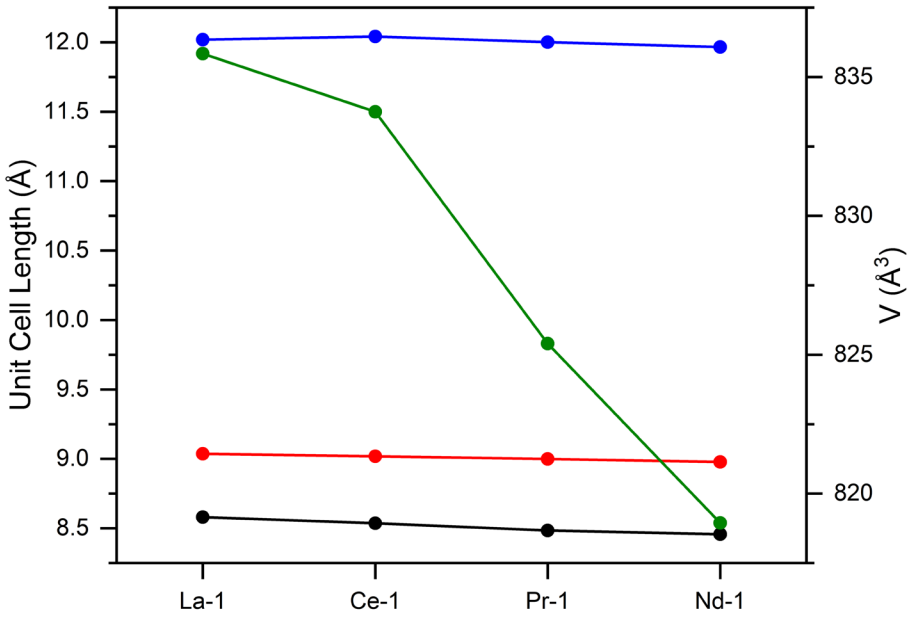

Figure 5.6. Unit cell *a* (black), *b* (red), and *c* (blue) dimensions, as well as unit cell volume (green) for La-1–Nd-1 at room temperature. Values determined from Pawley refinements.

TGA was performed to investigate the stability of La-1–Nd-1 (Figure 5.7). For each MOF there are two stages of solvent loss, the first complete by ~50 °C and the second by ~120 °C. Both solvent loss steps correspond to an approximately 7.5% weight loss, consistent with a loss of four H_2O molecules per step. The first solvent loss is therefore assigned to four pore H_2O molecules, while the second is attributed to the four H_2O molecules directly bonded to the Ln sites. The MOFs then exhibit no further weight loss until framework decomposition at a temperature of 340–360 °C. This is similar to the decomposition temperature of other lanthanide MOFs with carboxylate ligands and reflects the high thermal stability of lanthanide MOFs in general.[35, 36]

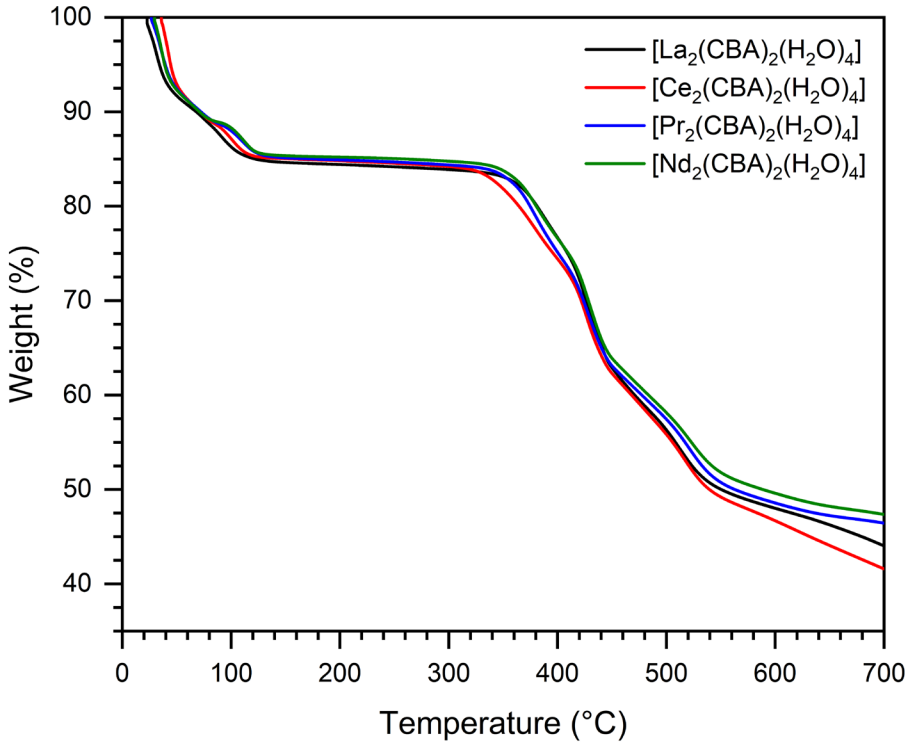

Figure 5.7. TGA of La-1 (black), Ce-1 (red), Pr-1 (blue), and Nd-1 (green), measured at a ramp rate of 2 °C/min under a nitrogen atmosphere.

5.3.3 MOFs With Other Lanthanides

Attempts to form MOFs with H_3CBA and other lanthanides (Sm, Eu, Gd) were performed using the same conditions as for La-1–Nd-1. These experiments yielded opaque agglomerates, in contrast to the transparent crystals of La-1–Nd-1. The Sm–Gd materials were nonetheless crystalline – as revealed by PXRD – and are likely MOFs (Figure 5.8). Furthermore, the PXRD patterns of the Eu and Gd MOFs are clearly different to those of La-1–Nd-1 (Figure 5.8), indicating a different MOF structure and/or topology. These structures are henceforth referred to as Eu-2 and Gd-2; here, the 2 signifies the different topology. Interestingly, when Sm was used a mixed phase of both topologies was formed, i.e. Sm-1 and Sm-2. The different topology is likely explained by the lanthanide contraction,[32, 33] wherein the smaller radii of the later Ln^{3+} cations promotes a different coordination environment and thus overall MOF structure. This is not uncommon, with changes in topology and coordination number moving along the lanthanide series reported in other MOF systems.[37-41] No crystals of Sm-2–Gd-2 suitable for SCXRD have yet been obtained despite repeated efforts using a variety of solvent ratios, temperatures, and concentrations. Therefore, the exact structure of Sm-2–Gd-2 are yet to be determined. Additionally, the PXRD patterns of Eu-2 and Gd-2 have an amorphous component (broad hump) above a 2θ of 22°, suggesting they have worse crystallinity than La-1–Nd-1.

Since the 2θ values of the first diffraction peak in the PXRD patterns of Sm-2–Gd-2 are smaller than those in La-1–Nd-1 (~6.0 vs ~7.6), it can be implied that the longest unit cell dimension of Sm-2–Gd-2 is larger than the longest unit cell dimension of La-1–Nd-1.

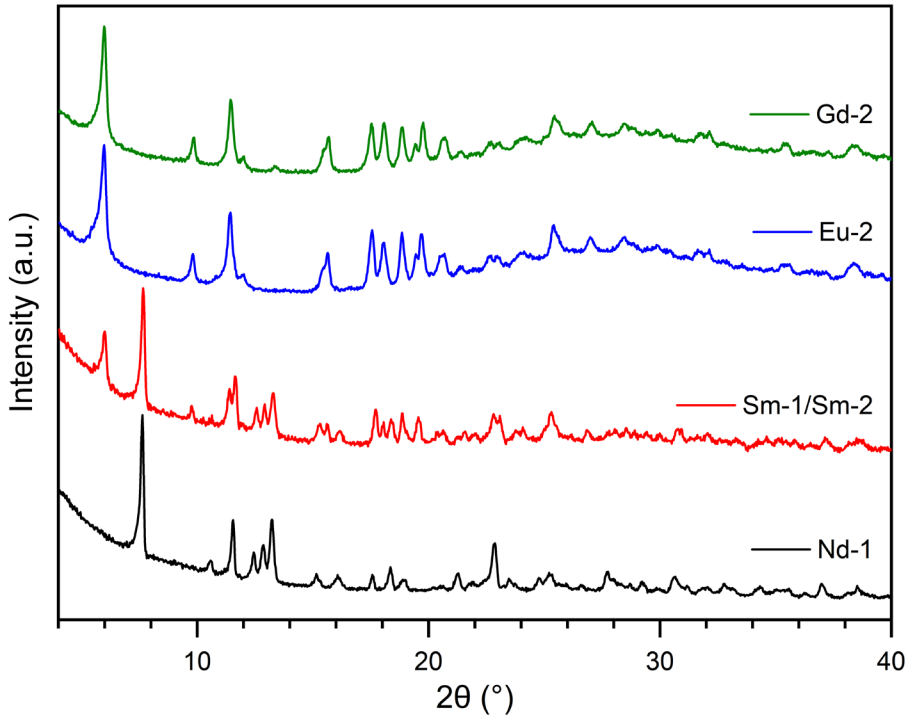

Figure 5.8. PXRD patterns of Nd-1 (black), Sm-1/2 (red), Eu-2 (blue), and Gd-2 (green).

5.3.4 Optical Properties of La-1–Nd-1

The UV-vis spectrum of La-1 is dominated by absorbance of the CBA^{3-} ligand in the UV region (Figure 5.9). The solid-state spectrum of H_3CBA has a peak at 245 nm, which is redshifted by 7 nm compared to H_3CBA in MeCN solution. Notably, the weak shoulder observed in solution is more defined in the solid-state with bands observed at 292 nm and 305 nm, however the precise origin of these transitions could not be determined. In La-1 the ligand absorbance is further redshifted to 252 nm and the shoulder band is less well defined. This could be caused by slight alterations of the ligand's electronic structure due to deprotonation and coordination to La. Comparing La-1–Nd-1, all displayed similar spectra in the UV region, with maxima between 248 and 252 nm, arising from absorbance of the CBA^{3-} ligand (Figure 5.10). This peak is slightly broadened in Ce-1–Nd-1 compared to La-1, indicating that the shoulder band is more intense in these frameworks.

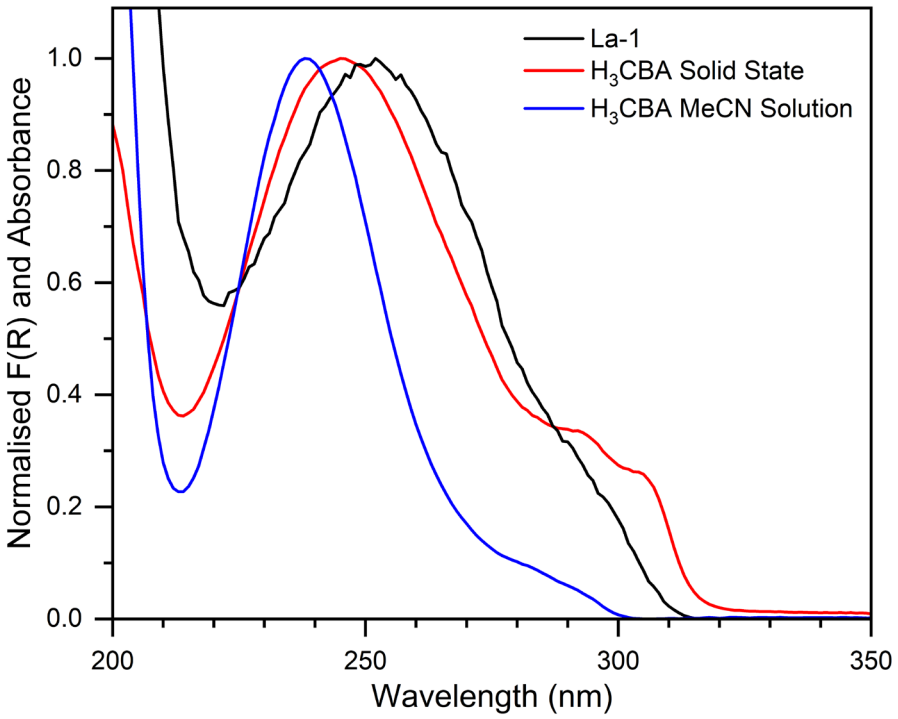

Figure 5.9. Solid-state diffuse reflectance spectra of La-1 (black) and H_3CBA (red). Spectrum of H_3CBA in MeCN (blue) shown for comparison.

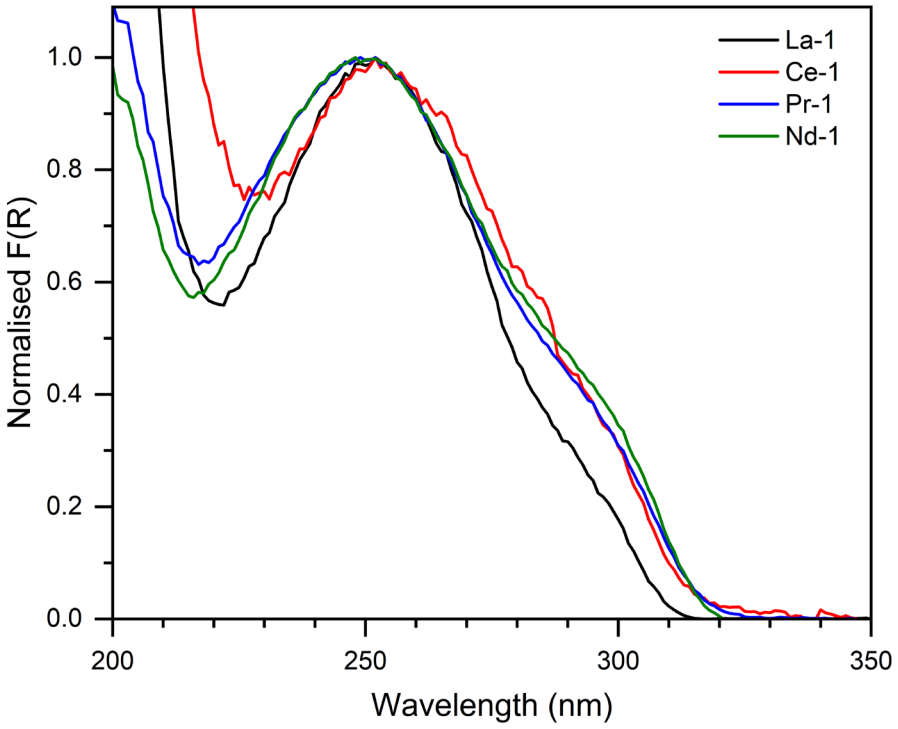

Figure 5.10. Solid state diffuse reflectance spectra of La-1 (black), Ce-1 (red), Pr-1 (blue), and Nd-1 (green) in the UV region.

In the visible region, lanthanide f–f transitions were observed for Pr-1 and Nd-1 (Figure 5.11). These transitions are much weaker than the ligand absorbance because f–f transition are Laporte forbidden and typically exhibit small extinction coefficients (sometimes less than <1

$M^{-1}cm^{-1}$).[42-46] The 4f orbitals do not play a major role in bonding due to shielding from the occupied $5s^2$ and $5p^6$ orbitals.[42, 45, 46] Therefore, there is little vibronic coupling in f–f transitions, giving rise to sharp, narrow absorbance bands.[45, 46] A further consequence of this shielding is that f–f transitions are relatively unaffected by the ligand environment and vary little between different complexes, making f–f transitions characteristic for each lanthanide.[45, 46] In Pr-1 f–f transitions were observed at 445, 469, 483, and 590 nm, consistent with other Pr compounds.[47, 48] The spectrum of Nd-1 displayed many f–f transitions, the most prominent occurring at 356, 524, 581, and 743 nm, in agreement with other Nd complexes.[49, 50] No visible transitions were observed for La-1 and Ce-1, the former due to its lack of f electrons and the latter because Ce^{3+} often exhibits $4f^1$–$5d^1$ transitions which absorb deeper into the UV (<300 nm),[51-53] in this case obscured by the absorbance of CBA^{3-}.

Fluorescence experiments found both Pr-1 and Nd-1 to be nonemissive. The likely reason for this is that the lanthanide nodes in these frameworks are each coordinated by two water molecules. Coordination of water or alcohol to lanthanides is known to quench their fluorescence due to efficient energy transfer to OH vibrational overtones.[54] This is compounded by the weak absorbance of lanthanide ions, which already makes direct excitation difficult. Excitation of the CBA^{3-} did not result in lanthanide fluorescence, indicating that CBA^{3-} is a poor sensitiser of lanthanide fluorescence.

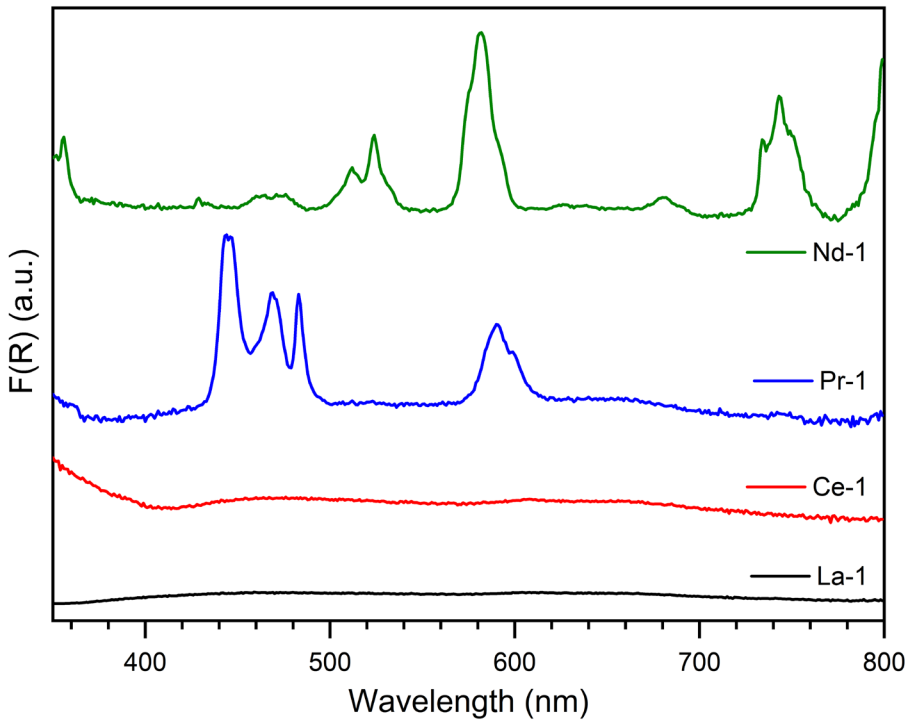

Figure 5.11. Solid-state diffuse reflectance spectra of La-1 (black), Ce-1 (red), Pr-1 (blue), and Nd-1 (green) in the visible region.

The crystal structures of La-1, Ce-1, and Pr-1 indicated that they are achiral due to ligand racemisation and therefore not expected to exhibit CD. While PXRD provided strong evidence that these crystal structures were representative of the bulk, CD was nonetheless performed on La-1 in case there was any chiral, amorphous material present. These experiments showed no CD signals (Figure 5.12), confirming that La-1 is achiral and free of chiral impurities.

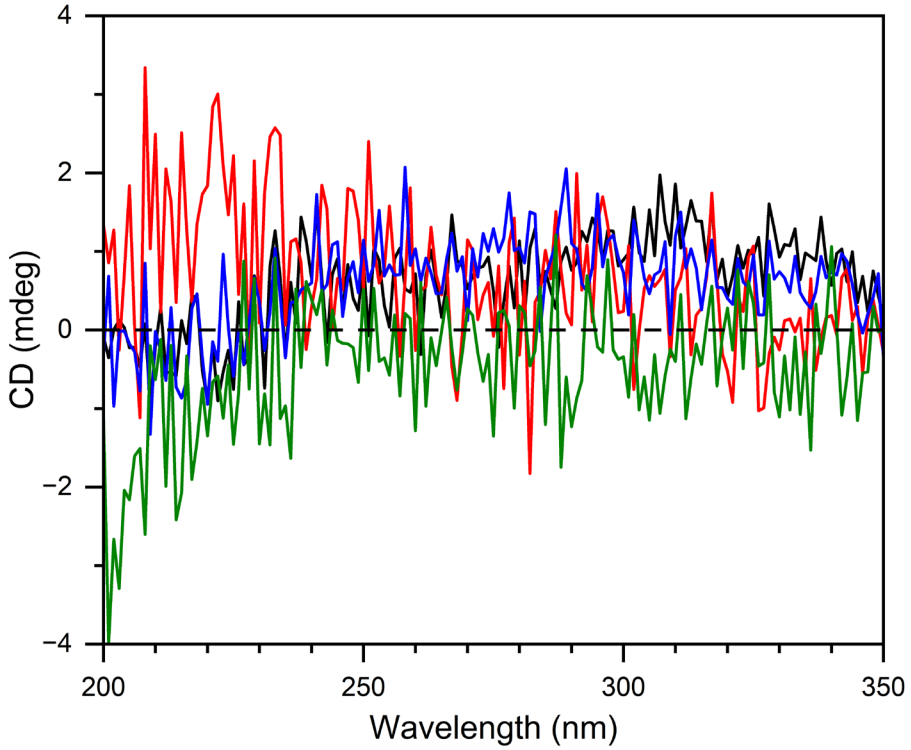

Figure 5.12. Solid-state CD spectra of four different batches of La-1 showing the lack of clear Cotton signals. Measurements were performed on a small amount of powder sandwiched between two quartz slides.

5.3.5 Attempts to Avoid Racemisation

The racemisation of H_3CBA during synthesis was highly unexpected. The solvothermal conditions used to synthesise La-1–Nd-1 (75 °C for 18 h) are much milder compared to those used in the successful synthesis of enantiopure MOFs from many other chiral ligands derived from amino acids. For example, some chiral frameworks have been synthesised in conditions as harsh as 120 °C for 3–4 days, including with ligands structurally similar to H_3CBA which contain amide functionalisation of the amino acid N-terminus.[55-57]

Amino acids are known to undergo racemisation over long periods of time at elevated temperatures in acidic or basic solution.[58, 59] Aspartic acid happens to have one of the fastest rates of racemisation of all the proteinogenic amino acids.[60] This can be explained by

considering the mechanism of racemisation in acidic solution, which proceeds through enolisation of the α-carboxylic acid (Figure 5.13).[60] The enol form of the amino acid contains a double bond and is planar. Tautomerisation back to the carboxylic acid form regenerates the stereocentre, but with no preference for the L- or D-enantiomer, leading to eventual loss of enantiopurity. The CH_2COOH side chain of aspartic acid can also undergo a similar tautomerisation process.[60] The enol form of the side chain stabilises the enol form of the α-carboxylic acid (and vice versa) due to double bond conjugation.[60] Consequently, tautomerisation – and therefore racemisation – is enhanced in aspartic acid compared to other amino acids in acidic solution. It has been experimentally shown that racemisation of aspartic acid is fastest at pH 3.[58-60] It can be inferred from the work of Bada that the racemisation half-life of aspartic acid at this pH is roughly two days at 100 °C.[59] Bada did not report data for 75 °C; however, the racemisation half-life is strongly temperature-dependent and can be estimated to be at least one order of magnitude larger at this temperature (for comparison the half-life at 25 °C is approximately 350 years).[59] If similar racemisation rates were observed in H_3CBA, only minimal racemisation would be expected under the solvothermal conditions employed in the synthesis of La-1–Nd-1. However, the amide functionalised N-terminus in H_3CBA may promote faster racemisation compared to aspartic acid itself.

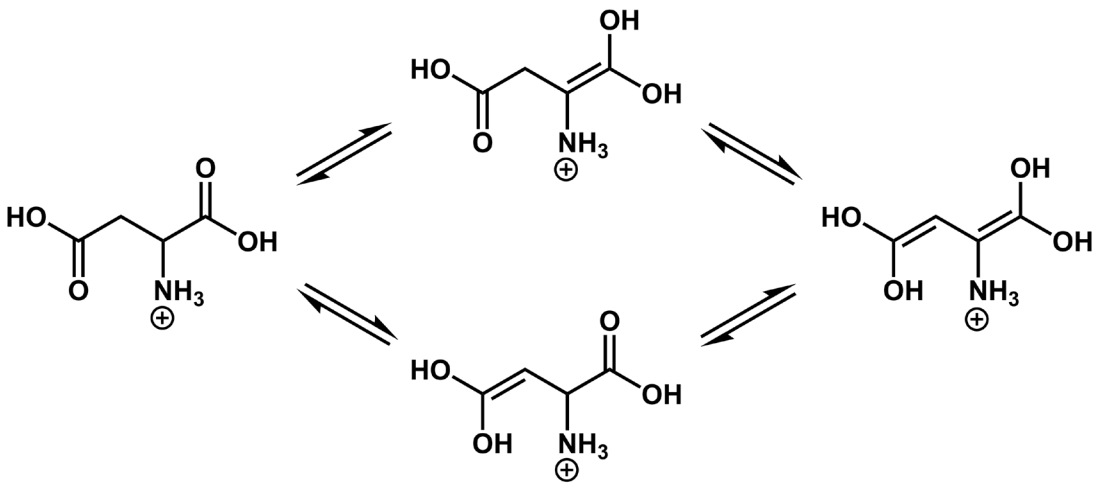

Figure 5.13. Mechanism of aspartic acid racemisation by tautomerisation in acidic conditions.

Another possible explanation is that the Ln^{3+} cations are catalysing racemisation. Various metal ions including Cu^{2+}, Co^{3+}, Cr^{3+}, Al^{3+}, Pd^{2+}, and Pt^{2+} have been shown to accelerate the racemisation of amino acids in neutral and alkaline conditions.[58, 61, 62] However, such investigations have not yet been extended to the effect of lanthanides on racemisation rates in acidic environments. If racemisation of H_3CBA is being catalysed by lanthanide ions, it likely arises from specific interactions determined by the structure of the ligand, rather than a general

rule. To underscore this point: there are already examples of homochiral MOFs containing lanthanides synthesised from amino acid-derived ligands at temperatures ranging from 80–120 °C without racemisation.[63, 64]

Another possibility was that the loss of enantiopurity could have occurred during the synthesis of H_3CBA itself. This is, however, deemed unlikely since both steps of the ligand synthesis and subsequent purifications were carried out at mild temperatures, with the maximum temperature being 40 °C during rotary evaporation. This is certainly not hot enough to cause racemisation on such a timescale. Furthermore, the chirality of H_3CBA was already demonstrated through CD measurements, as described earlier (Figure 5.3).

One approach to mitigate racemisation is to reduce the temperature of reaction. However, solvothermal reactions performed at lower temperature (55 °C) were unsuccessful, highlighting how elevated temperatures are important in the solvothermal approach for MOF formation. Thus, a room temperature diffusion synthesis was carried out between H_3CBA and $La(NO_3)_3 \cdot 6H_2O$ in DMF:H_2O (1:1). LiOH was used as a base to generate CBA^{3-} to facilitate metal coordination. A vial-in-vial approach was used so that the metal and deprotonated ligand solutions were initially in separate compartments; the slow diffusion of reactants facilitates MOF formation without the need for temperature-induced error correction. The obtained crystals were analysed by PXRD and were found to be a new phase distinct from La-1 (Figure 5.14). This new material is henceforth called La-3; here, the 3 signifies the different topology compared to the structures described previously. This is a promising result and suggests that a novel, chiral MOF containing enantiopure CBA^{3-} ligand has been formed. The crystals of La-3 which formed were opaque, white agglomerates (in contrast to the well-formed clear crystals of La-1) and proved unsuitable for SCXRD analysis. Therefore, the crystal structure of La-3 could not be determined. The poor crystallinity is evident in the PXRD pattern, with a broad, amorphous component between 15 and 40° 2θ. Diffusion reactions performed with other solvent systems (EtOH:H_2O and MeCN:H_2O) likewise failed to produce satisfactory crystals for SCXRD analysis. It is also unclear whether any lithium was incorporated into the structure.

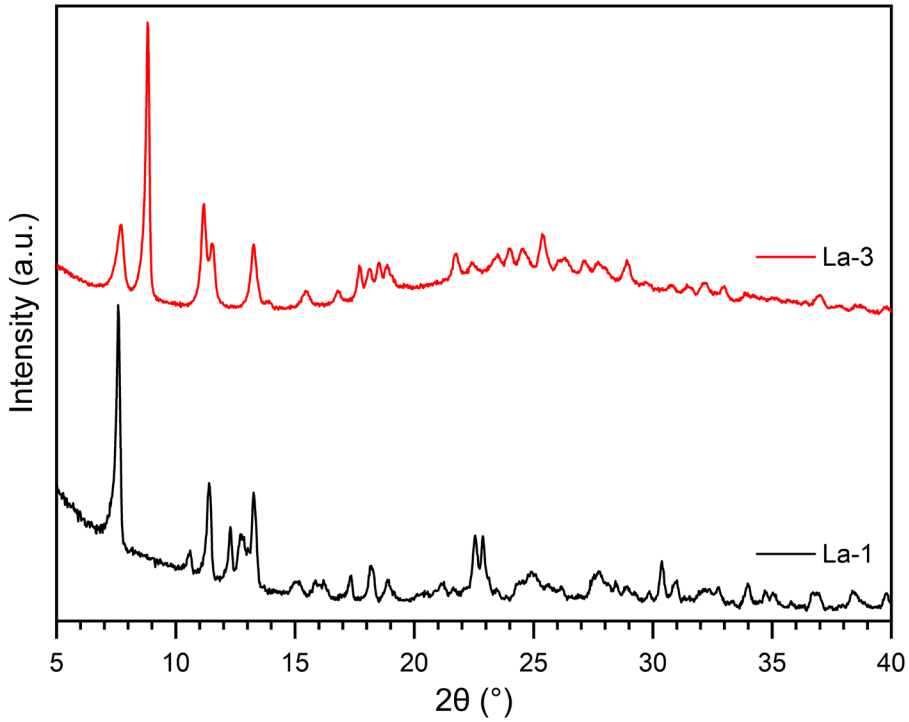

Figure 5.14. PXRD patterns of La-1 (black) and La-3 (red).

Solid-state CD experiments were performed to see if La-3 was chiral, however no consistent CD signals could be detected from two measurements of the same batch (Figure 5.15). This does not necessarily mean that La-3 is achiral; the large amount of scattering and inhomogeneity in the solid-state means the threshold for unambiguous detection of a chiral signal is higher than for solution state. This indicates that if La-3 is indeed chiral, it is only very weakly so and has a small g_{abs}.

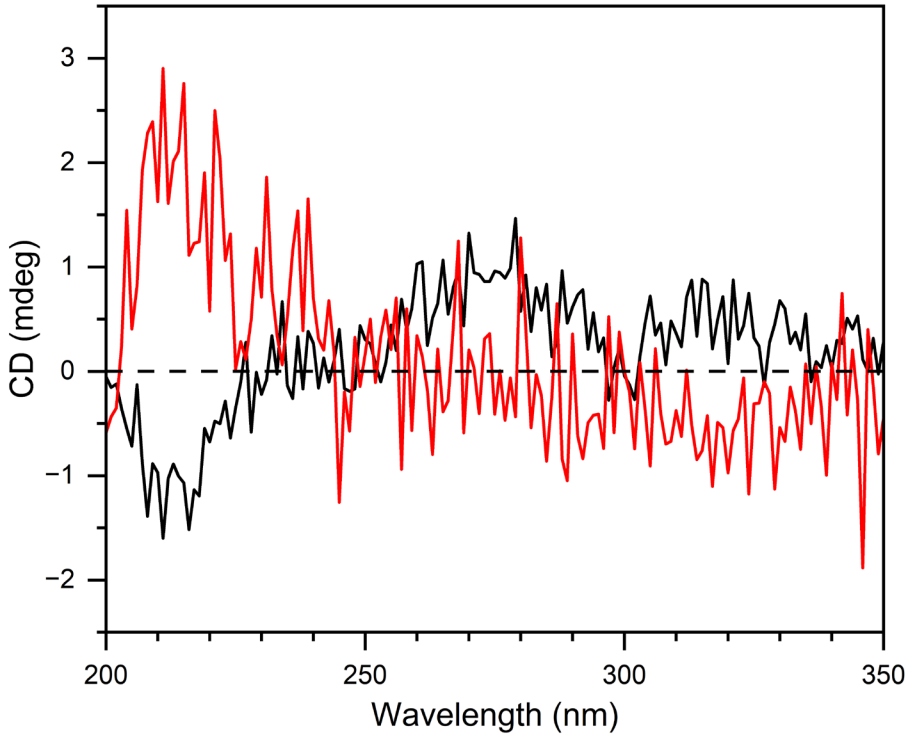

Figure 5.15. Solid-state CD spectra of La-3, performed on two separate portions from the same batch. Measurements were performed on a small amount of powder sandwiched between two quartz slides.

5.4 *N*-(4-carboxyphenyl)-L-alanine (H_2CPA)

5.4.1 Synthesis of H_2CPA

Given the difficulties attaining chiral MOFs with H_3CBA described in the previous section, an alternate approach to synthesising chiral MOFs was undertaken. The chiral ligand *N*-(4-carboxyphenyl)-L-alanine (H_2CPA) was synthesised in a two-step procedure as shown in Figure 5.16. Firstly, L-alanine methyl ester was coupled to methyl 4-iodobenzoate in a copper catalysed Ullmann-type *N*-arylation reaction based on similar published procedures.[65, 66] In this reaction K_2CO_3 was used as a non-nucleophilic base and L-proline served as a ligand to solubilise the copper catalyst. As a sterically hindered secondary amine, L-proline is less reactive towards the aryl iodide than primary amines, allowing it to catalyse the reaction without significantly outcompeting the desired coupling of L-alanine.[65, 66] Additionally, the conditions (60 °C) employed here are even milder than those reported in similar reactions that were observed to preserve enantiopurity of the amino acid despite the presence of copper which, as noted previously, can catalyse racemisation.[67] In the second step, ester deprotection with NaOH was performed to afford H_2CPA in an overall yield of 14% for the two steps.

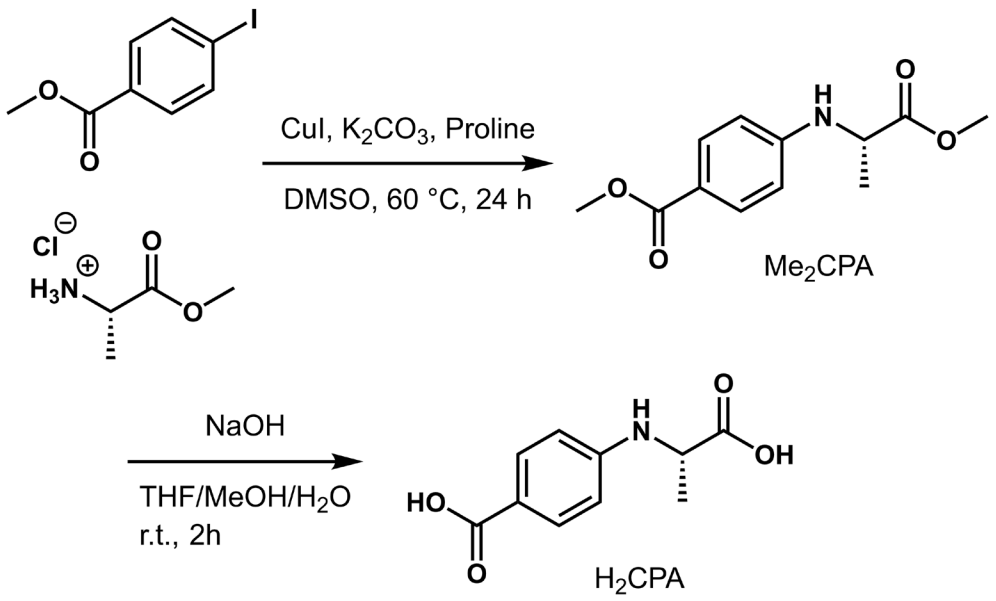

Figure 5.16. Synthesis scheme for H_2CPA.

H_2CPA was designed to address two of the challenges encountered with H_3CBA. Firstly, H_2CPA contains no amide bond and therefore should not suffer from hydrolysis under solvothermal synthesis conditions. This allows for additionally solvothermal conditions without DMF/DEF to be trialled, making H_2CPA a more versatile ligand. Secondly, alanine has been found to racemise at slower rates than aspartic acid,[58, 60, 68] reducing the likelihood that achiral MOFs will be obtained. Being a dicarboxylate ligand, H_2CPA will have a −2 charge when deprotonated. Therefore, the primary focus will be on forming chiral MOFs with divalent transition metals rather than lanthanides. It was also hoped that the linear geometry of H_2CPA would result in MOFs with larger accessible pore spaces than La-1–Nd-1, which had small channels due to the nonlinear geometry of CBA^{3-}. An additional benefit of incorporating alanine into the ligand design is that the small methyl side chain should have minimal intrusion into any pore spaces. Sufficiently large pores would enable chiroptical switching modulated by host-guest interactions. The precise choice of guest would depend on the geometry of the chiral pores, since a close fit facilitates a more effective chirality transfer from the host framework to the guest.[12]

5.4.2 Optical and Chiroptical Properties of H_2CPA

The UV-vis spectrum of H_2CPA is shown in Figure 5.17 and features a main absorbance peak at 294 nm (ε = 9930 $M^{-1}cm^{-1}$) and a smaller peak at 221 nm (ε = 3640 $M^{-1}cm^{-1}$). The CD spectrum confirms the chirality of H_2CPA and shows negative Cotton signals at 280 and 234

nm and a positive Cotton signal at 218 nm (Figure 5.17). H_2CPA has a g_{abs} of -1.75×10^{-3} at 234 nm, which is more than 10 times larger than the g_{abs} of H_3CBA.

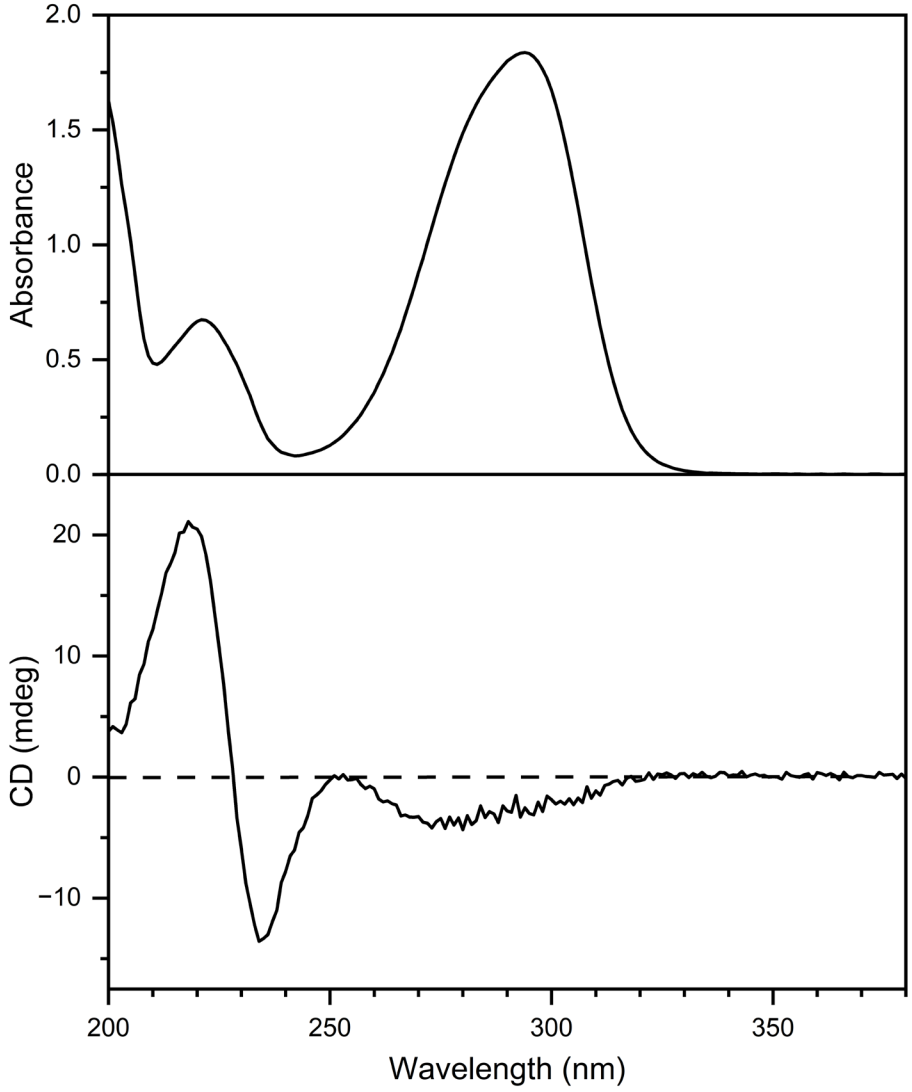

Figure 5.17. Absorbance (top) and CD (bottom) spectra of H_2CPA in MeCN (185 μM).

5.4.3 H_2CPA MOFs

The solvothermal synthesis of H_2CPA and $Cd(NO_3)_2 \cdot 4H_2O$ was performed in DMF:EtOH (3:1) solution at 80 °C for 21 h and yielded small, white crystals of a new material, hereafter referred to as Cd-1. PXRD indicates Cd-1 is crystalline and likely a MOF, however the overall crystallinity was poor, as evidenced by the large amorphous component in the 15–35° 2θ range (Figure 5.18). The obtained crystals had an acicular crystal habit and were thus unsuitable for SCXRD analysis. As a result, the structure and topology of Cd-1 could not be determined. Here, efforts to tweak the synthetic conditions to obtain better quality crystals for structure elucidation would be very useful, as this would reveal the size of the pore spaces (if any).

Knowing the size of the pore spaces would thus allow a rational choice of guest with a compatible size for more effective chirality transfer.

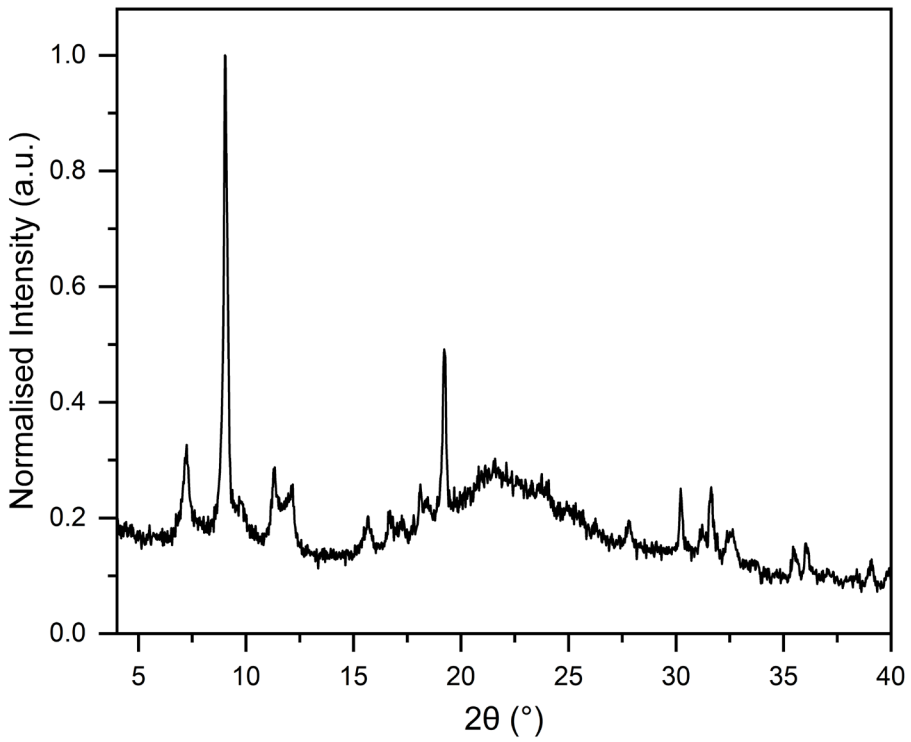

Figure 5.18. PXRD pattern of the material obtained from solvothermal synthesis of H_2CPA and $Cd(NO_3)_2 \cdot 4H_2O$.

To investigate the optical and chiroptical properties of Cd-1, solid-state UV-vis and CD experiments were performed on powdered crystals of Cd-1 (Figure 5.19). The UV-vis spectrum of Cd-1 shows absorbance bands at 261 and 202 nm, attributed to absorbance of the CPA^{2-} ligand. This is blueshifted by 20-30 nm compared to H_2CPA and could be caused by slight changes in the electronic structure due to deprotonation of the carboxylates and coordination to Cd. As expected of measurements on powdered samples, there was a large baseline effect, evidenced by the measured absorbance of ~0.55 at 450 nm. This can be attributed to both scattering and the inherent inhomogeneity of powdered samples, in which some particles are big enough to block the light entirely. The CD spectrum of Cd-1 shows negative Cotton peaks at 311 and 227 nm. Chiral scattering also contributes to the observed CD, evidenced by the nonzero CD measured at 450 nm. While the chiral scattering and CD contributions to the observed CD spectrum could not be individually quantified, this result nonetheless confirms that Cd-1 is indeed chiral, validating the design of H_2CPA as a ligand intended to reduce racemisation.

Unfortunately, the synthesis of H_2CPA and Cd-1 were both low yielding. The overall amount of Cd-1 obtained was very small and insufficient for investigating host-guest interactions for chiroptical switching. Evidently, efforts to improve the yields and scale-up the synthesis of Cd-1 are needed.

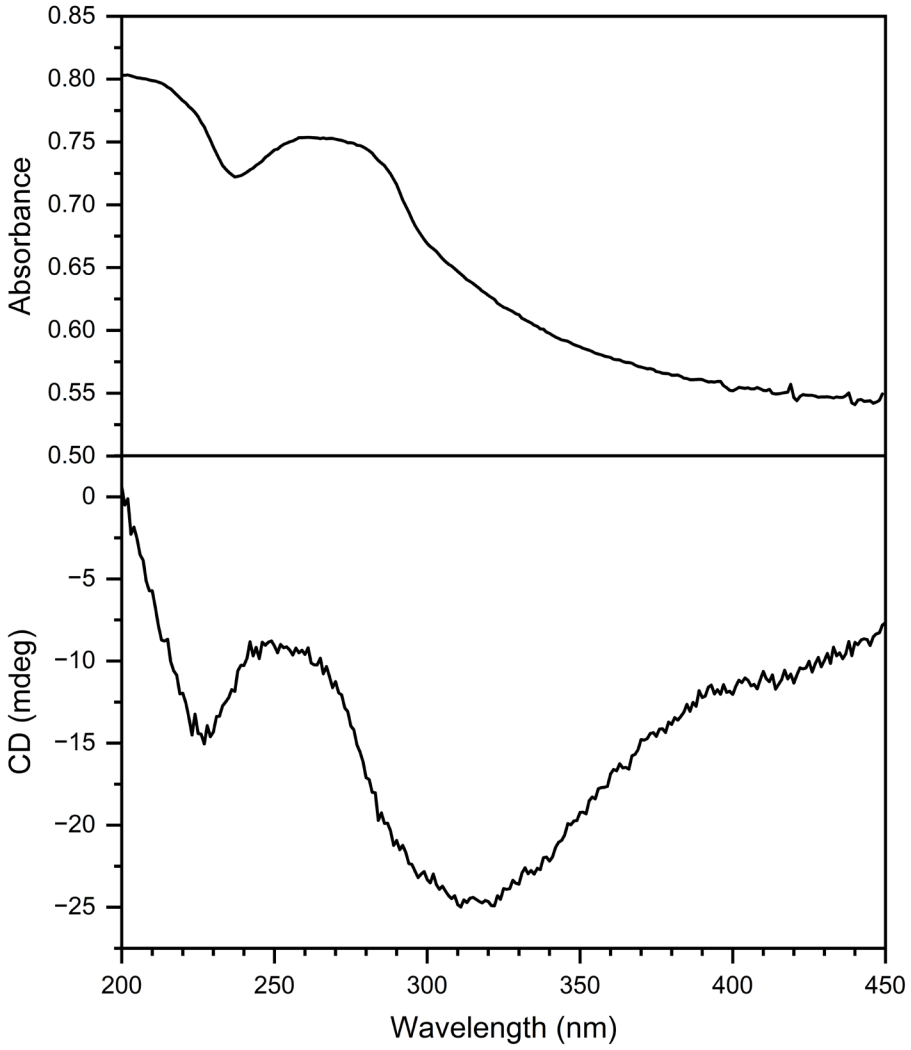

Figure 5.19. Solid-state absorbance (top) and CD (bottom) spectra of Cd-1. Measurements were performed on a small amount of powder sandwiched between two quartz slides.

5.5 Conclusions

In conclusion, this chapter outlines the synthesis of a series of novel lanthanide MOFs, La-1–Nd-1, of the from $[Ln_2(CBA)_2(H_2O)_4]\cdot 4H_2O$ (Ln = La, Ce, Pr, Nd). La-1–Nd-1 were found to be achiral due to racemisation of H_3CBA during synthesis, a surprising result given the relatively mild synthetic conditions. The exact reason for racemisation is unclear, however it is possible that H_3CBA is simply more susceptible to thermal racemisation that related amino-acid derived ligands, or that Ln^{3+} ions are catalysing racemisation. In an effort to avoid

racemisation, room temperature diffusions between H_3CBA and $La(NO_3)_3 \cdot 6H_2O$ were performed, resulting in a new phase, La-3. The precise structure of La-3 could not be determined, however CD measurements indicated that if it is chiral, it has a weak chiroptical response.

Interestingly, the reaction between H_3CBA and other lanthanides (Sm, Eu, Gd) yielded a new MOF topology, with Sm resulting in a mixed batch containing both structures. This topological change was attributed to a difference in the preferred coordination geometry of these later lanthanides due to the lanthanide contraction. However, the structure of this new phase could not be determined due to the poor crystallinity of the crystals.

In response to the challenges faced with H_3CBA, a new chiral ligand, H_2CPA, was synthesised via the *N*-arylation of L-alanine with methyl 4-iodobenzoate. H_2CPA was designed to mitigate racemisation to increase the chances of obtaining a chiral MOF. The reaction of H_2CPA and $Cd(NO_3)_2 \cdot 4H_2O$ led to the formation of a new phase, Cd-1, which PXRD indicated was likely a MOF. Furthermore, Cd-1 was found to be chiral, justifying the development of H_2CPA. Obtaining the crystal structure of Cd-1 and scaling up the synthesis of both H_2CPA and Cd-1 are clear directions for future research. This would enable assessment of Cd-1 as a platform for chiroptical switching mediated by host-guest interactions.

Overall, this work underscores the difficulties in synthesising chiral MOFs and obtaining crystals of sufficient quality to enable structure determination by SCXRD analysis.

5.6 Future Work

One of the major challenges faced during this work was the racemisation of H_3CBA. To completely remove any concerns about ligand racemisation, a new ligand design was envisioned based on 1,1′-binaphthalene-2,2′-diol (BINOL), which is highly resistant to thermal racemisation with a racemisation half-life of 180 h at 190 °C.[69] To coordinate Ln^{3+} ions, the BINOL scaffold would be functionalised with dipicolinic acid (2,6-pyridine dicarboxylic acid) groups. Dipicolinc acid was chosen because it is known to form isostructural 9-coordinate complexes across the whole lanthanide series without any coordinated solvent molecules.[70, 71] This is important because the coordination of two H_2O molecules to each lanthanide in Pr-1 and Nd-1 resulted in them being nonemissive. The proposed structure of this ligand, (*S*)-2,2′-bis((2,6-dicarboxypyridin-4-yl)oxy)-1,1′-binaphthalene ((*S*)-H_4DCPB) is shown in Figure 5.20a. To date the tetraethyl-protected precursor, (*S*)-Et_4DCPB, has been successfully

synthesised. Surprisingly, an initial attempt at base catalysed ester deprotection was unsuccessful, however further refinement of the synthetic procedures should be able to resolve this issue.

Designing and synthesising novel MOFs is often a time-consuming process requiring lengthy trial-and-error testing of suitable synthesis conditions in order to obtain MOF crystals appropriate for SCXRD. A quicker approach would be to simply synthesise an existing chiral MOF with known synthesis conditions. For example, the chiral ligand trimesoyl tris(L-alanine) (H_3TMTA) shown in Figure 5.20b has been reported to form homochiral MOFs with Co, Ni, Zn, and Cd, both with and without 4,4′-bipyridine as co-ligand.[72-75] These frameworks contain accessible pore spaces; encapsulation of luminophores of compatible size would thus enable CPL through host-to-guest chirality transfer. This would form the basis of host-guest modulated chiroptical switching with CPL as the chiroptical readout. Initial steps in this direction have been carried out, with a batch of H_3TMTA having already been synthesised.

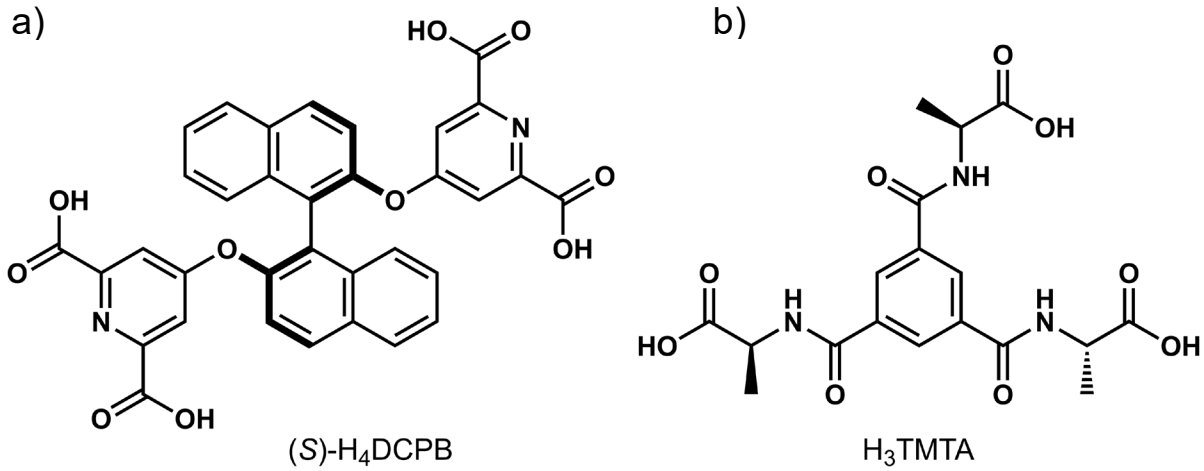

Figure 5.20. (a) The structure of (*S*)-H_4DCPB. (b) The structure of H_3TMTA.

5.7 References

(1) Greenfield, J. L.; Wade, J.; Brandt, J. R.; Shi, X.; Penfold, T. J.; Fuchter, M. J. Pathways to increase the dissymmetry in the interaction of chiral light and chiral molecules. *Chem. Sci.* **2021**, *12*, 8589-8602.

(2) Lakhwani, G.; Meskers, S. C. J. Insights from Chiral Polyfluorene on the Unification of Molecular Exciton and Cholesteric Liquid Crystal Theories for Chiroptical Phenomena. *J. Phys. Chem. A* **2012**, *116*, 1121-1128.

(3) Wan, L.; Zhang, R.; Cho, E.; Li, H.; Coropceanu, V.; Brédas, J.-L.; Gao, F. Sensitive near-infrared circularly polarized light detection via non-fullerene acceptor blends. *Nat. Photonics* **2023**, *17*, 649-655.

(4) Watanabe, K.; Osaka, I.; Yorozuya, S.; Akagi, K. Helically π-Stacked Thiophene-Based Copolymers with Circularly Polarized Fluorescence: High Dissymmetry Factors Enhanced by Self-Ordering in Chiral Nematic Liquid Crystal Phase. *Chem. Mater.* **2012**, *24*, 1011-1024.

(5) Yang, X.-X.; Li, N.; Li, C.; Jin, Z.-B.; Ma, Z.-Z.; Gu, Z.-G.; Zhang, J. Chiral Liquid Crystalline Metal–Organic Framework Thin Films for Highly Circularly Polarized Luminescence. *J. Am. Chem. Soc.* **2024**, *146*, 16213-16221.

(6) Zhao, B.; Li, N.; Wang, X.; Chang, Z.; Bu, X.-H. Host–Guest Engineering of Coordination Polymers for Highly Tunable Luminophores Based on Charge Transfer Emissions. *ACS Appl. Mater. Interfaces* **2017**, *9*, 2662-2668.

(7) Nishida, J.; Fayer, M. D. Guest Hydrogen Bond Dynamics and Interactions in the Metal–Organic Framework MIL-53(Al) Measured with Ultrafast Infrared Spectroscopy. *J. Phys. Chem. C* **2017**, *121*, 11880-11890.

(8) Chang, X.-H.; Qin, W.-J.; Zhang, X.-Y.; Jin, X.; Yang, X.-G.; Dou, C.-X.; Ma, L.-F. Angle-Dependent Polarized Emission and Photoelectron Performance of Dye-Encapsulated Metal–Organic Framework. *lnorg. Chem.* **2021**, *60*, 10109-10113.

(9) Zhang, C.; Yan, Z. P.; Dong, X. Y.; Han, Z.; Li, S.; Fu, T.; Zhu, Y. Y.; Zheng, Y. X.; Niu, Y. Y.; Zang, S. Q. Enantiomeric MOF Crystals Using Helical Channels as Palettes With Bright White Circularly Polarized Luminescence. *Adv. Mater.* **2020**, *32*, 2002914.

(10) Gheorghe, A.; Strudwick, B.; Dawson, D. M.; Ashbrook, S. E.; Woutersen, S.; Dubbeldam, D.; Tanase, S. Synthesis of Chiral MOF-74 Frameworks by Post-Synthetic Modification by Using an Amino Acid. *Chem. Eur. J.* **2020**, *26*, 13957-13965.

(11) Gao, P.; Zhang, K.; Ren, D.; Liu, H.; Zhang, H.; Fu, H.; Ma, L.; Li, D. Host-Guest Chemistry of Chiral MOFs for Multicolor Circularly Polarized Luminescence Including Room Temperature Phosphorescence. *Adv. Funct. Mater.* **2023**, *33*, 2300105.

(12) Hu, L.; Li, K.; Shang, W.; Zhu, X.; Liu, M. Emerging Cubic Chirality in γCD-MOF for Fabricating Circularly Polarized Luminescent Crystalline Materials and the Size Effect. *Angew. Chem. Int. Ed.* **2020**, *59*, 4953-4958.

(13) Zhao, Y.-W.; Wang, Y.; Zhang, X.-M. Homochiral MOF as Circular Dichroism Sensor for Enantioselective Recognition on Nature and Chirality of Unmodified Amino Acids. *ACS Appl. Mater. Interfaces* **2017**, *9*, 20991-20999.

(14) Zhao, T.; Han, J.; Shi, Y.; Zhou, J.; Duan, P. Multi-Light-Responsive Upconversion-and-Downshifting-Based Circularly Polarized Luminescent Switches in Chiral Metal–Organic Frameworks. *Adv. Mater.* **2021**, *33*, 2101797.

(15) Gao, Z.; Xu, B.; Zhang, T.; Liu, Z.; Zhang, W.; Sun, X.; Liu, Y.; Wang, X.; Wang, Z.; Yan, Y.; et al. Spatially Responsive Multicolor Lanthanide-MOF Heterostructures for Covert Photonic Barcodes. *Angew. Chem. Int. Ed.* **2020**, *59*, 19060-19064.

(16) da Luz, L. L.; Milani, R.; Felix, J. F.; Ribeiro, I. R. B.; Talhavini, M.; Neto, B. A. D.; Chojnacki, J.; Rodrigues, M. O.; Júnior, S. A. Inkjet Printing of Lanthanide–Organic Frameworks for Anti-Counterfeiting Applications. *ACS Appl. Mater. Interfaces* **2015**, *7*, 27115-27123.

(17) Yu, H.; Liu, Q.; Li, J.; Su, Z.-M.; Li, X.; Wang, X.; Sun, J.; Zhou, C.; Hu, X. A dual-emitting mixed-lanthanide MOF with high water-stability for ratiometric fluorescence sensing of Fe^{3+} and ascorbic acid. *J. Mater. Chem. C* **2021**, *9*, 562-568.

(18) Harada, T.; Nakano, Y.; Fujiki, M.; Naito, M.; Kawai, T.; Hasegawa, Y. Circularly Polarized Luminescence of Eu(III) Complexes with Point-and Axis-Chiral Ligands Dependent on Coordination Structures. *lnorg. Chem.* **2009**, *48*, 11242-11250.

(19) Hasegawa, Y.; Miura, Y.; Kitagawa, Y.; Wada, S.; Nakanishi, T.; Fushimi, K.; Seki, T.; Ito, H.; Iwasa, T.; Taketsugu, T.; et al. Spiral Eu(iii) coordination polymers with circularly polarized luminescence. *Chem. Commun.* **2018**, *54*, 10695-10697.

(20) Kumar, J.; Marydasan, B.; Nakashima, T.; Kawai, T.; Yuasa, J. Chiral supramolecular polymerization leading to eye differentiable circular polarization in luminescence. *Chem. Commun.* **2016**, *52*, 9885-9888.

(21) Li, H.; Han, W.; Lv, R.; Zhai, A.; Li, X.-L.; Gu, W.; Liu, X. Dual-Function Mixed-Lanthanide Metal–Organic Framework for Ratiometric Water Detection in Bioethanol and Temperature Sensing. *Anal. Chem.* **2019**, *91*, 2148-2154.

(22) Wang, S.; Jiang, J.; Lu, Y.; Liu, J.; Han, X.; Zhao, D.; Li, C. Ratiometric fluorescence temperature sensing based on single- and dual-lanthanide metal-organic frameworks. *J. Lumin.* **2020**, *226*, 117418.

(23) Xia, C.; Yu, C.; Cao, M.; Xia, J.; Jiang, D.; Zhou, G.; Zhang, D.; Li, H. A Eu and Tb co-doped MOF-5 compound for ratiometric high temperature sensing. *Ceram. Int.* **2018**, *44*, 21040-21046.

(24) Han, Z.; Shi, W.; Cheng, P. Synthetic strategies for chiral metal-organic frameworks. *Chin. Chem. Lett.* **2018**, *29*, 819-822.

(25) Sharifzadeh, Z.; Berijani, K.; Morsali, A. Chiral metal–organic frameworks based on asymmetric synthetic strategies and applications. *Coord. Chem. Rev.* **2021**, *445*, 214083.

(26) Işık, M.; Dündar, E.; Şahin, E.; Tanyeli, C. A boron dipyrromethene chiral at boron and carbon with a bent geometry: synthesis, resolution and chiroptical properties. *Chem. Commun.* **2022**, *58*, 7188-7191.

(27) Kitayama, Y.; Amako, T.; Suzuki, N.; Fujiki, M.; Imai, Y. Enhancing circularly polarised luminescence by extending the π-conjugation of axially chiral compounds. *Org. Biomol. Chem.* **2014**, *12*, 4342-4346.

(28) Lauwick, H.; Kertész, E.; Garami, K. N.; Huadsai, W.; Duffy, M. P.; Foundi, R.; Chemin, A.; Roisnel, T.; Vanthuyne, N.; Benkő, Z.; et al. Phosphetene-Based Polyaromatics: Structure-Property Relationships and Chiroptical Tuning. *Angew. Chem. Int. Ed.* **2024**, *63*, e202409988.

(29) Pascal, S.; Besnard, C.; Zinna, F.; Di Bari, L.; Le Guennic, B.; Jacquemin, D.; Lacour, J. Zwitterionic [4]helicene: a water-soluble and reversible pH-triggered ECD/CPL chiroptical switch in the UV and red spectral regions. *Org. Biomol. Chem.* **2016**, *14*, 4590-4594.

(30) Rekis, T. Crystallization of chiral molecular compounds: what can be learned from the Cambridge Structural Database? *Acta Cryst. B* **2020**, *76*, 307-315.

(31) Rowland, R. S.; Taylor, R. Intermolecular Nonbonded Contact Distances in Organic Crystal Structures: Comparison with Distances Expected from van der Waals Radii. *J. Phys. Chem.* **1996**, *100*, 7384-7391.

(32) Jordan, R. B. Lanthanide Contraction: What is Normal? *lnorg. Chem.* **2023**, *62*, 3715-3721.

(33) Seitz, M.; Oliver, A. G.; Raymond, K. N. The Lanthanide Contraction Revisited. *J. Am. Chem. Soc.* **2007**, *129*, 11153-11160.

(34) Silva, G. S.; Dutra, J. D. L.; da Costa, N. B., Jr.; Alves, S., Jr.; Freire, R. O. Lanthanide Contraction in Lanthanide Organic Frameworks: A Theoretical and Experimental Study. *J. Phys. Chem. A* **2020**, *124*, 7678-7684.

(35) Lu, T.-Q.; Cheng, L.-T.; Wang, X.-T.; Chen, C.; Zheng, J.; Lu, D.-F.; Zheng, X.-Y. Lanthanide Metal–Organic Frameworks with High Chemical Stability as Multifunctional Materials: Cryogenic Magnetic Cooler and Luminescent Probe. *Cryst. Growth Des.* **2022**, *22*, 4917-4925.

(36) Patra, K.; Pal, H. Lanthanide-based metal–organic frameworks (Ln-MOFs): synthesis, properties and applications. *RSC Sustain.* **2025**, *3*, 629-660.

(37) Barsukova, M. O.; Cherezova, S. V.; Sapianik, A. A.; Lundovskaya, O. V.; Samsonenko, D. G.; Fedin, V. P. Lanthanide contraction effect and white-emitting luminescence in a series of metal–organic frameworks based on 2,5-pyrazinedicarboxylic acid. *RSC Adv.* **2020**, *10*, 38252-38259.

(38) Gao, J.-Y.; Xiong, X.-H.; Chen, C.-J.; Xie, W.-P.; Ran, X.-R.; Yue, S.-T.; Liu, Y.-L.; Cai, Y.-P. Effect of lanthanide contraction on structures of 3D lanthanide organic frameworks from 5-nitroisophthalic acid and picolinic acid. *Inorg. Chem. Commun.* **2013**, *31*, 5-12.

(39) Kumar, M.; Li, L.-Q.; Zaręba, J. K.; Tashi, L.; Sahoo, S. C.; Nyk, M.; Liu, S.-J.; Sheikh, H. N. Lanthanide Contraction in Action: Structural Variations in 13 Lanthanide(III) Thiophene-2,5-dicarboxylate Coordination Polymers (Ln = La–Lu, Except Pm and Tm) Featuring Magnetocaloric Effect, Slow Magnetic Relaxation, and Luminescence-Lifetime-based Thermometry. *Cryst. Growth Des.* **2020**, *20*, 6430-6452.

(40) Wang, H.-S.; Li, J.; Li, J.-Y.; Wang, K.; Ding, Y.; Xia, X.-H. Lanthanide-based metal-organic framework nanosheets with unique fluorescence quenching properties for two-color intracellular adenosine imaging in living cells. *NPG Asia Mater.* **2017**, *9*, e354-e354.

(41) Xu, J.; Cheng, J.; Su, W.; Hong, M. Effect of Lanthanide Contraction on Crystal Structures of Three-Dimensional Lanthanide Based Metal–Organic Frameworks with Thiophene-2,5-Dicarboxylate and Oxalate. *Cryst. Growth Des.* **2011**, *11*, 2294-2301.

(42) Binnemans, K. Lanthanide-Based Luminescent Hybrid Materials. *Chem. Rev.* **2009**, *109*, 4283-4374.

(43) Bünzli, J.-C. G. On the design of highly luminescent lanthanide complexes. *Coord. Chem. Rev.* **2015**, *293-294*, 19-47.

(44) Døssing, A. Luminescence from Lanthanide(3+) Ions in Solution. *Eur. J. Inorg. Chem.* **2005**, *2005*, 1425-1434.

(45) Eliseeva, S. V.; Bünzli, J.-C. G. Lanthanide luminescence for functional materials and bio-sciences. *Chem. Soc. Rev.* **2010**, *39*, 189-227.

(46) Moore, E. G.; Samuel, A. P. S.; Raymond, K. N. From Antenna to Assay: Lessons Learned in Lanthanide Luminescence. *Acc. Chem. Res.* **2009**, *42*, 542-552.

(47) Lakshman, S. V. J.; Buddhudu, S. Optical absorption spectra of praseodymium acetate complexes in solution. *Polyhedron* **1983**, *2*, 403-408.

(48) Woudenberg, J. P. M. The absorption of praseodymium in solutions. *Physica* **1942**, *9*, 217-224.

(49) Migdisov, A. A.; Reukov, V. V.; Williams-Jones, A. E. A spectrophotometric study of neodymium(III) complexation in sulfate solutions at elevated temperatures. *Geochim. Cosmochim. Acta* **2006**, *70*, 983-992.

(50) Seminara, A.; Musumeci, A. Absorption and emission spectra of neodymium(III) and europium(III) complexes. *Inorg. Chim. Acta* **1984**, *95*, 291-307.

(51) Kaizu, Y.; Miyakawa, K.; Okada, K.; Kobayashi, H.; Sumitani, M.; Yoshihara, K. Aqualigand Dissociation of $[Ce(OH_2)_9]^{3+}$ ion in the 5d ← 4f Excited State. *J. Am. Chem. Soc.* **1985**, *107*, 2622-2626.

(52) Keller, B.; Legendziewicz, J.; Gliński, J. Investigation of optical properties of praseodymium and cerium chlorides in nonaqueous solutions. *Spectrochim. Acta A* **1998**, *54*, 2207-2213.

(53) Qin, X.; Liu, X.; Huang, W.; Bettinelli, M.; Liu, X. Lanthanide-Activated Phosphors Based on 4f-5d Optical Transitions: Theoretical and Experimental Aspects. *Chem. Rev.* **2017**, *117*, 4488-4527.

(54) Horrocks, W. D., Jr.; Sudnick, D. R. Lanthanide ion probes of structure in biology. Laser-induced luminescence decay constants provide a direct measure of the number of metal-coordinated water molecules. *J. Am. Chem. Soc.* **1979**, *101*, 334-340.

(55) Boer, S. A.; Hawes, C. S.; Turner, D. R. Engineering entanglement: controlling the formation of polycatenanes and polyrotaxanes using π interactions. *Chem. Commun.* **2014**, *50*, 1125-1127.

(56) Ge, Y.; Teng, B.; Lv, L.; Chen, R.; Wu, B. Homochiral Metal–Organic Frameworks of Lead(II) and Cadmium(II) Constructed by Amino Acid-Functionalized Isophthalic Acids: Synthesis, Structure Diversity, and Optical Properties. *Cryst. Growth Des.* **2020**, *20*, 486-497.

(57) Guo, W.-X.; Wang, Y.-Y.; Hu, X.-L.; Yue, Q.; Gao, E.-Q. Homochiral Helical Coordination Architectures Built from Biphenyl-Based Amino Acid Derivatives: Structural Diversity Tuned by Varying Conformation and Configuration of N-Donor Ligands, Sensing of Acidic Amino Acids, and Photoluminescence Properties. *Cryst. Growth Des.* **2020**, *20*, 5072-5085.

(58) Bada, J. L. Kinetics of the Nonbiological Decomposition and Racemization of Amino Acids in Natural Waters. In *Nonequilibrium Systems in Natural Water Chemistry*, Advances in Chemistry, Vol. 106; American Chemical Society, 1971; pp 309-331.

(59) Bada, J. L. Kinetics of racemization of amino acids as a function of pH. *J. Am. Chem. Soc.* **1972**, *94*, 1371-1373.

(60) Frank, H.; Woiwode, W.; Nicholson, G.; Bayer, E. Determination of the rate of acidic catalyzed racemization of protein amino acids. *Liebigs Ann. Chem.* **1981**, *1981*, 354-365.

(61) Bada, J. L. Racemization of Amino Acids. In *Chemistry and Biochemistry of the Amino Acids*, Barrett, G. C. Ed.; Springer Netherlands, 1985; pp 399-414.

(62) Smith, G. G.; Khatib, A.; Reddy, G. S. The effect of nickel(II) and cobalt(III) and other metal ions on the racemization of free and bound L-alanine. *J. Am. Chem. Soc.* **1983**, *105*, 293-295.

(63) Kuk, Y.; Ok, K. M. Homochiral three-dimensional noncentrosymmetric lanthanide coordination polymers directed by chiral linkers: syntheses, crystal structures, and optical properties. *CrystEngComm* **2021**, *23*, 3701-3709.

(64) Wang, R.-Y.; Huang, A.-P.; Wang, W.-B.; Sun, H.-Z.; Teng, B.-S.; Ma, Y.-J.; Wu, B.-L. Three-dimensional homochiral coordination polymers of Eu(III) and Tb(III): Synthesis, structure determination, and optical properties. *J. Solid State Chem.* **2020**, *292*, 121702.

(65) Ma, D.; Cai, Q.; Zhang, H. Mild Method for Ullmann Coupling Reaction of Amines and Aryl Halides. *Org. Lett.* **2003**, *5*, 2453-2455.

(66) Zhang, H.; Cai, Q.; Ma, D. Amino Acid Promoted CuI-Catalyzed C−N Bond Formation between Aryl Halides and Amines or N-Containing Heterocycles. *J. Org. Chem.* **2005**, *70*, 5164-5173.

(67) Ma, D.; Zhang, Y.; Yao, J.; Wu, S.; Tao, F. Accelerating Effect Induced by the Structure of α-Amino Acid in the Copper-Catalyzed Coupling Reaction of Aryl Halides with α-Amino Acids. Synthesis of Benzolactam-V8. *J. Am. Chem. Soc.* **1998**, *120*, 12459-12467.

(68) Smith, G. G.; Williams, K. M.; Wonnacott, D. M. Factors affecting the rate of racemization of amino acids and their significance to geochronology. *J. Org. Chem.* **1978**, *43*, 1-5.

(69) Patel, D. C.; Woods, R. M.; Breitbach, Z. S.; Berthod, A.; Armstrong, D. W. Thermal racemization of biaryl atropisomers. *Tetrahedron: Asymmetry* **2017**, *28*, 1557-1561.

(70) Harrowfield, J. M.; Kim, Y.; Skelton, B. W.; White, A. H. Mixed Transition Metal/Lanthanide Complexes: Structural Characterization of Solids Containing Cage Amine Chromium(III) Cations and Tris(dipicolinato)lanthanide Anions. *Aust. J. Chem.* **1995**, *48*, 807-823.

(71) Tancrez, N.; Feuvrie, C.; Ledoux, I.; Zyss, J.; Toupet, L.; Le Bozec, H.; Maury, O. Lanthanide Complexes for Second Order Nonlinear Optics: Evidence for the Direct Contribution of f Electrons to the Quadratic Hyperpolarizability. *J. Am. Chem. Soc.* **2005**, *127*, 13474-13475.

(72) Chen, Z.; Liu, X.; Zhang, C.; Zhang, Z.; Liang, F. Structure, adsorption and magnetic properties of chiral metal–organic frameworks bearing linear trinuclear secondary building blocks. *Dalton Trans.* **2011**, *40*, 1911-1918.

(73) Chen, Z.; Zhang, C.; Liu, X.; Zhang, Z.; Liang, F. Synthesis, Structure, and Properties of a Chiral Zinc(II) Metal-Organic Framework Featuring Linear Trinuclear Secondary Building Blocks. *Aust. J. Chem.* **2012**, *65*, 1662-1666.

(74) Li, Y.; Chen, S.; Xu, Z.-X.; Wu, X.; Zhang, H.; Zhang, J. Asymmetric metal–organic frameworks with double helices for enantioselective recognition. *CrystEngComm* **2021**, *23*, 4748-4751.

(75) Zhu, C.; Zhang, A. M.; Li, Y.; Li, H.-X.; Qian, Y.; Fu, Y.; Wu, X.; Li, Y. A biomimetic metal–organic framework with cuboid inner cavities for enantioselective separation. *Inorg. Chem. Front.* **2022**, *9*, 2683-2690.

Chapter 4

Dual-Responsive Chiroptical Switching in an Enantiomeric Pair of Chiral Ferrocene Derivatives

4.1 Overview

Dual-responsive chiroptical switches can be reversibly modulated with two different stimuli. For certain applications of chiroptical switches such as optical computing and data storage (in which even basic logic gates need two input channels),[1, 2] this enhanced functionality is essential. In Chapter 3, chiroptical switching was achieved with electric potential and demonstrated in-principle for magnetic field. The aim of this chapter is to realise 'true' dual-responsive chiroptical switching, in which the chiroptical changes are monitored *in-situ*. To accomplish this, amino acid conjugates of 1,1′-ferrocenedicarboxylic acid are identified as suitable candidates for dual-responsive chiroptical switching.

4.1.1 Amino Acid Conjugates of 1,1′-Ferrocenedicarboxylic Acid

The reaction between 1,1′-ferrocenedicarboxylic acid and an amino acid (in this case valine methyl ester) was first performed by Herrick and coworkers in 1996.[3] They observed that in solution state there were two intramolecular hydrogen bonds between the NH of each valine and the ester carbonyl of the other valine. Due to the chirality of the valine units themselves, this favourable hydrogen bonding interaction can only occur when the two cyclopentadienyl rings are arranged in a specific orientation with respect to one another, providing the molecule with axial chirality. This arrangement became known as the 'Herrick conformation' and has been observed for many other ferrocene diamino acid and dipeptide conjugates.[4-8] However, in some cases an alternate conformation is observed in which only a single intramolecular hydrogen bond is formed between the amine of one amino acid and the amide carbonyl of the other. This arrangement is termed the 'van Staveren conformation'.[9] Finally, if no intramolecular hydrogen bonds are present the open 'Xu conformation' is obtained in which

the two amino acid arms freely rotate with no dominant orientation, leading to no overall chirality.[10] This conformation is particularly prominent when proline is used as the tertiary amide formed lacks a N–H bond. The structures of the different conformations are shown below in Figure 4.1. For both the Herrick and van Staveren conformations, L amino acids induce *P*-helicity while D amino acids induce *M*-helicity of the ferrocene unit.[11] Bioconjugates of ferrocene with amino acids and peptides have been the subject of intense research due to their propensity to mimic the antiparallel *β*-sheets of proteins when in the Herrick conformation.[3, 7, 12]

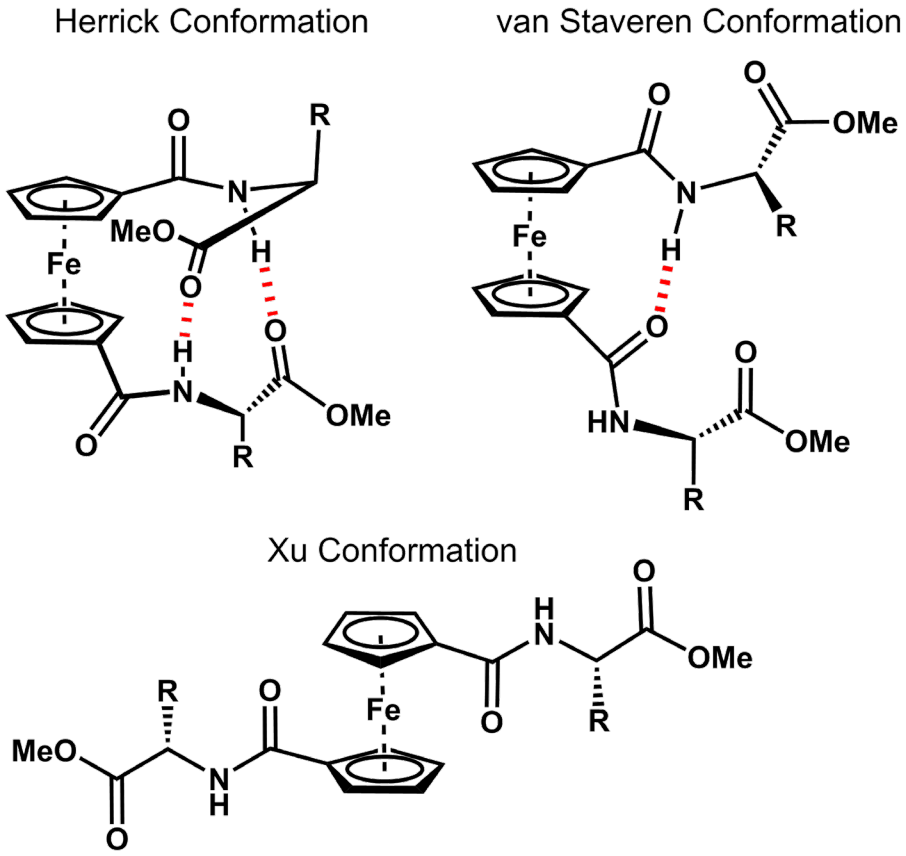

Figure 4.1. The Herrick, van Staveren, and Xu conformations of diamino acid conjugates of 1,1′-ferrocenedicarboxylic acid. Intramolecular hydrogen bonds are shown in red. R = amino acid side groups.

Ferrocene bis(amino acid) derivatives are promising candidates for realising dual-responsive chiroptical switches as they have been shown to respond to a wide range of stimuli. Firstly, the ferrocene core is redox-active and can be converted to the ferrocenium cation under relatively mild potentials. Given the ferrocene/ferrocenium cation redox couple is commonly used as an internal standard in non-aqueous electrochemistry due to its high reversibility,[13] redox is thus an obvious choice of stimulus. Despite this, of the many ferrocene bis(amino acid) derivatives

reported to date, only one has exploited redox to achieve switching and this was done chemically for only one cycle.[4] The use of electrochemical oxidation/reduction of ferrocene bis(amino acid) derivatives for chiroptical switching is thus underutilised and warrants a more thorough investigation.

Another way to effect chiroptical switching in ferrocene bis(amino acid) derivatives is to alter or break the intramolecular hydrogen bonds between the amino acids in some way since they are what holds the molecule in a chiral configuration. A range of stimuli can achieve this such as temperature,[4, 6, 8] hydration,[6] metal coordination,[5, 14] and anion binding.[15] Of these, temperature is arguably the most convenient for performing multiple switching cycles. The mechanism is very straightforward: increasing the temperature should lead to a decrease in CD signal as there is more thermal energy to break the intramolecular hydrogen bonds, causing more molecules to adopt the open, achiral conformation.

This chapter thus describes the synthesis of a pair of ferrocene amino acid bioconjugates, L-Fc(MeLeu)$_2$ and D-Fc(MeLeu)$_2$, formed by the amide coupling between L/D-leucine methyl ester and 1,1′-ferrocenedicarboxylic acid. Their fundamental optical and chiroptical properties are subsequently explored through analysis of their solvent-dependent CD response. Next, variable temperature (VT) and spectroelectrochemical CD experiments are performed to show that L/D-Fc(MeLeu)$_2$ operate as dual-responsive chiroptical switches in response to both temperature and electric potential as stimuli. Their magneto-optical properties are also investigated using MCD spectroscopy. Finally, thin films of L/D-Fc(MeLeu)$_2$ are prepared to study their solid-state chiroptical properties.

4.2 Synthesis and Characterisation of L- and D-Fc(MeLeu)$_2$

4.2.1 Synthesis of L- and D-Fc(MeLeu)$_2$

L- and D-Fc(MeLeu)$_2$ were synthesised via a simple three step-procedure from ferrocene (Figure 4.2). Firstly, ferrocene was converted to 1,1′-diacetylferrocene in a Friedel-Crafts acylation with acetyl chloride in 61% yield. Next, the diacetylferrocene was converted to 1,1′-ferrocenedicarboxylic acid in a haloform reaction using sodium hypochlorite in a 76% yield. Careful control of temperature was important for this step. Both reactions scale well and could be performed on the multi-gram scale, affording a large amount of the ferrocene dicarboxylic acid. Finally, L-Fc(MeLeu)$_2$ and D-Fc(MeLeu)$_2$ were synthesised by the amide coupling of L- or D-leucine methyl ester hydrochloride with 1,1′-ferrocenedicarboxylic acid using HATU as

the coupling agent and triethylamine as the base. The final products were obtained following column chromatography in 94% and 95% yields (approximately 44% overall yield) for L-Fc(MeLeu)$_2$ and D-Fc(MeLeu)$_2$, respectively.

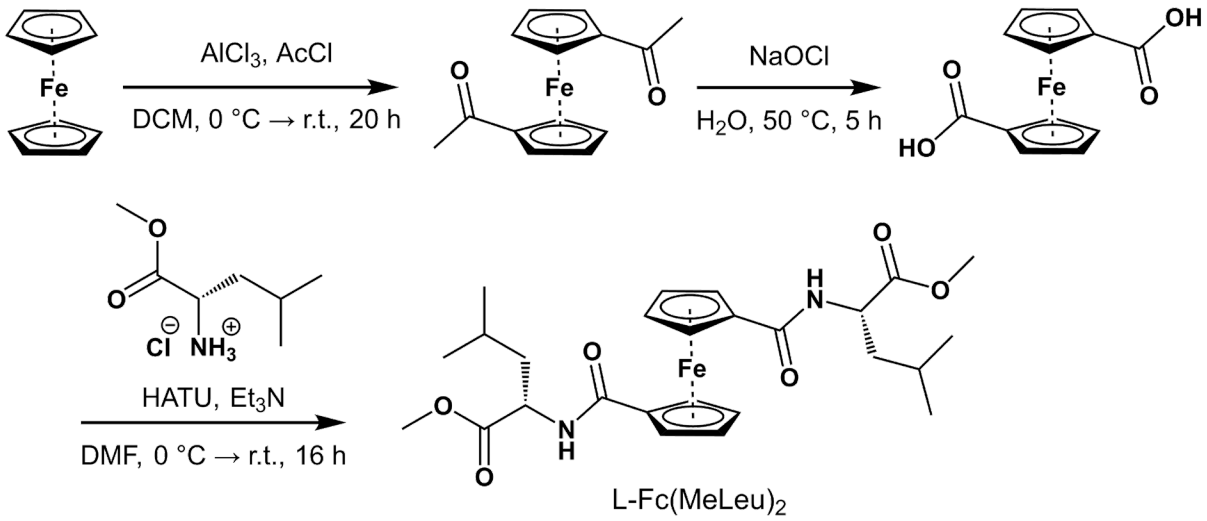

Figure 4.2. Synthesis scheme of L-Fc(MeLeu)$_2$. D-Fc(MeLeu)$_2$ is synthesised by the same method except using D-leucine methyl ester hydrochloride instead.

A few key spectroscopic benchmarks have been developed to determine the particular conformation of ferrocene bis(amino acid) derivatives in solution.[3, 9, 11] According to these criteria, both L-Fc(MeLeu)$_2$ and D-Fc(MeLeu)$_2$ exist in the Herrick conformation. Firstly, in $CDCl_3$ (a non-hydrogen bonding solvent) the ^{1}H NMR of the amide NH protons of both enantiomers show a single signal with an integral of 2H and chemical shift of 7.76 ppm. If the compounds were in a van Staveren conformation, two amide NH peaks would be expected, one for the hydrogen bonded proton and another for the non-hydrogen bonded proton. Furthermore, a chemical shift > 7 ppm is indicative of hydrogen bonded amide protons, discounting the Xu conformation. Additionally, the FTIR spectra of L-Fc(MeLeu)$_2$ and D-Fc(MeLeu)$_2$ in DCM show N-H stretches at 3373 and 3372 cm^{-1}, respectively. These are assigned to intramolecular hydrogen bonds since amide stretches less than 3400 cm^{-1} are typical of hydrogen bonded NH protons. Finally, the CD spectra (discussed in the next section) of both enantiomers are characteristic of other ferrocene bis(amino acid) derivatives which exist in the Herrick conformation.

4.2.2 Optical and Chiroptical Properties of L- and D-Fc(MeLeu)$_2$

The UV-vis and CD spectra of L-Fc(MeLeu)$_2$ and D-Fc(MeLeu)$_2$ acquired in toluene are shown in Figure 4.3. The UV-vis of L-Fc(MeLeu)$_2$ is characterised by absorbance bands at 346 nm (ε = 427 $M^{-1}cm^{-1}$) and 443 nm (ε = 256 $M^{-1}cm^{-1}$), both assigned to the ferrocene d–d transition.[16-18] These transitions are fairly weak because d–d transitions are Laporte forbidden. The CD spectrum exhibits positive Cotton signals at 485 and 309 nm, and negative Cotton signals at 417 and 356 nm. These spectral features are consistent with the Herrick conformation and *P*-helicity, in accordance with well-known spectroscopic benchmarks.[11, 19] As expected for enantiomers, D-Fc(MeLeu)$_2$ shows the same absorbance but mirror image CD spectra compared to L-Fc(MeLeu)$_2$.

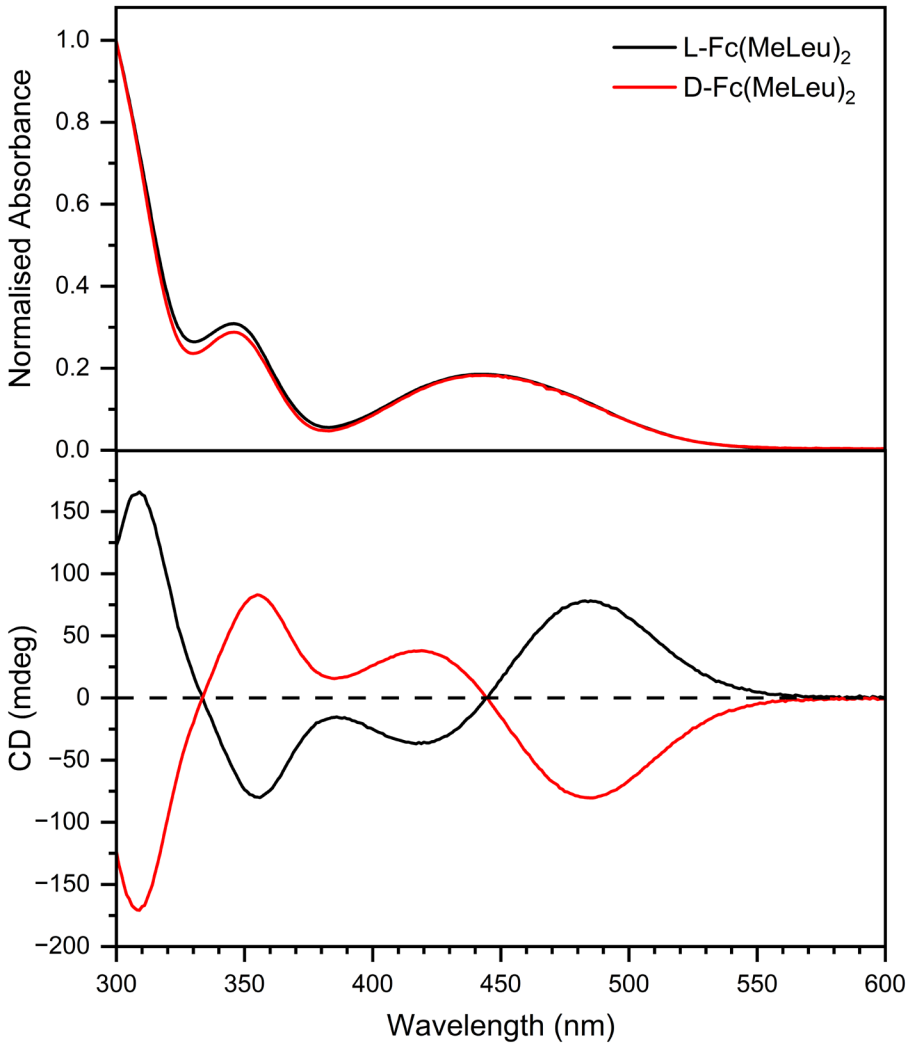

Figure 4.3. Normalised absorbance (top) and CD (bottom) of L-Fc(MeLeu)$_2$ (black) and D-Fc(MeLeu)$_2$ (red) in toluene. Sample concentrations were approximately 1.36 mM.

The spectra reported in Figure 4.3 were measured in toluene, a nonpolar solvent that would not be expected to display a significant interaction with the amide or carbonyl groups involved in intramolecular hydrogen bonding. To gain insight into whether other solvents would alter the solution-state behaviour of L/D-Fc(MeLeu)$_2$, UV-vis and CD spectra of L-Fc(MeLeu)$_2$ were measured in a range of organic solvents with differing polarity, including some with the ability to act as hydrogen bond donors (Figure 4.4). The choice of solvent clearly had a significant impact on the magnitude of the observed CD signal, following an overall trend of decreasing CD signal with increasing solvent polarity. The absorbance dissymmetry factor, g_{abs}, was largest in chloroform at 1.21×10^{-2}, while DMF had the smallest g_{abs} of 3.7×10^{-3}. This behaviour can be rationalised by considering the L-Fc(MeLeu)$_2$ molecules as existing in an equilibrium between the hydrogen bonded Herrick (chiral) conformation and the open Xu (achiral) conformation. More polar solvents are generally better able to disrupt the intramolecular hydrogen bonds and thus shift the equilibrium further towards the achiral side. However, even in the most polar solvent tested – DMF – there is still a CD signal, indicating that at least some of the L-Fc(MeLeu)$_2$ molecules retain intramolecular hydrogen bonds. In contrast to the variation in intensity, the overall shape of the CD spectra remained relatively unchanged across all the solvents measured. Similar effects of solvent polarity have been observed in other ferrocene amino acid conjugates.[6, 8] The effect of different solvents on the absorbance of L-Fc(MeLeu)$_2$ were less pronounced, although some variation in the absorbance intensity were observed. The main d–d transition had absorbance maxima between 442–445 nm in all solvents, consistent with a transition confined to the iron centre with little charge transfer character and somewhat shielded from solvent interactions by the bulky ligands. The higher energy d–d transition displayed slightly more variability, appearing as a shoulder in MeOH and DMF rather than a distinct peak.

To better quantify the solvent-dependence of the chiroptical signal, the relationship between g_{abs} and solvent polarity was compared. Since there is no definitive measure of solvent polarity, several different metrics were explored (Table 4.1). The specific parameters were the solvent dipole moment, the solvent dielectric constant, Snyder's polarity index (P′),[20] the Et(30) polarity parameter,[21] and the hydrogen bond basicity (i.e. ability to act as a hydrogen bond acceptor).[22] While the dipole moment and dielectric constant are inherent properties of a solvent, the other metrics were developed through experimentation and therefore emphasise different aspects of polarity depending on the chemical systems against which the polarity metric was validated. The polarity index P′ is based on a solvent's ability to engage in proton-

accepting, proton-donating, and dipole-dipole interactions with polar solutes in liquid and gas chromatography. The Et(30) values measure solvent polarity through solvatochromism and are defined by the molar transition energy of the lowest energy electronic transition in Reichardt's dye in the particular solvent. Finally, the hydrogen bond basicity is derived from log(K) values for the complexation of a solute (the base) with a reference acid in carbon tetrachloride, providing a thermodynamic scale of hydrogen bond basicity. Since hydrogen bonding is essential to the chirality of L-Fc(MeLeu)$_2$, it was expected that the hydrogen bond basicity would best describe the observed g_{abs} in different solvents. Interestingly, the strongest predictor of the observed g_{abs} was simply the dipole moment of the solvent, which showed a linear correlation with a R^2 of 0.81 (Figure 4.5). While demonstrating a broad trend, it is apparent that the relationship between dipole moment and CD intensity is not perfect. For example, the g_{abs} of toluene and 2-propanol are almost identical even though 2-propanol has a much larger dipole moment – and is also a hydrogen bond donor – and would thus be expected to inflict greater disruption on the intramolecular hydrogen bonds. A potential explanation is that as well as a general trend with dipole moment, each solvent makes specific interactions with L-Fc(MeLeu)$_2$ which may have a meaningful impact on the observed CD. DFT calculations on other ferrocene amino acid conjugates have shown that the CD signal is highly sensitive to the dihedral angle between the two amino acid arms, as well as small rotations of both the amide bond and the bond between the cyclopentadiene ring and carbonyl carbon.[6, 8] Since each solvent will solvate the Herrick form of L-Fc(MeLeu)$_2$ in a slightly different way, the equilibrium bond geometries – and thus CD of the Herrick form itself – will also vary slightly in each solvent. Such effects could potentially explain the slight deviations from the general trend.

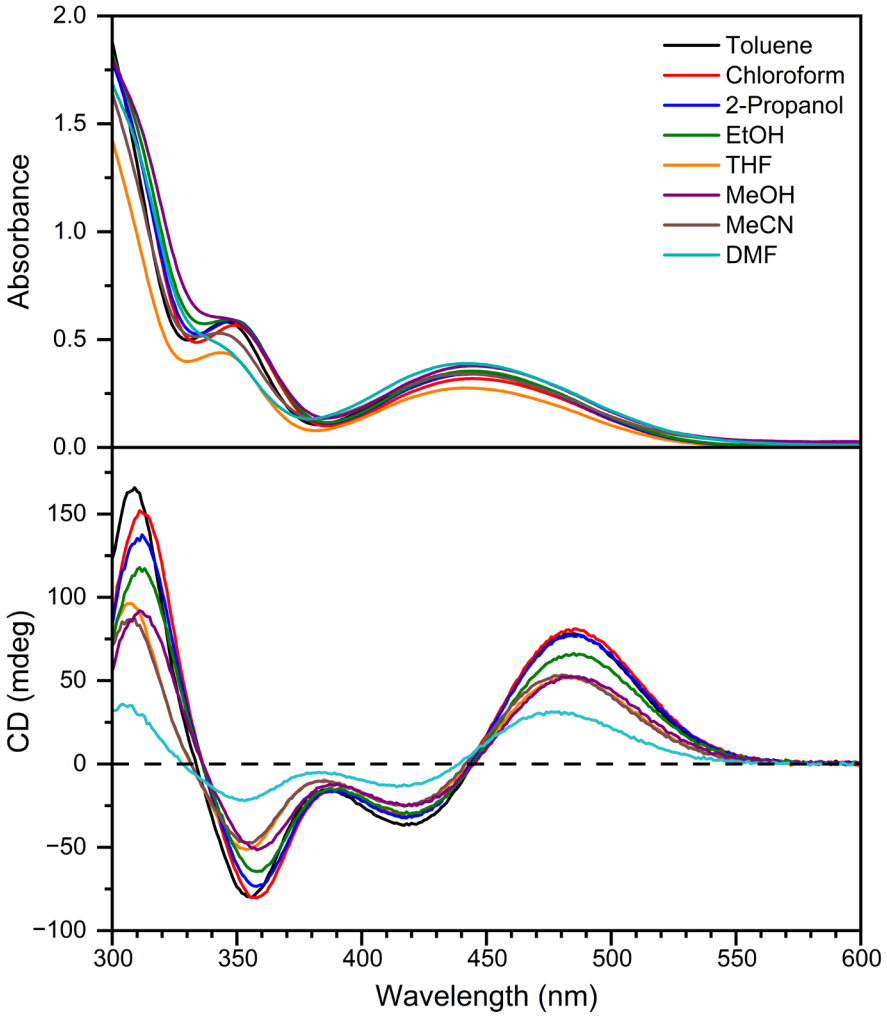

Figure 4.4. UV-vis (top) and CD (bottom) of L-Fc(MeLeu)$_2$ in different solvents. Sample concentrations were approximately 1.36 mM.

Table 4.1. Comparison of trends between the g_{abs} of L-Fc(MeLeu)$_2$ in different solvents and various metrics for solvent polarity.

Solvent	**g_{abs} × 10^3**	**Dipole Moment (D)**	**Dielectric Constant**	**P′**	**Et(30) (kcal/mol)**	**Hydrogen bond basicity**
Toluene	11.0	0.31	2.38	2.4	33.9	0.14
Chloroform	12.1	1.15	4.81	4.1	39.1	0.02
2-Propanol	11.0	1.66	19.92	3.9	48.6	0.56
EtOH	9.1	1.69	24.3	4.3	51.9	0.48
THF	9.4	1.75	7.58	4.0	37.4	0.48
MeOH	6.4	2.87	32.7	5.1	55.5	0.47
MeCN	7.3	3.44	37.5	5.8	46.0	0.32
DMF	3.7	3.86	36.71	6.4	43.8	0.74

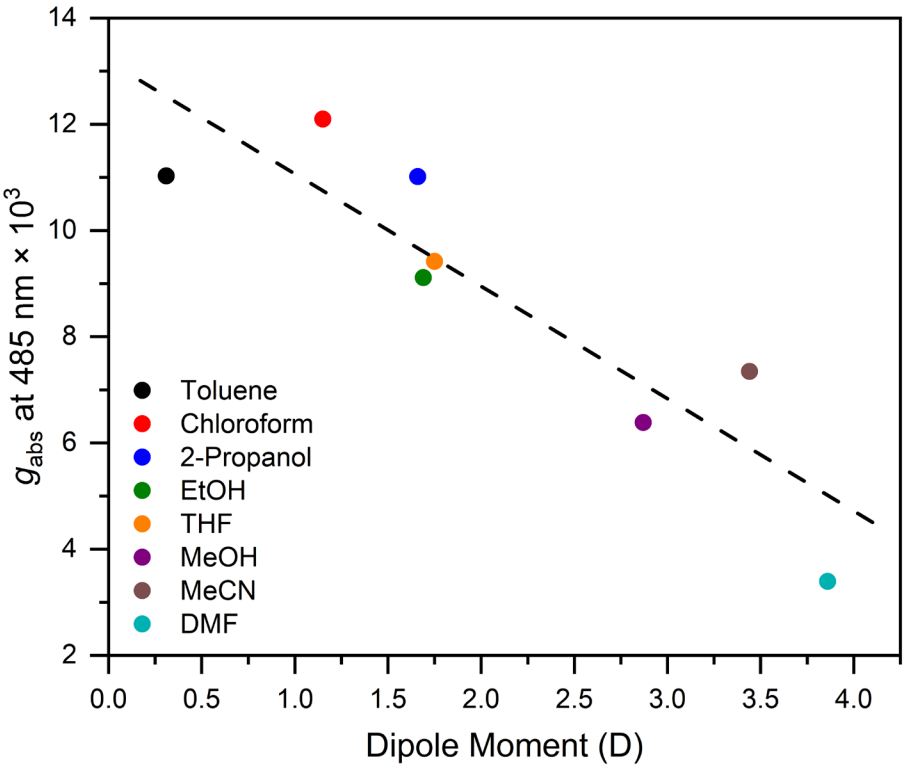

Figure 4.5. The relationship between g_{abs} of L-Fc(MeLeu)$_2$ and the dipole strength of the solvent. The dashed line represents the line of best fit and has an R^2 value of 0.81.

To confirm that the observed CD was solely due to the intramolecular arrangement of the amino acid arms and not due to the formation of chiral supramolecular aggregates, the g_{abs} of L-Fc(MeLeu)$_2$ in toluene was measured at a range of concentrations (Figure 4.6). As can be seen, g_{abs} is essentially independent of concentration with only a slight variation between 360–400 nm, likely due to the sensitivity of g_{abs} calculations in regions with low absorbance. Alternatively, the slight variations in g_{abs} could be due to small changes in ambient temperature between measurements (the temperature-dependent CD of L-Fc(MeLeu)$_2$ is analysed in section 4.3). The observed CD is thus an intensive property of L-Fc(MeLeu)$_2$.[23, 24]

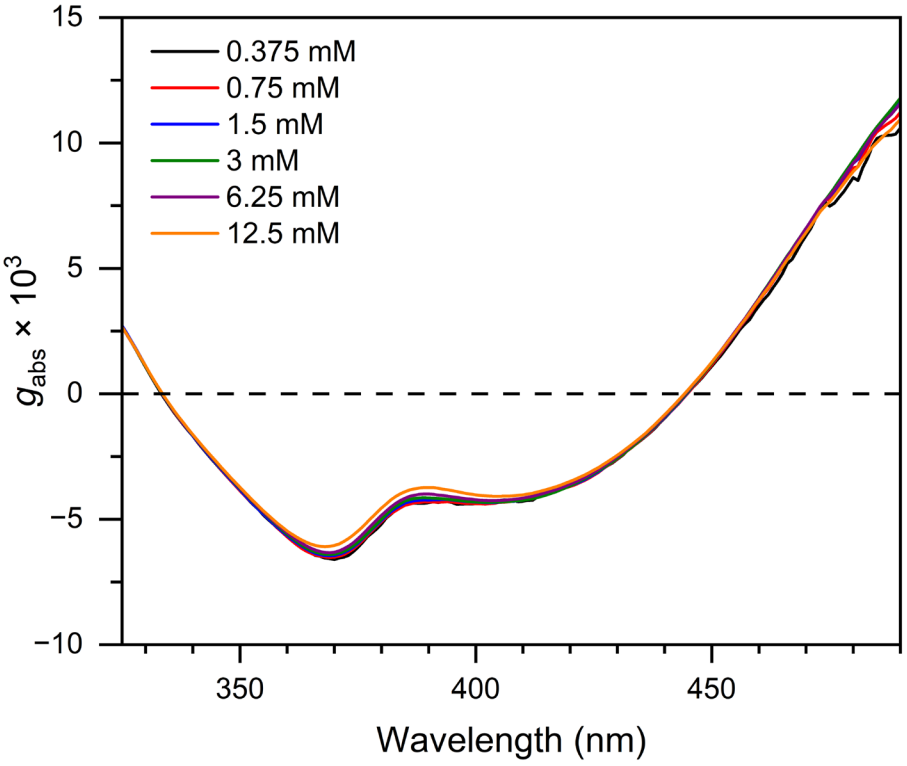

Figure 4.6. Absorbance dissymmetry factor, g_{abs}, of L-Fc(MeLeu)$_2$ in toluene at different concentrations.

4.3 Temperature-Modulated Chiroptical Switching of L- and D-Fc(MeLeu)$_2$

Given that the chirality of L- and D-Fc(MeLeu)$_2$ derives from intramolecular hydrogen bonds, it was expected that the CD intensity could be influenced by changes in temperature. Higher temperatures provide greater thermal energy to break these hydrogen bonds and decrease the proportion of molecules in the chiral, Herrick conformation. This is demonstrated by variable temperature (VT) UV-vis and CD spectra of L-Fc(MeLeu)$_2$ in toluene as shown in Figure 4.7. As the temperature was decreased from 100 °C to 0 °C, there was a consistent increase in CD intensity across the whole spectrum, with a 55% increase of the d–d band at 485 nm. The corresponding g_{abs} at 485 nm increased from 8.4×10^{-3} to 1.3×10^{-2} over the same temperature range. This change was highly reversible; heating the sample from 0 °C back to 100 °C restored the original CD spectrum. For both heating and cooling, the variation of CD was found to be linear with the change in temperature (Figure 4.9). Moreover, no hysteresis was observed, indicating that the ratio of L-Fc(MeLeu)$_2$ molecules in the Herrick and Xu conformations adjusts rapidly to the change in temperature. The absorbance also varied with temperature, showing a modest increase across the entire spectrum as the temperature was cooled. The

spectral changes were comparatively smaller than those seen in CD, with the d–d band exhibiting a 28% increase at 443 nm.

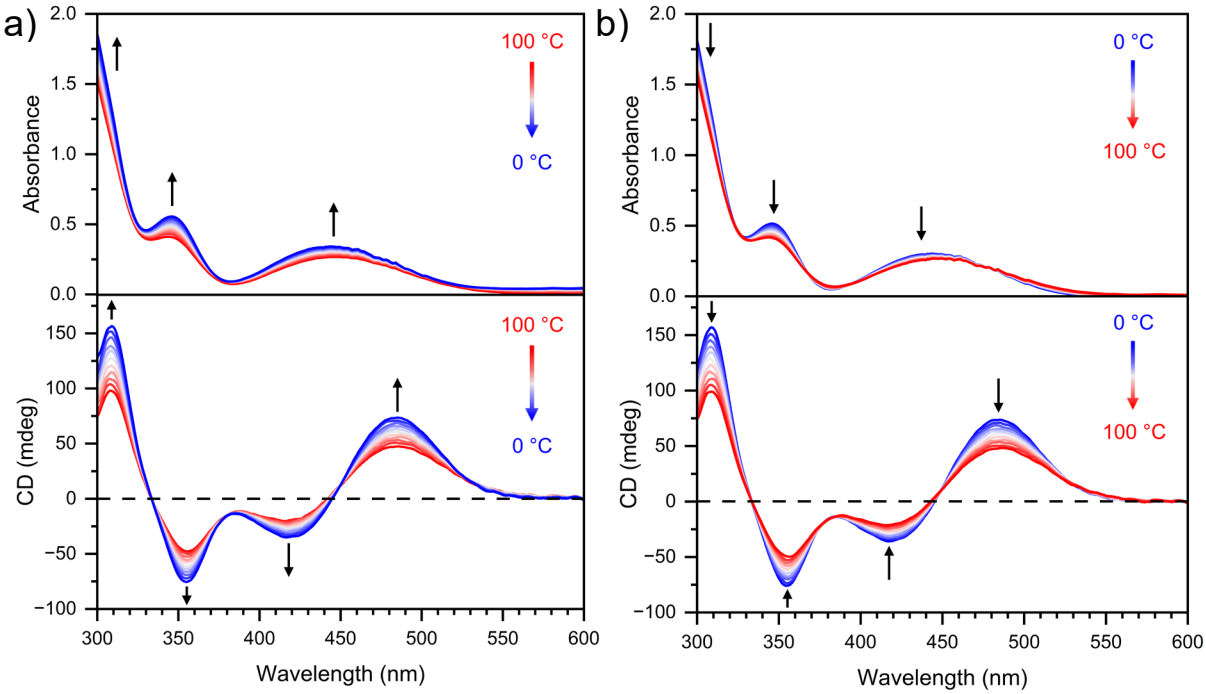

Figure 4.7. Variable temperature UV-vis (top) and CD (bottom) spectra of L-Fc(MeLeu)$_2$ during cooling from 100 °C to 0 °C (a), and heating from 0 °C to 100 °C (b). Spectra were acquired at 10 °C intervals. Sample concentration was 1.36 mM in toluene. Temperature ramp rate = 0.75 °C/min.

To investigate whether this behaviour was dependent on the solvent polarity, VT experiments were also performed on L-Fc(MeLeu)$_2$ in DMF (Figure 4.8 and Figure 4.9). Since the chiroptical signal was weakest in DMF, it was speculated that the CD intensity would drop to zero at high temperatures in DMF. However, the result was similar to that observed in toluene, with a linear increase in CD intensity as the temperature was decreased from 100 °C to 0 °C. While the overall CD was lower in DMF due to its greater polarity, the proportional response to changing temperature was larger than in toluene, with a 106% increase of the d–d band at 477 nm. The corresponding g_{abs} at 477 nm increased from 2.0×10^{-3} to 3.6×10^{-3} over the same temperature range. The energetic favourability of the intramolecular hydrogen bonds is underscored by the residual CD signal observed even at 100 °C in such a highly polar solvent. As seen in toluene, the spectral changes are reversed upon heating back to 100 °C. Additionally, the absorbance of L-Fc(MeLeu)$_2$ increased as the temperature was reduced, with the d–d band exhibiting a 27% increase at 441 nm.

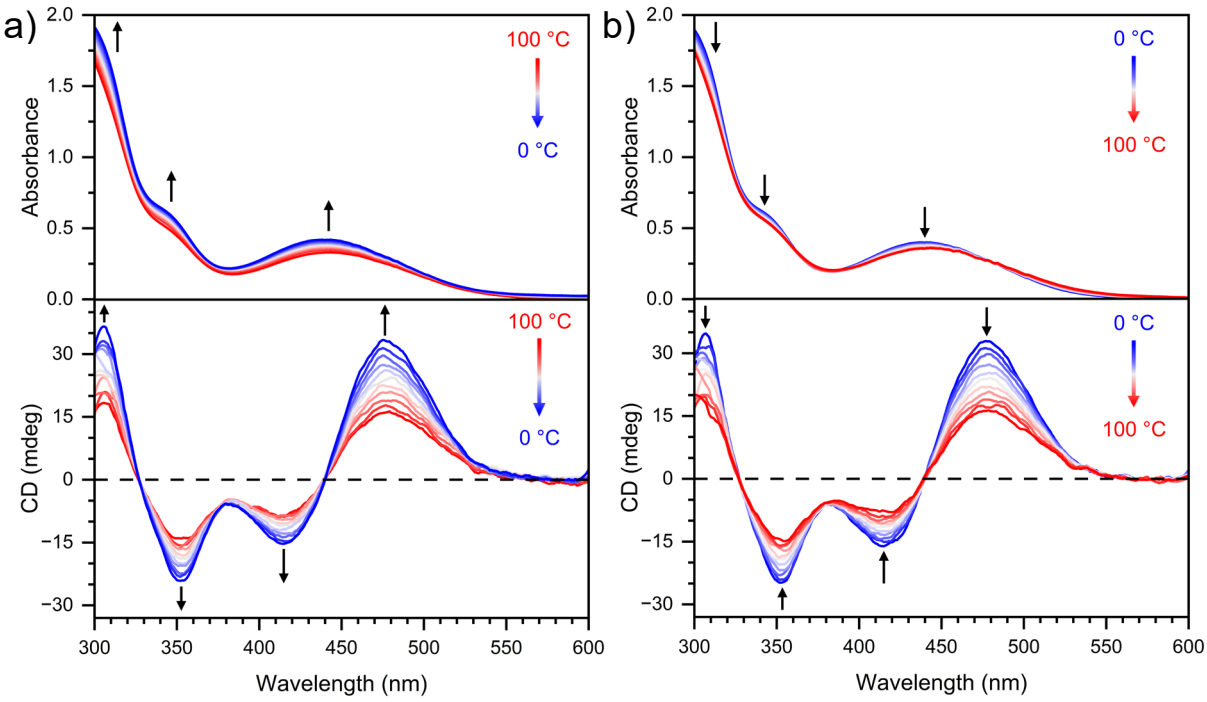

Figure 4.8. Variable temperature UV-vis (top) and CD (bottom) spectra of L-Fc(MeLeu)$_2$ during cooling from 100 °C to 0 °C (a), and heating from 0 °C to 100 °C (b). Spectra were acquired at 10 °C intervals. Sample concentration was 1.36 mM in DMF. Temperature ramp rate = 0.75 °C/min.

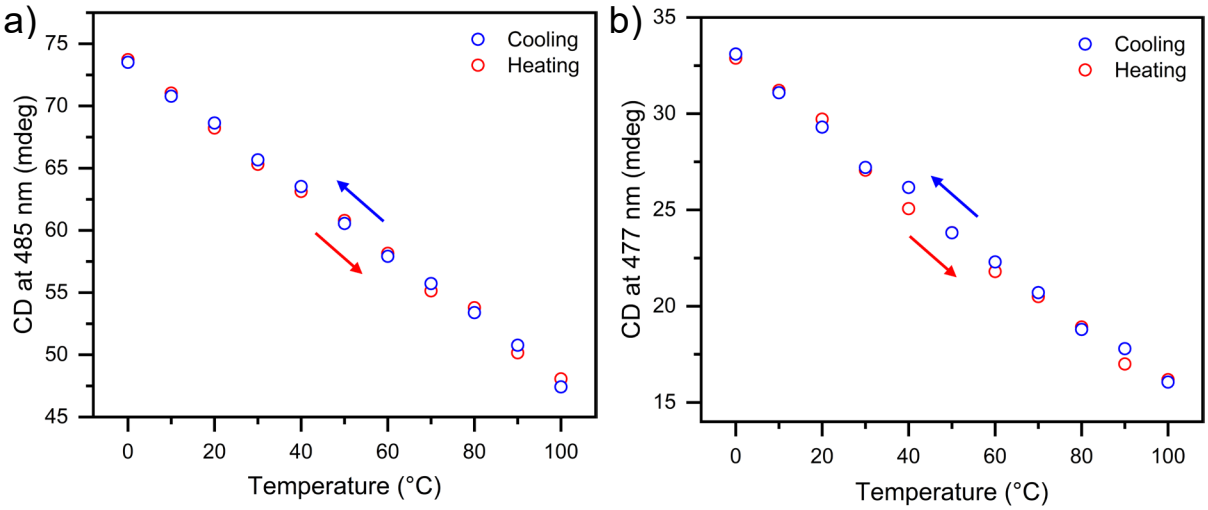

Figure 4.9. Linear trend between CD and temperature at specified wavelengths for L-Fc(MeLeu)$_2$ in toluene (a) and DMF (b). Cooling and heating are represented as blue and red open circles, respectively. Sample concentrations were 1.36 mM. Temperature ramp rate = 0.75 °C/min.

These results demonstrate that L-Fc(MeLeu)$_2$ can act as a reversible, temperature-controlled chiroptical switch in both polar and nonpolar environments. Furthermore, in both toluene and DMF, the change in CD was larger than the change in absorbance, highlighting how chiroptical switches can outperform purely optical switches in certain situations. As expected, analogous behaviour was observed for D-Fc(MeLeu)$_2$ in both toluene and DMF (Figures B1 – B3).

In the literature, comparable temperature-dependent CD has been observed in other ferrocene amino acid conjugates.[4, 6, 8, 25] However, some compounds with dipeptide or tripeptide arms have shown notably smaller changes in CD with varying temperature,[6, 25] indicating that the intramolecular interactions in these molecules are stronger, likely due to the presence of additional intramolecular hydrogen bonds. Whether longer peptide arms lead to more intramolecular hydrogen bonds and greater resistance to temperature changes will no doubt depend on the constituent amino acids and their steric compatibility.

4.4 Redox-Modulated Chiroptical Switching of L- and D-Fc(MeLeu)$_2$

4.4.1 Electrochemistry of L- and D-Fc(MeLeu)$_2$

To investigate the redox behaviour of L- and D-Fc(MeLeu)$_2$, cyclic voltammetry experiments were performed in MeCN using 0.1 M [(*n*-C_4H_9)$_4$N]PF_6 as the supporting electrolyte. The cyclic voltammogram of L-Fc(MeLeu)$_2$ shows a single oxidative process with $E_{1/2}$ = 0.39 V vs Fc/Fc^+ (Figure 4.10a). This process is assigned to a one-electron oxidation of the ferrocene core and is electrochemically reversible, with a ΔE of 91 mV. The anodic shift compared to unsubstituted ferrocene is attributed to the electron-withdrawing effect of the amide groups on the cyclopentadienyl rings. Additionally, the process is diffusion-limited due to the linear relationship between the peak current and the square root of the scan rate according to the Randles-Sevcik equation (Figure 4.10b). As expected, D-Fc(MeLeu)$_2$ displayed the same electrochemistry as L-Fc(MeLeu)$_2$, exhibiting a single, reversible oxidation with $E_{1/2}$ = 0.39 V vs Fc/Fc^+ (Figure B4). This electrochemical behaviour is consistent with ferrocene-based oxidations,[26-28] and indicates that L/D-Fc(MeLeu)$_2$ are suitable for redox-modulated chiroptical switching.

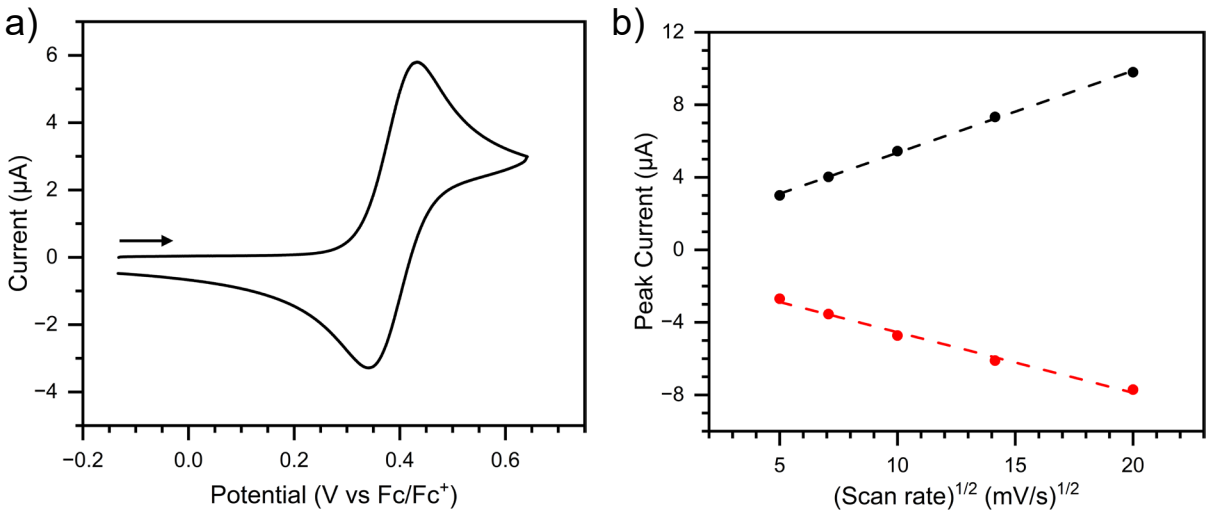

Figure 4.10. (a) Cyclic voltammogram of L-Fc(MeLeu)$_2$ in MeCN with 0.1 M [(n-C_4H_9)$_4$N]PF_6 supporting electrolyte. The arrow shows the direction of the potential sweep. Scan rate = 100 mV/s and the potentials are referenced to Fc/Fc^+ at 0 V. (b) Linear fits of anodic (black) and cathodic (red) peak current vs the square root of scan rate for L-Fc(MeLeu)$_2$ in MeCN with 0.1 M [(n-C_4H_9)$_4$N]PF_6 supporting electrolyte. The anodic and cathodic linear fits have R^2 values of 0.9989 and 0.9919, respectively.

4.4.2. Spectroelectrochemistry of L- and D-Fc(MeLeu)$_2$

The redox-modulated chiroptical switching of L-Fc(MeLeu)$_2$ was investigated with UV-vis and CD SEC (Figure 4.11). The spectroelectrochemical data for D-Fc(MeLeu)$_2$ are analogous to that of L-Fc(MeLeu)$_2$ and are presented in Appendix B (Figure B5). DCM was chosen as the solvent in these experiments for three reasons: (1) its suitable electrochemical window; (2) as a non-hydrogen bonding solvent, it should not meaningfully disrupt the intramolecular hydrogen bonding in L/D-Fc(MeLeu)$_2$, meaning that stronger signals would be observed; (3) the neutral and oxidised states of L/D-Fc(MeLeu)$_2$ are both readily soluble and stable in DCM.

As L-Fc(MeLeu)$_2$ was oxidised, a new absorbance band appeared at 656 nm ($\varepsilon = 575\ M^{-1}cm^{-1}$), attributed to the characteristic ligand-to-metal charge-transfer (LMCT) transition of the ferrocenium core.[17, 18, 29, 30] This is somewhat redshifted from that of ferrocenium itself (617 nm) due to the effect of the electron-withdrawing amide substituents, but is consistent with reports of other ferrocene bis(amino acid) conjugates.[4, 31] Additionally, the LMCT band has a very broad shoulder on the high energy side which is due to several d–d transitions of the ferrocenium core which are not fully resolved.[17] The small shoulder at 380 nm can similarly be attributed to a d–d transition.[17]

Before analysing the CD SEC, it is worth noting that in this experiment neutral L-Fc(MeLeu)$_2$ had a g_{abs} of 8.8 × 10^{-3} at 485 nm, which is somewhat less than the g_{abs} in chloroform despite the similarities between DCM and chloroform. However, it was unclear whether this is due to the inherent properties of DCM, or caused by the high concentration of [(n-C$_4$H$_9$)$_4$N]PF$_6$ electrolyte which could possibly interfere with the intramolecular hydrogen bonding. As L-Fc(MeLeu)$_2$ was oxidised, the Cotton signals at 485 and 355 nm decreased, while a new CD spectrum appeared featuring a positive Cotton signal at 513 nm and negative Cotton signal at 453 nm, corresponding to the ferrocenium species, [L-Fc(MeLeu)$_2$]$^+$. This confirms that chirality is preserved upon oxidation and that the intramolecular hydrogen bonds are retained. The g_{abs} of [L-Fc(MeLeu)$_2$]$^+$ was 2.6 × 10^{-3} at 513 nm and −3.3 × 10^{-3} at 453 nm, indicating that [L-Fc(MeLeu)$_2$]$^+$ has a lower intrinsic chirality than L-Fc(MeLeu)$_2$. Nonetheless, the largest Δg_{abs} is an impressive 1.0 × 10^{-2} at 487 nm. No comparisons with literature could be made as the only other report of CD SEC on a ferrocene bis(amino acid) conjugate merely noted that Cotton signals were present without including the relevant spectrum.[31]

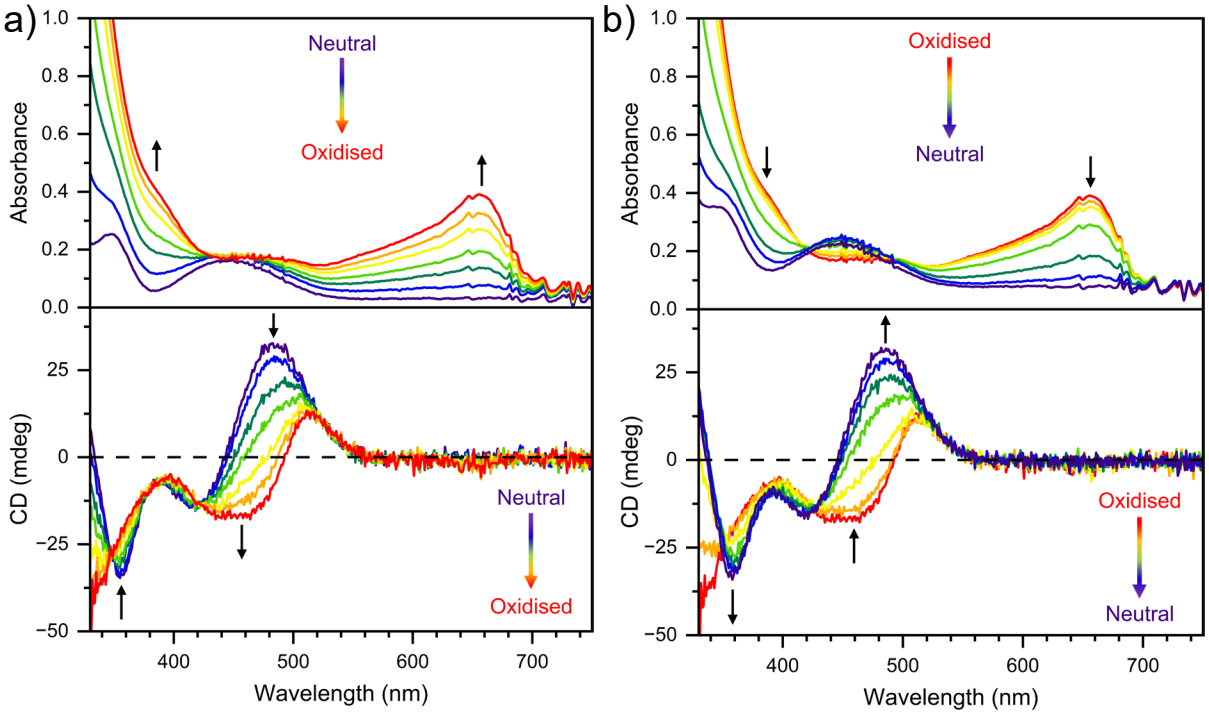

Figure 4.11. (a) UV-vis (top) and CD (bottom) spectra of L-Fc(MeLeu)$_2$ during oxidation to the ferrocenium species over a 70 min time interval. (b) UV-vis (top) and CD (bottom) spectra of L-Fc(MeLeu)$_2$ during subsequent reduction from the ferrocenium to neutral state over a 105 min time interval. The concentration of L-Fc(MeLeu)$_2$ was approximately 10 mM. Spectra were acquired in DCM with 0.25 M [(n-C$_4$H$_9$)$_4$N]PF$_6$ as supporting electrolyte.

Interestingly, there also appears to be a very weak chiroptical signal centred around 650 nm, arising from the LMCT transition. This feature is more distinct when the CD spectra of [L-Fc(MeLeu)$_2$]$^+$ and [D-Fc(MeLeu)$_2$]$^+$ are shown together (Figure 4.12). It was not possible to determine a precise g_{abs} of the ferrocenium absorbance band due to the poor signal-to-noise ratio of the CD response, however a rough estimate gives a g_{abs} of approximately $\pm 2 \times 10^{-4}$ for D- and L-Fc(MeLeu)$_2$, respectively.

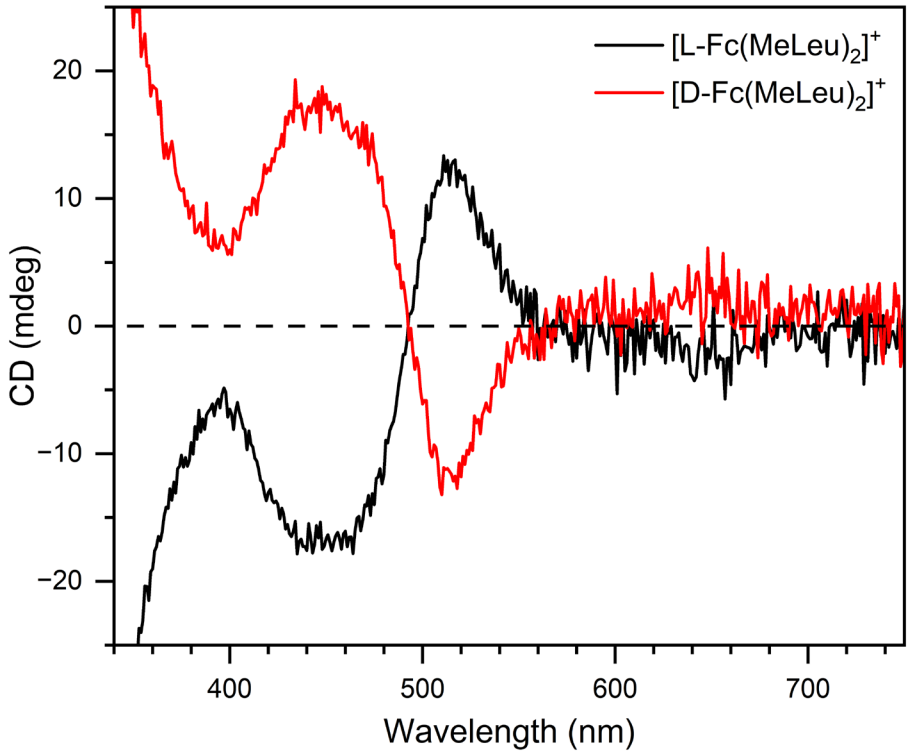

Figure 4.12. CD spectra of [L-Fc(MeLeu)$_2$]$^+$ (black) and [D-Fc(MeLeu)$_2$]$^+$ (red) from SEC experiments. The very weak chirality of the LMCT transition is evident around 650 nm.

In both UV-vis and CD SEC, the original spectra were recovered upon reduction back to the neutral state (Figure 4.11b), confirming that L-Fc(MeLeu)$_2$ can perform as a redox-modulated chiroptical switch. The CD spectra of L-Fc(MeLeu)$_2$ and [L-Fc(MeLeu)$_2$]$^+$ are easily distinguishable in the 450–500 nm range, with 476 nm deemed to be best for monitoring switching. Given that both L-Fc(MeLeu)$_2$ and [L-Fc(MeLeu)$_2$]$^+$ have similar absorbance in this region, the contrast in CD is much greater than in absorbance. Conversely, the change in absorbance is much greater at 656 nm and L-Fc(MeLeu)$_2$ would function better as an optical switch in this region.

Performing UV-vis and CD SEC of L/D-Fc(MeLeu)$_2$ were not easy experiments, primarily because of the high concentration needed (10 mM) due to their low extinction coefficients and the narrow pathlength of the SEC cell (0.068 cm). The high concentration had negative

implications for reversibility and repeated cycling given the difficulty of attaining complete oxidation of L/D-Fc(MeLeu)$_2$ in the cuvette part of the SEC cell. Figure 4.13 shows the CD intensity at 476 nm during two oxidation/reduction cycles of L-Fc(MeLeu)$_2$. The cycling experiment is characterised by very long switching times, with the first cycle taking 68 min for the oxidation half-cycle and 25 min for the reduction half-cycle. For comparison, the switching times for (*S*)-BNI and (*R*)-BNI presented in Chapter 3 were on the order of 4–8 min. The stark difference is attributed to the higher concentration of L-Fc(MeLeu)$_2$ as there are simply many more molecules to oxidise/reduce. Nonetheless, there was only a 2% drop in CD intensity after the first cycle. However, after the second cycle the CD intensity had dropped by 36% overall.

The challenges of obtaining complete oxidation/reduction without the presence of a counter species were explained in Chapter 3. Unfortunately, these challenges only become more difficult as the concentration of analyte increases. In an attempt to improve the switching performance of L-Fc(MeLeu)$_2$, the cycling experiment was repeated with phenazine added as a redox counter-species to the frit containing the counter electrode. Phenazine was selected for the following two reasons: (1) it undergoes electrochemical reduction,[32, 33] allowing it to complement the oxidation of L-Fc(MeLeu)$_2$ at the working electrode; (2) it has previously demonstrated excellent reversibility in bulk electrochemical experiments,[33] so that the electrochemical reversibility of phenazine should not be a limiting factor. The experiment was conducted by adding 50 µL of a 100 mM phenazine solution (dissolved in the DCM/[(n-$C_4H_9)_4N]PF_6$ electrolyte) to the glass frit containing the counter electrode. The high concentration of phenazine was chosen because the surface area of the counter electrode is smaller than the surface area of the working electrode. The inclusion of phenazine clearly improved the reversibility, showing a 2% drop in CD intensity after one cycle and a cumulative decrease of 18% after two cycles, which was only half of the decrease observed without phenazine (Figure 4.13). Furthermore, the observed CD signal reached a minimum of −12.4 mdeg, which was about 20% lower than without added phenazine. This suggests that the presence of phenazine helped to achieve a more complete oxidation of L-Fc(MeLeu)$_2$ at the working electrode. The cycling times were still very long, with the first oxidation half-cycle taking 74 min, which was slightly more than without phenazine. This is likely a consequence of the electrochemical reactions being limited by the diffusion of reactive species to the working electrode surface, which would not be expected to change significantly with the addition of phenazine at the counter electrode.

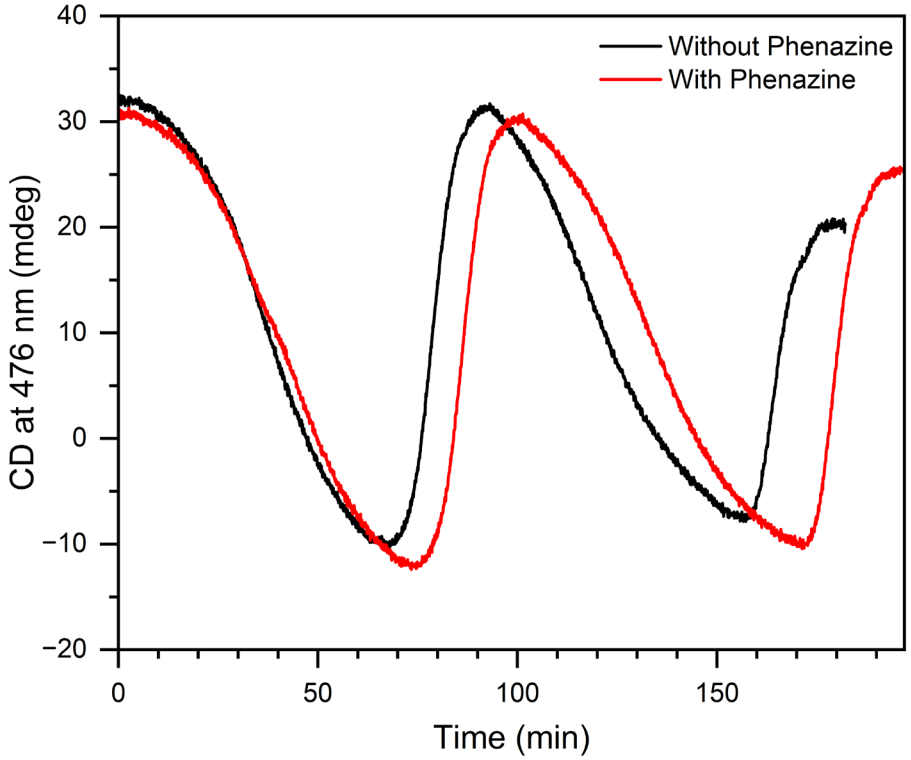

Figure 4.13. CD response of L-Fc(MeLeu)$_2$ at 476 nm during two consecutive oxidation and reduction cycles both with (red) and without (black) added phenazine. For the experiment performed with phenazine, approximately 50 µL of the electrolyte solution containing 100 mM phenazine was added to the frit containing the counter electrode. Data were acquired in DCM with 0.25 M [(n-C_4H_9)$_4$N]PF_6 as supporting electrolyte.

Despite the improved performance with the addition of phenazine, the overall cycling times and reversibility were still relatively poor. A possible reason is that the counter electrode could still be the site of the limiting redox process. The high concentration of phenazine may not have sufficiently compensated for the lower surface area of the counter electrode (wire) versus the working electrode (mesh). Essentially, when an oxidising potential was applied at the working electrode, the number of L-Fc(MeLeu)$_2$ molecules available for oxidation was larger than the corresponding number of phenazine molecules that could be reduced at the counter electrode. To maintain charge balance other species would also need to be reduced; DCM being the most likely candidate as it has a milder reduction potential than [(n-C_4H_9)$_4$N]PF_6. However, the reduction of DCM has been observed to have slow kinetics,[34, 35] especially at platinum electrodes.[36, 37] The proposed mechanism involves the adsorption of DCM and reaction intermediates to the electrode surface, which can inhibit the further reaction of DCM molecules at these sites until the reaction products desorb.[34, 35, 37] Under such a scenario it is possible that the counter electrode would be unable to reach the current density that would otherwise be

attained at the working electrode, thereby artificially lowering the rate of L-Fc(MeLeu)$_2$ oxidation and leading to the observed long cycle times.

It is also likely that some degradation of [L-Fc(MeLeu)$_2$]$^+$ is occurring. Electron-withdrawing substituents – such as the amide groups on [L-Fc(MeLeu)$_2$]$^+$ – are known to destabilise ferrocenium cations.[38-40] This makes them highly susceptible to decomposition from nucleophilic attack by solvents such as water, alcohols, DMF, and DMSO; as well as destruction by chelating ligands such as 2,2′-bipyridine and 1,10-phenanthroline.[39, 41] But the SEC experiments were performed in DCM, so [L-Fc(MeLeu)$_2$]$^+$ should be stable excepting any trace water or oxygen present. However, consider the way in which DMF acts as a nucleophile: through a zwitterionic resonance structure in which a negative charge is localised on the carbonyl oxygen. A similar process could theoretically occur in [L-Fc(MeLeu)$_2$]$^+$, since the very amide substituents which destabilise it will also have a nucleophilic, zwitterionic resonance form. Such a decomposition route would presumably be bimolecular – with self-attack sterically prevented – and therefore depend on the concentration of [L-Fc(MeLeu)$_2$]$^+$. The extent to which these resonance forms dominate in [L-Fc(MeLeu)$_2$]$^+$ is unknown, however the zwitterionic form of amides can be significant contributors, accounting for 28% in acetamide, for example.[42] Regardless, of the exact mechanism of decomposition, the long cycling times provide ample opportunity for degradation of [L-Fc(MeLeu)$_2$]$^+$.

Overall, the relative contributions of limitations at the counter electrode and degradation of L-Fc(MeLeu)$_2$ on the observed cycling behaviour cannot be distinguished. This result underscores the need for a redesigned spectroelectrochemical cell – with ample space for a large surface area counter electrode and dedicated analyte and counter-species half cells separated by an ion-exchange membrane – in order to guarantee that reactions at the counter electrode are not a limiting factor. This would allow for true estimates of the degradation and bulk electrochemical reversibility of a system.

4.4.3 Spectroelectrochemistry of L- and D-Fc(MeLeu)$_2$ in Dilute Solution

A clear way to alleviate the issues with cycling described in the previous section would be to perform the SEC experiments with much lower concentrations of L/D-Fc(MeLeu)$_2$. This was not feasible in the visible range due to the weakness of the parity forbidden transitions in this region. However, ferrocene displays transitions at higher energies which are not forbidden and thus have far larger extinction coefficients, allowing measurement at much lower

concentrations. These experiments were performed in MeCN since the UV cutoff of DCM is too high.

The UV-vis and CD spectra of L/D-Fc(MeLeu)$_2$ acquired in MeCN are shown in Figure 4.14. L-Fc(MeLeu)$_2$ exhibits absorbance bands at 256 nm ($\varepsilon = 9600$ M^{-1}cm^{-1}) and 217 nm ($\varepsilon = 30100$ M^{-1}cm^{-1}). The band at 256 nm is likely a ferrocene-based transition while the band at 217 nm likely contains contributions from the ferrocene core and amino acid arms, which both absorb in this region.[17] The CD spectra display multiple Cotton signals, with the most prominent being at 255 nm and 217 nm. The g_{abs} values are 1.0×10^{-3} at 255 nm and 8.2×10^{-4} at 217 nm, which is roughly one order of magnitude smaller than the g_{abs} of the visible transitions. Once again, D-Fc(MeLeu)$_2$ shows the same absorbance but mirror image CD compared to L-Fc(MeLeu)$_2$.

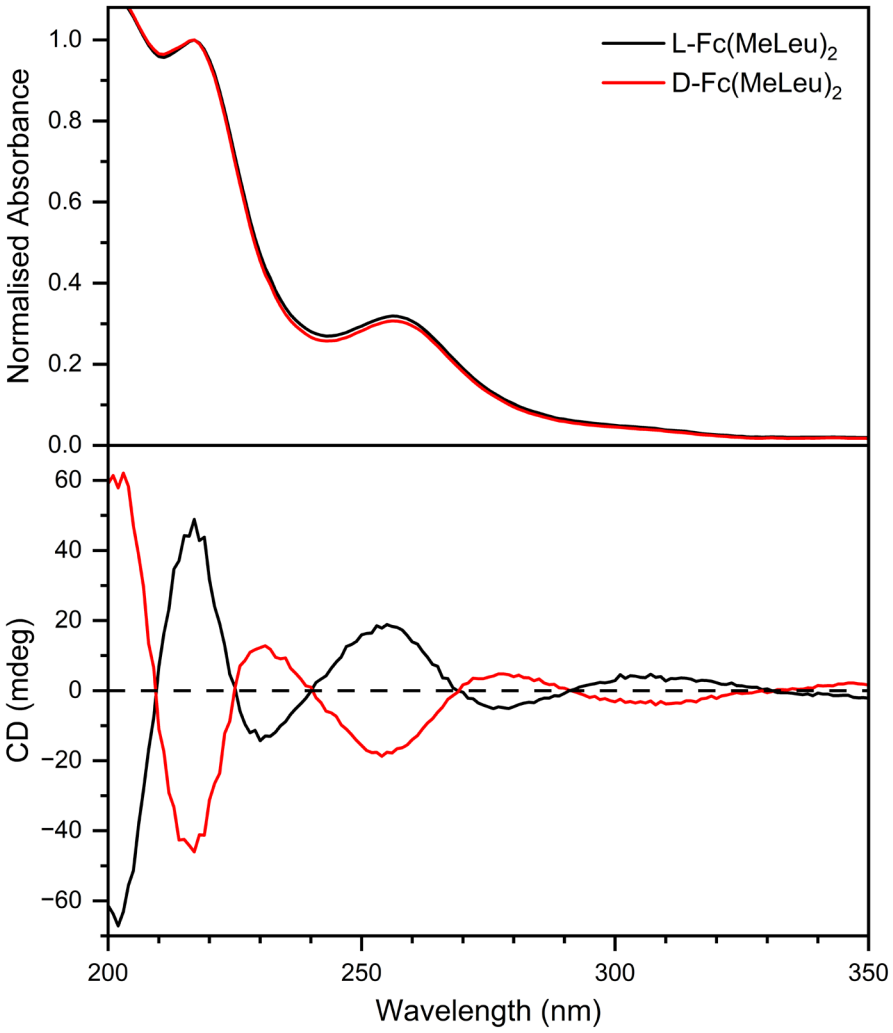

Figure 4.14. Absorbance (normalised to the peak at 217 nm; top) and CD (bottom) of L-Fc(MeLeu)$_2$ (black) and D-Fc(MeLeu)$_2$ (red) in MeCN. Sample concentrations were 60 μM.

With the basic chiroptical properties of L/D-Fc(MeLeu)$_2$ in this spectral region understood, their UV-vis and CD SEC are now discussed. As L-Fc(MeLeu)$_2$ was oxidised, the absorbance

band at 217 nm was diminished while two new bands appeared at 303 nm (ε = 7440 $M^{-1}cm^{-1}$) and 264 nm (ε = 11500 $M^{-1}cm^{-1}$), as shown in Figure 4.15a. Both of these bands can be assigned to LMCT transitions of the ferrocenium core.[17] The CD SEC of L-Fc(MeLeu)$_2$ was characterised by a reversal of handedness in the 275–330 nm range and a general diminishing of chirality elsewhere (Figure 4.15a). The CD spectrum of [L-Fc(MeLeu)$_2$]$^+$ shows one major Cotton signal at 211 nm which has a g_{abs} of 6.4 × 10^{-4}. This indicates that the intrinsic chirality of [L-Fc(MeLeu)$_2$]$^+$ is also lower than that of L-Fc(MeLeu)$_2$ in the higher energy regime as well. The largest Δg_{abs} was 2.5 × 10^{-3} at 317 nm.

Reduction of [L-Fc(MeLeu)$_2$]$^+$ restored the original spectra in both UV-vis and CD, confirming that L-Fc(MeLeu)$_2$ can also act as a chiroptical switch at these wavelengths (Figure 4.15b). The spectra of L-Fc(MeLeu)$_2$ and [L-Fc(MeLeu)$_2$]$^+$ show major differences, with 254 and 217 nm being the best wavelengths to monitor chiroptical switching. The difference in measured CD was slightly larger at 217 nm, thus this wavelength was chosen as the readout for cycling experiments. The UV-vis and CD SEC of D-Fc(MeLeu)$_2$ are comparable to that for L-Fc(MeLeu)$_2$ and are presented in Figure B6.

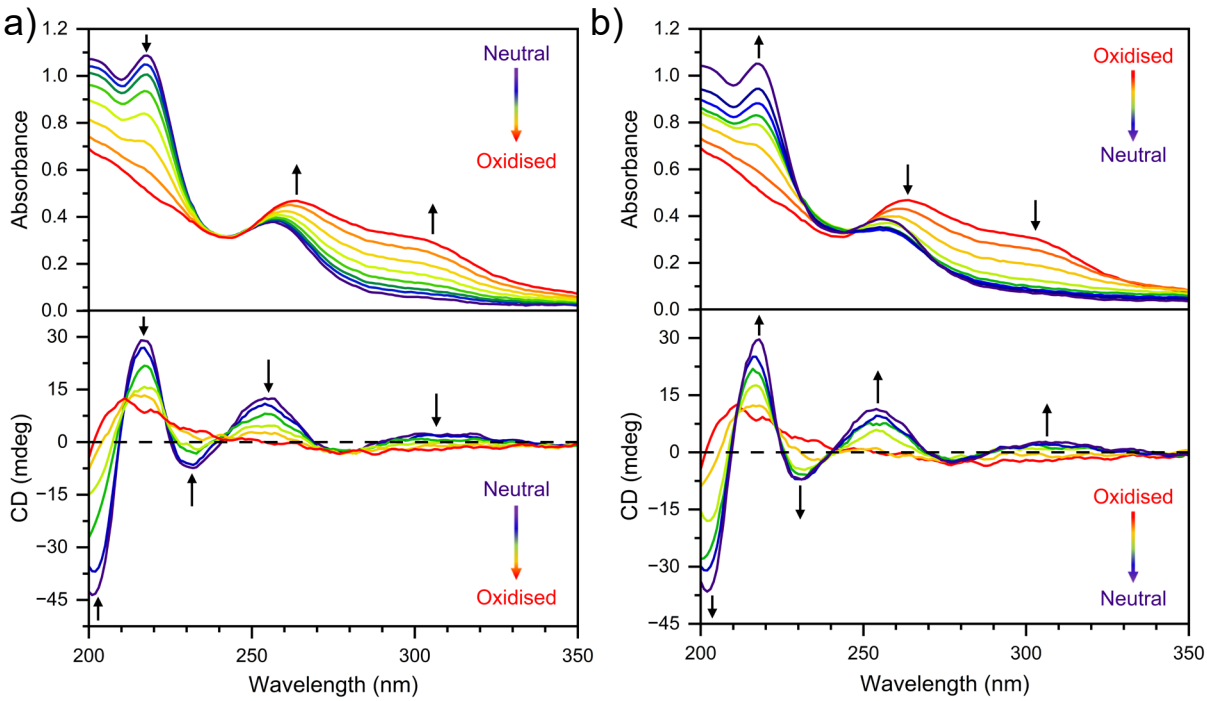

Figure 4.15. (a) UV-vis (top) and CD (bottom) spectra of L-Fc(MeLeu)$_2$ during oxidation to the ferrocenium species over a 45 min time interval. (b) UV-vis (top) and CD (bottom) spectra of L-Fc(MeLeu)$_2$ during subsequent reduction from the ferrocenium to neutral state over a 100 min time interval. The concentration of L-Fc(MeLeu)$_2$ was approximately 0.6 mM. Spectra were acquired in MeCN with 0.25 M [(n-C_4H_9)$_4$N]PF_6 as supporting electrolyte.

Given the much lower concentration of L-Fc(MeLeu)$_2$ in these experiments, it was envisioned that repeated cycling would be more successful. This hypothesis was confirmed, with chiroptical switching of L-Fc(MeLeu)$_2$ successfully demonstrated over 10 successive oxidation and reduction cycles at 217 nm (Figure 4.16). The switching times were also much faster, with oxidation and reduction half-cycles each taking around 3–5 min. The CD intensity showed an initial drop of 37% after the first cycle, however the next 9 cycles only displayed a cumulative decrease of 10%. This is quite similar to the behaviour of (*S*/*R*)-BNI observed in Chapter 3, in which a large initial loss of reversibility is followed by good reversibility in the subsequent cycles. Regardless of the initial reduction of signal intensity, the neutral and oxidised states remained easily distinguishable after 10 cycles, indicating that L-Fc(MeLeu)$_2$ performs well as a redox-modulated chiroptical switch under these conditions. This result was replicated with D-Fc(MeLeu)$_2$ over the same number of cycles (Figure B7).

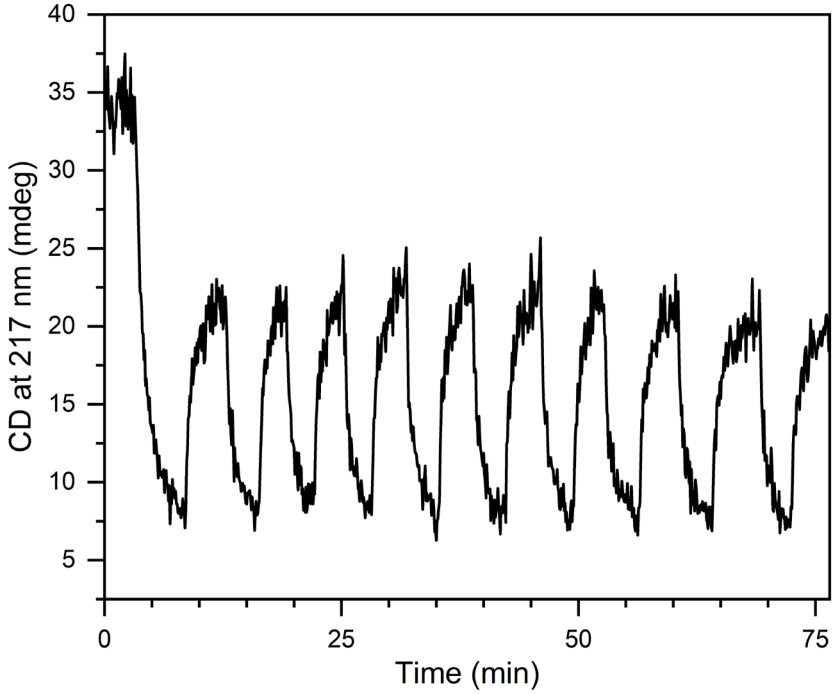

Figure 4.16. CD response of L-Fc(MeLeu)$_2$ at 217 nm during ten consecutive oxidation and reduction cycles. The concentration of L-Fc(MeLeu)$_2$ was approximately 0.7 mM. Data was acquired in MeCN with 0.25 M [(n-C_4H_9)$_4$N]PF_6 as supporting electrolyte.

The improvement in kinetics and reversibility is attributed to the lower concentration of L/D-Fc(MeLeu)$_2$. Firstly, a lower concentration of L/D-Fc(MeLeu)$_2$ means a lower current density flowing through the circuit. Therefore, the required rate of reduction/oxidation of the solvent or electrolyte needed to maintain charge balance at the counter electrode is significantly lower and can be maintained by the counter electrode, despite its smaller surface area. Additionally,

if the degradation of [L/D-Fc(MeLeu)$_2$]$^+$ is indeed a bimolecular decomposition, then this would be significantly suppressed at lower concentrations as the chance of two [L/D-Fc(MeLeu)$_2$]$^+$ molecules colliding is much lower. Furthermore, shorter cycle times mean that there will be much less degradation of [L/D-Fc(MeLeu)$_2$]$^+$ per cycle. The combination of these effects results in an overall much lower decomposition rate, as evidenced by the good stability of the last 9 cycles.

4.5 Magneto-Optical Properties of L- and D-Fc(MeLeu)$_2$

The magneto-optical properties of L/D-Fc(MeLeu)$_2$ were investigated using MCD spectroscopy. The MCD$_{N\rightarrow S}$ spectra of L-Fc(MeLeu)$_2$ in toluene show two main absorbance-like peaks at 357 and 304 nm (Figure 4.17a). There is also a very weak MCD signal in the 430–530 nm region with a derivative-like shape and peaks at 456 and 497 nm (Figure 4.17b). In order to exhibit MCD A or C terms, a molecule must have either a three-fold or higher rotational symmetry or be paramagnetic.[43-45] Since L-Fc(MeLeu)$_2$ fulfills neither of these criteria, all the observed bands can be assigned to MCD B terms that result from electronic mixing of states. The magnetic field normalised MCD dissymmetry factors, g_{MCD}, were 3.3×10^{-4} at 357 nm and 2.8×10^{-4} at 304 nm. In the visible region, the g_{MCD} values were -1.1×10^{-4} at 456 nm and 2.5×10^{-4} at 497 nm. These values are several orders of magnitude smaller than what has been observed in some metal complexes,[46-48] however other d^6 metal complexes have also shown weaker MCD.[49] These results show how magnetic field could also be employed as a stimulus for chiroptical switching since the MCD signal increases in intensity as the strength of the magnetic field is increased and changes sign with reversal of the magnetic field polarity. Analogous results were obtained for D-Fc(MeLeu)$_2$ (Figure B8).

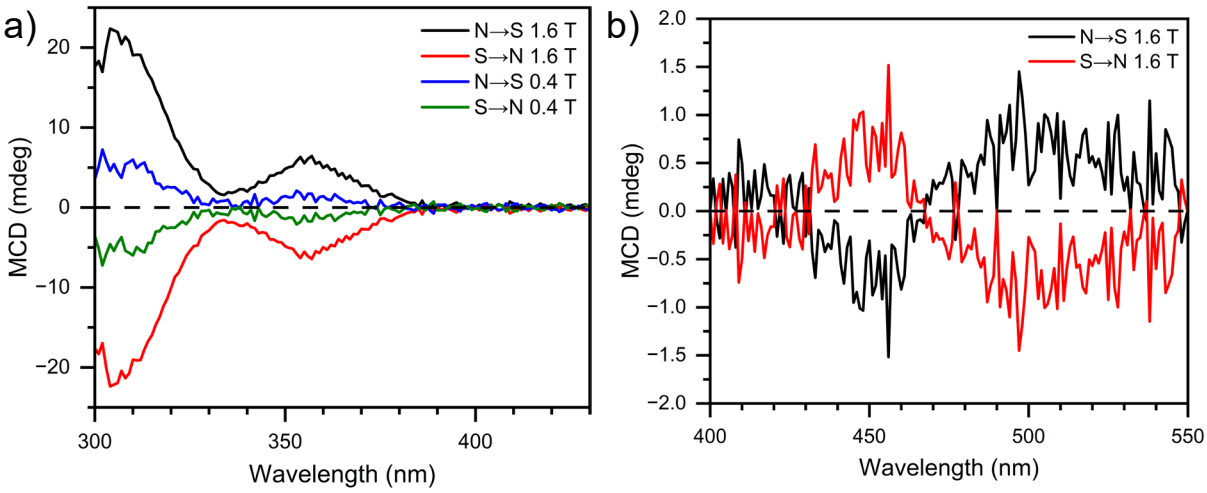

Figure 4.17. (a) MCD spectra of L-Fc(MeLeu)$_2$ in toluene with different magnetic field strengths and orientations. (b) The weak MCD peaks in the visible range. Sample concentration was 2.5 mM.

To see if the magneto-optical properties of L/D-Fc(MeLeu)$_2$ were solvent dependent, MCD was also performed in MeCN. Comparing the MCD$_{N\rightarrow S}$ spectra in the two solvents, it is evident that the spectral shape is the same, although the intensity is slightly lower in MeCN (Figure 4.18). The values of g_{MCD} were 2.4×10^{-4} at 357 nm and 2.2×10^{-4} at 304 nm in MeCN. The intensity of MCD B-terms are inversely proportional to the energy gap between the intermixing electronic states.[44, 50] Therefore, the lower MCD intensity in MeCN suggests that the energy gap between the mixing states is slightly larger than in toluene.

The presence of both CD and MCD means that L/D-Fc(MeLeu)$_2$ will display MChD, provided the MChD intensity is strong enough to be detected. The strength of MChD for L/D-Fc(MeLeu)$_2$ was estimated as the product of CD and MCD as follows: $g_{MChD} \approx g_{abs} \times g_{MCD}$.[51, 52] With a magnitude in the 10^{-6} range, the estimated MChD strength of L/D-Fc(MeLeu)$_2$ was roughly four times as large as for (*S*)-BNI. However, the MChD response of L/D-Fc(MeLeu)$_2$ was still too low to be detected.

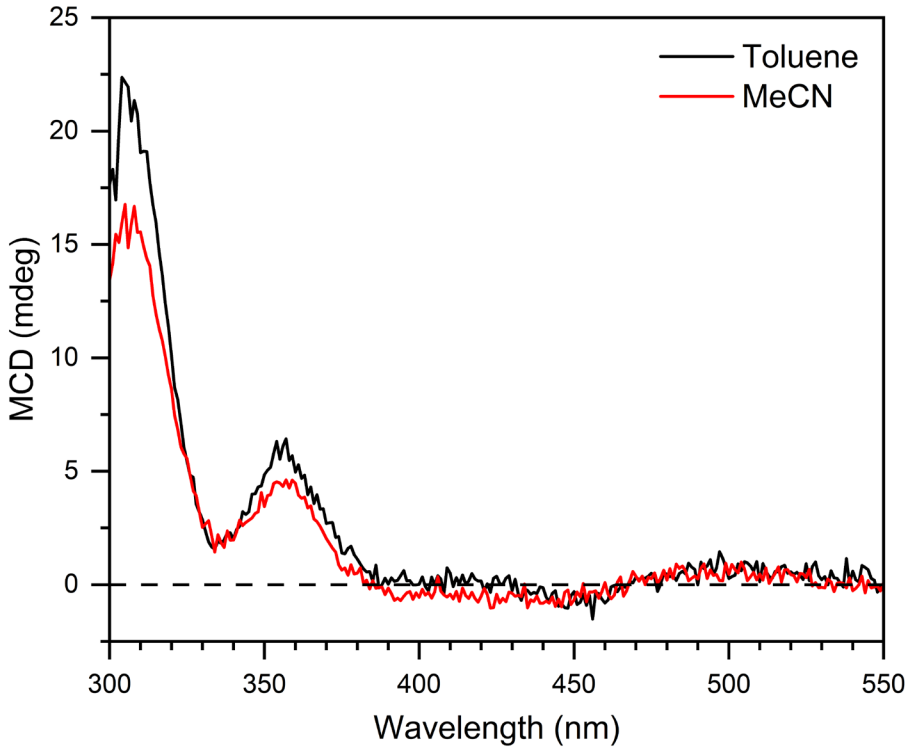

Figure 4.18. $MCD_{N\rightarrow S}$ spectra of L-Fc(MeLeu)$_2$ in toluene (black) and MeCN (red) acquired at a magnetic field strength of 1.6 T. Sample concentrations were 2.5 mM.

4.6 L- and D-Fc(MeLeu)$_2$ Thin Films

To explore the solid-state behaviour of L/D-Fc(MeLeu)$_2$, thin films were prepared by spin-coating from chloroform solution onto quartz slides. The UV-vis and CD spectra of L/D-Fc(MeLeu)$_2$ thin films are shown in Figure 4.19. The absorbance spectrum of the L-Fc(MeLeu)$_2$ thin film was essentially identical to the spectrum in MeCN solution, with both absorbance peaks redshifted by 2 nm – to 258 and 219 nm – in the solid-state (Figure 4.20). The CD of the film also closely matched the solution spectrum and displayed a similarly small redshift, with Cotton signals at 309, 256, and 218 nm. Additionally, a peak corresponding to the main d–d transition is observed centred around ~487 nm. The thin film of L-Fc(MeLeu)$_2$ had g_{abs} of 1.94×10^{-3} at 309 nm, which was ~5% smaller than in MeCN solution. The g_{abs} of the peak at 487 nm could not be precisely calculated due to poor signal-to-noise but was approximately 3×10^{-3}, also smaller than in solution.

There are numerous crystal structures of other ferrocene bis(amino acid) compounds in which all the molecules adopt the Herrick conformation in the solid state.[6, 8, 31, 53] It was therefore expected that the thin films of L/D-Fc(MeLeu)$_2$ would show larger g_{abs} than their solution-state counterparts, with the presumption that the intramolecular hydrogen bonds would become

locked into place as the film solidified. That this was not observed suggests that the rapid precipitation of L/D-Fc(MeLeu)$_2$ during spin-coating led to an amorphous structure in which not all molecules were able to adopt a hydrogen bonded Herrick conformation.

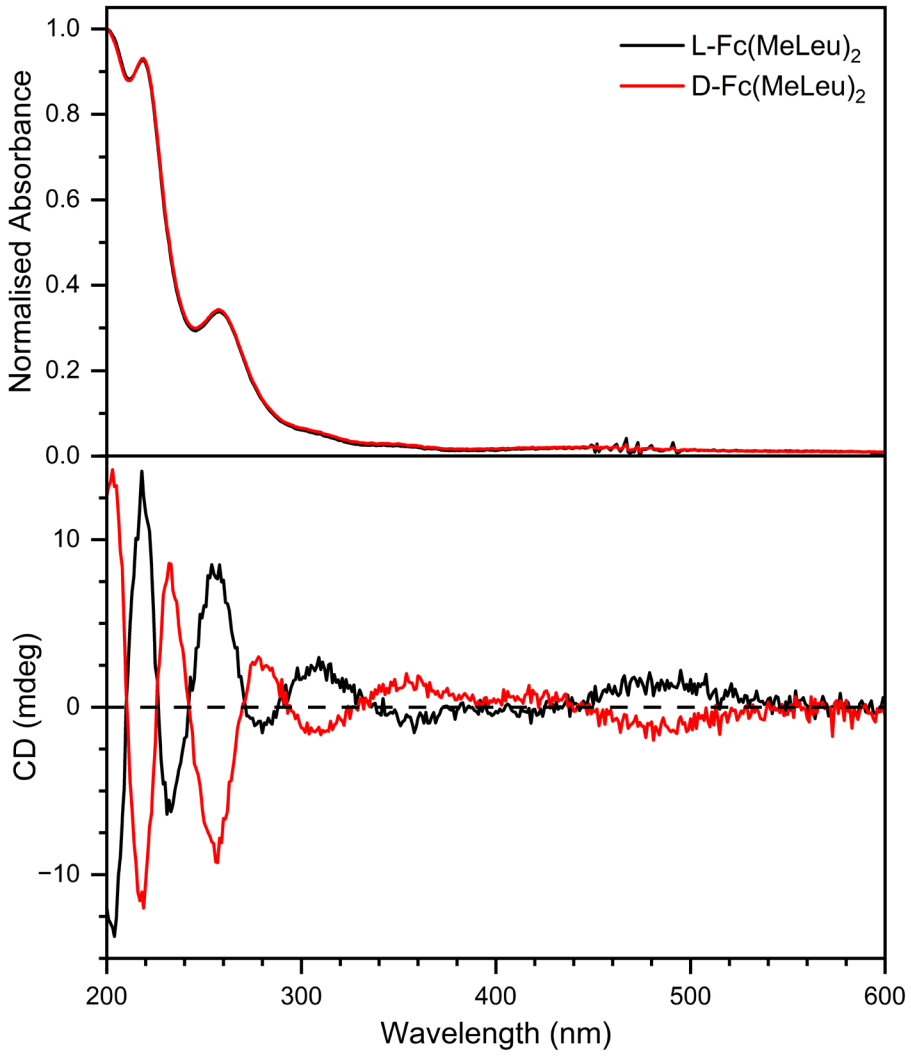

Figure 4.19. Normalised absorbance (top) and CD (bottom) of L-Fc(MeLeu)$_2$ (black) and D-Fc(MeLeu)$_2$ (red) thin films.

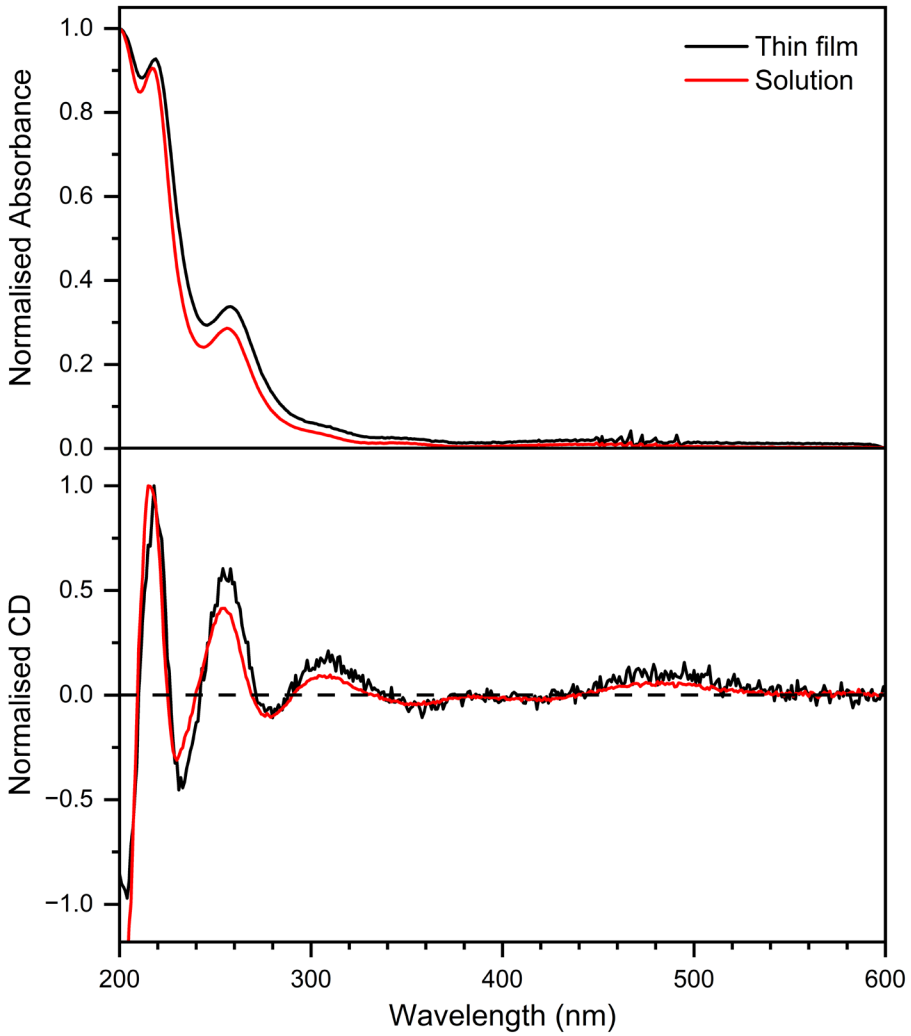

Figure 4.20. Normalised absorbance (top) and CD (bottom) of L-Fc(MeLeu)$_2$ thin film (black) and in 65 μM MeCN solution (red).

4.7 Conclusions

To summarise, this chapter successfully demonstrates temperature- and redox-modulated dual-responsive chiroptical switching in a pair of enantiomers, L/D-Fc(MeLeu)$_2$, constructed from a ferrocene core substituted with methyl ester-protected leucine groups via an amide linkage. The chirality of L/D-Fc(MeLeu)$_2$ – which derives from intramolecular hydrogen bonding – was found to be solvent-dependent, with more polar solvents promoting weaker chiroptical responses. The chiroptical properties of L/D-Fc(MeLeu)$_2$ thin films closely aligned with solution state measurements, albeit with a slightly weaker response, suggesting that an enhancement in intramolecular hydrogen bonding was not attained in a solvent-free environment – at least during rapid solidification. Temperature was also used to influence the intramolecular hydrogen bonds in L/D-Fc(MeLeu)$_2$, with the CD strength found to vary

linearly – and reversibly – with temperature. This behaviour was observed in both toluene and DMF, with the percentage change in CD intensity greater in the more polar DMF.

The redox-active ferrocene core was also harnessed to facilitate chiroptical switching in L/D-Fc(MeLeu)$_2$. Oxidation to the ferrocenium species, [L/D-Fc(MeLeu)$_2$]$^+$, produced large spectral changes, as determined by UV-vis and CD SEC experiments. Interestingly, the reversibility and kinetics of this switching was found to be better at lower concentrations of L/D-Fc(MeLeu)$_2$. This was likely due to the limited ability of the counter electrode to sustain a sufficient current density needed for charge balance, an effect that would be expected to be worse at higher concentrations. Attempts to overcome this problem by addition of phenazine as a redox counter-species were largely unsuccessful. Decomposition of [L/D-Fc(MeLeu)$_2$]$^+$ was also possible and a potential bimolecular decomposition pathway was outlined, although further experiments would be needed to reach a more definitive understanding.

Throughout Chapters 3 and 4, we have now seen how molecular systems can be used to construct stable, reversible, and sensitive chiroptical switches. However, there is also value in developing chiroptical switches based on framework materials such as chiral MOFs. For example, the ordered arrangement of these materials can lead to cooperative interactions between chromophores which may greatly enhance the chiroptical response. Additionally, chiral pore spaces can be harnessed for chirality transfer to an achiral guest. To explore framework materials in greater depth, the focus of the following chapter with thus shift to chiral MOFs.

4.8 Future Work

There are many directions for future work to explore. An obvious extension of this project would be to perform VT SEC experiments to investigate the temperature-dependent chiroptical response of the ferrocenium states. This is important because simultaneous control of both stimuli is essential for the operation of molecular logic gates. There would presumably be a decrease in the intensity of the CD response for [L/D-Fc(MeLeu)$_2$]$^+$ as the temperature increased, analogous to what was observed for L/D-Fc(MeLeu)$_2$. However, given the stability issues observed for [L-Fc(MeLeu)$_2$]$^+$ at room temperature, it would be useful to get an insight into decomposition rates at elevated temperatures.

A more complete understanding of the magneto-optical properties of L/D-Fc(MeLeu)$_2$ could be gained through MCD measurements of the oxidised states. Ferrocenium cations are low-

spin d^5 complexes, containing one unpaired electron.[54] Therefore, in the presence of a magnetic field, there will be a ground state degeneracy and MCD C terms would be observed. MCD C terms are temperature-dependent because the relative populations of the two degenerate ground states depends on the amount of thermal energy.[44, 50, 55] VT SEC experiments would thus allow modulation of both the chiroptical and magnetic-optical properties of L/D-Fc(MeLeu)$_2$. Additionally, MCD C terms typically have greater intensity compared to A and B terms (even at room temperature),[44, 50, 55, 56] hence the expected strength of MChD would be larger for [L/D-Fc(MeLeu)$_2$]$^+$ than for L/D-Fc(MeLeu)$_2$ and could potentially be intense enough to detect. Moreover, the applied magnetic field itself could be used as a stimulus for chiroptical switching. This would be best pursued using an electromagnet as the magnetic field strength and polarity can be easily varied. This would enable chiroptical switching with three different stimuli (temperature, electric potential, and magnetic field), an exceptionally rare feat.

There is also potential to functionalise L/D-Fc(MeLeu)$_2$ through further reaction at the amino acid carboxyl sites. This would first require a deprotection step to remove the ester, allowing a range of subsequent reactions to be conducted. One strategy would be to design a fluorophore with an amine or hydroxy group and attach it to the amino acid carboxylic acids via an amide or ester linkage. The fluorophores would thus be held in a chiral orientation and could exhibit circularly polarised luminescence (CPL). However, ferrocene is known to quench fluorescence, through either photo-induced electron transfer (PET) or energy transfer, depending on the nature of the fluorophore and the nature of their covalent linkage.[57-60] Oxidation to ferrocenium should deactivate these quenching mechanisms. For PET this is because the electron-donating ability of ferrocenium is much less than that of ferrocene. For energy transfer this occurs when the spectral overlap of the fluorophore with ferrocenium is much less than with ferrocene. Therefore, the observed fluorescence (and CPL) intensity and quantum yields should depend strongly on the oxidation state of ferrocene core and could be monitored spectroelectrochemically. The switching of fluorescence intensity by oxidation of a ferrocene moiety covalently tethered to a fluorophore has been demonstrated multiple times,[58, 60-62] providing a solid proof-of-concept for this approach. Though to date this strategy has yet to be extended to chiral systems for the electrochemical modulation of CPL.

Preliminary work in this direction has already been made, with the synthesis of the fluorophore 2-(4-aminophenyl)benzothiazole (Figure 4.21). Deprotection of L/D-Fc(MeLeu)$_2$ and the coupling of the fluorophore still need to be undertaken to obtain the final product. A benzothiazole-based fluorophore was selected as they are known to be highly fluorescent and

have good photostability.[63, 64] The fluorescence spectra of 2-(4-aminophenyl)benzothiazole are presented in Figure B9 and confirm its luminescent properties. Notably, the fluorescence of 2-(4-aminophenyl)benzothiazole shows an emission maximum at 402 nm and there is virtually no overlap with the main ferrocenium absorbance peak of $[L\text{-}Fc(MeLeu)_2]^+$ at 656 nm. This is important because if the emission did overlap with the ferrocenium absorbance then energy transfer could still occur and the desired fluorescence enhancement would be diminished.

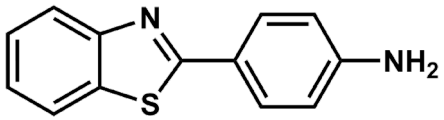

Figure 4.21. Structure of 2-(4-aminophenyl)benzothiazole.

4.9 References

(1) de Silva, A. P.; McClenaghan, N. D. Molecular-Scale Logic Gates. *Chem. Eur. J.* **2004**, *10*, 574-586.
(2) Erbas-Cakmak, S.; Kolemen, S.; Sedgwick, A. C.; Gunnlaugsson, T.; James, T. D.; Yoon, J.; Akkaya, E. U. Molecular logic gates: the past, present and future. *Chem. Soc. Rev.* **2018**, *47*, 2228-2248.
(3) Herrick, R. S.; Jarret, R. M.; Curran, T. P.; Dragoli, D. R.; Flaherty, M. B.; Lindyberg, S. E.; Slate, R. A.; Thornton, L. C. Ordered conformations in bis(amino acid) derivatives of 1,1′-ferrocenedicarboxylic acid. *Tetrahedron Lett.* **1996**, *37*, 5289-5292.
(4) Adhikari, B.; Afrasiabi, R.; Kraatz, H.-B. Ferrocene–Tryptophan Conjugate: An Example of a Redox-Controlled Reversible Supramolecular Nanofiber Network. *Organometallics* **2013**, *32*, 5899-5905.
(5) Adhikari, B.; Lough, A. J.; Barker, B.; Shah, A.; Xiang, C.; Kraatz, H.-B. Bis-amino Acid Derivatives of 1,1′-Ferrocenedicarboxylic Acid: Structural, Electrochemical, and Metal Ion Binding Studies. *Organometallics* **2014**, *33*, 4873-4887.
(6) Liu, B.; Hao, A.; Xing, P. Water-Mediated Folding Behaviors and Chiroptical Inversion of Ferrocene-Conjugated Dipeptides. *J. Phys. Chem. Lett.* **2021**, *12*, 6190-6196.
(7) Moriuchi, T. Helical Chirality of Ferrocene Moieties in Cyclic Ferrocene-Peptide Conjugates. *Eur. J. Inorg. Chem.* **2022**, *2022*, e202100902.
(8) Zong, Z.; Cao, Z.; Hao, A.; Xing, P. Dynamic axial chirality of ferrocene diamino acids: hydration effects and chiroptical applications. *J. Mater. Chem. C* **2021**, *9*, 12191-12200.
(9) van Staveren, D. R.; Weyhermüller, T.; Metzler-Nolte, N. Organometallic β-turn mimetics. A structural and spectroscopic study of inter-strand hydrogen bonding in ferrocene and cobaltocenium conjugates of amino acids and dipeptides. *Dalton Trans.* **2003**, 210-220.
(10) Xu, Y.; Saweczko, P.; Kraatz, H.-B. 1,1′-Ferrocenoyl–oligoprolines. A synthetic, structural and electrochemical study. *J. Organomet. Chem.* **2001**, *637-639*, 335-342.
(11) Kirin, S. I.; Kraatz, H.-B.; Metzler-Nolte, N. Systematizing structural motifs and nomenclature in 1,n′-disubstituted ferrocene peptides. *Chem. Soc. Rev.* **2006**, *35*, 348-354.
(12) van Staveren, D. R.; Metzler-Nolte, N. Bioorganometallic Chemistry of Ferrocene. *Chem. Rev.* **2004**, *104*, 5931-5986.
(13) Gagne, R. R.; Koval, C. A.; Lisensky, G. C. Ferrocene as an internal standard for electrochemical measurements. *lnorg. Chem.* **1980**, *19*, 2854-2855.

(14) Han, G.-C.; Ferranco, A.; Feng, X.-Z.; Chen, Z.; Kraatz, H.-B. Synthesis, Characterization of Some Ferrocenoyl Cysteine and Histidine Conjugates, and Their Interactions with Some Metal Ions. *Eur. J. Inorg. Chem.* **2014**, *2014*, 5337-5347.
(15) Qing, G.-Y.; Sun, T.-L.; Wang, F.; He, Y.-B.; Yang, X. Chromogenic Chemosensors for N-Acetylaspartate Based on Chiral Ferrocene-Bearing Thiourea Derivatives. *Eur. J. Org. Chem.* **2009**, *2009*, 841-849.
(16) Duhović, S.; Diaconescu, P. L. An experimental and computational study of 1,1′-ferrocene diamines. *Polyhedron* **2013**, *52*, 377-388.
(17) Gray, H. B.; Sohn, Y. S.; Hendrickson, N. Electronic structure of metallocenes. *J. Am. Chem. Soc.* **1971**, *93*, 3603-3612.
(18) Paul, A.; Borrelli, R.; Bouyanfif, H.; Gottis, S.; Sauvage, F. Tunable Redox Potential, Optical Properties, and Enhanced Stability of Modified Ferrocene-Based Complexes. *ACS Omega* **2019**, *4*, 14780-14789.
(19) Kirin, S. I.; Schatzschneider, U.; de Hatten, X.; Weyhermüller, T.; Metzler-Nolte, N. 1,n′-Disubstituted ferrocenoyl amino acids and dipeptides: Conformational analysis by CD spectroscopy, X-ray crystallography, and DFT calculations. *J. Organomet. Chem.* **2006**, *691*, 3451-3457.
(20) Snyder, L. R. Classification off the Solvent Properties of Common Liquids. *J. Chromatogr. Sci.* **1978**, *16*, 223-234.
(21) Reichardt, C. Empirical Parameters of Solvent Polarity as Linear Free-Energy Relationships. *Angew. Chem. Int. Ed. Engl.* **1979**, *18*, 98-110.
(22) Abraham, M. H. Scales of solute hydrogen-bonding: their construction and application to physicochemical and biochemical processes. *Chem. Soc. Rev.* **1993**, *22*, 73-83.
(23) Lakhwani, G.; Gielen, J.; Kemerink, M.; Christianen, P. C. M.; Janssen, R. A. J.; Meskers, S. C. J. Intensive Chiroptical Properties of Chiral Polyfluorenes Associated with Fibril Formation. *J. Phys. Chem. B* **2009**, *113*, 14047-14051.
(24) Lakhwani, G.; Meskers, S. C. J. Insights from Chiral Polyfluorene on the Unification of Molecular Exciton and Cholesteric Liquid Crystal Theories for Chiroptical Phenomena. *J. Phys. Chem. A* **2012**, *116*, 1121-1128.
(25) Adhikari, B.; Singh, C.; Shah, A.; Lough, A. J.; Kraatz, H.-B. Amino Acid Chirality and Ferrocene Conformation Guided Self-Assembly and Gelation of Ferrocene–Peptide Conjugates. *Chem. Eur. J.* **2015**, *21*, 11560-11572.
(26) Khan, F. S. T.; Waldbusser, A. L.; Carrasco, M. C.; Pourhadi, H.; Hematian, S. Synthetic, spectroscopic, structural, and electrochemical investigations of ferricenium derivatives with weakly coordinating anions: ion pairing, substituent, and solvent effects. *Dalton Trans.* **2021**, *50*, 7433-7455.
(27) Nie, Z.; Nijhuis, C. A.; Gong, J.; Chen, X.; Kumachev, A.; Martinez, A. W.; Narovlyansky, M.; Whitesides, G. M. Electrochemical sensing in paper-based microfluidic devices. *Lab Chip* **2010**, *10*, 477-483.
(28) Tsierkezos, N. G. Cyclic Voltammetric Studies of Ferrocene in Nonaqueous Solvents in the Temperature Range from 248.15 to 298.15 K. *J. Solution Chem.* **2007**, *36*, 289-302.
(29) Prins, R. Visible absorption spectra of substituted ferricenium cations. *J. Chem. Soc. D* **1970**, 280b-281.
(30) Swearingen, C.; Wu, J.; Stucki, J.; Fitch, A. Use of Ferrocenyl Surfactants of Varying Chain Lengths To Study Electron Transfer Reactions in Native Montmorillonite Clay. *Environ. Sci. Technol.* **2004**, *38*, 5598-5603.
(31) Nomoto, A.; Moriuchi, T.; Yamazaki, S.; Ogawa, A.; Hirao, T. A highly ordered ferrocene system regulated by podand peptide chains. *Chem. Commun.* **1998**, 1963-1964.
(32) Mugnier, Y.; Roullier, L.; Laviron, E. Reduction mechanism of phenazine in tetrahydrofuran. Influence of added proton donors. *Electrochim. Acta* **1991**, *36*, 803-809.

(33) Wenger, S. R.; D'Alessandro, D. M. Improving the Sustainability of Electrochemical Direct Air Capture in a 3D Printed Redox Flow Cell. *ACS Sustainable Chem. Eng.* **2024**, *12*, 4789-4794.
(34) Horányi, G.; Torkos, K. Electrocatalytic reduction of some halogenated derivatives of methane and acetic acid at a platinized platinum electrode in acid medium. *J. Electroanal. Chem. Interfacial Electrochem.* **1982**, *140*, 329-346.
(35) Muftikian, R.; Fernando, Q.; Korte, N. A method for the rapid dechlorination of low molecular weight chlorinated hydrocarbons in water. *Water Res.* **1995**, *29*, 2434-2439.
(36) Kotsinaris, A.; Kyriacou, G.; Lambrou, C. H. Electrochemical reduction of dichloromethane to higher hydrocarbons. *J. Appl. Electrochem.* **1998**, *28*, 613-616.
(37) Sonoyama, N.; Ezaki, K.; Sakata, T. Continuous electrochemical decomposition of dichloromethane in aqueous solution using various column electrodes. *Adv. Environ. Res.* **2001**, *6*, 1-8.
(38) Huang, W. H.; Jwo, J.-J. Kinetics of the Decomposition of Ferrocenium Ion and Its Derivatives. *J. Chin. Chem. Soc.* **1991**, *38*, 343-350.
(39) Khobragade, D. A.; Mahamulkar, S. G.; Pospíšil, L.; Císařová, I.; Rulíšek, L.; Jahn, U. Acceptor-Substituted Ferrocenium Salts as Strong, Single-Electron Oxidants: Synthesis, Electrochemistry, Theoretical Investigations, and Initial Synthetic Application. *Chem. Eur. J.* **2012**, *18*, 12267-12277.
(40) Prins, R. Electronic structure of the ferricenium cation. *Mol. Phys.* **1970**, *19*, 603-620.
(41) Prins, R.; Korswagen, A. R.; Kortbeek, A. G. T. G. Decomposition of the ferricenium cation by nucleophilic reagents. *J. Organomet. Chem.* **1972**, *39*, 335-344.
(42) Kemnitz, C. R.; Loewen, M. J. "Amide Resonance" Correlates with a Breadth of C−N Rotation Barriers. *J. Am. Chem. Soc.* **2007**, *129*, 2521-2528.
(43) Gabbani, A.; Taddeucci, A.; Bertuolo, M.; Pineider, F.; Aronica, L. A.; Di Bari, L.; Pescitelli, G.; Zinna, F. Magnetic Circular Dichroism Elucidates Molecular Interactions in Aggregated Chiral Organic Materials. *Angew. Chem. Int. Ed.* **2024**, *63*, e202313315.
(44) Kobayashi, N.; Muranaka, A.; Mack, J. Theory of Optical Spectroscopy. In *Circular Dichroism and Magnetic Circular Dichroism Spectroscopy for Organic Chemists*, The Royal Society of Chemistry, 2012; pp 1-41.
(45) Sharma, A.; Wojciechowski, J. P.; Liu, Y.; Pelras, T.; Wallace, C. M.; Müllner, M.; Widmer-Cooper, A.; Thordarson, P.; Lakhwani, G. The Role of Fiber Agglomeration in Formation of Perylene-Based Fiber Networks. *Cell Rep. Phys. Sci.* **2020**, *1*, 100148.
(46) Cahya Adi, L.; Willis, O. G.; Gabbani, A.; Rikken, G. L. J. A.; Di Bari, L.; Train, C.; Pineider, F.; Zinna, F.; Atzori, M. Magneto-Chiral Dichroism of Chiral Lanthanide Complexes in the Context of Richardson's Theory of Optical Activity. *Angew. Chem. Int. Ed.* **2024**, *63*, e202412521.
(47) Lu, H.; Qi, F.; Wang, H.; He, T.; Sun, B.; Gao, X.; Comstock, A. H.; Gull, S.; Zhang, Y.; Qiao, T.; et al. Strong Magneto-Chiroptical Effects through Introducing Chiral Transition-Metal Complex Cations to Lead Halide. *Angew. Chem. Int. Ed.* **2024**, e202415363.
(48) Raupach, E.; Rikken, G. L. J. A.; Train, C.; Malézieux, B. Modelling of magneto-chiral enantioselective photochemistry. *Chem. Phys.* **2000**, *261*, 373-380.
(49) McCaffery, A. J.; Stephens, P. J.; Schatz, P. N. Magnetic optical activity of d→d transitions. Octahedral chromium (III), cobalt (III), cobalt (II), nickel (II), and manganese (II) complexes. *lnorg. Chem.* **1967**, *6*, 1614-1625.
(50) Mason, W. R. Theoretical Framework: Definition of MCD Terms. In *A practical guide to magnetic circular dichroism spectroscopy*, John Wiley & Sons, 2007; pp 14-35.
(51) Atzori, M.; Rikken, G. L. J. A.; Train, C. Magneto-Chiral Dichroism: A Playground for Molecular Chemists. *Chem. Eur. J.* **2020**, *26*, 9784-9791.

(52) Ishii, K.; Hattori, S.; Kitagawa, Y. Recent advances in studies on the magneto-chiral dichroism of organic compounds. *Photochem. Photobiol. Sci.* **2020**, *19*, 9-19.
(53) Ferranco, A.; Basak, S.; Lough, A.; Kraatz, H.-B. Metal coordination of ferrocene–histidine conjugates. *Dalton Trans.* **2017**, *46*, 4844-4859.
(54) Toma, Š.; Šebesta, R. Applications of Ferrocenium Salts in Organic Synthesis. *Synthesis* **2015**, *47*, 1683-1695.
(55) Wolford, N. J.; Radovic, A.; Neidig, M. L. C-Term magnetic circular dichroism (MCD) spectroscopy in paramagnetic transition metal and f-element organometallic chemistry. *Dalton Trans.* **2021**, *50*, 416-428.
(56) Buckingham, A. D.; Stephens, P. J. Magnetic Optical Activity. *Annu. Rev. Phys. Chem.* **1966**, *17*, 399-432.
(57) Fery-Forgues, S.; Delavaux-Nicot, B.; Lavabre, D.; Rurack, K. Intermolecular quenching of excited singlet states by ferrocenyl derivatives: study with ketocyanine dyes. *J. Photochem. Photobiol., A* **2003**, *155*, 107-114.
(58) Gan, J.; Tian, H.; Wang, Z.; Chen, K.; Hill, J.; Lane, P. A.; Rahn, M. D.; Fox, A. M.; Bradley, D. D. C. Synthesis and luminescence properties of novel ferrocene–naphthalimides dyads. *J. Organomet. Chem.* **2002**, *645*, 168-175.
(59) Guldi, D. M.; Maggini, M.; Scorrano, G.; Prato, M. Intramolecular Electron Transfer in Fullerene/Ferrocene Based Donor−Bridge−Acceptor Dyads. *J. Am. Chem. Soc.* **1997**, *119*, 974-980.
(60) Martínez, R.; Ratera, I.; Tárraga, A.; Molina, P.; Veciana, J. A simple and robust reversible redox–fluorescence molecular switch based on a 1,4-disubstituted azine with ferrocene and pyrene units. *Chem. Commun.* **2006**, 3809-3811.
(61) Karmakar, M.; Bhatta, S. R.; Giri, S.; Thakur, A. Oxidation-Induced Differentially Selective Turn-On Fluorescence via Photoinduced Electron Transfer Based on a Ferrocene-Appended Coumarin–Quinoline Platform: Application in Cascaded Molecular Logic. *Inorg. Chem.* **2020**, *59*, 4493-4507.
(62) Wang, Z.; Chen, K.; Tian, H. Intramolecular Fluorescence Quenching in Ferrocene-Naphthalimide Dyads. *Chem. Lett.* **2003**, *28*, 423-424.
(63) Das, S.; Indurthi, H. K.; Asati, P.; Saha, P.; Sharma, D. K. Benzothiazole based fluorescent probes for the detection of biomolecules, physiological conditions, and ions responsible for diseases. *Dyes Pigm.* **2022**, *199*, 110074.
(64) Yan, F.; Sun, J.; Zang, Y.; Sun, Z.; Zhang, H.; Wang, X. Benzothiazole applications as fluorescent probes for analyte detection. *J. Iran. Chem. Soc.* **2020**, *17*, 3179-3203.

Epilogue

Final Conclusions

The overarching aim of this thesis was to create novel chiroptical switches through the targeted design of stimuli-responsive chiral molecules and MOFs. Reflecting on the results of the previous chapters, it is clear this was successfully achieved in chiral molecular systems, while challenges remain to be overcome in the domain of chiral MOFs. Nevertheless, the insight gained through this research has enabled promising future directions to be proposed in each chapter.

In Chapter 3, the redox-active 1,1′-binaphthalene derivatives, (*S*)-BNI and (*R*)-BNI were shown to undergo redox-modulated chiroptical switching in response to successive cycles of reduction and oxidation. These switches exhibited excellent sensitivity in both UV and visible wavelengths, allowing unambiguous determination of the dominant redox species present. Furthermore, (*S*)-BNI and (*R*)-BNI displayed good reversibility, with only minimal loss of intensity after 10 cycles. While nonemissive in solution, spin-coated thin films of (*S*)-BNI and (*R*)-BNI were found to exhibit aggregation-induced emission. CPL measurements on these films showed that (*S*)-BNI and (*R*)-BNI had different CPL responses, however the pure CPL signals could not be differentiated from other effects such as chiral scattering. (*S*)-BNI and (*R*)-BNI displayed clear MCD signals, indicating that MCD would likely be able to function as a highly sensitive chiroptical readout in response to redox cycling.

In Chapter 4, dual-responsive chiroptical switching was successfully achieved in an enantiomeric pair of ferrocene amino acid bioconjugates, L-Fc(MeLeu)$_2$ and D-Fc(MeLeu)$_2$ using temperature and electric potential as stimuli. In response to temperature, a linear amplification of the chiroptical response was observed. In response to oxidation, a combined amplification and peak shift of the chiroptical response was observed in the visible range, while in the UV region the chiroptical response was largely diminished. Interestingly, the electrochemical reversibility was found to be much better at lower concentrations, likely due to the inability of the SEC cell to sustain adequate current densities for charge balance. This result emphasises how SEC cell design and sample concentration play a major role in the

performance of redox-modulated chiroptical switches. The magneto-optic properties of L-Fc(MeLeu)$_2$ and D-Fc(MeLeu)$_2$ were explored through MCD. Once again, MCD could serve as a valuable chiroptical readout during electrochemical switching, especially if combined with variable temperature measurements.

In Chapter 5, the chiral ligand H_3CBA was used to create a series of lanthanide MOFs, La-1–Nd-1, which were synthesised and structurally characterised. Unfortunately, they were found to be achiral due to *in situ* racemisation of the ligand during solvothermal synthesis. When other lanthanides were used, a different MOF topology was formed, however this was unable to be structurally characterised due to the poor crystallinity of the resulting material. Efforts to prevent racemisation through room-temperature diffusion syntheses yielded a new phase, La-3, however if it is chiral it only has a weak chiroptical response. Finally, a chiral MOF, Cd-1, was successfully synthesised using a different chiral ligand, H_2CPA. Overall, these results underscore the unpredictability inherent to MOF chemistry and the challenge of obtaining highly crystalline, chiral frameworks.

Outlook and Perspective

Chiroptical switching lies at the intersection of structural chirality, chiroptics, and stimuli-responsive materials. As such, chiroptical switching represents an exciting launchpad from which to explore the properties and dynamics of complex systems ranging from the molecular scale to extended materials. However, beyond such fundamental studies – which are nonetheless valuable in their own right – a bigger picture view of chiroptical switching necessarily considers their applied uses. Here, the choice of stimuli is of great importance. Those that can be easily and rapidly switched, such as electric potential, temperature, magnetic field, and light are more broadly useful, while less convenient stimuli such as pH, mechanical grinding, or solvent may be more suited to niche uses.

In the field of chiroptical switching, CD has been – and still is – the dominate choice of chiroptical readout.[1-3] In many cases, CD is well-suited to its role as a chiroptical readout, however, the ubiquity of CD has perhaps overshadowed the development of chiroptical switches optimised for other chiroptical readouts. For example, magneto-optic techniques such as MCD and MChD are comparatively underutilised readouts for chiroptical switches. An obvious use case for such techniques is in temperature-modulated switching of magnetic materials between magnetically ordered and disordered states. However, chiroptical switching could also be achieved using magnetic field as a stimulus by exploiting a key feature of both

MCD and MChD: that reversing the applied magnetic field direction results in a signal inversion, one of the most favoured types of chiroptical response since it inherently provides good sensitivity. This inversion of the chiroptical response occurs at all temperatures (unlike some magnetic materials with very low or very high Curie temperatures),[4, 5] allowing the chiroptical switch to operate under ambient conditions. Furthermore, magnetic fields can be alternated rapidly (> 1 MHz),[6] enabling the fast switching needed for optoelectronic applications. Magnetic field is also a non-destructive stimulus, therefore switching should be possible for many cycles without loss of reversibility.

Finally, it is worth noting that chiral molecules and materials also have uses in other research areas. For example, all chiral molecules and materials are inherently noncentrosymmetric, meaning they are also candidates for nonlinear optics (NLO).[7-9] This allows them to act as media to facilitate photon-photon interactions such as second-harmonic generation (SHG) and sum-frequency generation (SFG).[7-9] Photon-photon interactions are the basis for ultrafast all-optical switching, in which logic gates are constructed by using one optical signal (the input signal) to control another optical signal (the output signal).[10] A breakthrough in this area has the potential to revolutionise the telecommunications industry through the development of new technologies such as all-optical devices, light-mediated telecommunications, and optical computing.[10, 11] Stimuli-responsive materials with switchable NLO properties are also of great interest for such applications. Therefore, many of the concepts explained in this thesis would be directly applicable for research into materials for switchable NLO.

References

(1) Canary, J. W.; Mortezaei, S.; Liang, J. Transition metal-based chiroptical switches for nanoscale electronics and sensors. *Coord. Chem. Rev.* **2010**, *254*, 2249-2266.

(2) Feringa, B. L.; van Delden, R. A.; Koumura, N.; Geertsema, E. M. Chiroptical Molecular Switches. *Chem. Rev.* **2000**, *100*, 1789-1816.

(3) Zhang, L.; Wang, H.-X.; Li, S.; Liu, M. Supramolecular Chiroptical Switches. *Chem. Soc. Rev.* **2020**, *49*, 9095-9120.

(4) Huebener, R. P. Magnetism: Order Among the Elementary Magnets. In *Conductors, Semiconductors, Superconductors: An Introduction to Solid State Physics*, Springer International Publishing, 2016; pp 163-181.

(5) Zhang, Y.; Guo, D.; Geng, S.; Lu, X.; Wilde, G. Structure, magnetic and cryogenic magneto-caloric properties in intermetallic gallium compounds RE_2Co_2Ga (RE = Dy, Ho, Er, and Tm). *J. Appl. Phys.* **2018**, *124*.

(6) Garaio, E.; Collantes, J. M.; Plazaola, F.; Garcia, J. A.; Castellanos-Rubio, I. A multifrequency eletromagnetic applicator with an integrated AC magnetometer for magnetic hyperthermia experiments. *Meas. Sci. Technol.* **2014**, *25*, 115702.

(7) Di Bella, S. Second-order nonlinear optical properties of transition metal complexes. *Chem. Soc. Rev.* **2001**, *30*, 355-366.

(8) Shen, Y. R. Surface properties probed by second-harmonic and sum-frequency generation. *Nature* **1989**, *337*, 519-525.

(9) Suresh, S.; Ramanand, A.; Jayaraman, D.; Mani, P. Review On Theoretical Aspect of Nonlinear Optics. *Rev. Adv. Mater. Sci.* **2012**, *30*, 175-183.

(10) Chai, Z.; Hu, X.; Wang, F.; Niu, X.; Xie, J.; Gong, Q. Ultrafast All-Optical Switching. *Adv. Opt. Mater.* **2017**, *5*, 1600665.

(11) Minzioni, P.; Lacava, C.; Tanabe, T.; Dong, J. J.; Hu, X. Y.; Csaba, G.; Porod, W.; Singh, G.; Willner, A. E.; Almaiman, A.; et al. Roadmap on all-optical processing. *J. Opt.* **2019**, *21*, 063001.

Appendices

Appendix A: Supplementary Information for Chapter 3

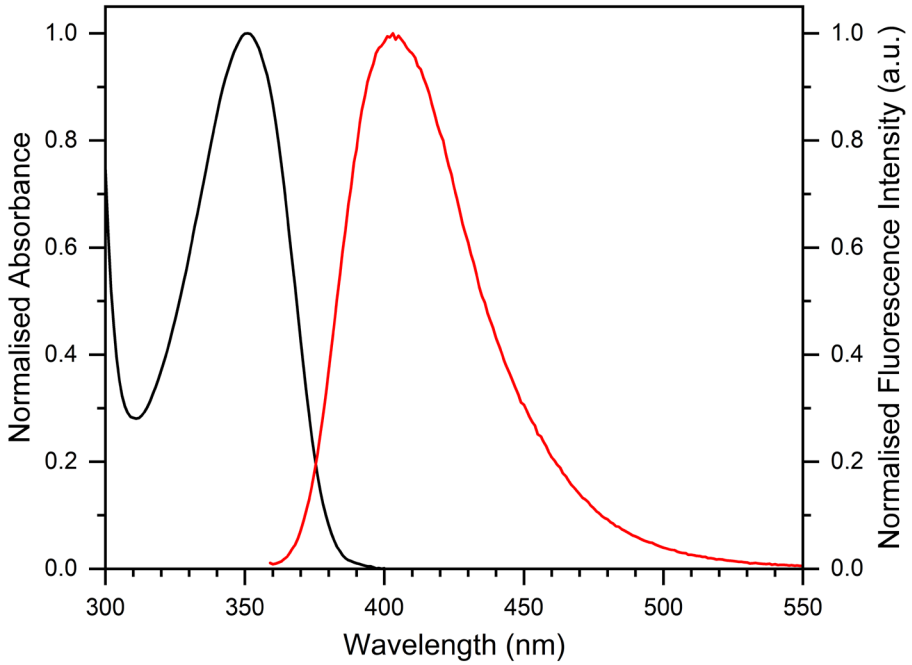

Figure A1. Normalised absorbance (black) and normalised fluorescence emission intensity (red) of (*R*)-BINAM in MeCN. Excitation wavelength was 351 nm. Spectra were acquired at 120 μM for absorbance and 6 μM for fluorescence.

Table A1. Crystal data and structure refinement for (*S*)-BNI.

CCDC number	2386163
Empirical formula	$C_{44}H_{24}N_2O_4$
Formula weight	644.65
Temperature (K)	150(2)
Crystal system	monoclinic
Space group	$P2_1$
a (Å)	9.6007(2)
b (Å)	15.3777(3)
c (Å)	11.5145(3)
β (°)	114.619(3)
V (Å^3)	1545.43(7)
Z (Z')	2 (1)
ρ_{calc} (g cm^{-3})	1.385
μ (mm^{-1})	0.716
Absorption correction	Gaussian
F(000)	668
Crystal size (mm^3)	0.098 × 0.031 × 0.026
Radiation	Cu-Kα (λ = 1.54184 Å)
2Θ range for data collection (°)	8.446 to 147.684
Index ranges	$-11 \leq h \leq 11$, $-18 \leq k \leq 16$, $-13 \leq l \leq 14$
Reflections collected	35717
Independent reflections	5212 [R_{int} = 0.0414, R_{sigma} = 0.0380]
Data/restraints/parameters	5212/1/451
Goodness-of-fit on F^2	1.097
Final R indexes [$I \geq 2\sigma(I)$]	R_1 = 0.0417, wR_2 = 0.1014
Final R indexes [all data]	R_1 = 0.0639, wR_2 = 0.1217
Largest diff. peak/hole (e Å^{-3})	0.21/−0.27
Flack parameter	0.02(11)

Table A2. Crystal data and structure refinement for (*R*)-BNI**.**

CCDC number	2386164
Empirical formula	$C_{51}H_{32}N_2O_4$
Formula weight	736.78
Temperature (K)	150(2)
Crystal system	monoclinic
Space group	*C*2
a (Å)	20.9775(6)
b (Å)	9.4690(4)
c (Å)	18.4363(6)
β (°)	92.098(3)
V (Å^3)	3659.7(2)
Z (*Z*')	4 (1)
ρ_{calc} (g cm^{-3})	1.337
μ (mm^{-1})	0.674
Absorption correction	Gaussian
F(000)	1536
Crystal size (mm^3)	0.197 × 0.021 × 0.015
Radiation	Cu-Kα (λ = 1.54184 Å)
2Θ range for data collection (°)	4.796 to 124.766
Index ranges	$-24 \le h \le 24$, $-10 \le k \le 9$, $-21 \le l \le 21$
Reflections collected	18610
Independent reflections	5466 [R_{int} = 0.0685, R_{sigma} = 0.0653]
Data/restraints/parameters	5466/91/556
Goodness-of-fit on F^2	0.976
Final *R* indexes [$I \ge 2\sigma(I)$]	R_1 = 0.0543, wR_2 = 0.1352
Final *R* indexes [all data]	R_1 = 0.0744, wR_2 = 0.1531
Largest diff. peak/hole (e Å^{-3})	0.20/−0.26
Flack parameter	−0.1(4)

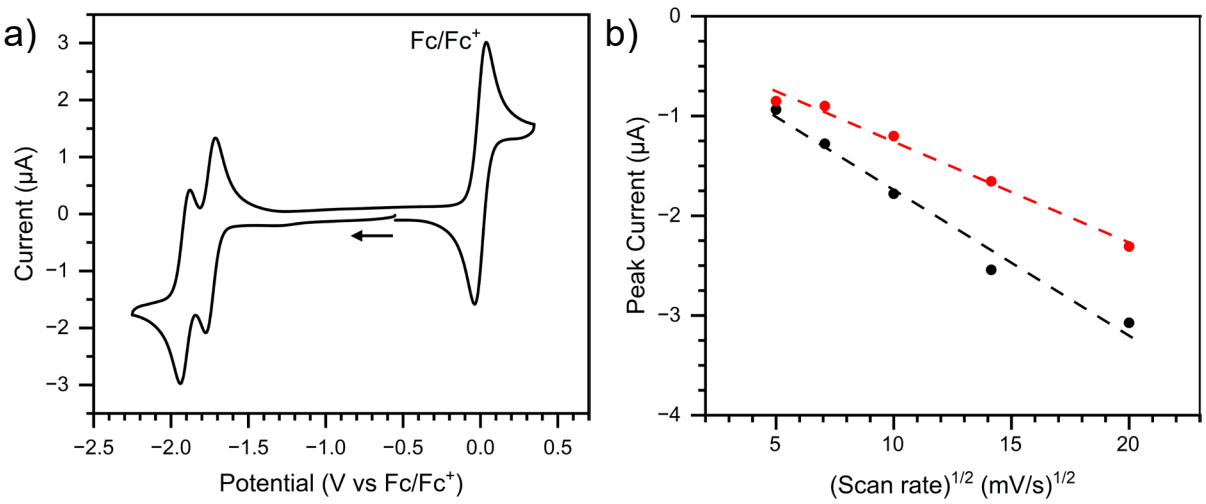

Figure A2. (a) Cyclic voltammogram of (*R*)-BNI in MeCN with 0.1 M $[(n\text{-}C_4H_9)_4N]PF_6$ supporting electrolyte. The arrow shows the direction of the potential sweep. Scan rate = 100 mV/s and the potentials are referenced to Fc/Fc^+ at 0 V. (b) Linear fits of cathodic peak current vs the square root of scan rate for (*R*)-BNI in MeCN with 0.1 M $[(n\text{-}C_4H_9)_4N]PF_6$ supporting electrolyte. Black = first reduction process, red = second reduction process. The first and second reductions have R^2 values of 0.9796 and 0.9873, respectively.

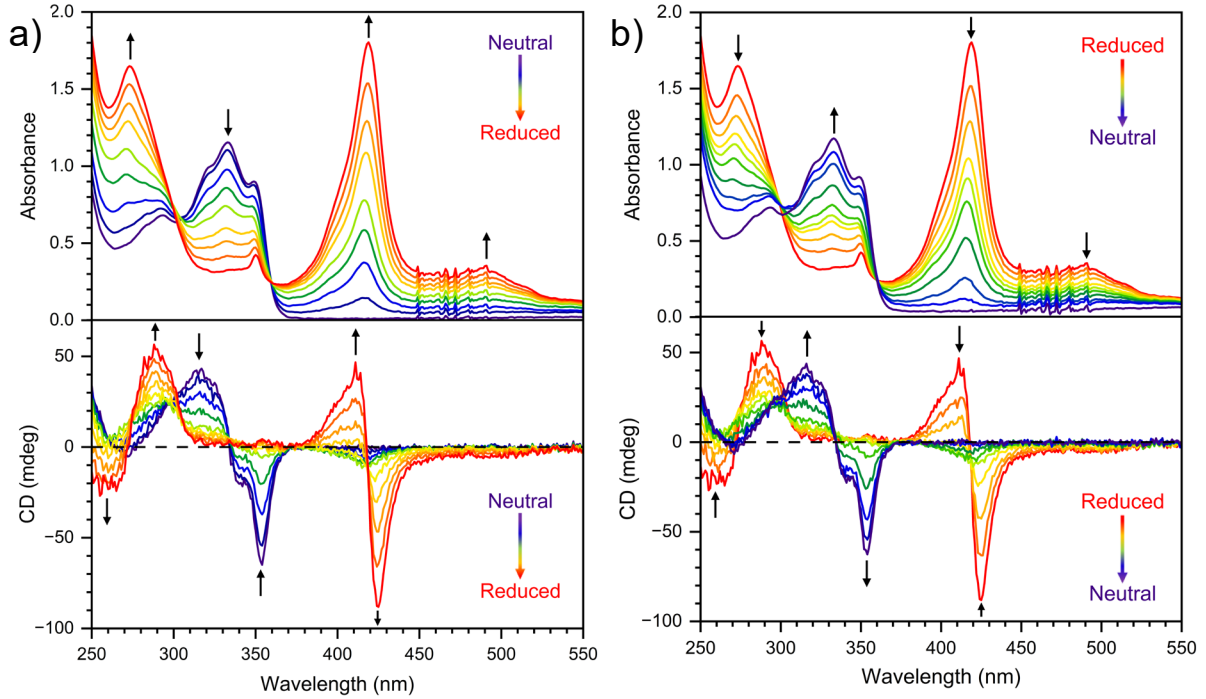

Figure A3. (a) UV-vis (top) and CD (bottom) spectra of (*R*)-BNI during reduction from the neutral to the dianion state over a 70 min time interval. (b) UV-vis (top) and CD (bottom) spectra of (*R*)-BNI during subsequent oxidation from the dianion to the neutral state over an 85 min interval. The concentration of (*R*)-BNI was approximately 0.68 mM. Spectra were acquired in MeCN with 0.25 M $[(n\text{-}C_4H_9)_4N]PF_6$ as supporting electrolyte.

Table A3. Δε of (*R*)-BNI and (*R*)-BNI^{2-} and corresponding |ΔΔε| at selected wavelengths as calculated from CD SEC measurements.

Wavelength (nm)	(*R*)-BNI Δε ($M^{-}1cm^{-}1$)	(*R*)-BNI^{2-} Δε ($M^{-1}cm^{-1}$)	|ΔΔε| ($M^{-1}cm^{-1}$)
261	3.2	−15.0	18.2
288	7.9	37.0	29.1
318	27.3	1.4	25.9
354	−42.5	2.9	45.4
411	0	30.6	30.6
425	0	−57.7	−57.7

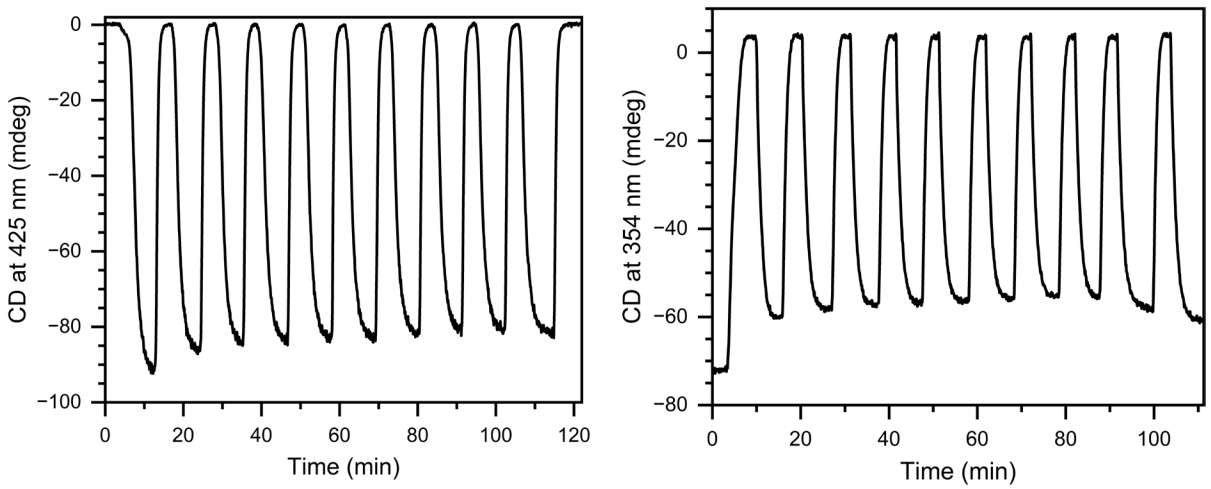

Figure A4. CD response of (*R*)-BNI at 425 nm (left) and 354 nm (right) during 10 consecutive reduction and oxidation cycles. The concentration of (*R*)-BNI was approximately 0.75 mM. Spectra were acquired in MeCN with 0.25 M $[(n\text{-}C_4H_9)_4N]PF_6$ as supporting electrolyte.

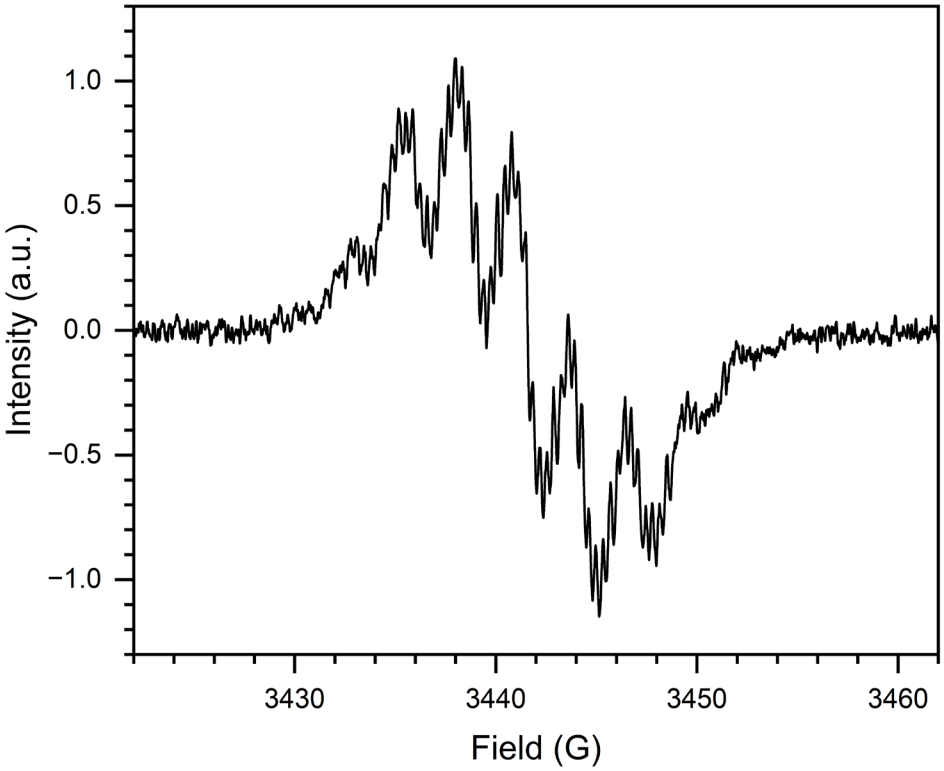

Figure A5. EPR spectrum of (*R*)-BNI^{2-} generated by reduction of a 2.0 mM solution of (*R*)-BNI in DMF with 0.1 M [(n-C_4H_9)$_4$N]PF_6 as supporting electrolyte. Instrument parameters: microwave frequency = 9.648 GHz; modulation amplitude = 50 mG; modulation frequency = 100 kHz; microwave power = 10 mW.

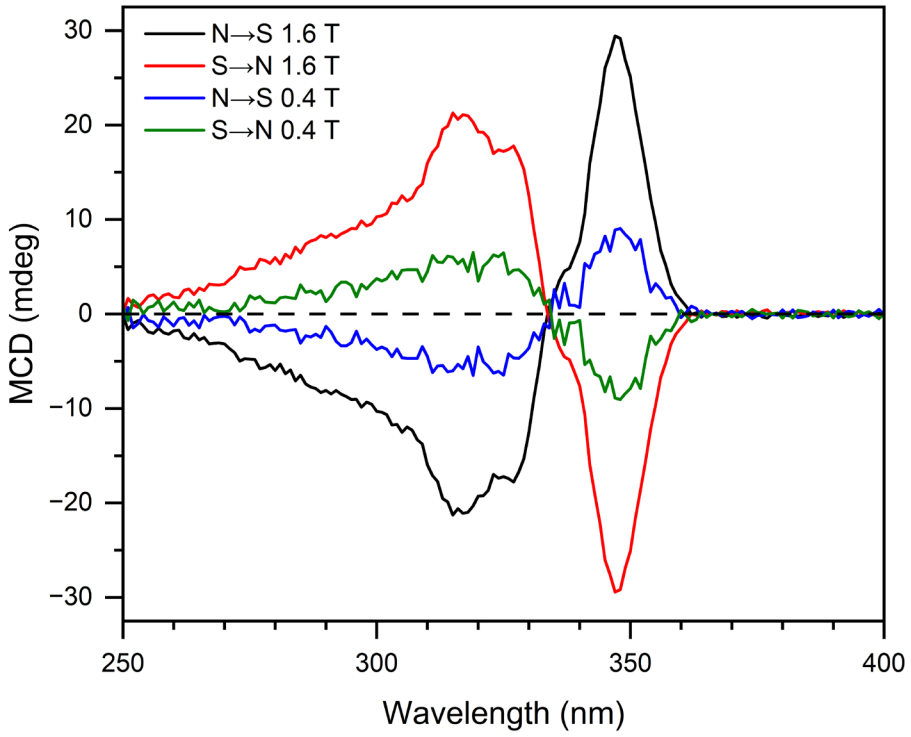

Figure A6. MCD spectra of (*R*)-BNI in MeCN with different magnetic field strengths and orientations. Sample concentration was 110 μM.

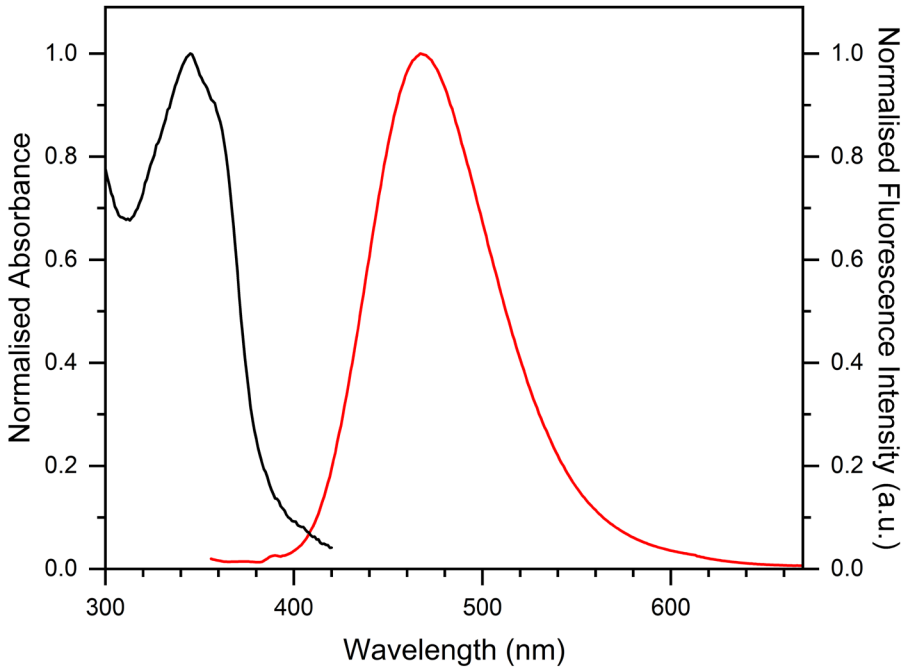

Figure A7. Normalised absorbance (black) and normalised fluorescence emission intensity (red) of (*R*)-BNI thin films. Excitation wavelength = 344 nm.

Appendix B: Supplementary Information for Chapter 4

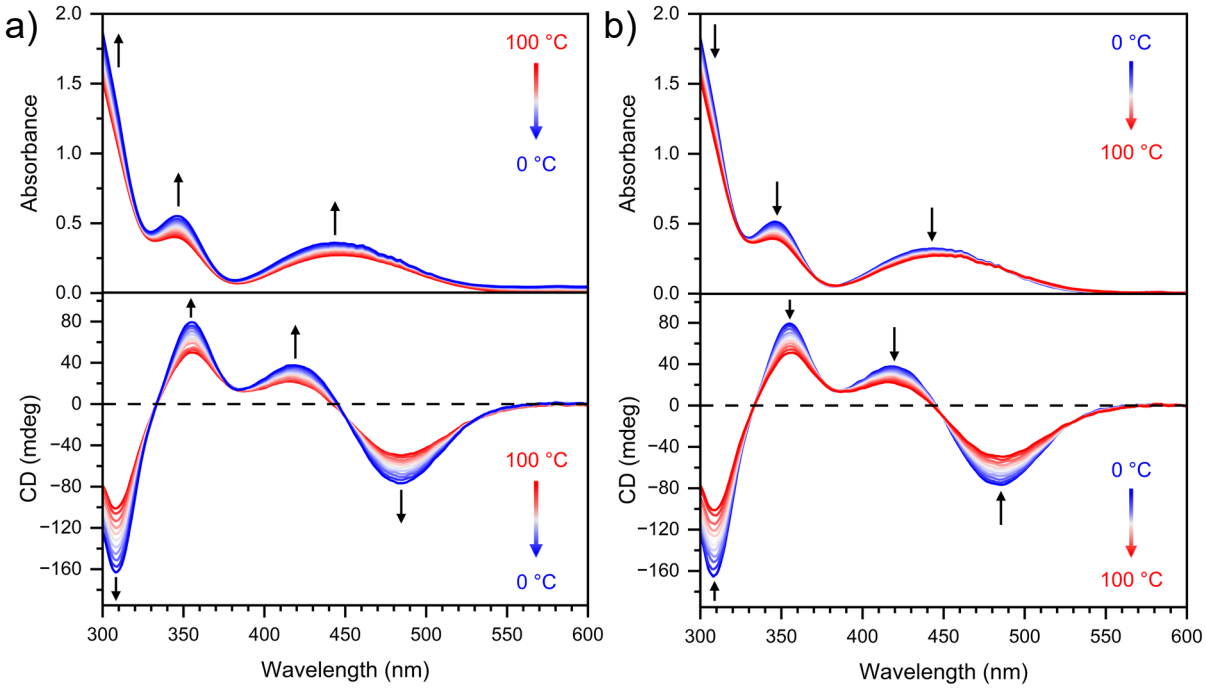

Figure B1. Variable temperature UV-vis (top) and CD (bottom) spectra of D-Fc(MeLeu)$_2$ during cooling from 100 °C to 0 °C (a), and heating from 0 °C to 100 °C (b). Spectra were acquired at 10 °C intervals. Sample concentration was 1.36 mM in toluene. Temperature ramp rate = 0.75 °C/min.

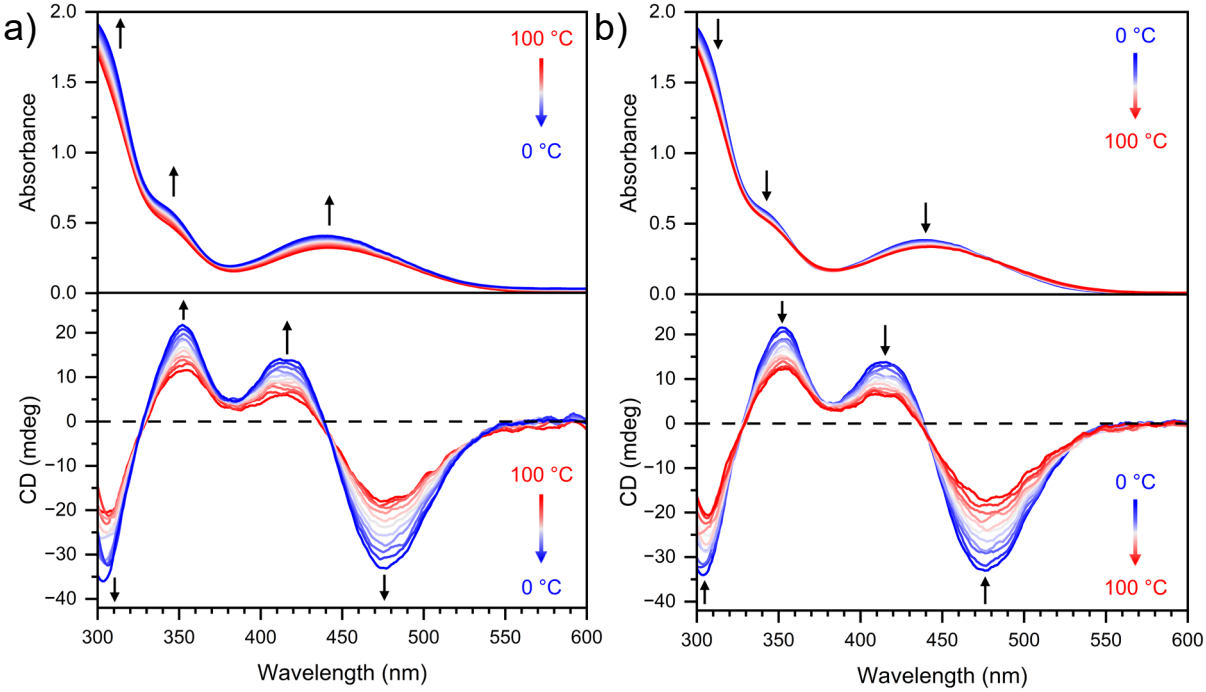

Figure B2. Variable temperature UV-vis (top) and CD (bottom) spectra of D-Fc(MeLeu)$_2$ during cooling from 100 °C to 0 °C (a), and heating from 0 °C to 100 °C (b). Spectra were acquired at 10 °C intervals. Sample concentration was 1.36 mM in DMF. Temperature ramp rate = 0.75 °C/min.

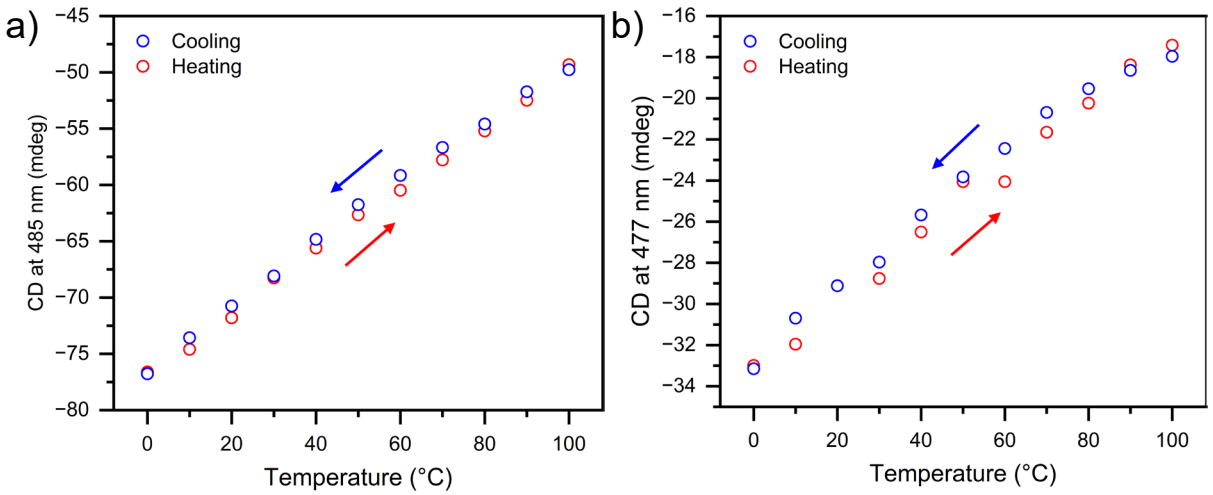

Figure B3. Linear trend between CD and temperature at specified wavelengths for D-Fc(MeLeu)$_2$ in toluene (a) and DMF (b). Cooling and heating are represented as blue and red open circles, respectively. Sample concentrations were 1.36 mM. Temperature ramp rate = 0.75 °C/min.

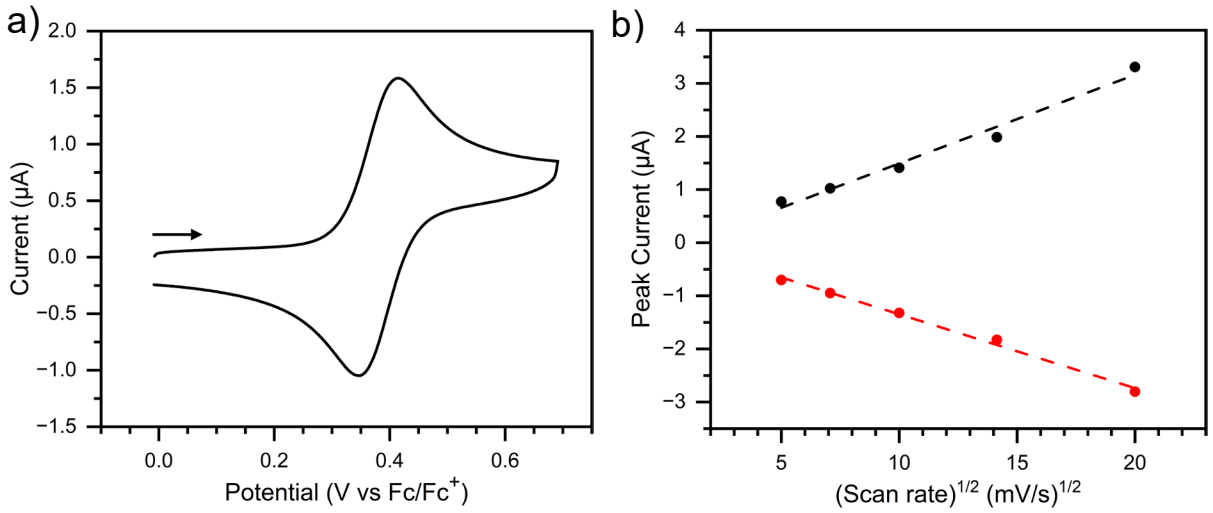

Figure B4. (a) Cyclic voltammogram of D-Fc(MeLeu)$_2$ in MeCN with 0.1 M [(n-C_4H_9)$_4$N]PF_6 supporting electrolyte. The arrow shows the direction of the potential sweep. Scan rate = 100 mV/s and the potentials are referenced to Fc/Fc^+ at 0 V. (b) Linear fits of anodic (black) and cathodic (red) peak current vs the square root of scan rate for D-Fc(MeLeu)$_2$ in MeCN with 0.1 M [(n-C_4H_9)$_4$N]PF_6 supporting electrolyte. The anodic and cathodic linear fits have R^2 values of 0.9801 and 0.9939, respectively.

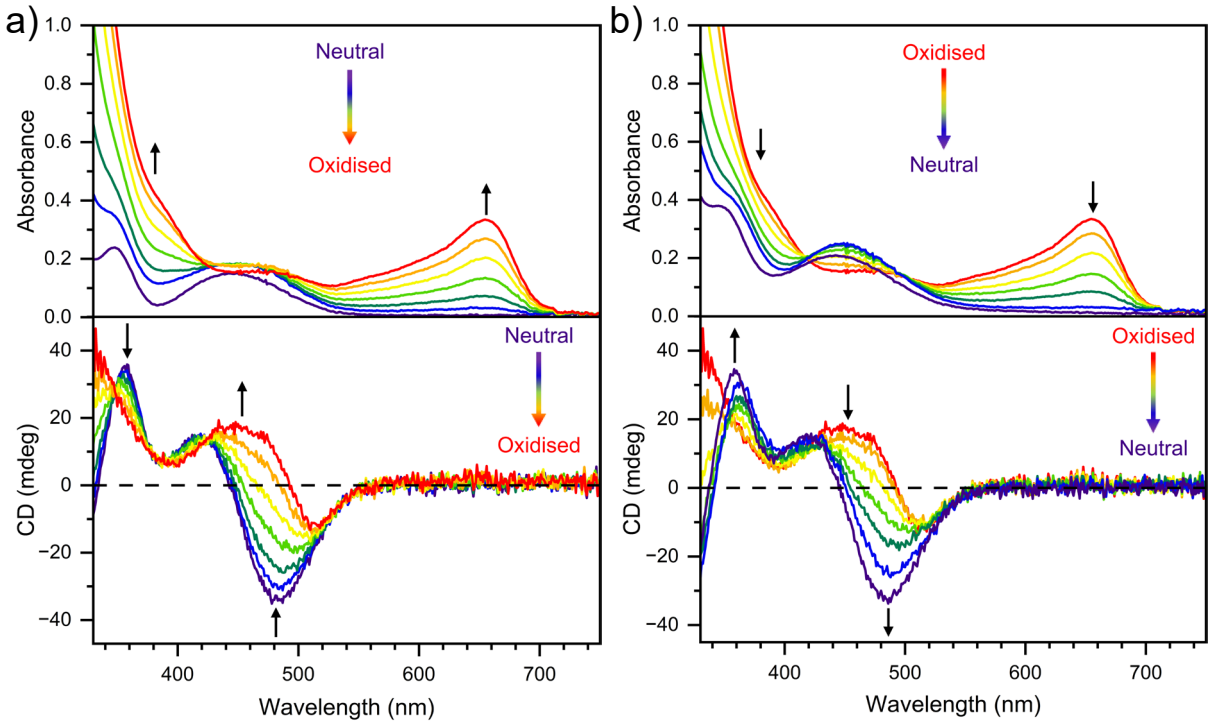

Figure B5. (a) UV-vis (top) and CD (bottom) spectra of D-Fc(MeLeu)$_2$ during oxidation to the ferrocenium species over a 95 min time interval. (b) UV-vis (top) and CD (bottom) spectra of D-Fc(MeLeu)$_2$ during subsequent reduction from the ferrocenium to neutral state over a 135 min time interval. The concentration of D-Fc(MeLeu)$_2$ was approximately 10 mM. Spectra were acquired in DCM with 0.25 M [(n-C_4H_9)$_4$N]PF_6 as supporting electrolyte.

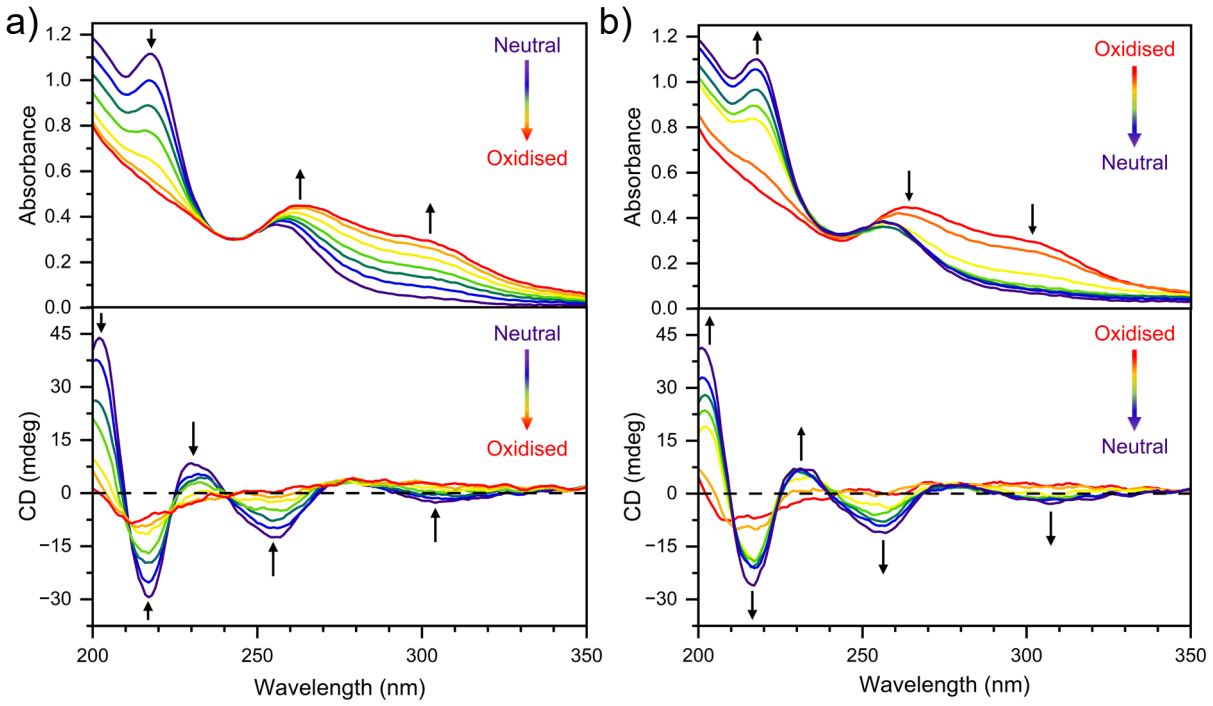

Figure B6. (a) UV-vis (top) and CD (bottom) spectra of D-Fc(MeLeu)$_2$ during oxidation to the ferrocenium species over a 30 min time interval. (b) UV-vis (top) and CD (bottom) spectra of D-Fc(MeLeu)$_2$ during subsequent reduction from the ferrocenium to neutral state over a 75 min time

interval. The concentration of D-Fc(MeLeu)$_2$ was approximately 0.6 mM. Spectra were acquired in MeCN with 0.25 M [(n-C_4H_9)$_4$N]PF_6 as supporting electrolyte.

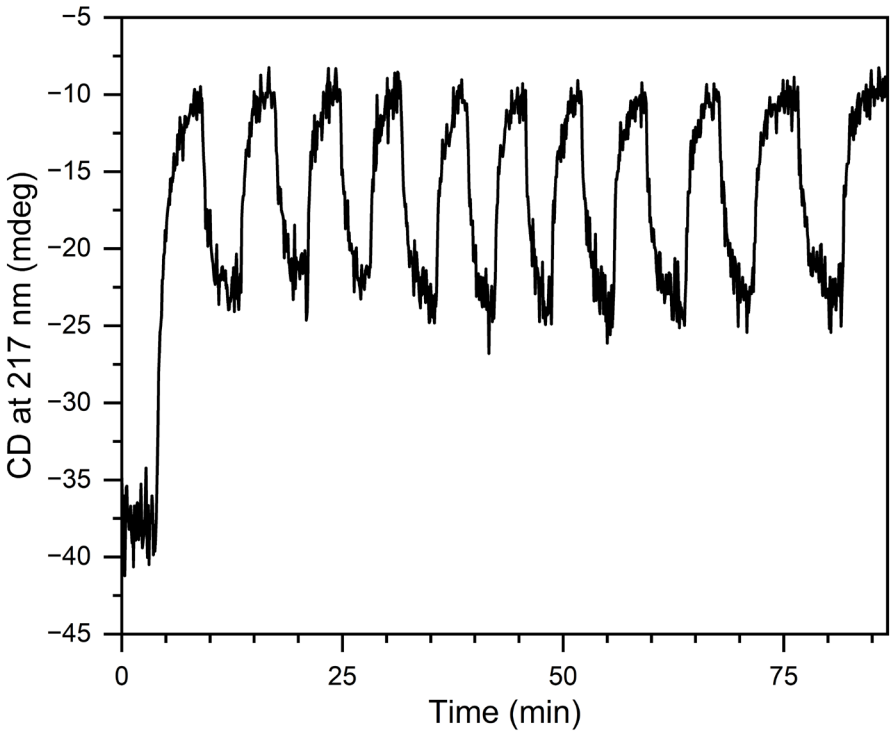

Figure B7. CD response of D-Fc(MeLeu)$_2$ at 217 nm during ten consecutive oxidation and reduction cycles. The concentration of D-Fc(MeLeu)$_2$ was approximately 0.7 mM. Data was acquired in MeCN with 0.25 M [(n-C_4H_9)$_4$N]PF_6 as supporting electrolyte.

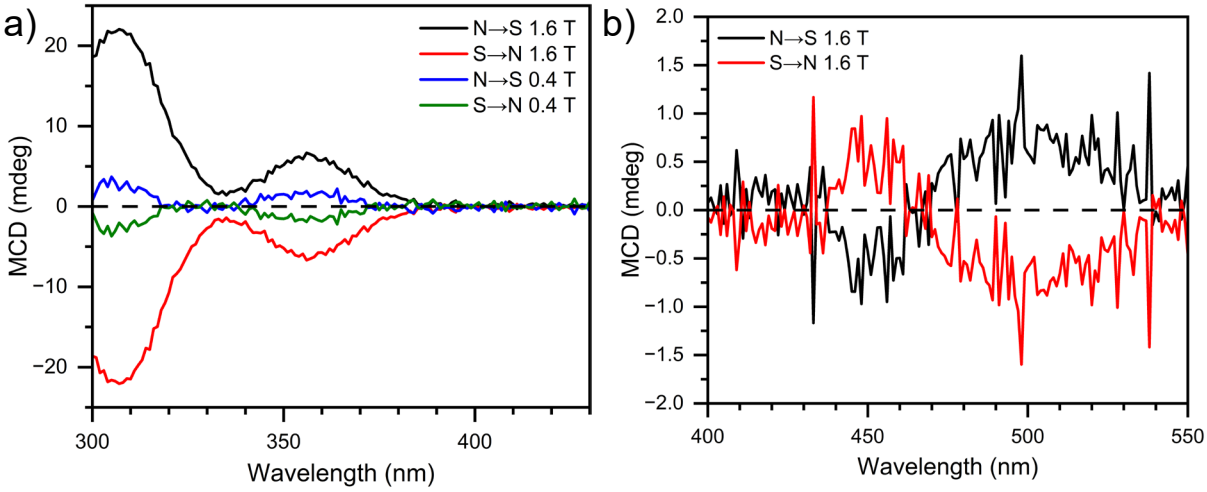

Figure B8. (a) MCD spectra of D-Fc(MeLeu)$_2$ in toluene with different magnetic field strengths and orientations. (b) The weak MCD peaks in the visible range. Sample concentration was 2.5 mM.

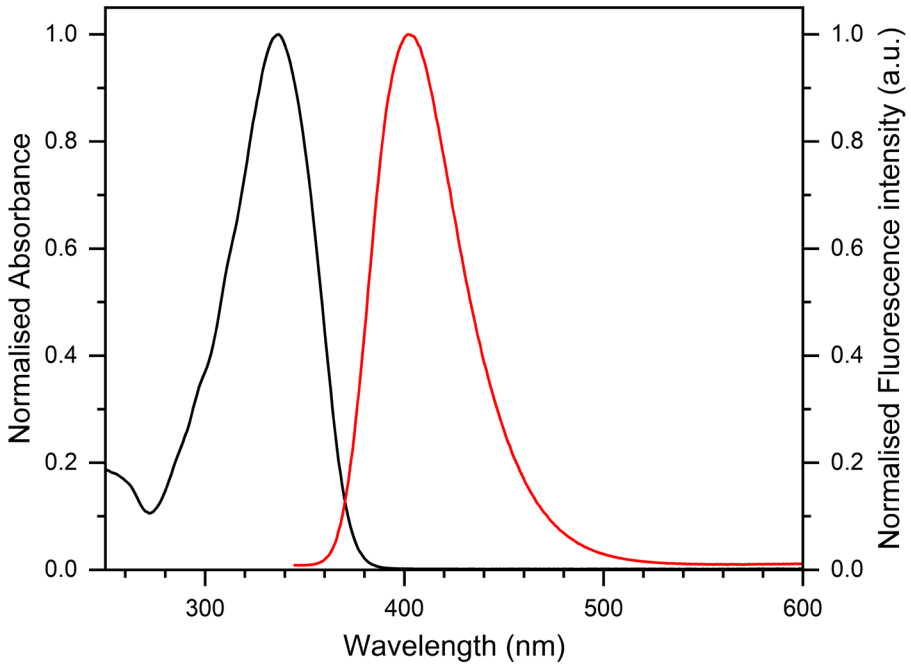

Figure B9. Normalised absorbance (black) and normalised fluorescence emission intensity (red) of 2-(4-aminophenyl)benzothiazole in MeCN. Spectra were acquired at 40 μM for absorbance and 2 μM for fluorescence. Excitation wavelength = 337 nm.

Appendix C: Supplementary Information for Chapter 5

Table C1. Crystal data and structure refinement for La-1.

Empirical formula	$C_{12}H_{12}LaNO_9$
Formula weight	453.14
Temperature (K)	100.15
Crystal system	triclinic
Space group	*P*-1
a (Å)	8.5061(5)
b (Å)	9.0168(5)
c (Å)	11.9108(6)
α (°)	80.884(4)
β (°)	75.074(5)
γ (°)	68.722(5)
V (Å^3)	820.39(8)
Z (*Z*')	2
ρ_{calc} (g cm^{-3})	1.834
μ (mm^{-1})	20.550
Absorption correction	Gaussian
F(000)	440.0
Crystal size (mm^3)	0.11 × 0.04 × 0.03
Radiation	Cu-Kα (λ = 1.54184)
2Θ range for data collection (°)	10.556 to 144.904
Index ranges	$-10 \leq h \leq 9$, $-11 \leq k \leq 11$, $-14 \leq l \leq 14$
Reflections collected	24388
Independent reflections	3111 [R_{int} = 0.0927, R_{sigma} = 0.0413]
Data/restraints/parameters	3111/0/210
Goodness-of-fit on F^2	1.032
Final *R* indexes [$I \geq 2\sigma(I)$]	R_1 = 0.0801, wR_2 = 0.2132
Final *R* indexes [all data]	R_1 = 0.0869, wR_2 = 0.2190
Largest diff. peak/hole (e Å^{-3})	4.19/-1.90

Table C2. Crystal data and structure refinement for Ce-1

Empirical formula	$C_{12}H_{12}CeNO_9$
Formula weight	454.35
Temperature (K)	100.15
Crystal system	triclinic
Space group	*P*-1
a (Å)	8.4658(2)
b (Å)	8.9887(2)
c (Å)	11.8536(3)
α (°)	81.300(2)
β (°)	75.758(2)
γ (°)	68.529(2)
V (Å^3)	811.75(4)
Z (*Z*')	2
ρ_{calc} (g cm^{-3})	1.859
μ (mm^{-1})	22.099
Absorption correction	Gaussian
F(000)	442.0
Crystal size (mm^3)	0.1 × 0.06 × 0.02
Radiation	Cu-Kα (λ = 1.54184)
2Θ range for data collection (°)	7.712 to 144.462
Index ranges	$-10 \leq h \leq 9$, $-11 \leq k \leq 10$, $-14 \leq l \leq 14$
Reflections collected	33558
Independent reflections	3101 [R_{int} = 0.0696, R_{sigma} = 0.0319]
Data/restraints/parameters	3101/0/210
Goodness-of-fit on F^2	1.073
Final *R* indexes [$I \geq 2\sigma(I)$]	R_1 = 0.0592, wR_2 = 0.1589
Final *R* indexes [all data]	R_1 = 0.0631, wR_2 = 0.1643
Largest diff. peak/hole (e Å^{-3})	3.50/-1.62

Table C3. Crystal data and structure refinement for Pr-1

Empirical formula	$C_{12}H_{12}PrNO_9$
Formula weight	455.14
Temperature (K)	150.15
Crystal system	triclinic
Space group	*P*-1
a (Å)	8.4694(3)
b (Å)	8.9831(3)
c (Å)	11.8763(3)
α (°)	82.338(2)
β (°)	76.178(2)
γ (°)	68.376(3)
V (Å^3)	814.62(5)
Z (*Z*')	2
ρ_{calc} (g cm^{-3})	1.856
μ (mm^{-1})	23.372
Absorption correction	Gaussian
F(000)	444.0
Crystal size (mm^3)	0.09 × 0.08 × 0.02
Radiation	Cu-Kα (λ = 1.54184)
2Θ range for data collection (°)	10.608 to 144.528
Index ranges	$-10 \le h \le 10$, $-10 \le k \le 11$, $-14 \le l \le 14$
Reflections collected	32185
Independent reflections	3110 [R_{int} = 0.1065, R_{sigma} = 0.0436]
Data/restraints/parameters	3110/0/209
Goodness-of-fit on F^2	1.037
Final *R* indexes [$I \ge 2\sigma(I)$]	R_1 = 0.0838, wR_2 = 0.2047
Final *R* indexes [all data]	R_1 = 0.0882, wR_2 = 0.2070
Largest diff. peak/hole (e Å^{-3})	3.88/-2.61

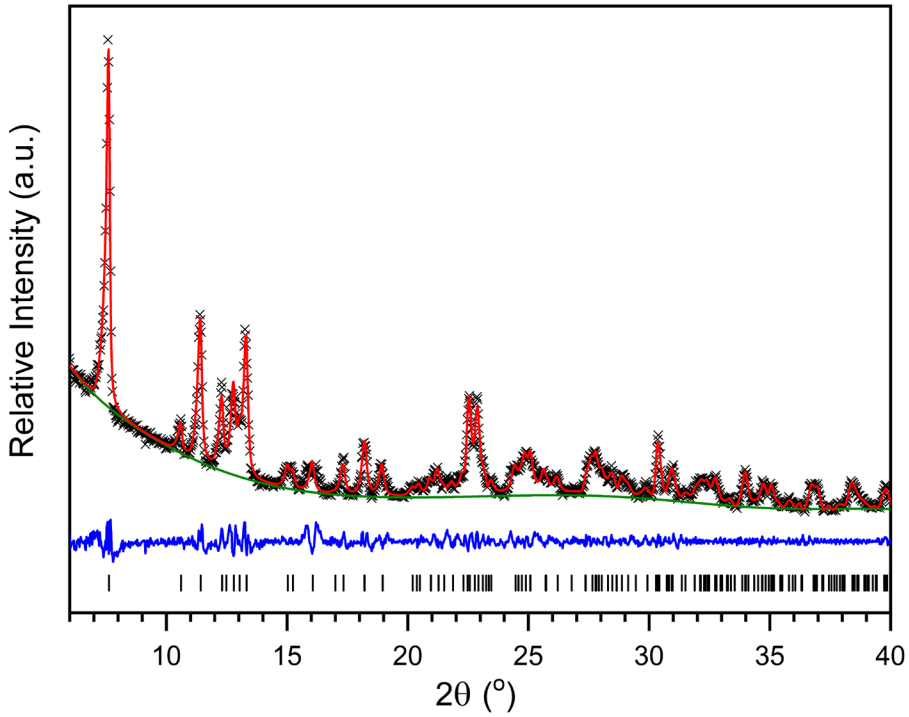

Figure C1. Pawley refinement of La-1 showing experimental (crosses) and calculated (red) diffraction patterns, background (green), difference (blue), and *hkl*s (vertical lines). Rw = 4.564.

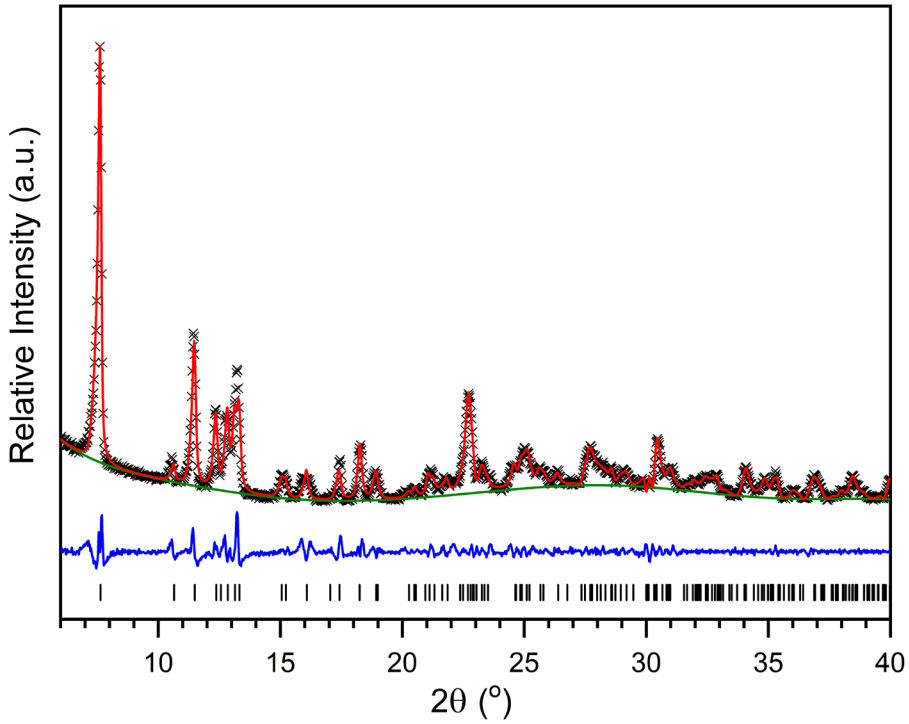

Figure C2. Pawley refinement of Ce-1 showing experimental (crosses) and calculated (red) diffraction patterns, background (green), difference (blue), and *hkl*s (vertical lines). Rw = 5.238.

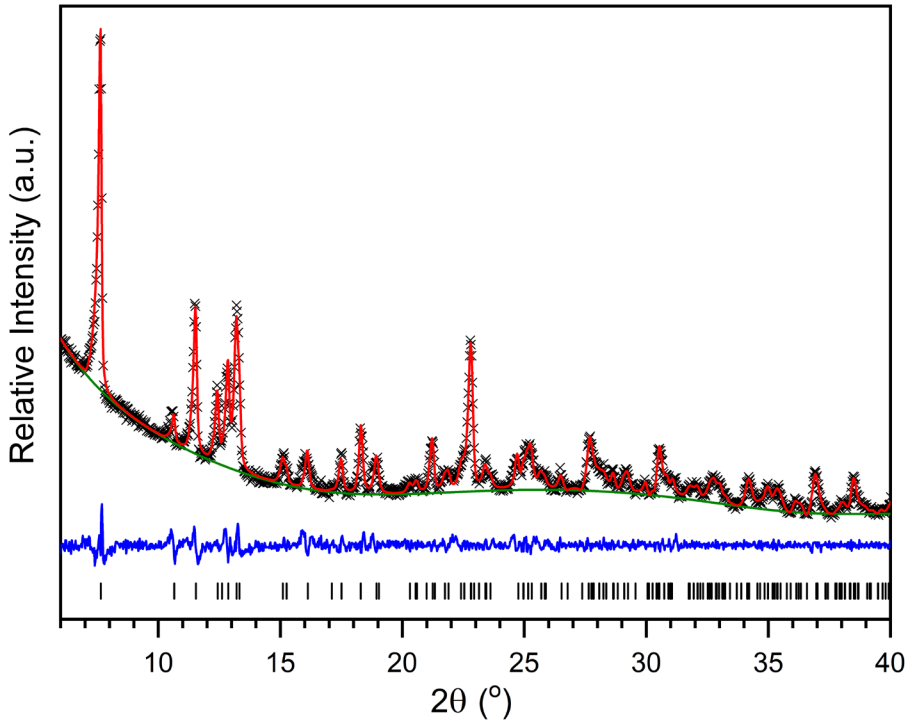

Figure C3. Pawley refinement of Pr-1 showing experimental (crosses) and calculated (red) diffraction patterns, background (green), difference (blue), and *hkl*s (vertical lines). Rw = 3.738.

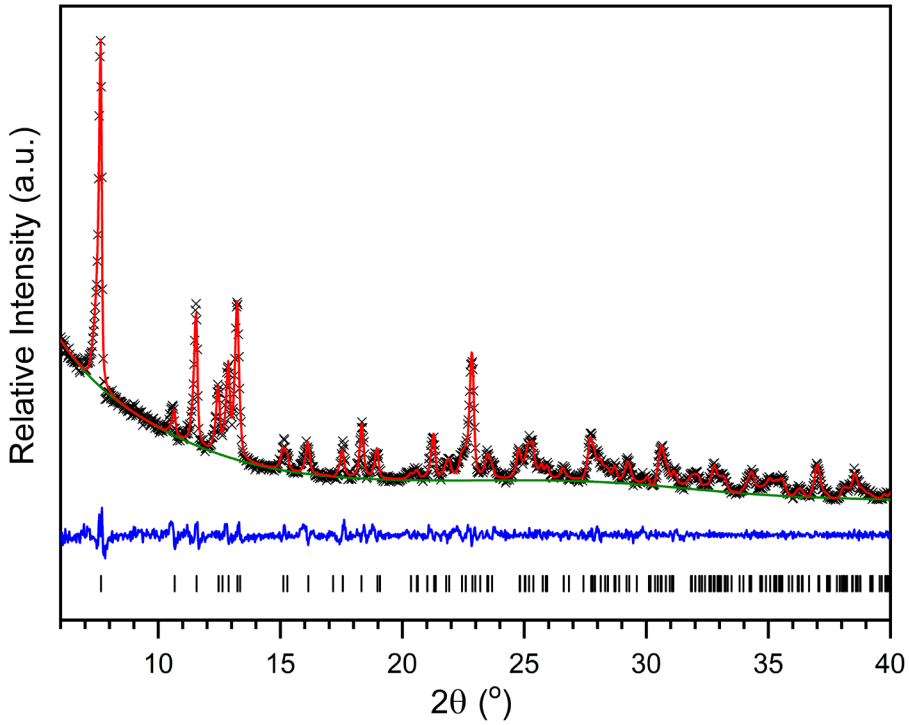

Figure C4. Pawley refinement of Nd-1 showing experimental (crosses) and calculated (red) diffraction patterns, background (green), difference (blue), and *hkl*s (vertical lines). Rw = 3.390.

Table C4. Unit cell parameters of La-1–Nd-1 determined by Pawley refinement on room temperature PXRD patterns.

Parameter	La-1	Ce-1	Pr-1	Nd-1
a (Å)	8.58029	8.5368	8.48448	8.45711
b (Å)	9.03677	9.01861	8.99946	8.97775
c (Å)	12.0196	12.04199	12.00068	11.96618
α (°)	82.484	82.821	82.998	83.03
β (°)	75.822	76.089	76.259	76.364
γ (°)	67.800	67.997	68.119	68.152
V (Å^3)	835.844	833.750	825.403	818.945
Rw	4.564	5.238	3.738	3.390